Measurement of the Mechanical Loss of Test Mass Materials for Advanced Gravitational Wave Detectors

Peter G Murray, M.Sci.

Department of Physics and Astronomy,
University of Glasgow

Presented as a thesis for the degree of Ph.D.
in the University of Glasgow, University Avenue,
Glasgow G12 8QQ

May 22, 2008

Contents

List of Figures

List of Tables

Acknowledgements

It took a while to produce, but I have finally completed my PhD thesis. This has been achieved not only through hard work on my part but also with a lot of help and support from many colleagues, family members and friends.

First of all I would like to thank my supervisors Jim Hough, Sheila Rowan and Geppo Cagnoli for all their support, encouragement and, probably most importantly patience over the last four years. A big thank you is also due to the members of the Institute for Gravitational Research and colleagues in the Department of Physics and Astronomy at the University of Glasgow for providing an environment that was pleasant to work (and not to work) in. I would like to thank STFC and the then UK research council PPARC for providing the funding required to carry out all the research presented in this thesis.

I would particularly like to thank Stuart Reid for all the many useful discussions about our research work and for all the technical advice (not just about building and over-clocking computers) he gave me throughout the time we spent working in the laboratory together. This thanks is due despite his semi-successful attempt to burn the laboratory down and buying himself a nice camera lens in Japan instead of one for me.

Thanks are also due to Eleanor Chalkley who had to put up not only with my music in the laboratory while we both worked but also occasionally with my singing and dancing. It did not happen, but I will work on the plans for a rave in 215. A thank you should also go to all the people I have worked with on many different projects in

the laboratory including Peter Sneddon, David Crooks, Alastair Heptonstall, Eoin Elliffe, Mariëlle van Veggel, Iain Martin and Alan Cumming. A special thanks needs to go to our group technicians Colin Craig and Stephen Craig for the number of parts and vacuum fittings they have manufactured for me, bolts they have unfastened after I have overtightened them and for holding up heavy pieces of cryostat while I fastened them in place.

Outwith the laboratory many colleagues have also been great help and provided much entertainment during coffee breaks, lunchtimes and outwith working hours. Thanks are due to: Jen Toher, the fussiest vegetarian I have ever met, Bob Taylor who was willing to host many social gatherings, John Veitch and Christian Killow who were willing to attend many social gatherings, Matt Pitkin for his entertaining rambles, Siong Heng for being a *respectable* academic and Johanna Bogenstahl, the craziest German I have ever met, who constantly prodded me to get on with my thesis. It has been a privilege to work with them and all the other group members.

Outside the University I would like to thank Paul Turner for the many years in the Osprey pretending to understand what I do, for getting me interested in photography and for only once locking us out of his car when Glencoe was at what felt like cryogenic temperatures. Thanks are due to John O'Brien and his colleagues at the Eastwood High School Physics Department, without them I would never have applied to do my undergraduate degree in Physics and Mathematics.

I want to specially thank Kirsty McKay for her love, encouragement, support and MATLAB knowledge while I finished off my thesis. She has been very patient with me over the last year, particulary with my culinary endeavours.

Finally, I would like to thank my parents, grand parents, Edmund and Helen my brother and sister for their endless support, financing the past twenty one years of my education and putting up with me continually disassembling and reassembling things at home from an early age. A particular thanks is due to my mum for reading through my thesis and checking my grammar and and misspelt words.

"Imagination is more important than knowledge..."

Albert Einstein

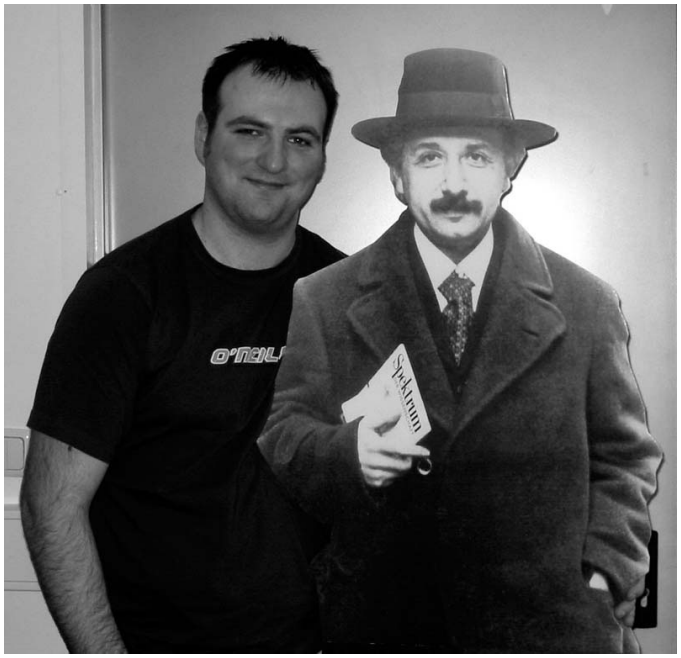

Figure 1: Peter Murray and Albert Einstein (cutout) at the GEO600 Detector.

Preface

This thesis is an account of research undertaken between September 2003 and September 2007 at the University of Glasgow contributing to the investigation of the mechanical loss of test mass materials for advanced gravitational wave detectors.

In Chapter One the nature of gravitational waves and the different sources which may produce them is discussed and also the differing ways in which they may be detected is introduced. It highlights the difficulties arising from various noise sources which must be overcome for gravitational waves to be detected. It provides an account of the gravitational wave detectors in operation today, details some proposed upgrades to them and describes new gravitational wave detectors which are planned.

In Chapter Two aspects of the theory of thermal noise are described to provide a background into the research presented in this thesis. It details the quantification of thermal noise and how it affects the detection of gravitational waves. Through understanding the processes which give rise to thermal noise, methods can be developed to minimise it.

Chapter Three focusses on the measurement of the mechanical loss factor of bulk samples of fused silica coated with multi-layer dielectric coatings. The experiments were mostly performed by the author with the measurements of the samples provided by LMA[1] undertaken in conjunction with S. Reid, and some of the measurements of the doped multi-layer coated samples provided by CSIRO[2] undertaken in conjunction with A. Cumming. The finite element analysis was conducted by the author, except in the case of the coating analysis of the LMA samples where the modelling was carried out by D. Crooks. The measurements using the EELS technique were performed by I. MacLaren.

Chapter Four introduces the chemistry of hydroxide-catalysis bonding and the necessity for its use. Mechanical loss measurements of the 50 mm and 70 mm long fused silica samples were made by the author in partnership with S. Reid. The bonded sample studied in this chapter, and the witness samples were bonded by J. Hough and S. Rowan with mechanical loss measurements of the bonded sample made by the author. Sawing and polishing of the witness samples was undertaken by the author and S. Reid. Scanning Electron, Transmission Electron and Atomic Microscope imaging was achieved with the help of J. Scott and W. Smith.

In Chapter Five the mechanical loss measurement of bulk samples of a-axis sapphire are detailed. The calculation of the elastic properties of sapphire was undertaken by the author and J. Toher after discussions with J. Hough, S. Rowan and A. Long. Loss measurements of the different polished samples were taken by the author and S. Reid. The finite element analysis and measurements of the mechanical loss of all the coated samples were performed by the author. The nodal support was designed by E. Chalkley and J. Faller, with the loss measurements using this support taken by E. Chalkley. Mechanical loss measurements of all the tantala/silica coated sapphire substrates was undertaken by the author with the thermoelastic loss contributions calculated by D. Crooks.

[1] Laboratoire des Matériaux Avancés http://lma.in2p3.fr/Lmagb.htm

[2] Commonwealth Scientific and Industrial Research Organisation http://www.csiro.au/

Chapter Six details the mechanical loss measurements made on different orientations and aspect ratios of silicon substrates. The mechanical loss measurements and finite element analysis were conducted predominately by the author with the losses of the 100 mm and 150 mm long samples measured by the author and S. Reid.

Appendix A details the processes undertaken by the author to polish cross-sections of one inch diameter witness bond samples studied in Chapter Four.

Appendices B and C contain tutorials written by the author detailing the Finite Element Analysis techniques used to determine the strain energy stored in hydroxide-catalysis bond of the 120 mm long fused silica sample investigated in Chapter Four.

Summary

Measurement of the Mechanical Loss of Test Mass Materials for Advanced Gravitational Wave Detectors

Einstein's General Theory of Relativity (1916) predicted the existence of gravitational waves. These waves can be considered as fluctuations, or ripples, in the curvature of space-time. Until now there has been only indirect evidence, produced by Hulse and Taylor, of their existence. However, for many years various groups of scientists around the world have been developing ultra-sensitive instruments and techniques which are expected to be capable of detecting gravitational wave signals. The direct detection of these waves will provide new information about the astrophysical processes and sources which produce them.

Gravitational radiation is quadropole in nature, producing orthogonal stretching and squeezing of space. The resulting fluctuations in distance are, however, very small, with gravitational waves emitted from violent astrophysical phenomena expected to produce strains in space of the order $\sim 10^{-22}$ over relevant timescales.

One technique for detecting such strains is based on a Michelson Interferometer. The Institute for Gravitational Research at the University of Glasgow under the leadership of its director Professor James Hough, has been an active contributor of research targeted towards the detection of gravitational waves for over 35 years. A strong collaboration exists with the Albert-Einstein-Intitut in Hanover and Golm, the University of Hanover and the University of Cardiff. This collaboration has

developed and constructed a laser interferometer, with arms of 600 m length, in Germany named GEO600. GEO600 operates in a range of $\sim$ 50 Hz to a few kHz with strain sensitivities reaching the order of 10^{-22} $/\sqrt{\text{Hz}}$ in this frequency range.

The research presented in this thesis details experiments undertaken on materials and techniques used in current interferometric detectors and for proposed future detectors. The aim of this research is to investigate methods of reducing the levels of mechanical loss associated with the detector optics and thereby minimise the impact of thermal noise on the overall sensitivity of detectors.

Chapter One explains the nature of gravitational waves, the sources which are expected to yield the largest signals and also details the development of resonant bar and interferometric gravitational wave detectors. This is followed by a description in Chapter Two of thermal noise which is one of the principle limitations of the sensitivity of detectors. Reducing this thermal noise in interferometric detectors is a major challenge and studies have been made to establish the sources of thermal noise associated with the suspended, coated, test mass mirrors used in such detectors.

A significant source of thermal noise in the optics of interferometric gravitational wave detectors currently in operation arises from the mechanical loss associated with the coatings applied onto the test masses to create highly reflective mirrors. The results presented in Chapter Three show that the mechanical loss of these coatings is associated predominantly with the tantala component of the silica/tantala coatings used and that doping the tantala with titania can reduce the mechanical loss by approximately 40%. Results show other dopants such as lutetium may also reduce the mechanical loss, but not to the extent seen with titania and that the use of a heavier sputter gas such as xenon in the manufacture of the coatings can lead to a reduction of the mechanical loss. This is of importance in the determination of the optimum composition of coatings for the planned Advanced LIGO detectors.

Another significant technique to reduce thermal noise is the construction of monolithic fused silica suspensions. This involves the use of hydroxide-catalysis bonding as is used in the jointing of the monolithic suspensions of the GEO600 detector and

which will be used in the Advanced LIGO detectors. In Chapter Four investigations into the loss of hydroxide-catalysis bonds are presented which show that the levels of mechanical loss could be as much as four times lower than previous experiments by E. Elliffe and P. Sneddon suggested.

In Chapters Four to Six mechanical loss measurements of bulk mirror substrates for current and future interferometric gravitational wave detectors are detailed. Fused silica, *a*-axis sapphire and single-crystal silicon samples yielded values for the mechanical loss of $\phi_{\text{silica}} = 2.4\times10^{-8}$, $\phi_{\text{sapphire}} = 4.6\times10^{-9}$ and $\phi_{\text{silicon}} = 8.5\times10^{-9}$. The lowest loss values obtained for Heraeus type 311 fused silica were used to modify the semi-empirical model for the loss of fused silica developed by S. Penn et al. The low levels of loss in bulk silicon samples are of interest for use in the third generation of gravitational wave detectors. Measurements also suggest that the mechanical losses of (111) orientated silicon samples are lower than that of (100) orientated silicon substrates. Silicon also has a high thermal conductivity which is relevant for these detectors where significant thermal loading is anticipated due to the increased levels of laser power required to improve the levels of shot noise.

Finally, in Chapter Seven studies of silicon at cryogenic temperatures at the University of Glasgow are discussed. The author was involved in the commissioning of the two cryostats in operation. Early research shows that the measured mechanical loss of silicon flexures of single crystal silicon generally decreases as the samples are cooled to liquid nitrogen temperatures.

Chapter 1

Gravitational Wave Detection

1.1 Introduction

Einstein's General Theory of Relativity [5] describes gravitational waves as distortions of space-time produced by the non-uniform acceleration of mass. The solutions of the linearised Einstein Equations predict the existence of gravitational waves, *ripples in space-time*, travelling at the speed of light. Research towards detecting these gravitational waves began in earnest in the 1960s as a result of experimental work undertaken by Weber at the University of Maryland [6, 7].

The direct detection of gravitational waves is not only important in the field of fundamental physics because it will provide confirmation of Einstein's predictions made in 1916, but also to astronomy because detection will open up a new window onto the Universe. This will allow astronomers to study in much greater detail the properties of objects such as neutron stars and black holes and also, perhaps, to see early interactions from the *Big Bang*.

As yet no direct measurement of gravitational waves has been made, but this possibility grows nearer as a world-wide network of gravitational wave detectors is currently operating at, or near, their design sensitivities.

There is, however, indirect evidence of the existence of gravitational waves after Hulse and Taylor discovered the binary pulsar PSR $1913 + 19$ in 1975 [8, 9] and observed its orbital decay over a period of years [10, 11]. They noted that the orbit of this binary system decayed at a particular rate with the associated loss of energy being consistent with a model based on the emission of gravitational waves. In 1993 this discovery won Hulse and Taylor the Nobel Prize for Physics [12] for

> *"the discovery of a new type of pulsar, a discovery that has opened up the possibilities for the study of gravitation".*

1.2 Production of Gravitational Waves

General relativity restricts the number and type of polarisation states of gravitational radiation. Electromagnetic waves are generated by the acceleration of charge and in a similar way, gravitational waves are produced by the acceleration of mass. The conservation of mass is equivalent to the conservation of charge in electromagnetism eliminating the possibility of monopole gravitational wave radiation. However, the conservation of momentum also rules out the existence of dipole gravitational radiation. In electromagnetism, dipole radiation can exist due to the acceleration of both positive and negative electrical charges whereas gravitational radiation results from the acceleration of *positive* masses. Gravitational waves are therefore only produced by the non-axisymmetric acceleration of matter and are quadropole, or of higher pole, in nature.

Gravitational waves produce ripples, or waves, in the curvature in space-time and can be considered as tidal strains in space. There exist two polarisations of gravitational waves, which have amplitudes denoted h_+ and $h_\times$. They can be pictured as arriving at 45° to each other on the Earth from a distant source. The effect of such a wave passing perpendicularly through a ring of test particles is shown in figure 1.1.

This incident wave distorts the ring of diameter L so that it is stretched in one

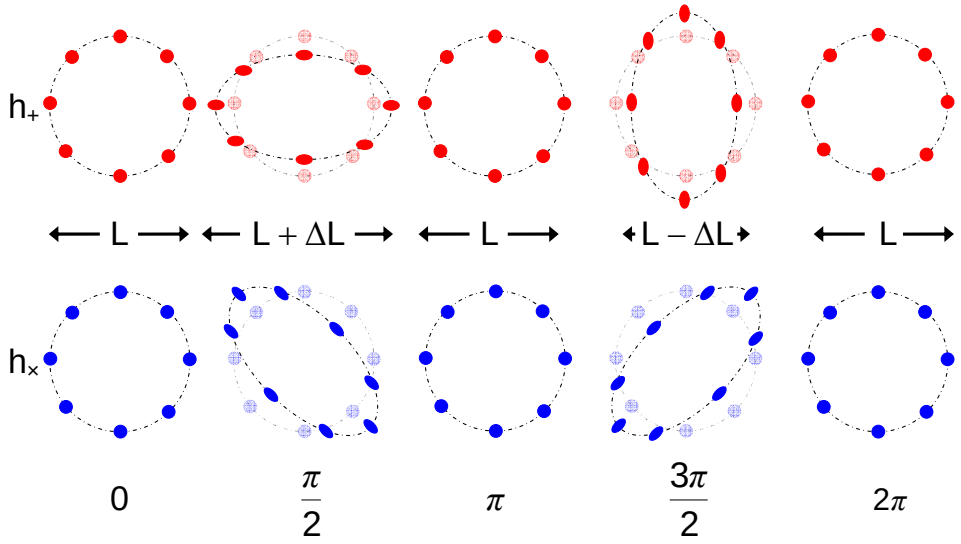

Figure 1.1: The effect of the h_+ and $h_\times$ polarisations of a gravitational wave on a ring of test particles, incident perpendicular to the page.

direction by ΔL and compressed in the orthogonal direction by an equal amount. The amplitude of the resultant strain is defined as

$$h = \frac{2\Delta L}{L}. \tag{1.1}$$

Gravity is the weakest of the four forces of nature. The relative strengths of the strong (nuclear), electromagnetic, weak (radioactive decay) and gravitational forces are $1 : 10^{-25} : 10^{-37} : 10^{-39}$ respectively. Consequently, for the effect of a gravitational wave to be significant very large masses and accelerations are required.

1.3 Sources of Gravitational Waves

Heinrich Hertz was the first person to obtain experimental evidence of electromagnetic waves in 1887 [13] following the prediction of their existence in 1862 by James Clerk Maxwell [14, 15]. His receiver was made up of a coil with a small air gap between two conducting electrodes. This receiver was placed several yards from an oscillator consisting of a high voltage inductor, capacitor and another spark gap. He

showed that when the oscillator was turned on the sparks from it would induce a current in the unconnected receiver loop which would send sparks across the gap. This experiment demonstrated the first transmission and reception of electromagnetic waves.

It would be ideal if it was also possible to generate gravitational waves in a similar laboratory environment. A "typical" generator of gravitational waves is described by Saulson [16], consisting of two masses, each weighing a tonne, separated by two metres and rotating about a common central axis with a rotational frequency of 1 kHz. The magnitude of h which this generator could produce was calculated to be $\sim 1 \times 10^{-38}$ at a distance of one wavelength from this source. The corresponding displacement caused by this strain over a length of several kilometers would be in the order of 1×10^{-35} m. This is too small to be detected by any of the existing, or currently proposed, gravitational wave detectors which are discussed in sections 1.6 and 1.7.

Instead we must look at large scale astronomical objects to find sources of detectable gravitational waves. There are several sources of gravitational waves which potentially emit radiation with both a suitable level and frequency to be detectable by a gravitational wave detector, for example, the coalescence of a compact binary system to a black hole or the spinning of an asymmetric neutron star. Some of the expected sources of measurable gravitational waves and their predicted stain amplitudes are discussed in the following sections.

1.3.1 Burst Sources

Burst sources are events which occur over a short timescale ranging from only a few milliseconds to several minutes.

Coalescing Binary Systems

Compact Binaries are systems consisting of pairs of high density stars which rotate about their common centre of mass. There are three main types of binary system which are of interest here:

black hole / black hole	(BH/BH),	
neutron star / neutron star	(NS/NS)	and
neutron star / black hole	(NS/BH)	binaries.

This rotational orbital motion produces gravitational radiation which carries energy away from the system. This results in the orbit decreasing until the inspiralling trajectory causes the two objects to merge. This sequence of events produces a distinct *chirp signal* of gravitational waves.

PSR 1913 + 19, which was mentioned in section 1.1, is an example of a NS/NS binary. Its orbital frequency, and consequently the frequency of gravitational waves radiated, increases with time until eventually the two stars will coalesce in $\sim 10^8$ years. The periodic signal increases in amplitude and frequency right up until the final merger. The signals from this sweep from low frequency through the bandwidth of all the different types of gravitational wave detectors (described in section 1.4). Detection of the merger of other NS/NS binaries which coalesce much sooner is one likely candidate for initial gravitational wave searches.

For a coalescing NS/NS binary comprising of two stars of mass $m_1 M_\odot$ and $m_2 M_\odot$, where $M_\odot$ is the solar mass, the approximate strain amplitude h is calculated by Schutz [17] to be;

$$h \approx 1 \times 10^{-23}\ {m_{\mathrm{T}}}^{\frac{2}{3}}\ \mu \left(\frac{f}{100\ \mathrm{Hz}}\right)^{\frac{2}{3}} \left(\frac{100\ \mathrm{Mpc}}{r}\right) \tag{1.2}$$

for f, the frequency of radiation emitted from a system at a distance r from Earth where

$$m_{\mathrm{T}} = m_1 + m_2 \tag{1.3}$$

and

$$\mu = \frac{m_1 m_2}{m_1 + m_2} \tag{1.4}$$

is the reduced mass of the system.

BH/BH and NS/BH binaries are expected to be rarer than NS/NS binaries, but as they have a greater mass the correspondingly larger wave amplitude makes them detectable at a larger distance. There are hundreds of known neutron stars, but only several are located in a binary system. The number of neutron star binaries along with the rate at which new ones are born can be used to estimate the event rate of coalescing binary systems. The estimated detection rates for the initial LIGO detectors, as described later in section 1.6, are presented in table 1.1 [18].

Binary System	**LIGO Detection Rate ($\mathbf{yr^{-1}}$)**
NS/NS	$1 \times 10^{-4} - 0.03$
NS/BH	$\leqslant 1 \times 10^{-4} - 0.3$
BH/BH	$\leqslant 3 \times 10^{-3} - 0.5$

Table 1.1: Estimated detection rates of coalescing binary systems for the LIGO detectors network.

Supernovae

Supernovae are some of the most spectacular events to occur in the universe. A supernova is the explosion of a star, but there are however two classifications of supernovae: *Type I* and *Type II*. Type I supernovae are thought to involve binary systems of low mass stars such as white dwarfs. The white dwarf accretes matter from its companion in the binary system until the inward pressure due to gravity is significantly greater than the outward radiation pressure and subsequently the star detonates. This explosion if asymmetric, is thought to generate gravitational radiation.

Type II supernovae are the product of a violent collapse of a massive stellar core which produces a neutron star or black hole. If this collapse is symmetric then no

gravitational waves would be produced, but if, instead, the collapse is asymmetric due to the core of the star having a large angular momentum then a burst of gravitational radiation will be emitted. The exact waveform produced by this kind of occurrence is very difficult to predict. The detection of such a supernova could be used to assist the efforts being made to model these events.

Schutz however has estimated the strain amplitude h from a star becoming a supernova [19] to be:

$$h \approx 5 \times 10^{-22} \left(\frac{E}{10^{-3}\ M_{\odot} c^2} \right)^{\frac{1}{2}} \left(\frac{15\ \text{Mpc}}{r} \right) \left(\frac{1\ \text{kHz}}{f} \right) \left(\frac{1\ \text{ms}}{\tau} \right)^{\frac{1}{2}} \tag{1.5}$$

where E is the energy of gravitational radiation emitted by the source at a distance r from the detector and predominately at a frequency f for time τ. However, later work on this by Müller using more realistic models of core-collapse supernovae suggests that the expected strain amplitude may be lower than this [20].

1.3.2 Continuous Sources

The gravitational waves produced throughout the lifetime of a binary system have too low a frequency, until their last few seconds of life, to be observed by ground-based detectors hence they are observed as burst sources. However, a space-based detector, as discussed in section 1.7, should be able to observe such sources over a much longer timescale. For ground-based detectors there are other potential *continuous sources*. The signal-to-noise ratio of all these sources can be improved by integrating over a long time.

Pulsars

Neutron stars are the collapsed remnants of massive stars. A neutron star is only about 20 km in diameter but has a mass about 1.4 times larger than that of the

Sun. This means that the matter contained within such a star is thousands of times more dense than ordinary matter.

Pulsars were first discovered by Jocelyn Bell Burnell in 1967 [21] and are highly magnetised spinning neutron stars which have vast jets of particles streaming out of their magnetic poles. These jets sweep round as the pulsar rotates and can be observed on Earth as regular flashes of radiation occurring at twice the pulsar rotational frequency f_{rot}. If the pulsar has small irregularities on the surface, or it has elliptical geometry, then such a non-axisymmetric pulsar will emit gravitational waves. An estimation of the likely amplitude h from this kind of pulsar observed over time $\mathrm{T_{obs}}$ is [22]

$$h \approx 4 \times 10^{-20} \left(\frac{f_{\mathrm{rot}}}{500\ \mathrm{Hz}}\right)^{\frac{5}{2}} \left(\frac{\mathrm{T_{obs}}}{\frac{1}{3}\ \mathrm{yr}}\right)^{\frac{1}{2}} \left(\frac{1\ \mathrm{kpc}}{r}\right) \left(\frac{\varepsilon}{10^{-6}}\right) \tag{1.6}$$

where the equatorial ellipticity ε is a measure of how asymmetric a star is and r is the distance of the pulsar from Earth. The most accurately measured upper limit of the gravitational strain from a known pulsar is 2.6×10^{-25} for PSR $J1603-7207$ [23].

Low-Mass X-ray Binaries

Low-Mass X-ray binaries are systems where the strong gravitational field of a neutron star pulls matter from a normal companion star. The accretion process results in a gain of angular momentum of the neutron star until it reaches a limit known as the Chandrasekhar-Friedman-Schutz instability point [24] where the rotation becomes non-axisymmetric and produces gravitational waves [25]. A neutron star exhibiting this instability is known as a *Wagoner Star*.

X-ray emissions are observed as matter is accreted towards the surface of the neutron star and eventually a steady state is reached. This occurs when the increasing instability from the continued accretion is balanced by the energy lost from the

emission of X-rays and gravitational radiation. The amplitude of gravitational waves expected from such Low-Mass X-ray Binaries is defined in terms of the time-averaged X-ray flux l_γ such that [25]

$$h \approx 3 \times 10^{-27} \left(\frac{1 \text{ kHz}}{mf}\right) \left(\frac{l_\gamma}{10^{-19} \text{ Wm}^{-2}}\right) \tag{1.7}$$

where the mode number m is approximately 4 and f is the frequency of gravitational radiation.

1.3.3 Stochastic Background

The final type of gravitational radiation is in the form of a *stochastic background*. A random background of gravitational waves is expected to exist from the superposition of random, uncorrelated signals which cannot be easily be resolved. These signals are only distinguishable from the noise within a single detector by the cross-correlation of data from two or more detectors.

There have been many different predictions of the formation of the Universe including the cosmic string scenario for galaxy formation and cosmic inflation theory. If strings were the seeds around which galaxies condensed, then their decay must produce gravitational radiation which is observable through the cross-correlation between several detectors. The magnitude of h predicted for the stochastic background, using the cosmic string scenario for galaxy formation is [26]

$$h \approx 1.8 \times 10^{-25} \left(\frac{H_0}{100 \text{ kms}^{-1} \text{ Mpc}^{-1}}\right) \left(\frac{\Omega_{\text{gw}}}{10^{-8}}\right)^{\frac{1}{2}} \left(\frac{f}{100 \text{ Hz}}\right)^{-\frac{3}{2}} \left(\frac{B}{2 \text{ Hz}}\right)^{\frac{1}{2}} \tag{1.8}$$

within a bandwidth B about a frequency f, where H_0 is the present value of the Hubble's Constant and Ω_{gw} is the energy density per logarithmic frequency interval required to close the universe.

Another possible source of a stochastic background is from cosmic inflation theory. Gravitational waves are produced from the early inflationary period of the Universe $\sim 10^{-24}$ s after the Big Bang. The observation of a gravitational wave stochastic background would provide interesting insights into the dynamics of the early universe.

For periodic sources such as pulsars and low-mass X-ray binaries and also from the stochastic background, integrating over a long observation time can improve the signal-to-noise ratio. This increases the likelihood of the detection of gravitational waves.

1.4 Gravitational Wave Detectors

Despite the vast scale of these astronomical events, it can be understood from the previous discussion that in order to see gravitational waves on Earth, devices sensitive to extremely small strains, h of 10^{-23}, over relevant timescales are required. Historically there has been two approaches to constructing suitable devices; resonant bar detectors, and long baseline interferometers.

1.4.1 Resonant Bar Detectors

The experimental search for gravitational waves began over forty years ago when Joseph Weber planned and constructed a pair of *resonant bar detectors*. The design of each of these detectors consisted of a large cylindrical aluminium bar suspended from vibration isolation stages and placed under vacuum to further isolate the bar from seismic and acoustic noise. A description of these sources of noise is given later in section 1.5. Strain gauges were attached in several locations around the cylinders to monitor the amplitude of the resonant modes.

The principle of operation is based on the premise that when a gravitational wave

with frequency components spanning the resonant frequency of the cylinder ($\sim$ 1600 Hz) passes through the detector, the bar will become excited. The sensitivity of these detectors was limited to $h \sim 2 \times 10^{-16}$ $/\sqrt{\text{Hz}}$ by the electronic noise from the sensing system and the collective thermal motion of the molecules making up the bar itself, a noise source, discussed in detail in chapter 2.

After several years of data collection and refinements to his apparatus, in 1968 Weber reported coincident signals between two detectors placed 2 km apart, thought to be from the detection of gravitational waves [27]. He continued to report coincidences appearing over the following years [28, 29].

Research groups in the Bell-Laboratories (Rochester-Holmdel, United States of America) [30], Munich-Frascati (Germany) [31], Glasgow (United Kingdom) [32], Moscow (Russia) [33] and Tokyo (Japan) [34, 35] constructed similar experiments but none of them were able to repeat or confirm the claims of Weber [36]. This was consistent with expectations because the sensitivity of these original detectors was several orders of magnitude above the levels theoretically predicted for the amplitudes of gravitational waves produced by typical astronomical sources.

The focus of research then moved into reducing the thermal noise levels in these bar detectors by cooling them to cryogenic temperatures. The improved detectors have burst source sensitives approaching 10^{-20} $/\sqrt{\text{Hz}}$ over a $\sim$ 100 Hz bandwidth. There are four such advanced resonant bar detectors operating today:

Allegro: A 2296 kg aluminium bar detector located in Baton Rouge (Louisiana, USA). This detector has been operational since 1991 and is cooled to 4.2 K and has two resonant frequencies at 895 Hz and 920 Hz. The strain sensitivity at resonance in 2006 of this detector was 4×10^{-21} $/\sqrt{\text{Hz}}$ [37] with an operating bandwidth of 60 Hz. However, this detector is shortly going to cease operation.

Auriga: A 2230 kg aluminium bar detector located in Legnaro (Padova, Italy) which has been in operation since 1997. Auriga can be cooled to ultra-cryogenic temperatures of 200 mK [38] with two resonant frequencies at 912 Hz

and 930 Hz. In 2006, the strain sensitivity at 4.5 K was reported to be $\sim 2 \times 10^{-21}$ $/\sqrt{\text{Hz}}$ with the detector operating bandwidth of 110 Hz [39].

Explorer: A 2270 kg aluminium bar detector located at CERN (Geneva, Switzerland). This detector has been in operation since 1990 and is cooled to 2.6 K with resonances at 905 Hz and 921 Hz [40]. After some improvements to the readout system for the detector, the peak sensitivity at resonance in this detector was reported to be 7×10^{-22} $/\sqrt{\text{Hz}}$ following a year long run from March 2004 [41]. The bandwidth of this detector is however only 5 Hz.

Nautilus: A 2260 kg aluminium bar detector located in Frascati (Rome, Italy). Operational since 1995, it can be run at ultra-cryogenic temperatures of 100 mK [42] with resonances at 908 Hz and 924 Hz . In the $2004-2005$ science run the Nautilus detector reached a strain sensitivity at resonance of 7×10^{-22} $/\sqrt{\text{Hz}}$ while operating at the higher temperature of 3 K [41], again with only a 5 Hz bandwidth. Better performances may be obtained when the antenna is cooled to 100 mK temperatures.

Bar detectors have a fundamental disadvantage: they are only sensitive to signals which have a significant spectral energy in a $\sim$ 100 Hz band around the frequency of the fundamental longitudinal resonance mode of the detector at $\sim$ 900 Hz. However, improvements in the directional sensitivity have been made through the use of spherical detectors.

Spherical detectors are omnidirectional whereas bar detectors are limited in this respect. A sphere has five equivalent quadropole modes compared to the one in a bar. Therefore when a gravitational wave passes through such a detector the ratio of the amplitude of the five resonant modes can be used to determine both the direction and polarisation of the wave. Details of two spherical bar detectors under development are summarised below:

MiniGRAIL: A 1300 kg CuAl(6%), 0.68 m diameter spherical detector in LION (Leiden, Netherlands). It is designed to operate at 50 mK, but at 4.2 K a strain

sensitivity of 5×10^{-20} $/\sqrt{\text{Hz}}$ has been obtained at the ~ 2980 Hz resonance and it operates with a 30 Hz bandwidth [43].

Mario Schenberg: A second 1300 kg CuAl(6%) spherical detector currently being commissioned at the Universidade de São Paulo (Brazil). It has a target sensitivity of $h \sim 2 \times 10^{-21}$ $/\sqrt{\text{Hz}}$ at 3200 Hz and to operate with a 60 Hz bandwidth [44].

Unfortunately, a significant disadvantage in the operation of spherical bar detectors is their physical dimensions which limit them to a narrow frequency bandwidth.

Bonaldi, Cerdonio and others have developed a scheme where the operating bandwidth is extended by using a dual resonant mass detector [45, 46]. In this proposed set up a solid Molybdenum cylinder is nested within a larger hollow cylinder where the resonant frequency of the larger cylinder is two to three times lower than the smaller one. A gravitational wave which passes between the resonant frequencies of the two cylinders, will induce two motions which are 180° out of phase. This enables the resulting differential vibrations to be sensed by a displacement readout. Such a dual detector should be able to reach strain sensitivities of 2×10^{-23} $/\sqrt{\text{Hz}}$ over a bandwidth of several kilohertz.

1.4.2 Long Baseline Interferometers

In 1963 Soviet physicists Gertenshtein and Pustovoit suggested the use of freely suspended test masses forming a Michelson Interferometer to detect gravitational waves [47]. Such detectors provide the possibility of higher sensitivity over a much broader frequency range. Forward [48] and Weiss [49] began research with similar detectors in the 1970s. A diagram of a simple Michelson Interferometer is shown in figure 1.2.

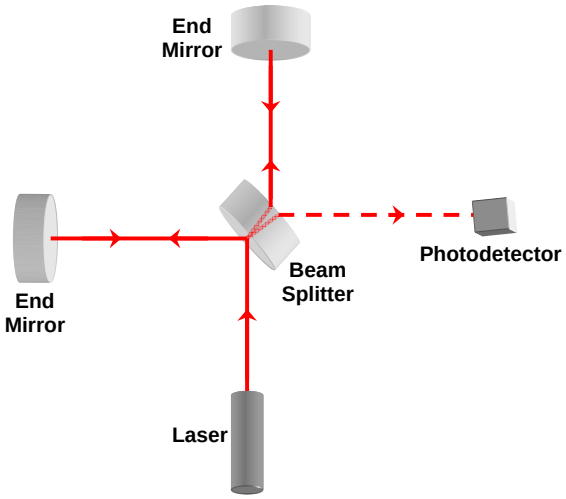

Figure 1.2: Diagram of a Simple Michelson Interferometer.

Laser light is split into two beams by the beam splitter and directed along two orthogonal arms of the interferometer. These beams are then reflected at the end mirrors back towards the beam splitter where they are recombined and steered towards a photodiode. The end mirrors are hung as freely suspended pendulums to isolate them from seismic noise.

An optimally orientated gravitational wave incident on the detector will increase the optical path length of one arm by δL and correspondingly reduce the path length in the other orthogonal arm by the same amount. This gives a total change in the relative optical path length of $2\delta L$. This results in a relative phase shift between the return beams of laser light in the interferometer, which, when they are recombined, is detected as a change in the light power at the photodetector.

A major advantage of the laser interferometer design is that the signal from a gravitational wave can be increased by having a longer arm length. This results in a correspondingly larger δL. However, the curvature of the earth limits the arm lengths of these interferometers to the kilometer scale.

Delay-Line Interferometers

There are several techniques which can be implemented to increase the effective arm length of an interferometer. The first method is by increasing the length of the optical path of the laser light within the interferometer. Weiss proposed such a scheme incorporating optical *Delay-Lines* [50]. This utilises an optical path folded by the addition of a secondary mirror reflecting the light to mirrors positioned back near the beam splitter. A simplified version of this is shown in figure 1.3. This folded delay-line configuration is used as the basis of the layout of the GEO600 detector discussed in section 1.6.

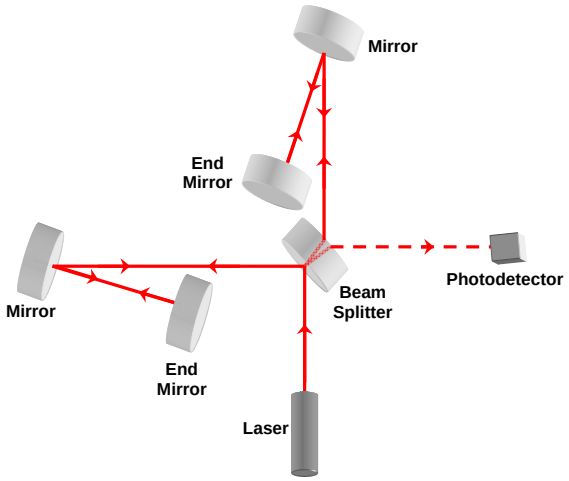

Figure 1.3: Diagram of a Michelson Interferometer where the optical path length is increased by folding the optical path.

The optical path length of a delay-line interferometer can be increased by the addition of mirrors, each of which has a small input hole, placed close to the beam splitter in each arm as shown in figure 1.4 [51]. If the mirrors are designed with a small curvature then multiple, non-overlapping beams can co-exist within each arm of the interferometer. Researchers at the Max-Planck-Institut für Quantenoptik (Garching, Germany) [52] developed a configuration where the laser light in the interferometer exited each arm through the same input hole where it entered [53].

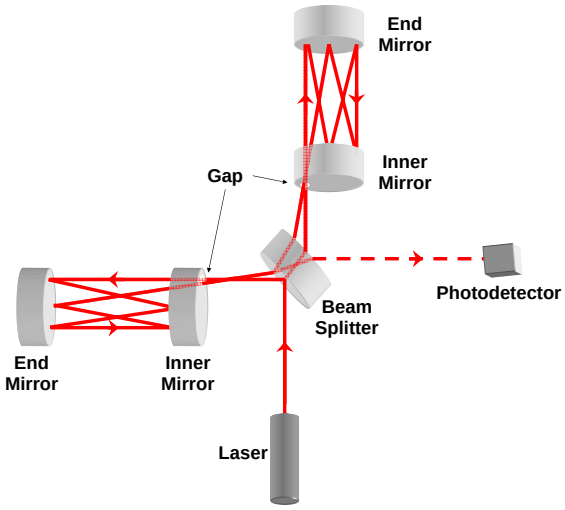

Figure 1.4: Diagram of a delay-line Michelson Interferometer.

Fabry-Perot Interferometers

Another technique for increasing the optical path length of the laser light within the arms of an interferometer is through the use of Fabry-Perot cavities, as shown in figure 1.5. Each cavity is formed by the placing, in each arm, of one mirror situated near the beam splitter and one highly reflective end mirror.

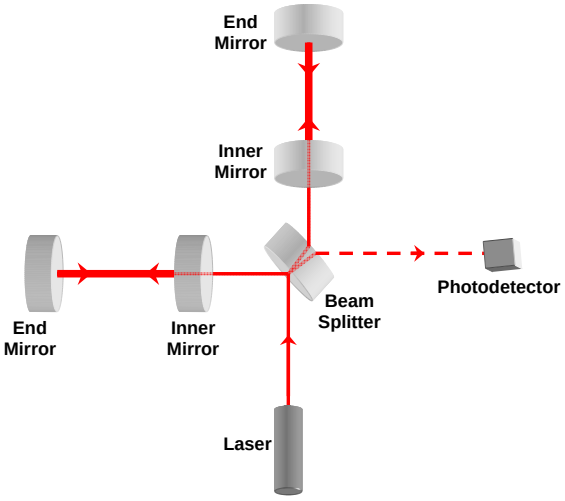

Figure 1.5: Diagram of a Michelson Interferometer with Fabry-Perot cavities formed in each arm between the end and inner test masses.

The addition of Fabry-Perot cavities makes the interferometer much more complex and a significant amount of servo-control is required to hold them on resonance. However, one advantage of a Fabry-Perot Interferometer over a Delay-Line Interferometer is that the multiple beams can be overlapped and so mirrors of smaller diameter can be used. In addition, the effects of scattered light within each of the interferometers arms is greatly reduced [54].

Prototype Fabry-Perot detectors were constructed in Glasgow and Caltech in California. The arms of the Glasgow detector were 10 m in length and those of the Caltech detector 40 m long. The minimum displacement noise spectral densities of these detectors were 4×10^{-19} m/$\sqrt{\text{Hz}}$ and $\sim 5 \times 10^{-20}$ m/$\sqrt{\text{Hz}}$ respectively [55, 56].

1.5 Sensitivity Limits: Sources of Noise

There is a number of noise sources which are known to limit the sensitivity achievable by interferometric gravitational wave detectors. Some of the most important of these different noise sources are discussed below.

1.5.1 Photoelectron Shot Noise

The output signal of the interferometer is held just off the dark fringe because at this point the signal-to-noise ratio of the instrument is best [57]. To maintain the interferometer in this condition the output signal at the photodiode is monitored and, when necessary, a signal is fed to a transducer which adjusts the position of one of the test mirrors. Information about the change in arm length from a passing gravitational wave can then be determined by monitoring the feedback signal.

A gravitational wave interferometer needs to resolve differences of less than 10^{-20} m/$\sqrt{\text{Hz}}$ in the lengths of the arms of the interferometer [58]. This is a minute displacement compared with the wavelength of light which is approximately 10^{-6} m. The statis-

tical fluctuations in the number of photons n detected at the output over time τ introduces a source of noise. According to Poisson counting statistics, the shot noise of a folded interferometer of length L with N bounces is dependant on the input power P_{in} of the laser with wavelength λ, such that [59]:

$$h_{\text{shot}}(f) = \frac{1}{NL}\left(\frac{\hbar c\lambda}{2\pi P_{\text{in}}}\right)^{\frac{1}{2}} \sqrt{\text{Hz}} \tag{1.9}$$

where c is the speed of light and $\hbar$ is the reduced Planck's Constant (1.05×10^{-34} Js). It is assumed that the photodetectors have a quantum efficiency of 1.

Therefore for an interferometer using a laser with a wavelength of $\sim 1\times10^{-6}$ m, a laser power of more than 10^8 W is needed for a single bounce to reach the desired detector sensitivity [58]. Increasing the power of the laser to this level is a formidable task, but the effective power in the interferometer can be built up by the use of Fabry-Perot cavities, as discussed in section 1.4, and through the recycling of power within the interferometer. The Fabry-Perot cavities of the 4 km Hanford LIGO detector [60], detailed later in section 1.6, have an arm cavity finesse of 219 [61].

Power Recycling

Power Recycling is a technique used to enhance the output signal of an interferometric gravitational wave detector [62]. As mentioned previously, these detectors are operated with the reflected beams interfering destructively to give a dark fringe at the photodetector. This means that most of the laser power entering the interferometer is reflected back towards the laser.

By inserting an additional partially transmitting mirror between the laser and the beam splitter, as shown in figure 1.6, the back-reflected beam can be *re-used* by reflecting it back into the interferometer. Similar to the use of a Fabry-Perot cavity, power recycling increases the power levels within the interferometer without having to increase the laser-source power.

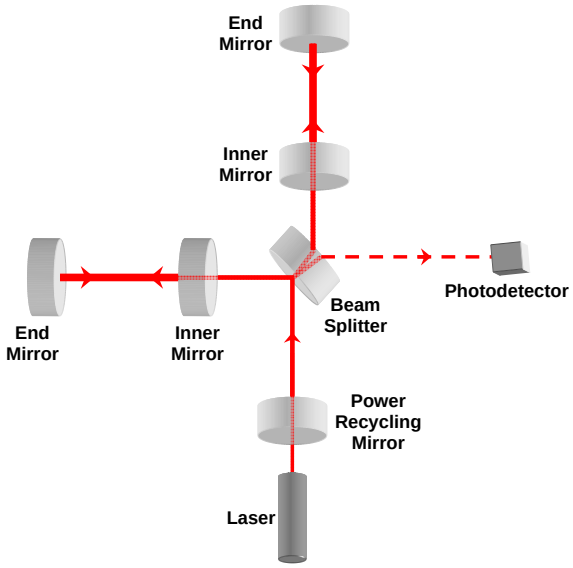

Figure 1.6: Diagram of a Michelson Interferometer with a Fabry-Perot cavity and the addition of a power recycling mirror placed between the laser and the beam splitter.

Signal Recycling

Signal Recycling is based on the same premise as power recycling in that a partially reflecting mirror is used to reflect outgoing light back into the interferometer, but this time by re-using the *signal* light at the photodetector [62]. As discussed earlier in section 1.4, the passage of a gravitational wave through an interferometer results in a differential change in the arm lengths of the detector producing laser light at the photodetector.

If a mirror with a suitably chosen reflectivity is placed between the beam splitter and the photodetector, as shown, in figure 1.7, then this signal is recycled back into the interferometer arms where it resonates, increasing the signal size over a given bandwidth.

Signal recycling may be used in gravitational wave detectors to increase sensitivity in a narrow bandwidth. This is particularly useful when searching for continuous gravitational waves sources, such as those described in section 1.3.

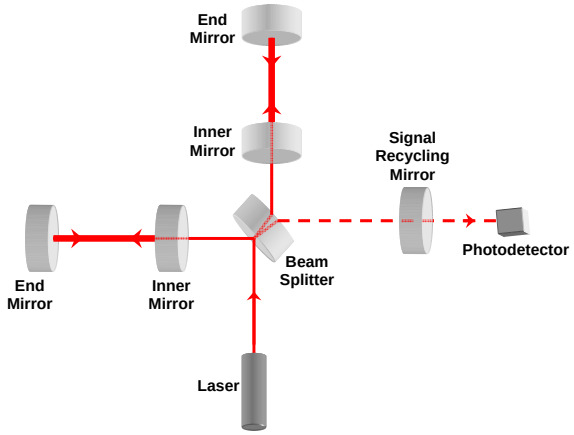

Figure 1.7: Diagram of a Michelson Interferometer with a Fabry-Perot cavity and the addition of a signal recycling mirror placed before the photodiode.

1.5.2 Radiation Pressure Noise

Increasing the effective laser power in the arms of the interferometer increases the levels of *Radiation Pressure Noise*. This noise arises from fluctuations in the number of photons reflecting off the surface of the test mass mirrors. There is a force exerted on the interferometer mirrors from the transfer of momentum during this reflection. The force on the mirror varies with the fluctuating numbers of photons. For a Delay-Line interferometer of length L with mirrors of mass m, with N bounces, the strain sensitivity levels h_{rp} caused by these fluctuations, for a laser with wavelength λ and input power P_{in}, can be expressed as [16]

$$h_{\mathrm{rp}}(f) = \frac{N}{mf^2L}\sqrt{\frac{2\hbar P_{\mathrm{in}}}{\pi^3 c\lambda}}\ \frac{1}{\sqrt{\mathrm{Hz}}}. \tag{1.10}$$

It can be seen from equation 1.10 that $h_{\mathrm{rp}} \propto \frac{1}{f^2}$, therefore the level of radiation noise diminishes as the frequency increases. Also, if the power is increased, the levels of noise from radiation pressure will increase.

1.5.3 The Standard Quantum Limit

Both shot noise and radiation pressure noise are sources associated with the quantum nature of light. Assuming that these two effects are statistically independent, it is possible to combine these sources to state them as a single *optical readout noise* expressed as [16]

$$h_{\mathrm{oro}}(f) = \sqrt{h^2{}_{\mathrm{shot}}(f) + h^2{}_{\mathrm{rp}}(f)}. \tag{1.11}$$

For low frequencies this expression is dominated by the term from the radiation pressure noise whereas at high frequencies the noise levels are set by shot noise, which is seen earlier in equation 1.9 to be frequency independent.

These combined effects have a minimum noise spectral density when the input laser power is set to an optimum level P_{opt}. At this power, $h_{\mathrm{shot}}(f) = h_{\mathrm{rp}}(f)$ which allows equations 1.9 and 1.10 to be equated to give

$$P_{\mathrm{opt}} = \pi c \lambda m f^2. \tag{1.12}$$

This is substituted into equation 1.11 to yield the locus of lowest possible noise referred to as the *Standard Quantum Limit* h_{QL}:

$$h_{\mathrm{QL}} = \frac{1}{\pi f L}\sqrt{\frac{\hbar}{m}}. \tag{1.13}$$

The standard quantum limit sets a limitation on the minimum differential displacement which can be measured between two test mirror masses in a simple interferometer.

In currently operating interferometric gravitational wave detectors the standard quantum limit is significantly below all other sources of noise. This limit becomes

important for more sensitive interferometers. It should be possible, however, to reach this limit in future interferometric detectors, at a tuned range of frequencies, by squeezing the vacuum field [63, 58].

In principle it may be possible to *beat* the standard quantum limit by constructing a cavity which has a strong optical spring [64, 65, 58] which couples the optical field to the mechanical system.

1.5.4 Seismic Noise

Natural phenomena such as earth tremors and ocean waves and also human activities like the movement of traffic and machinery, can all lead to significant levels of *seismic noise*. These levels are not constant; varying instead throughout the day, and with a dependence on site location. In a quiet environment the seismic noise levels in each of the three directions can be approximated by [66]:

$$\delta x = \frac{10^{-7}}{f^2}\ \mathrm{m}/\sqrt{\mathrm{Hz}}. \tag{1.14}$$

The target sensitivity of Advanced LIGO at 10 Hz is $\sim 1 \times 10^{-19}\ \mathrm{m}/\sqrt{\mathrm{Hz}}$ [67]. To achieve this it is necessary for the levels of seismic noise to be suppressed by $\sim 10^{10}$. Each mirror must therefore be isolated from the seismic motion of the surroundings over the entire operating frequency range of the gravitational wave detector. Cantilever springs can be used to isolate the system from vertical motion. In order to isolate the mirrors in the horizontal direction one technique is to suspend them as pendulums.

Pendulums attenuate ground motion above their resonant frequency. The transfer function of a single pendulum can be expressed as [16]

$$\frac{x_{\mathrm{mass}}}{x_{\mathrm{clamp}}} = \frac{f_0^2}{f_0^2 - f^2} \tag{1.15}$$

where x_{mass} is the displacement of the pendulum's mass, x_{clamp} is the displacement of the clamping point of the pendulum caused by seismic motion, f_0 is the resonant frequency of the pendulum and f is the frequency of the ground motion. When $f \gg f_0$ the degree of attenuation is approximately $-\frac{f_0^2}{f^2}$.

This attenuation can be enhanced by constructing a multi-stage pendulum system. For a system with N pendulums at a frequency f far greater than the resonant frequency of the pendulums f_0, the transfer function can be expressed as

$$\frac{x_{\text{mass}}}{x_{\text{ground}}} \approx \left(\frac{f_0^2}{f_0^2 - f^2}\right)^N . \tag{1.16}$$

Below the resonant frequency of the pendulum the equation 1.15 tends towards unity as $f_0^2 - f^2 \approx f_0^2$. This means that at such frequencies the pendulum acts as a rigid coupling between the ground and the suspended test mirror. Thus, to increase the low frequency sensitivity of interferometric detectors, multi-stage pendulums with very low resonant frequencies are necessary.

It appears that when $f = f_0$, the transfer function will be infinite. However, as discussed later in section 2.5, there is damping from internal friction which gives a more physical bounded value for the transfer function.

1.5.5 Gravity Gradient Noise

The direct gravitational coupling of seismic motions, sometimes referred to as Newtonian noise, and other fluctuations to the test mass mirrors provides a fundamental limit known as *Gravity Gradient Noise* [68]. In this case, vibration isolation techniques have no effect on reducing this noise. For initial interferometric gravitational wave detectors the levels of noise from these effects lie well below their sensitivities over most of the frequency range.

Unfortunately, such noise will limit the low frequency sensitivity of future detectors

below approximately $10 - 15$ Hz. A possible way to reduce this source of noise is to construct future detectors underground where gravity gradients are decreased. For example the planned Japanese *Large Scale Cryogenic Gravitational Wave Telescope* (LCGT) [69] has a proposed underground site in the Kamioka Mine in order to reduce this problem.

A second approach is to build a non-Earth based detector, such as the space-based LISA interferometric detector, discussed in section 1.7.3.

1.5.6 Residual Gas

In order to achieve the target sensitivities, interferometric gravitational wave detectors are required to be operated under ultra-high vacuum. However, any vacuum system contains some trace amounts of gas which is extremely difficult to remove from the system. Traces of gas in the beam-path will induce fluctuations in the refractive index of the arms. Residual gas particles bouncing off the mirrors can also increase the displacement noise.

1.5.7 Thermal Noise

The random vibrations of atoms in the test mirrors of an interferometer and their suspensions, which are at finite temperature and have a number of differing resonant modes, result in *thermal noise*.

Brownian Motion

Thermal noise results from the Brownian motion of the atoms and molecules. This motion is related to the thermal energy, specifically $\frac{1}{2}k_{\mathrm{B}}T$ energy per degree of freedom, where k_{B} is Boltzmann's Constant (1.38×10^{-23} J/K) and T is temperature. Thermal noise at all frequencies is dependent on the internal friction of the material.

Lowering the levels of this or reducing the operating temperature will produce a better thermal noise performance in future interferometric detectors.

Thermo-refractive Noise

The temperature of a body is not constant throughout its volume. Instead there are statistical fluctuations in temperature from point to point. The refractive indices of the test mass substrates, the mirror coatings applied to them and the material of the beam splitter all are a function of temperature. This leads to a source of noise known as *thermo-refractive noise*. The refractive index of the material is altered by temperature fluctuations, resulting in a phase fluctuations of the transmitted or reflected light.

The consequence of this is that there are levels of phase noise in the interference point of the interferometer. Braginsky, Gorodetsky and Vyatchanin showed in 2000 that the levels of thermo-refractive noise must be seriously considered for the mid-operating frequencies of the Advanced LIGO detectors and beyond [70]. In the GEO600 detector, discussed later in section 1.6, the levels of thermo-refractive noise is estimated at 100 Hz to be $\sim 7 \times 10^{-23}/\sqrt{\text{Hz}}$ [71].

Thermo-elastic Noise

A further form of thermal noise results from *thermo-elastic noise*. Levels of noise result from the statistical temperature fluctuations of a system which couple into mechanical movement, through the coefficient of thermal expansion of a material.

Thermal noise is one of the most significant noise sources in the sensitivities of current interferometric gravitational wave detectors. This makes it one of the most important areas of research in the field of gravitational wave detectors. Thermal noise will be discussed in greater detail in chapter 2.

1.5.8 Optical Distortion (A Technical Limitation)

A technical limitation to the performance of interferometric gravitational wave detectors which employ high laser powers is caused by thermally induced distortions of the optics [72]. The Gaussian intensity profile of the laser light used in the interferometers combined with the presence of absorption in the substrates and coatings of the optics results in non-uniform heating of the interferometer mirrors. This heating leads to thermal lensing of the substrate and thermally induced distortions associated with the coatings. These thermal effects can be significant, and can require active thermal compensation [73].

1.6 The Current Generation of Interferometric Gravitational Wave Detectors

There are several ground based interferometric gravitational wave detectors operating.

LIGO: The *Laser Interferometer Gravitational-Wave Observatory* (LIGO) [60] is a joint Caltech/MIT project consisting of three interferometers built at two different sites in the United States of America. In Hanford (Washington) there is a 4 km and a 2 km interferometer in the same vacuum system. There is also a 4 km arm length detector in Livingston (Louisiana). These three interferometers use Fabry-Perot cavities in each of their arms and utilise power recycling to reduce the effects of shot noise [60].

Each detector employs 10.7 kg fused silica mirrors which are suspended using a single loop of 0.62 mm diameter steel wire [74]. Magnets attached to the sides and back of the masses are used to control the movements of the suspensions. Each detector is operated under vacuum at a pressure of $\sim 10^{-9}$ mbar [75].

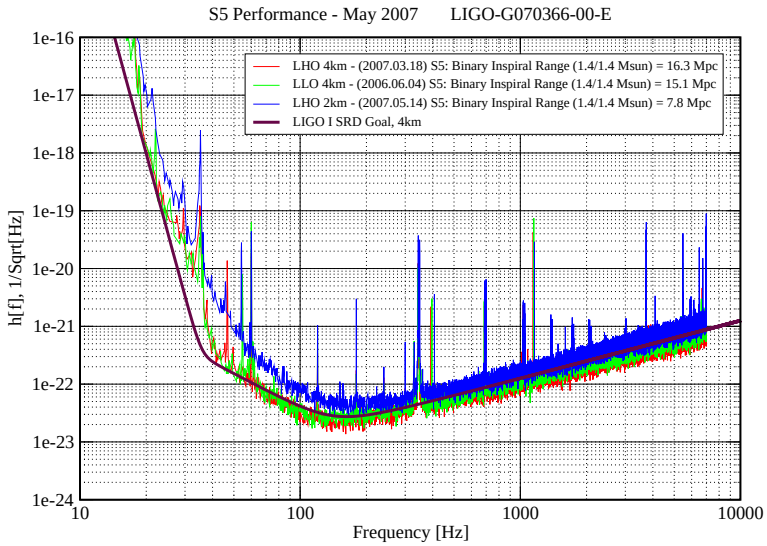

Figure 1.8: Sensitivity curves for the three LIGO interferometer detectors recorded during the S5 Science Run in May 2007.

The interferometers in the LIGO detector network are currently the most sensitive gravitational wave detectors in operation. During the recent S5 Science Run, discussed later in section 1.6.1, the strain sensitivity in the 4 km Hanford detector was seen to be $\sim 2 \times 10^{-23}$ $/\sqrt{\text{Hz}}$ at 150 Hz. The sensitivity curves from all three LIGO detectors during this science run are shown in figure 1.8 [76].

GEO600: The German/UK collaboration gravitational wave detector is located in Ruthe (Hanover, Germany) [77]. Its arm length is only 600 m but this is doubled by having folded arms. To enhance the signal-to-noise ratio in the detector both power and signal recycling techniques are employed. Thermal noise performance in the GEO600 detector is improved significantly by using very low-loss fused silica suspensions instead of steel wires [78]. These improvements enable the sensitivities of GEO600 above several hundred hertz to approach those of the LIGO and VIRGO detectors in their initial operation. It can be seen later from figure 1.11 that in June 2006 the sensitivity of the GEO600 detector was approaching $\sim 2 \times 10^{-22}$ $/\sqrt{\text{Hz}}$ at ~ 500 Hz.

VIRGO: The VIRGO detector, pictured in figure 1.9, is a French/Italian 3 km arm

length detector situated near Pisa (Italy). Construction of this detector was completed in June 2003 and since then it has undergone several commissioning science runs [79, 80].

Figure 1.9: Panorama of the VIRGO gravitational wave detector near Pisa (Italy) with 3 km arms at right angles to each other.

The optics are suspended from 10 m high *super-attenuators* - an elaborate system of seven compound pendulums [81] increasing the performance of the detector down to 10 Hz. In October 2007 the sensitivity of the VIRGO detector at 500 Hz was $\sim 7 \times 10^{-23}$ $/\sqrt{\text{Hz}}$ [82].

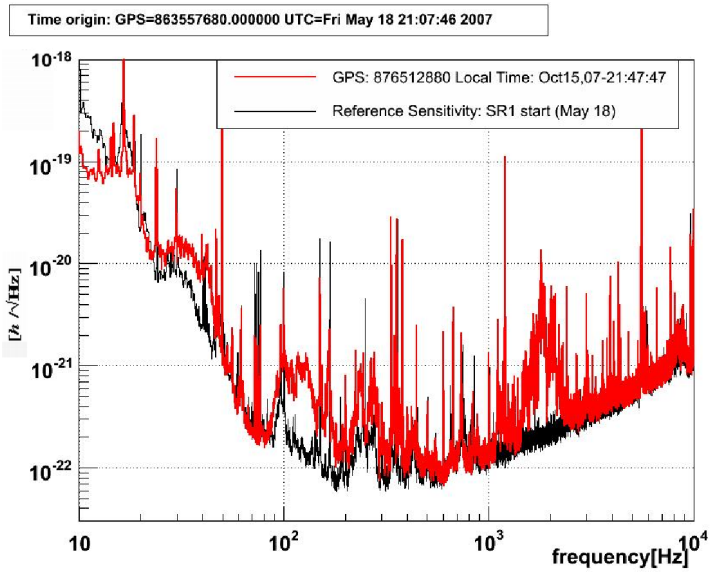

Figure 1.10: Sensitivity curves of the VIRGO interferometer detectors in October 2007.

TAMA300: The Japanese TAMA300 detector has a 300 m arm length and operates at the Tokyo Astronomical Observatory [83]. Like the current LIGO detectors it uses Fabry-Perot cavities in the arms and a power recycling mirror to enhance the laser power in the interferometer.

1.6.1 Gravitational Wave Searches (Science Runs)

For a gravitational wave to be distinguishable from all the different sources of noise, discussed earlier in section 1.5, it is desirable that it be seen in at least two independent interferometers. To date there have been five different science runs collecting coincident data from several gravitational wave detectors. The first science run $S1$ began with the LIGO and GEO600 detectors on the 23^{rd} August 2002 and ended on the 9^{th} September 2002. The fifth science run $S5$ was much longer, starting on the 4^{th} November 2005 and ended on the 1^{st} October 2007. A summary of the five science runs, and the detectors involved in these runs is given in table 1.2 [84]. Analysis of all the data collected throughout these runs is currently being undertaken, but as yet there has been no detection of gravitational radiation.

Science Run	Start Date	End Date	Detectors
S1	23^{rd} Aug 2002	9^{th} Sept 2002	LIGO, GEO600
S2	14th Feb 2003	14^{th} April 2003	LIGO, TAMA300
S3	31^{st} Oct 2003	9^{th} Jan 2004	LIGO, GEO600, TAMA300, ALLEGRO
S4	22^{nd} Feb 2005	23^{rd} Mar 2005	LIGO, GEO600, ALLEGRO, AURIGA
S5	4^{th} Nov 2005	1^{st} Oct 2007	LIGO, GEO600, VIRGO

Table 1.2: Summary of the five Science Runs involving the current network of gravitational wave detectors.

In between each of the five science runs improvements were constantly made to different aspects of the GEO600 detector resulting in correspondingly improved sensitivities as shown in figure 1.11 [71].

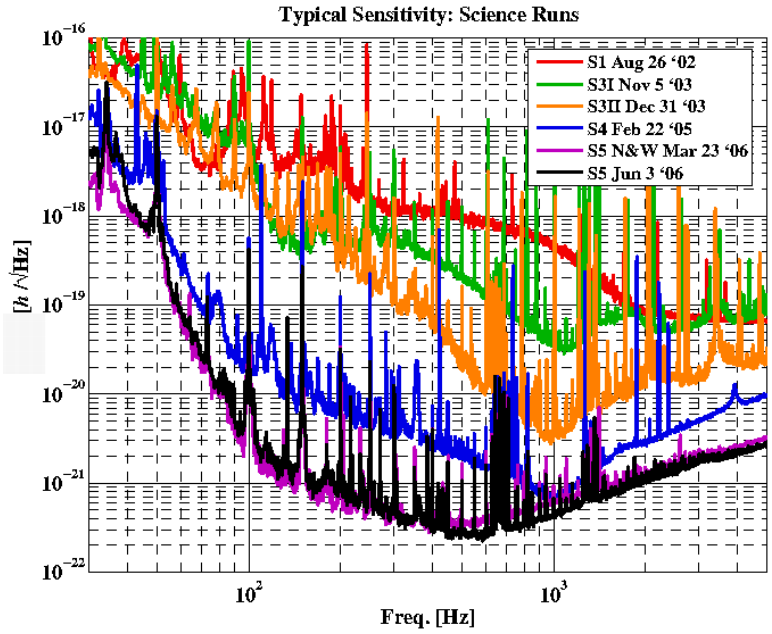

Figure 1.11: Sensitivity curves of the GEO600 detector during the S1, S3, S4 and S5 science runs.

1.7 The Next Generation of Gravitational Wave Detectors

The current bar and interferometric detectors provide the possibility for the first direct detection of gravitational waves. There is also a strong motivation to research and develop improved detectors with greater sensitivities because reducing the noise levels by one order of magnitude will increase the number of possible detectable sources by a factor of 1000, enhancing their use in the field of gravitational wave astronomy.

1.7.1 Second Generation (Advanced) Detectors

Enhanced LIGO: With the fifth science observing run complete a series of upgrades to the LIGO detectors will be implemented to provide an improved configuration called *Enhanced LIGO* [85]. The principal change in these de-

tectors is an increase in the laser power aimed at increasing the sensitivity above 100 Hz by a factor ~ 2.5. To reduce the effects of environmental noise the dark port sensing system will be placed under vacuum on a seismically isolated platform. A filter cavity will also be installed in the beam path to clean up the light and reduce shot noise.

Advanced LIGO: The LIGO Scientific Collaboration propose an *Advanced LIGO* detector network with sensitivities improved by more than a factor of ten. This increase would result in the one year observation time of the recently completed S5 science run to be equalled in roughly three hours [86]. Targets have been set to achieve this sensitivity including a reduction by a factor of 40 in seismic noise at 10 Hz, a reduction by a factor of 15 in thermal noise, and a 10 times reduction in photoelectron shot noise.

In order to achieve such goals several improvements need to be implemented including the adoption of fused silica fibres from the GEO600 detector [87] and improved seismic isolation systems [87, 67]. Signal recycling will be introduced, as discussed in section 1.4, along with the use of higher laser powers. The installation of these upgrades will begin around 2010 with the aim of commencing observations in 2014.

Advanced VIRGO: This will be a major upgrade to the VIRGO detector to be achieved in two steps. After the first set of improvements the *VIRGO+* detector [88] will have increased laser power and the introduction of a thermal compensation system to counteract optical distortions. At this stage it will also have new payloads, possibly with fused silica suspensions, as well as improvements to the electronics.

This will lead into the second set of upgrades creating an *Advanced VIRGO* detector which should have sensitivity over the entire detector bandwidth improved by an order of magnitude. The target of this research and development is to make Advanced VIRGO operational at the same time as the Advanced LIGO detectors.

GEO-HF: The shorter arm length of GEO600 results in it not being able to match the sensitivities of the Advanced LIGO and VIRGO detectors over their frequency range. Despite this, it will be able to continue operations during the down-time when the 4 km LIGO and VIRGO detectors are being upgraded. GEO600 will work along with the 2 km LIGO instrument and the bar detectors to provide an 'Astrowatch' function. Instead, the sensitivity of GEO600 for high frequencies will be improved in small sequential upgrades to reduce the thermal noise level and photoelectron shot noise. The development of prototypes and installation of suitable upgrades is called the *GEO-HF Project* [89].

GEO600 can operate with optimised tuning at low frequencies for continued network analysis, or tuned for high frequency performance as *GEO-HF*. The advantage of GEO600 is that it can be switched between either low or high frequency observations depending on the coverage of the LIGO and VIRGO detectors while their upgrades are implemented.

1.7.2 Third Generation Detectors

Increasing the sensitivity of interferometric gravitational wave detectors by a further order of magnitude will increase the number of detectable sources of gravitational waves by a further factor of 1000. However, improving sensitivities beyond the levels targeted by the second generation of interferometric gravitational wave detectors is challenging. Even with anticipated improvements to mirror coatings and substrate materials the thermal noise associated with the mirrors and their coatings will start to limit achievable sensitivities. The higher laser powers required to reduce photoelectron shot noise at higher frequencies and increased levels of power held inside the Fabry-Perot cavities increase the heat deposited in the substrate, the optical effects of which become increasingly difficult to control.

New techniques are likely to be required to alleviate these problems including the use of cryogenics to diminish thermal noise levels and possibly non-transmissive optical layouts to reduce thermal distortions. Squeezing light may be useful to improve the sensitivity of detectors because it may be possible to employ it to beat the standard quantum limit [90].

Discussions are underway for writing a White Paper for a third generation interferometric gravitational wave detector in the United States of America. There is also a design study beginning for a combined VIRGO/GEO European Detector called the '*Einstein Telescope*' (ET) [91] with research currently being undertaken across eighteen European laboratories as part of the STREGA project [92]. This project has the aim of reducing thermal noise in gravitational wave detectors at low temperatures.

1.7.3 Space-Based Detectors

The formation of a massive black hole with mass $10^3 - 10^6$ $M_\odot$ is the largest expected source of gravitational waves in the Universe. The signals from such events lie in the $10^{-4} - 10^{-1}$ Hz frequency range which due to Newtonian noise would be hard to detect using ground-based detectors. The only feasible way to detect signals in such a low frequency band is to use an interferometer in space.

A joint NASA/ESA mission is under development to create a space-based Laser Interferometer Space Antenna (*LISA*) [93]. LISA will consist of three drag-free spacecraft creating an equilateral triangle of three interferometers with arm lengths 5×10^6 km, as represented in figure 1.12 [94]. This array of spacecraft will fly in an Earth-like orbit around the Sun $\sim 20^\circ$ behind the Earth. Each craft accommodates two masses which form the end points of the three interferometers. A passing gravitational wave acting on LISA will change the length of one of the 5×10^6 km arms relative to the other. LISA is currently planned to be launched in 2015.

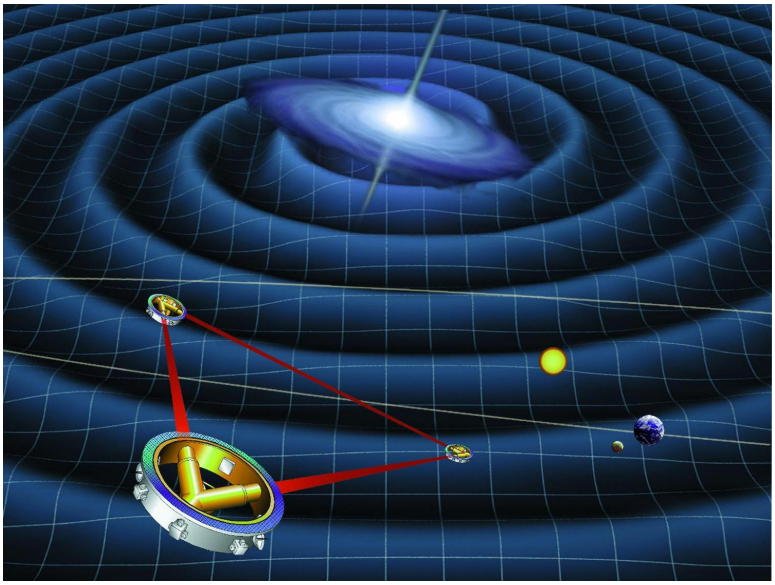

Figure 1.12: The Laser Interferometer Space Antenna consists of three spacecraft orbiting the sun in an equilateral triangular configuration, separated from each other by 5×10^6 km.

1.8 Conclusion

The experimental search for gravitational waves is a worldwide wide effort with several resonant bar and long-baseline interferometric detectors in operation around the world. They are now reaching sensitivities which allow the possibility of the detection of gravitational waves emitted from astronomical sources. The detection of this kind of radiation will open up an entirely new field in astronomy facilitating the study of known sources and discovery of new sources in our Universe.

However, to increase their use for gravitational wave astronomy, it is essential to improve the sensitivities of interferometric gravitational wave detectors. This introduces significant challenges in improving the levels of thermal noise in the test mass mirror substrates, the coatings applied to them and in the suspensions which are used to hang them. In addition the effects of thermal loading resulting from increased levels of laser power will need to be overcome.

The experimental research detailed in this thesis focusses on the measurement of mechanical loss of various substrate materials, coatings and chemical bonds proposed for use in future detectors. The third generation of detectors may need a non-transmissive optical layout with a material of high thermal conductivity such as silicon. Investigations relevant to that are reported later in this thesis.

Chapter 2

Thermal Noise in Interferometric Gravitational Wave Detectors

2.1 Introduction

Thermal noise associated with the coated mirror substrates and lower stage suspensions is one of the most significant noise sources at the lower operating frequency range of interferometric gravitational wave detectors. A mirror substrate suspended as a pendulum is a mechanical system which has many modes of oscillation. Each of these resonant modes has thermal energy associated with the vibrational, translational and rotational degrees of freedom of the system.

For a classical system, the Boltzmann distribution of energy from the Equipartition Theorem [95] states the mean energy of each of these degrees of freedom is equal to $\frac{1}{2}k_{\mathrm{B}}T$, where k_{B} is Boltzmann's Constant (1.38×10^{-23} JK^{-1}) and T is the temperature in Kelvin. This thermal energy influences the coherent motion of the entire system. In an interferometric gravitational wave detector the thermal energy of the mirrors and suspensions results in displacements of the mirror faces, forming a noise source in the instrument.

The effect of this thermally induced motion can be reduced in two ways. One technique is to cool the optics of the interferometer to reduce the levels of thermal energy within the mirrors and suspensions. However, cooling the optics while keeping a low-noise environment is not an easy task. This is being considered as a technique for use in a third generation of gravitational wave detectors, as discussed in section 1.7.2.

The second option is to use materials of low mechanical loss. In low loss systems the thermally induced motion lies predominantly within the narrow frequency band of the mechanical resonances of the system. For systems where the off-resonance thermal noise of each resonant modes is uncorrelated, the narrower the resonances the lower the off-resonance thermal displacement noise. Details of how this thermal noise appears in an interferometric gravitational wave detector is detailed in this chapter.

2.2 Brownian Motion

In 1827, Scottish botanist Robert Brown reported microscopical observations of particles of plant pollen which, when left to float freely on the surface of water, moved in a vigorous and irregular manner [96]. Almost 80 years later it was shown by Einstein that this motion was a result of the stochastic collisions of the molecules of water with the pollen grains - that is the motion was due to the fluid surrounding the pollen and not the particles themselves [97]. Einstein also realised that as a result of these impacts the pollen grains lost their initial kinetic energy while they moved through the water. This introduced a dissipation process [98].

2.3 The Fluctuation-Dissipation Theorem

The relationship described by Einstein was an early example of the Fluctuation-Dissipation Theorem developed later by Callen et al. [99, 100]. This provided a general relationship between the excitation of a system (fluctuation) and the friction (dissipation) for any linear system in thermal equilibrium.

The Fluctuation-Dissipation Theorem relates the power spectral density of the fluctuating mechanical driving force, $S_F(\omega)$, to the dissipative (real) part of the mechanical admittance, $\Re[Y(\omega)]$, such that

$$S_F(\omega) = \frac{4k_{\mathrm{B}}T}{\omega^2}\Re[Y(\omega)]. \tag{2.1}$$

The Fluctuation-Dissipation theorem enables predictions of thermal noise from dissipation. However, the analysis within equation 2.1 and the sections which follow deals with systems where the off-resonance thermal noise of each resonant mode is uncorrelated. Instead, for real, multi-mode systems such as gravitational wave detector mirror suspensions, further considerations must be taken into account, as discussed later in section 2.6.

2.4 Sources of Dissipation

2.4.1 External Sources of Dissipation

There exists a variety of external sources of dissipation which can have an effect on the cumulative levels of thermal noise within an interferometric gravitational wave detector. Some examples include:

Gas Damping External viscous damping is experienced by the mirrors and their suspensions due to the effects of residual gas molecules in the vacuum systems in which the suspensions are mounted.

Recoil Damping Energy may be lost from the pendulum suspension into a recoiling support structure.

Frictional Damping Friction at the suspension point and where suspension elements contact the test substrate may introduce stick-slip damping.

Careful design of the technical aspects of the suspensions is essential to ensure these types of damping are minimised - see for example [101].

2.4.2 Internal Sources of Dissipation

Once all the external sources of dissipation have been minimised, the dominant source of thermal noise is a result of the internal dissipation of the suspended optics. Internal dissipation can arise when a material responds anelastically to a force acted upon it.

When an ideal elastic material is acted upon by a force, a stress σ is produced for which there is a resultant strain within the material. This strain, ε, is related to the Modulus of Elasticity M such that

$$\sigma = M\varepsilon. \tag{2.2}$$

In an elastic response, the stress and strain are related to the compliance J of the material so that

$$\varepsilon = J\sigma \tag{2.3}$$

and J is related to the stored energy due to the induced deformation.

When a force is applied to anelastic materials the body returns to a new equilibrium state after a relaxation time. In experiments to study the behaviour of a material

a periodic stress is applied to a system. The stress and resulting strain can be modelled in complex form, where the strain ε follows the stress σ after a phase lag, ϕ, such that

$$\sigma = \sigma_0 e^{i\omega t} \tag{2.4}$$

where σ_0 is the stress amplitude and ω the angular frequency ($\omega = 2\pi f$, where f is the vibration frequency), and

$$\varepsilon = \varepsilon_0 e^{i(\omega t - \phi)}. \tag{2.5}$$

where ε_0 is the strain amplitude. ϕ is the angle the strain lags behind the stress and is commonly referred to as the loss angle, which for an ideal elastic material is $\phi = 0$. However, for the anelastic case ϕ is generally non-zero, so that the ratio $\frac{\sigma}{\varepsilon}$ is a complex quantity. From equation 2.2 the Modulus of Elasticity must therefore also be complex, defined as $M^*(\omega)$, noting that it is a function of ω.

It is useful to write

$$M^*(\omega) = M_1(\omega) + iM_2(\omega) \tag{2.6}$$

where $M_1(\omega)$ and $M_2(\omega)$ are the real and imaginary parts respectively and

$$\tan\phi = \frac{M_2}{M_1}. \tag{2.7}$$

It is then possible to calculate the energy stored and the energy dissipated in a cycle of the applied stress, taking $\varepsilon = \varepsilon_0 \cos\omega t$ and $\sigma = M^*\varepsilon$. The energy ΔE dissipated in a full cycle, per unit volume, is [102]

$$\Delta E = \oint \varepsilon d\sigma = \pi M_2 \varepsilon_0^2 \tag{2.8}$$

and the maximum stored energy E per unit volume is given by [102]

$$E = \int_{\omega t=0}^{\pi/2} \varepsilon d\sigma = \frac{1}{2} M_1 \varepsilon_0^2. \tag{2.9}$$

The ratio of energy dissipated to the maximum stored energy is then, from equation 2.7, related to the loss angle ϕ

$$\frac{\Delta E}{E} = 2\pi \frac{M_2}{M_1} = 2\pi \tan\phi. \tag{2.10}$$

Since $\tan\phi = \phi(1 + \frac{1}{3}\phi^2 + \frac{2}{15}\phi^4 + \ldots)$ from its Taylor Series expansion and the assumption that $\phi^2 \ll 1$, it can be approximated that $\tan\phi \simeq \phi$. Consequently equation 2.10 can be rearranged to give

$$\phi = \frac{1}{2\pi}\frac{\Delta E}{E}. \tag{2.11}$$

ϕ gives a measure of the fractional energy loss per cycle due to anelastic behaviour and is more commonly known as the *internal friction* of the material.

2.5 Power Spectral Density of Displacement Thermal Noise in a Simple Harmonic oscillator

The level of Brownian thermal noise can be obtained from a direct application of the Fluctuation-Dissipation Theorem. For simplicity, the thermal noise spectrum will be first derived for a damped harmonic oscillator represented by a mass m on a spring. For an elastic spring, the spring constant is k and the restoring force is defined as

$$F_{\text{restoring}} = -kx. \tag{2.12}$$

However, to include the effects of dissipation resulting from internal friction, equation 2.12 must be re-written in complex form, as represented in figure 2.1. Therefore the force associated with the spring becomes [102]

$$F_{\text{spring}}(\omega) = -k(1 + i\phi(\omega))x \tag{2.13}$$

where the loss factor $\phi(\omega)$ represents the phase lag between the instantaneous force and the displacement x of the spring.

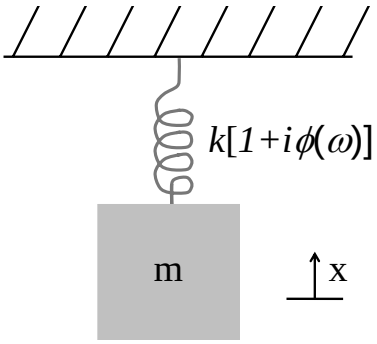

Figure 2.1: Oscillator consisting of mass m and a spring with complex spring constant $k(1 + i\phi(\omega))$.

The equation of motion for such a damped harmonic oscillator is

$$F(\omega) = m\ddot{x} + k(1 + i\phi(\omega))x \tag{2.14}$$

where $F(\omega)$ is the internal thermal driving force. If $x \propto e^{i\omega t}$ then $v = i\omega x$ and $\ddot{x} = i\omega v$, which allows equation 2.14 to be rewritten in terms of velocity

$$F(\omega) = i\omega m v - i\frac{k}{\omega}(1 + i\phi(\omega))v. \tag{2.15}$$

The fluctuating force is related to the impedance, $Z(\omega)$, such that

$$\begin{aligned} Z(\omega) &= \frac{F(\omega)}{v} \\ &= i\omega m - i\frac{k}{\omega}(1 + i\phi(\omega)) \\ &= i\left(\omega m - \frac{k}{\omega}\right) + \phi(\omega)\frac{k}{\omega}. \end{aligned} \tag{2.16}$$

From equation 2.16 the admittance can be obtained as $Y(\omega) = Z(\omega)^{-1}$

$$Y(\omega) = \frac{\omega}{k\phi(\omega) + i(\omega^2 m - k)}. \tag{2.17}$$

Multiplying both the numerator and denominator of equation 2.17 by the complex conjugate of the denominator $(k\phi(\omega) - i(\omega^2 m - k))$ gives

$$Y(\omega) = \frac{\phi(\omega)\frac{k}{\omega} - i\left(\omega m - \frac{k}{\omega}\right)}{[\phi(\omega)\frac{k}{\omega}]^2 + \left(\omega m - \frac{k}{\omega}\right)^2}. \tag{2.18}$$

Using the Fluctuation-Dissipation Theorem, the real part of equation 2.18 can be substituted into 2.1. This gives the power spectral density of displacement thermal noise, $S_x(\omega)$, of an oscillator with mass m at temperature T, associated with a resonant mode of frequency ω_0 of

$$S_x(\omega) = \frac{4k_{\mathrm{B}}T}{\omega m}\frac{\phi(\omega)\omega_0^2}{[(\omega_0^2 - \omega^2)^2 + \omega_0^4\phi(\omega)^2]} \tag{2.19}$$

where the angular resonant frequency $\omega_0^2 = \frac{k}{m}$ and $\phi(\omega)$ is the mechanical dissipation, or loss factor, of the oscillator [103].

At resonance, equation 2.19 may be simplified such that $S_x(\omega) \propto \frac{1}{\phi(\omega)}$ resulting in a large $S_x(\omega)$ if $\omega_0 \ll 1$. Also for frequencies far away from a resonant mode of frequency ω_0 the power spectral density of the displacement thermal noise is proportional to $\phi(\omega)$, which when $\omega_0 \ll 1$, results in a small $S_x(\omega)$ [104]. One limit to how accurately the position of the front face of the mirrors can be sensed using an interferometer is determined by off-resonance thermal displacement noise.

Consequently, the test masses and suspensions in interferometric gravitational wave detectors have been manufactured using materials of low mechanical loss $\phi(\omega)$. As discussed in section 1.6 all current interferometric detectors use fused silica for their mirror substrates because the mechanical loss of fused silica is known to be comparatively low [105, 106, 107]. The GEO600 gravitational wave detector also incorporates fused silica suspension fibres in the final suspension stage since silica has a significantly lower mechanical dissipation than carbon-steel [78].

However, the analysis derived from equation 2.1 deals with single resonant modes. In models based on the approach detailed in this section the laser beam reflected off the front face of a test mirror is considered to be sensing the incoherent sum of the displacement thermal noise in the 'tails' of the individual resonant modes. In reality, these losses are spatially inhomogeneous. Consequently, there are correlations between the fluctuations in the motions of different resonant modes, for which this summation does not account [108]. Instead, when dealing with *real* multi-mode mechanical systems, a different approach needed to be developed, as detailed in section 2.6.

2.6 Thermal Noise Resulting from Spatially Inhomogeneous Mechanical Dissipation

For spatially inhomogeneous mechanical loss it is necessary to use the approach described by Levin [109]. This allows the actual spatial distribution of mechanical loss and the detailed shape of the laser beam to be taken into account. Levin considered the effect of applying a notional oscillating pressure P to the front face of the test mass of the form

$$P = \frac{F_0}{\pi r_0^2} e^{-\frac{r^2}{r_0^2}} \cos(\omega t) \tag{2.20}$$

where F_0 is the amplitude of peak force and r_0 is the radius of the laser beam where the intensity of the beam has decreased to a level of $\frac{1}{e}$ of its maximum.

Levin then defines the real part of the mechanical admittance $\Re[Y(\omega)]$ in terms of the energy transferred into the test mass by the oscillating pressure and subsequently dissipated by thermoelastic heat flow: a form of dissipation discussed in section 2.9. From this, the power dissipated W_{diss} is then calculated, averaged over the period $\frac{2\pi}{\omega}$ of the pressure oscillations, to give

$$\Re[Y(\omega)] = \frac{2W_{\text{diss}}}{F_0^2}. \tag{2.21}$$

This produces a power spectral density of displacement thermal noise of

$$S_x(\omega) = \frac{8k_{\text{B}}T}{\omega^2}\frac{W_{\text{diss}}}{F_0^2}. \tag{2.22}$$

It can be shown that

$$W_{\text{diss}} = \omega \int_{\text{vol}} \varepsilon(x,y,z)\ \phi(x,y,z,\omega)\ d\text{V} \tag{2.23}$$

where ε is the energy density of the elastic deformation at the maximum applied notional pressure.

From equations 2.22 and 2.23 it is clear that there is no general formula which can be given for the case of inhomogeneous loss. However, for spatially homogeneous loss, and assuming that the diameter of the beam is considerably smaller than the dimensions of the mass, a test mass may be modelled as forming a half-infinite slab. It can then be shown that the thermal displacement noise due to Brownian motion of a test mass substrate having mechanical loss $\phi_{\text{substrate}}(\omega)$ is given by [110]

$$S_x(\omega) = \frac{4k_{\text{B}}T}{\omega}\ \frac{1-\nu^2}{\sqrt{2\pi}Yr_0}\ \phi_{\text{substrate}}(\omega) \tag{2.24}$$

where Y and ν are the Young's Modulus and Poisson's Ratio of the material and r_0 the radius of the laser beam where the intensity has fallen to $\frac{1}{e}$ of the maximum.

The notional force is applied to the front face of the test mass mirror. Deformation is biggest, closest to where the force is applied. Consequently, dissipation physically located close to the front surfaces of the mirrors contributes a greater level of thermal displacement noise than dissipation located far from the front face of the mirror.

This is of significant importance for the design of test mass suspensions for the next generation of interferometric gravitational wave detectors because in order to maintain low optical losses it is necessary to use ion-beam-sputtered multi-layer dielectric coatings. These coatings are applied to the front faces of the test substrates to give highly reflecting mirror surfaces. Unfortunately, such coatings are known to have much higher levels of mechanical loss of the order 10^{-4} [111] than that of the mirror substrate material $\sim 10^{-8}$ [105].

Decreasing the mechanical dissipation associated with the mirror coatings it therefore currently a substantial area of study. Measurements of the mechanical dissipation of test substrates with mirror coatings applied to them are presented in chapters 3 and 5.

2.7 Thermoelastic Dissipation

A component of the thermal noise significant in many crystalline materials, such as sapphire or silicon, results from statistical fluctuations in temperature. Thermoelastic displacement noise results from temperature fluctuations throughout the body of a test mass creating displacements in the front surface of the mirror due to coupling via the coefficient of thermal expansion α. These temperature fluctuations cause areas of the mass to expand or contract as they heat up or cool down. While the mass attempts to restore the thermal equilibrium, heat flows from the hotter areas to the cooler regions, which is a source of dissipation.

When the mechanical system is at rest, these local temperature fluctuations lead to motion through the coefficient of thermal expansion α. In the thin fibres used as suspension elements for the mirrors in gravitational wave detectors this dissipation mechanism $\phi(\omega)_{\mathrm{TE}}$ can be quantified via the model [102]

$$\phi(\omega)_{\mathrm{TE}} = \frac{Y\alpha^2 T}{\rho C} \frac{\omega\tau}{1+(\omega\tau)^2} \tag{2.25}$$

where Y is the Young's Modulus, α is the thermal coefficient of expansion, ρ is the

density of the substrate, C is the specific heat capacity per unit volume and τ is the relaxation time of the laser beam spot on the surface.

Additionally, Braginsky et al showed that thermoelastic dissipation is also relevant in test mass mirrors [112]. The power spectral density of thermoelastic displacement noise $S_{\mathrm{TE}}(\omega)$ in a test mass, approximated as half-infinite, where the laser beam diameter is much smaller than the dimensions of the mirror, is given as

$$S_{\mathrm{TE}}(\omega) = \frac{4\sqrt{2}}{\sqrt{\pi}} \frac{k_{\mathrm{B}} T^2 \alpha^2 (1+\nu)^2 \kappa}{\rho^2 C^2 r_0^3 \omega^2} \tag{2.26}$$

where the radius of the laser beam r_0 is much smaller than the radius of the mirror, ν is the Poisson's Ratio of the substrate and κ is the thermal conductivity.

For the case of a finite test mass, Liu and Thorne [110] determined a correction factor approximately equal to unity for a typical test substrate.

The level of this thermoelastic displacement noise can be equal to or larger than some other sources of thermal noise within the operating frequency band of interferometric gravitational wave detectors, as discussed later in section 2.9.

2.8 Brownian Noise Associated with Dielectric Mirror Coatings

As mentioned earlier, the application of dielectric coatings to the front faces of the test substrates to form highly reflective mirrors has been identified as a significant source of dissipation [113]. Typically, these coatings are formed with alternating layers of ion-beam sputtered amorphous silica SiO_2 and tantala Ta_2O_5 [114]. As detailed in section 2.6 for the approach by Levin, any dissipation physically located close to the front surfaces of the mirrors will contribute to a greater level of thermal displacement noise. Consequently the mechanical dissipation of these coatings strongly contributes to the noise in this region.

The power spectral density of Brownian motion associated with the mirror coatings may be expressed as [113, 115]

$$S_x(\omega) = \frac{4k_{\rm B}T}{\sqrt{\pi}} \frac{1}{\omega^2 Y} \left[\phi_{\rm substrate}(\omega) + \frac{2}{\sqrt{\pi}} \frac{d}{\omega} \left(\frac{Y'}{Y}\phi_{\parallel} + \frac{Y}{Y'}\phi_{\perp}\right)\right] \tag{2.27}$$

where Y and Y' are values of the Young's Modulus for the substrate and the coating respectively. $\phi_{\parallel}$ and $\phi_{\perp}$ are the values of the mechanical loss from a coating of thickness d for strains parallel and perpendicular to the coating surface.

2.9 Thermoelastic Noise Associated with Dielectric Mirror Coatings

An important limit to the sensitivity of interferometric gravitational wave detectors results from thermoelastic dissipation associated with the different thermo-mechanical properties of the layers which form the dielectric coatings [116, 2]. In the operating frequency band of an interferometric gravitational wave detector the power spectral density of thermoelastic dissipation from a multi-layer dielectric coating of a thickness d can be written as [117]

$$S_x(\omega) \approx \frac{8\sqrt{2}k_{\rm B}T^2}{\pi\sqrt{\omega}} \frac{d^2}{r_0^2} (1+\sigma_{\rm S})^2 \frac{C_{\rm avg}^2}{C_{\rm S}^2} \frac{\alpha_{\rm S}^2}{\sqrt{\kappa_{\rm S} C_{\rm S}}} \tilde{\Delta}^2 \tag{2.28}$$

where properties referring to the substrate are denoted by the subscript 's' and

$$\tilde{\Delta}^2 \equiv \left\{ \frac{C_{\rm S}}{2\alpha_{\rm S} C_{\rm avg}} \left(\frac{\alpha}{1-\sigma} \left[\frac{1+\sigma}{1+\sigma_{\rm S}} + (1-2\sigma_{\rm S}) \frac{Y}{Y_{\rm S}} \right] \right)_{\rm avg} - 1 \right\}^2 . \tag{2.29}$$

The averaging terms $(X)_{\rm avg}$ denote properties which are averaged in proportion to their fractional amounts. For a coating comprising of two alternating materials 'a' and 'b' of thicknesses $t_{\rm a}$ and $t_{\rm b}$ respectively, the volume averaging operator $(X)_{\rm avg}$ is defined as

$$(X)_{\rm avg} = \frac{t_{\rm a}}{t_{\rm a}+t_{\rm b}} X_{\rm a} + \frac{t_{\rm b}}{t_{\rm a}+t_{\rm b}} X_{\rm b}. \tag{2.30}$$

Recent interferometric studies of the displacement noise in suspended multi-layer optics are in broad agreement with the predictions using the above models for coating thermal noise [118].

2.10 Thermal Noise Sources in Interferometer Suspensions

2.10.1 Pendulum Modes

As discussed in section 1.5.4, the test masses are suspended as pendulums. The lengths of these suspensions are chosen such that the resonant frequency of the pendulum, typically $0.6 - 1$ Hz, lies well below the low frequency end of the detection band. These pendulums however also have thermal noise associated with the material from which the test mass mirrors are hung.

The mechanical loss of a pendulum of length l at resonant frequency ω_0 is related to the mechanical loss of the suspension material $\phi_{\mathrm{mat}}(\omega_0)$ by [119]

$$\phi_{\mathrm{pend}}(\omega_0) = \phi_{\mathrm{mat}}(\omega_0)\ \frac{\xi n\sqrt{TYI}}{2mgl} \tag{2.31}$$

for a suspension consisting of n suspension elements. T is the tension in each suspension element, Y is the Young's Modulus of the suspension material and I is the moment of the cross-sectional area. ξ takes the value of 1 or 2 depending on whether the attachment points of the suspension elements constrain the elements to bend at the top only or at both the top and bottom respectively [120].

The power spectral density of the displacement of the front face of a test mirror due to the pendulum mode can, above the pendulum resonant frequency ω_0, be approximated for a test mirror of mass m using equation 2.19

$$S_x(\omega) \approx \frac{4k_{\mathrm{B}}T}{m}\ \frac{\omega_0^2}{\omega^5}\ \phi_{\mathrm{pend}}(\omega). \tag{2.32}$$

This assumes that the laser beam impinges on the front face of the test mass so that the thermal noise from the pitch, yaw, rotational and torsional modes of the pendulums do not significantly couple.

2.10.2 Violin Modes

The suspension elements under tension themselves have resonant modes called *violin modes*. The violin modes form a harmonic series which lies within the operating frequency band of an interferometric gravitational wave detector. If the damping is considered to be homogeneous, then the losses associated with the violin modes of the suspension are related to the loss of the pendulum mode such that

$$\phi_{\text{violin}}(\omega) = 2\phi_{\text{pend}}(\omega) \tag{2.33}$$

which holds true depending on the position of the attachment points [120]. The resulting off-resonance displacement thermal noise introduced to the front face of the test mass from the violin modes of the suspension elements is much smaller than the displacement resulting from the pendulum modes and internal resonant modes of the test mass.

The suspensions are formed using low mechanical loss materials, therefore most of the thermally induced motion lies in narrow bands around the resonant frequencies of the violin modes. Techniques have been developed to remove the thermal displacement noise of the violin modes from the signals recorded by interferometric gravitational wave detectors [121].

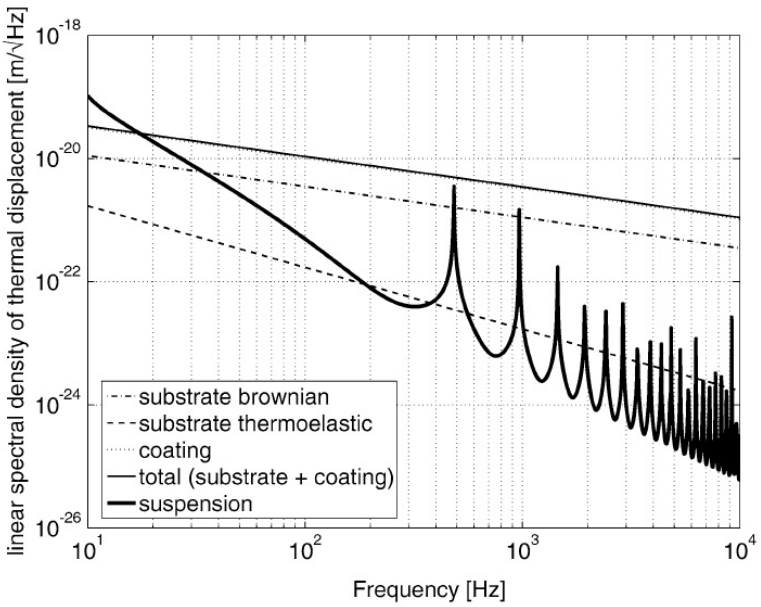

Figure 2.2: Levels of thermal and thermoelastic noise calculated in a single suspended tantala/silica coated fused silica mirror illuminated by a laser beam with radius $r_0 = 3.9$ cm.

2.11 Effect of Combined Thermal Noise in a Gravitational Wave Detector

To evaluate the effect of the total thermal noise in an interferometer on the achievable displacement sensitivity, it is necessary to combine the individual contributions to the thermally driven motion of the optics. This sums the loss components from the internal modes of the mirror substrate, equation 2.24, the mirror coatings, equation 2.28, the pendulum mode of the suspension, equation 2.32, and the violin resonances. The expected levels of thermal noise in a typical interferometer mirror planned to be used in the upgrades of the first generation of detectors is estimated in [122] as shown in figure 2.2 for a test mass substrate with a loss of 5×10^{-9}.

2.12 Conclusion

One of the limiting factors to the displacement sensitivities of ground-based interferometric gravitational wave detectors is thermal noise. Analysis of the different sources of loss from the mirror substrates, coatings and the suspensions from which they are hung, enable estimates of the levels of thermal displacement noise to be calculated.

Inspection of figure 2.2 shows that for a typical design of suspended test mirror the source dominating the levels of thermal noise is that from the coatings applied to the mirror substrates. Therefore, in order to proceed beyond the first set of upgrades to interferometric gravitational wave detectors ways must be found to reduce the levels of thermal noise from these coatings.

Chapter 3

Measurements of Mechanical Loss of Silica Substrates and Highly Reflective Coatings

As discussed in Chapter 2, an important limit to the sensitivity of long-baseline gravitational wave detectors is set by off-resonance thermal noise in the interferometer's mirrors and their suspensions. The bulk of the research presented in this thesis concentrates on the study of the mechanical dissipation, or loss, of materials being used, or proposed for use, as mirror substrates or mirror coatings in these detectors.

The magnitude of off-resonance thermal noise is related to the mechanical loss of the substrate material to the extent that materials with a low level of mechanical loss have lower levels of off-resonance thermal noise. As a consequence, the materials used for the interferometer mirrors and their suspensions must be carefully selected to ensure that their thermal noise is minimised. Further to the pre-requisite that the test mirror material must have a low mechanical loss at room temperature, to be suitable for use in an interferometric gravitational wave detector it must also satisfy a number of other requirements detailed below.

3.1 Requirements for Potential Test Mass Mirrors

There is a number of factors which affect the choice of material for the mirror substrates used in long-baseline gravitational wave detectors.

- As discussed, the material must have a low mechanical loss factor.
- It should be possible to produce mirrors in sizes suitable for use in a gravitational wave detector, in mass up to several tens of kilograms, with the aim of reducing the effects of photon recoil and the Heisenberg Uncertainty Principle [123].
- The interferometer is illuminated using a high-power laser beam. For interferometers using transmissive optics the material should be transparent and have a low optical loss at the wavelength of the laser light used (1064 nm in all current detectors) so that the heat deposited in the material is kept to a minimum [124].
- The mirror substrate should have a high thermal conductivity and a low thermal expansion so that when heat is deposited in it by absorption of residual laser light the resulting thermo-mechanical distortion is minimised [124].
- The material should be suitable for polishing to sub-angstrom surface roughness [125].
- The refractive index should change as little as possible with temperature to minimise the thermal lensing effects of transmitted laser beams [124].
- The material should be able to be bonded onto suspension elements by the low loss hydroxide catalysis bonding technique discussed in more detail in the following chapter [126, 127].

There is a small selection of materials which have low enough mechanical losses to be used potentially in a gravitational wave detectors. In particular, fused silica has

a range of properties which makes it appropriate for this purpose. It can be manufactured to have low optical absorption, can be polished and coated to appropriate specifications and is available in the sizes required. Experiments undertaken in a number of different laboratories suggest that the mechanical losses in different types of silica lie in the range of 1×10^{-6} to 5×10^{-9} [105, 106, 107].

The combination of these properties has led to all the current interferometric gravitational wave detectors utilising fused silica as a test mass material. It is also the baseline choice for the test mass substrate in the planned upgrades to the LIGO and Virgo detector systems. However, as will be discussed, the properties of fused silica set limits to the performance of all current and upgraded detectors. Therefore to improve detector performance further, different materials with lower mechanical losses are expected to be required. Research on the properties of other materials is presented in chapters 5 and 6 of this thesis.

3.2 Multi-Layer Dielectric Coatings

Interferometric gravitational wave detectors require test masses coated in such a way that they act as optically highly reflective mirrors. Metallic mirror coatings are not suitable because their optical absorption is too high. Instead, coatings are formed by applying ion-beam-sputtered dielectric layers to the front face of each test mass using alternate quarter wavelength layers of dielectric materials of different refractive indices in order to obtain a highly reflective surface. A schematic of such a coating, comprised of alternating materials with refractive index n_1 and n_2 respectively is shown in figure 3.1.

Each layer of dielectric material is $\lambda \setminus 4$ in optical thickness, where λ is the 1.064 μm wavelength of the Nd:YAG laser light used in an interferometric gravitational wave detector. The optical thickness of an individual layer is related to the physical thickness h such that

$$\frac{\lambda}{4} = nh \tag{3.1}$$

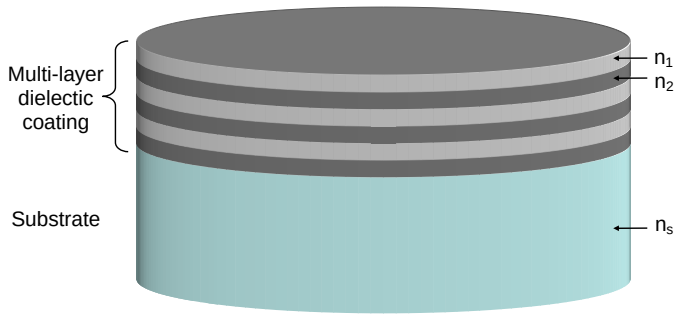

Figure 3.1: Schematic of a multi-layer dielectric coating sputtered onto a substrate, comprising of alternating layers of material with refractive index n_1 and n_2 respectively.

where n is the refractive index of the material at that wavelength.

These coatings are designed to be highly reflective at a narrow band around this wavelength of light, while having a very low optical absorption and scatter. All current interferometric detectors use mirrors whose coatings are formed from ion-beam-sputtered layers of tantalum pentoxide (Ta_2O_5) and silica (SiO_2) [114].

Although the test mass substrate materials used have low mechanical loss, the addition of coatings introduces another source of dissipation and thus of thermal noise in the detector [128]. It is therefore important to quantify the loss of these dielectric mirror coatings so that their thermal noise and the consequent limits to detector sensitivity can be calculated. This study is of immediate relevance to the planned upgrade of the LIGO detector system, *Advanced LIGO* [129] and, in addition, forms part of the Glasgow group's research contributing towards the design of the next generation of gravitational wave detectors.

3.3 Mechanical Loss of a Test Substrate - Measurement Principles

Each resonant mode of a test mass substrate can be modelled as a damped harmonic oscillator. The envelope of the amplitude A of freely decaying resonant motion of such an excited harmonic oscillator evolves as

$$A = A_0 \exp(-\frac{1}{2}\phi(\omega_0)\omega_0 \mathrm{t}) \tag{3.2}$$

where A_0 is the amplitude of the motion of the test mass's front face at the start of the decay, t is time, ω_0 is the resonant angular frequency and $\phi(\omega_0)$ is the loss at that frequency [130]. After taking the natural log of each side of equation 3.2, we find

$$\ln A = \ln A_0 - \frac{1}{2}\phi(\omega_0)\omega_0 \mathrm{t}. \tag{3.3}$$

If a mode is excited and then allowed to decay the natural log of the amplitude of motion can be plotted against time so that a straight line may be fitted to the ring down. The loss can then be determined using

$$\phi(\omega_0) = \frac{2\times \mid \text{gradient} \mid}{\omega_0} \tag{3.4}$$

where | gradient | is the magnitude of the gradient of the plot.

For the samples studied here, a Michelson interferometer is used to sense the motion of the front face of a mechanically excited test mass and the mechanical loss of each resonant mode of the sample found from the time taken for the motion to decay. As will be described, this arrangement can be used in the study of coating losses as well as studies of the effects of different test mass materials, sizes and aspect ratios on measured loss factors.

3.4 Experimental Procedure

To measure the mechanical loss of the resonant modes of a test mass it is necessary to mount the sample carefully to minimise any excess mechanical loss in the measurement. One of the most effective ways to isolate a mass from its surroundings is to hang it as a pendulum. A suspension formed from a single loop of silk thread has proved an effective choice, as shown in figure 3.2, and greasing the thread reduces frictional losses at the contact between the loop and test mass [125].

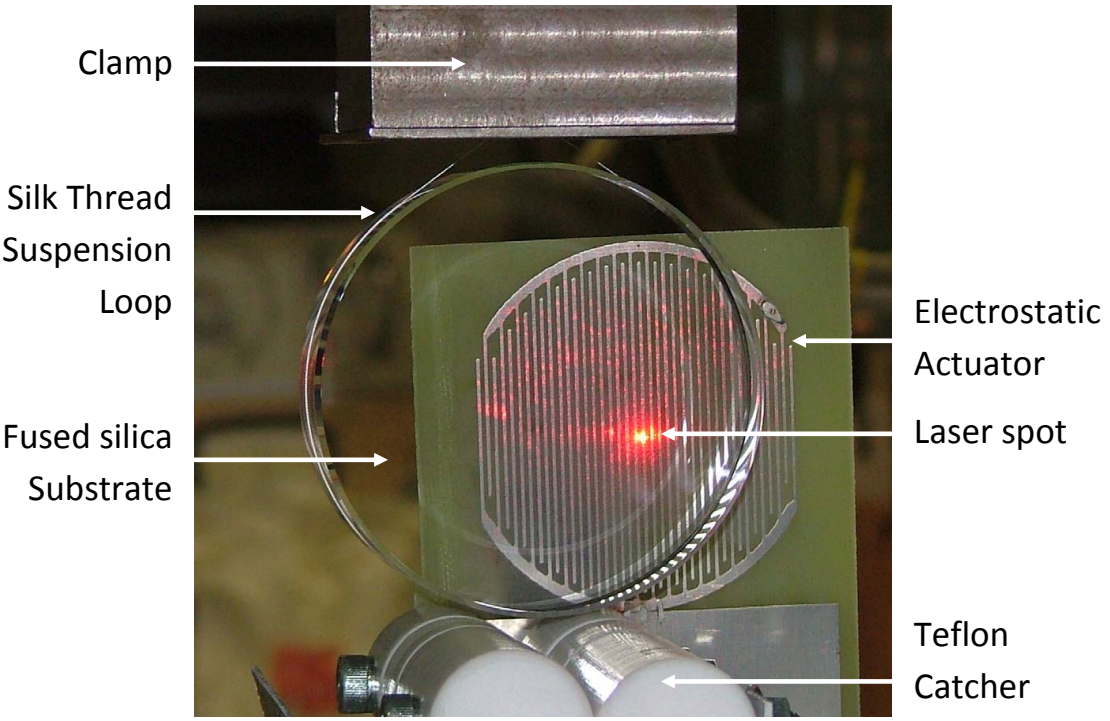

Figure 3.2: A 76.2 mm diameter by 25.4 mm thick fused silica test substrate suspended by a loop of silk thread.

To reduce the possibility of the test mass modes coupling with harmonics of the suspension "violin modes" and consequently increasing the measured loss, measurements are repeated for many different lengths of suspension loop [125]. To minimise gas damping of the excited motion the suspended mass is placed inside a vacuum tank, visible on the left-hand-side of figure 3.3, and the system pumped out to $\sim 10^{-5}$ mbar [16].

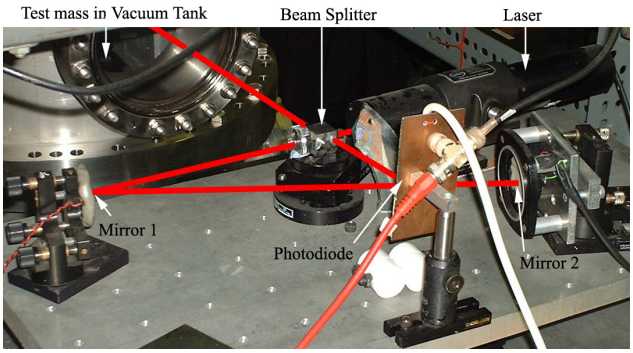

Figure 3.3: Michelson interferometer used for loss measurements

Low frequency bulk displacements of the test mass are of a greater magnitude than the laser wavelength, therefore it is important to remove the effects of lower frequency motion from the ring-down signal. This is done through the use of an electronic feedback system.

The first arm of the interferometer, used to sense test mass motion, is formed by reflecting laser light off the front face of the test mass. The second arm is folded and incorporates two mirrors, one mounted on a loudspeaker, '*Mirror 1*' in figure 3.3, and the other on a piezo-electric actuator, '*Mirror 2*'. The detected signal is then sent through a two-stage feedback system with suitable filtering such that the loudspeaker and piezo follow the low frequency bulk motion of the mass, while leaving high frequency motion $(10 - 90$ kHz) unaffected for recording.

The filtering stage takes the signal from the photodiode and firstly it is inverted. The signal is then amplified, or reduced, as required and the levels of D. C. adjusted. The signal is then sent, as shown in figure 3.4, to the piezo and through a second stage of filtering to a moving coil speaker. In this stage a low-noise pre-amplifier is used as a low-pass filer. Typically, the corner frequency of the filter was set to 3 Hz and the gain between 1 and 10, depending on the individual situation. A circuit diagram of this feedback system can be found in Appendix A of [104].

The frequency of each resonant mode is measured accurately using a spectrum analyser. These resonances can be excited by adding an A.C. signal of the ap-

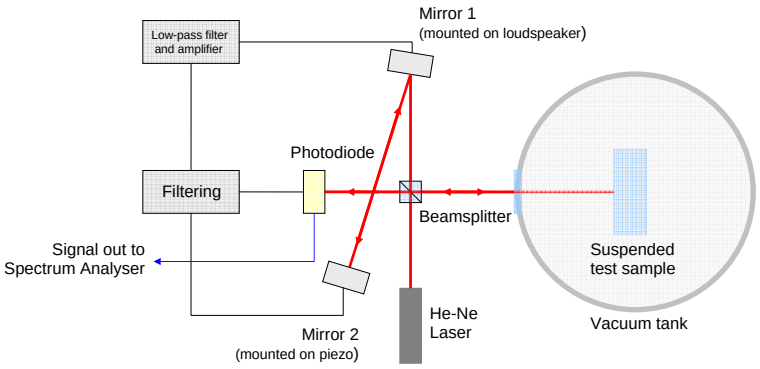

Figure 3.4: Schematic of the interferometer readout and filtering system used throughout this research for measuring the ring-downs of resonant modes of a test sample.

propriate frequency to a 750 volt D.C. bias on an electrostatic actuating plate close to one end of the mass. The electrostatic actuator can be seen positioned ~ 2 mm behind the suspended fused silica substrate in figure 3.2.

The decaying resonance signal, which has a typically frequency of a few tens of kHz, is at too high a frequency for the data acquisition program to handle easily. Instead, a lock-in amplifier is used to beat the signal down to ~ 5 Hz and the decaying signal can be captured by a LabVIEW script [131], a screen grab of which is shown in figure 3.5, and stored in a text file which is then fed into a spreadsheet for the mechanical loss to be extracted.

3.5 Modelling of Test Mass Resonant Mode Frequencies

In order to find the frequencies of the relevant mechanical modes preliminary calculation is required. Finite element analysis, (FEA), is a useful tool in the prediction of the resonant mode shapes and frequencies of the samples being tested. All the test masses used for these experiments were modelled using the ANSYS® Academic

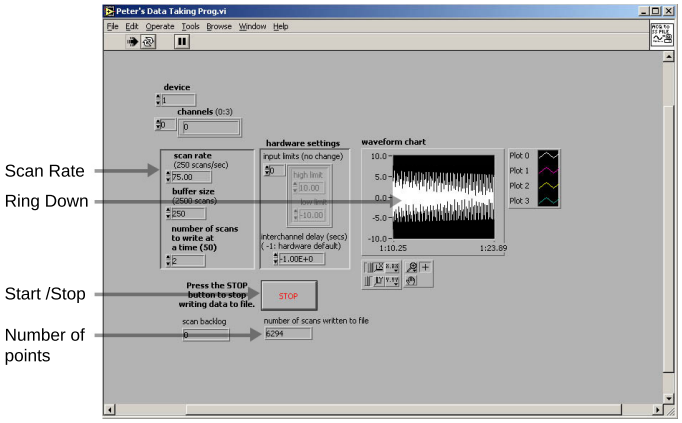

Figure 3.5: Screen capture of LabVIEW script used to capture the ring down of a decaying resonant mode.

Teaching Advanced v. 11.0 finite element analysis software package [132].

As well as providing information about the frequencies of resonant modes it is also possible in ANSYS® to show graphically the shape of each mode. This is important because not all resonant modes can be sensed using the interferometer described in section 3.4. Only those modes which have the greatest displacement of the front face of the test mass can be sensed using an interferometer. Two such mode shapes detectable by the current apparatus are the *"Clover 4"* $(16, n = 2)$ and *"Asymmetric Drum"* $(1, n = 0)$ modes, where the numbering denotes the symmetry classification of the modes, devised by G. McMahon [133]. These mode shapes, modelled in ANSYS®, for a 65 mm diameter by 70 mm long silica cylinder, are shown in figure 3.6.

In addition, *FEA* can be used to model the distribution of strain energy in each resonant mode of a mass. This information is essential to enable experimental measurements of dissipation to be interpreted correctly, as detailed later in section 3.7.

Interpretation of ring down measurement is more complicated when a mirror coating is present on the face of a mass to be measured. This situation will be addressed in the following sections.

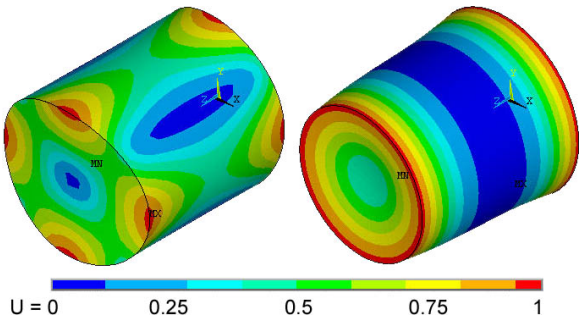

Figure 3.6: Clover 4 and Asymmetric Drum mode shapes for a 65 mm diameter by 70 mm long silica substrate where the relative displacements U $= \sqrt{x^2 + y^2 + z^2}$ are plotted in normalised, dimensionless units.

3.6 Calculation of Residual Coating Loss

The total level of loss for a system is found by summing all the separate loss factors contributed by different sources of dissipation. In general, the loss $\phi(\omega_0)$ is defined as [134]

$$\phi(\omega_0) = \frac{1}{2\pi} \frac{E_{\text{dissipated per cycle}}}{E_{\text{stored}}}. \tag{3.5}$$

Assuming that all other losses, for example surfaces losses, have been reduced to a negligible level, the measured mechanical loss of each individual resonant mode of a coated test substrate, $\phi(\omega_0)_{\text{coated}}$, is expressed as the sum of the intrinsic dissipation in the substrate material, $\phi(\omega_0)_{\text{substrate}}$, and the loss associated with the presence of a coating on the front face $\phi(\omega_0)_{\text{front face}}$

$$\phi(\omega_0)_{\text{coated}} = \phi(\omega_0)_{\text{substrate}} + \phi(\omega_0)_{\text{front face}}. \tag{3.6}$$

From equation 3.5 each loss term on the right hand side of equation 3.6 can be expressed in terms of the strain energy stored within the entire coated test substrate for each resonant mode so that

$$\phi(\omega_0)_{\text{coated}} = \frac{1}{2\pi} \frac{E_{\text{dissipated}_{\text{substrate}}} + E_{\text{dissipated}_{\text{coating}}}}{E_{\text{stored}_{\text{total.}}}} \tag{3.7}$$

Also from equation 3.5 it is possible to express the mechanical losses of the substrate and coating individually as

$$\phi(\omega_0)_{\text{substrate}} = \frac{1}{2\pi}\frac{E_{\text{dissipated}_{\text{substrate}}}}{E_{\text{stored}_{\text{substrate}}}} \tag{3.8}$$

$$\text{and} \qquad \phi(\omega_0)_{\text{coating}} = \frac{1}{2\pi}\frac{E_{\text{dissipated}_{\text{coating}}}}{E_{\text{stored}_{\text{coating}}}} \tag{3.9}$$

which can then be substituted into the numerator of equation 3.7 to express $\phi(\omega_0)_{\text{coated}}$ in terms of stored strain energy:

$$\phi(\omega_0)_{\text{coated}} = \frac{E_{\text{stored}_{\text{substrate}}}}{E_{\text{stored}_{\text{total}}}}\phi(\omega_0)_{\text{substrate}} + \frac{E_{\text{stored}_{\text{coating}}}}{E_{\text{stored}_{\text{total}}}}\phi(\omega_0)_{\text{coating}}. \tag{3.10}$$

The substrates tested are a few centimetres thick whereas the coatings applied to them are on the scale of only a few micrometres thick. This means that $E_{\text{stored}_{\text{substrate}}} \approx E_{\text{stored}_{\text{total}}}$ and consequently equation 3.10 can be simplified to

$$\phi(\omega_0)_{\text{coated}} = \phi(\omega_0)_{\text{substrate}} + \frac{E_{\text{stored}_{\text{coating}}}}{E_{\text{stored}_{\text{total}}}}\phi(\omega_0)_{\text{coating}}. \tag{3.11}$$

The term $\frac{^{E}\text{stored}_{\text{coating}}}{^{E}\text{stored}_{\text{total}}}$ is the ratio of the total elastic energy stored within the coating to the total energy in the coated test substrate. The coating loss must be calculated for each individual mode since the strain energy distribution is different for each resonant mode because each individual resonance has a different shape and occurs at a different frequency.

To determine the coating and residual losses it is necessary to measure the mechanical losses for the resonant frequencies of both an uncoated "*control*" mass and a similar but coated mass. The mechanical loss measurements of the control mass can provide $\phi(\omega_0)_{\text{substrate}}$ for each resonant mode, and the measured mechanical losses of the coated test substrate give $\phi(\omega_0)_{\text{coated}}$ [135].

The coating loss is the sum of losses attributed to Brownian noise and thermoelastic dissipation

$$\phi(\omega)_{\text{coating}} = \phi(\omega)_{\text{coating (Brownian)}} + \phi(\omega)_{\text{coating (thermoelastic)}}. \quad (3.12)$$

For each resonant mode $\phi(\omega_0)_{\text{coating}}$ may be expressed as

$$\phi(\omega_0)_{\text{coating}} = \phi(\omega_0)_{\text{residual}} + \frac{E_{\text{coating}_{\text{volume change}}}}{E_{\text{coating}_{\text{total}}}} \phi(\omega_0)_{\text{thermoelastic}} \quad (3.13)$$

where the first term, $\phi(\omega_0)_{\text{residual}}$, is the level of loss attributed to Brownian noise and the second term, $\phi(\omega_0)_{\text{thermoelastic}}$, is loss attributable to coating thermoelastic dissipation - damping associated with a coating, and the substrate to which it is applied - having dissimilar thermal and elastic properties. For each resonant mode $E_{\text{coating}_{\text{volume change}}}$ is the energy associated to the change of volume of the coating during the motion of the resonance. The ratio of the energy associated with volume change to the total energy stored in the coating was calculated for each resonant mode by D. Crooks. Once the residual losses of each resonant mode have been calculated they can all be combined to give an overall residual coating loss for that particular coating.

3.7 Calculation of Energy Ratios in ANSYS®

The loss for the coating itself is calculated once the fraction of the total strain energy stored in the coating is established. This can be found using ANSYS® Academic Teaching Advanced v.11.0 [132] for each resonant mode by treating the entire coating as consisting of one composite material rather than two separate materials [128].

3.7.1 Material Properties of Composite Coatings

The effective Young's Modulus, Y_{eff}, and Poisson's Ratio, ν_{eff}, for such a composite material can be calculated using [136]

$$Y_{\text{eff}} = \frac{Y_1 h_1 + Y_2 h_2}{h_1 + h_2} \tag{3.14}$$

and

$$\nu_{\text{eff}} = \frac{h_1 \nu_1 Y_1 (1 - \nu_1^2) + h_2 \nu_2 Y_2 (1 - \nu_2^2)}{h_1 Y_1 (1 - \nu_2^2) + h_2 Y_2 (1 - \nu_1^2)} \tag{3.15}$$

where Y_1, h_1, ν_1 are the Young's Modulus, physical thickness of each layer and Poisson's Ratio of the first material, and Y_2, h_2, ν_2 are the corresponding values for the second material which constitutes the dielectric coating.

For a coating consisting of two alternating materials of density ρ_1 and ρ_2 respectively, the volume averaging operator for density is defined as [137]

$$\rho_{\text{ave}} = \frac{h_1}{h_1 + h_2}\rho_1 + \frac{h_2}{h_1 + h_2}\rho_2. \tag{3.16}$$

The effective Young's Modulus, Poisson's ratio and density of a thirty layer silica/tantala coating comprising of $\lambda/4$ optically thick layers of coating material is calculated using the material properties given in table 3.1 [2], and substituting them into equations 3.14, 3.15 and 3.16.

Property	**Silica**	**Tantala**
n	1.45	2.03
h (μm)	0.183	0.131
Y (GPa)	72	140
ν	0.17	0.23
ρ (kgm^{-3})	2202	6850

Table 3.1: Material Properties of silica and tantala.

Property	Silica/Tantala
Y (GPa)	100
ν	0.204
ρ (kgm^{-3})	4139

Table 3.2: Effective material properties of a thirty layer silica/tantala coating

The calculated effective material properties of a thirty layer silica/tantala coating are presented in table 3.2.

3.7.2 Calculation of Energy Ratios in ANSYS®

The coating was modelled as a thin disc of appropriate properties and thickness at the front of the test substrate. For each resonant mode the ratio of the total energy contained in the coating and the total energy stored in the mass was found.

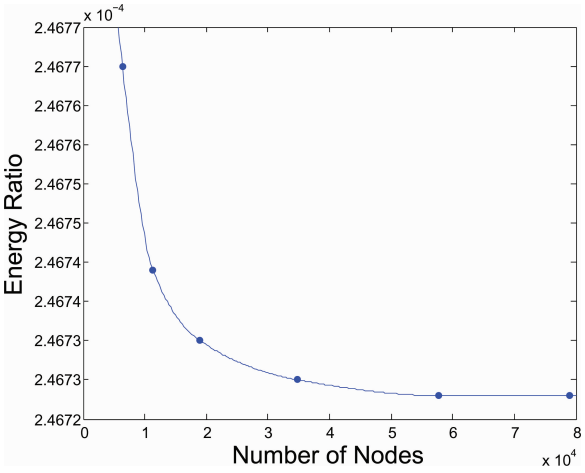

Figure 3.7: Convergence of Energy Ratio for the 47339 Hz Resonant Mode of a 30 layer silica/tantala coating on a 76.2 mm diameter by 25.4 mm long silica substrate.

To approximate an infinite point model, several models were run with an increasing number of nodes and a converged value for each energy ratio calculated. As an example, the convergence of the energy ratio for the 47339 Hz mode of a thirty layer silica/tantala coating of the type studied here, using the composite properties in

table 3.2, on a 76.2 mm diameter by 25.4 mm thick silica substrate, is shown in figure 3.7. It can also be noted that as the number of nodes increases the energy ratio converges to 2.246728×10^{-4}.

Using experimentally measured values for the mechanical losses of a set of modes of coated and uncoated samples, along with the results of finite element analysis models giving the fraction of energy stored in the coating for each mode, it is possible to calculate the intrinsic loss of the coatings.

3.8 Determination of the Source of Coating Dissipation

For the last few years, the study of these highly reflective dielectric coatings has been a project for several research groups within the gravitational wave community. All interferometric gravitational wave detectors currently operating use coatings consisting of alternating $\lambda/4$ layers of silica and tantala. Earlier investigations determined that the mechanical loss of these coatings was significant enough to be a limiting factor in the sensitivity of the next generation of gravitational wave detectors, and studies were made to determine the source of dissipation in these multi-layer coatings [111].

3.8.1 Potential Sources of Coating Dissipation

There are several possible sources of dissipation in a multi-layer dielectric coating. The first potential source of loss may be between the substrate and the coating itself, highlighted in figure 3.8.

Such dissipation could be introduced by the rubbing between these two objects, or damage done to the surface of the substrate by the coating deposition technique. If this were to be the dominant source of dissipation, then, for a number of coatings,

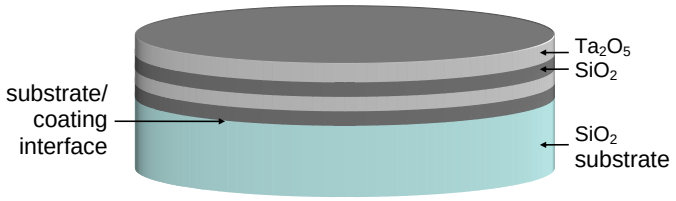

Figure 3.8: Illustration of the substrate/coating interface.

with different thicknesses and composition of layers, the mechanical loss would remain constant. This is because the loss would arise primarily from the deposition of the initial layer.

A second possible source of dissipation might be introduced between the interfaces between each of the layers of the multi-layer coatings, as indicated in figure 3.9. This could be due to discontinuities at the edges of each layer as a consequence of the ion-beam sputtering process. If such interfaces introduced mechanical loss, then for a series of coatings with the same composition of materials but increasing numbers of layers, and therefore more intra-coating interfaces, the mechanical loss would be seen to increase.

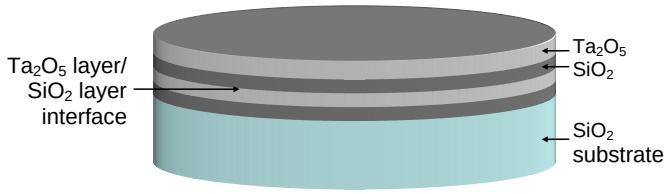

Figure 3.9: Illustration of the coating/coating interface.

The final source of dissipation could arise from the intrinsic loss of the materials used to create the multi-layer dielectric coatings. If this loss were to be the dominant source of dissipation, then, for a number of coatings with the same materials and number of layers, but differing proportions of material, the levels of dissipation would vary correspondingly.

3.8.2 Identification of the Source of Coating Dissipation

Harry et al. [114] investigated these three primary sources of dissipation in multilayer coatings, by measuring the mechanical losses of a set of coatings which had varied numbers and thicknesses of coating layers. Table 3.3 lists the five different coatings tested and states the individual coating losses which they calculated [114, 111][1]

Sample	**Layers**	**t SiO_2**	**t Ta_2O_5**	$\phi_{\mathbf{coating}}$ $(\times 10^{-4})$
A	0	0	0	n/a
B	2	$\lambda/4$	$\lambda/4$	0.9 ± 2.8
C	30	$\lambda/4$	$\lambda/4$	2.7 ± 0.7
D	60	$\lambda/8$	$\lambda/8$	2.7 ± 0.5
E	30	$\lambda/8$	$3\lambda/8$	3.7 ± 0.5
F	30	$3\lambda/8$	$\lambda/8$	1.9 ± 0.2

Table 3.3: Set of samples tested with different numbers of layers and optical thicknesses, t, of layer material to determine the mechanical loss in tantala/silica coatings.

If the dominant loss of dissipation in coatings was associated with the interface between substrate and coating, then the coating loss determined for each of the samples B-F would be approximately equal. It is clear from table 3.3 that the loss values were not all the same. If, on the other hand, the dissipation originated from the interfaces between the coating layers, one would expect the coating loss of sample C to be half the loss of sample D, which has the same physical thickness, but 30 and 60 layers respectively. From table 3.3 it can be seen that the coating losses of both these samples is identical, indicating that the intra-coating interfaces are not a dominant source of dissipation.

[1]Later analysis of three more coated samples identical to B yielded a coating loss of $(2.8 \pm 0.3) \times 10^{-4}$, which is in better agreement with samples C and D which have identical fractions of coating material.

It can also be seen from table 3.3, that as the proportions of coating materials are varied in coating types E, C and F, the coating loss increases with the increasing fraction of tantala present in the coating. This suggests that coating dissipation is due to the coating materials themselves, and also indicates that the tantalum pentoxide component of the coatings has a greater mechanical loss factor than the silica layers.

A coating split analysis was undertaken to separate the calculated coating losses into the individual losses for the two coating materials. This was determined by partitioning the energy in each of the five coatings into the amounts stored in its silica and tantala layers as

$$\phi_{\text{coating}} = \frac{t_{\text{Si}} Y_{\text{Si}} \phi_{\text{Si}} + t_{\text{Ta}} Y_{\text{Ta}} \phi_{\text{Ta}}}{t_{\text{Si}} Y_{\text{Si}} + t_{\text{Ta}} Y_{\text{Ta}}} \tag{3.17}$$

where t_i, Y_i and ϕ_i are the total thickness, Young's modulus and loss angle for the i^{th} coating material [114]. By solving simultaneously the fractions for the different coatings the loss of the silica and tantala components of the coating were calculated, as presented in table 3.4 [114, 137]. This quantified the suggestion that the mechanical loss of tantala/silica coatings is dominated by loss associated with the Ta_2O_5 component, showing that the loss angle of tantala is nearly four times greater than that of silica [114].

Material	ϕ_0 $(\times 10^{-4})$
Silica	1.0 ± 0.2
Tantala	3.8 ± 0.2

Table 3.4: Loss Angles for silica and tantala calculated from multi-layer coatings.

3.9 Single Layer Measurements

In an attempt to confirm by direct measurement the values for the losses of silica and tantala obtained from the multi-layer coatings, Laboratoire Matériaux Avancés (LMA) [138] in France produced two masses with single layers of coating to investigate the losses introduced by the individual coating materials. These coatings were applied to silica substrates 76.2 mm diameter and 25.4 mm tall. These dimensions are chosen to be of a similar aspect ratio to the full scale coated test substrates used in a gravitational wave detector, but scaled down to a smaller size to fit easily inside the coating ion-beam sputtering and loss measurement apparatus and which are also cheaper to produce.

The first substrate was coated with a single layer of silica equivalent to 25 quarter wavelengths, where 1.064 μm is the laser wavelength used in gravitational wave detectors, and the second was coated with the equivalent of 37 quarter wavelengths of tantala. The tantala coated sample was annealed at 600 °C, but small cracks appeared during the annealing process, as visible in figure 3.10.

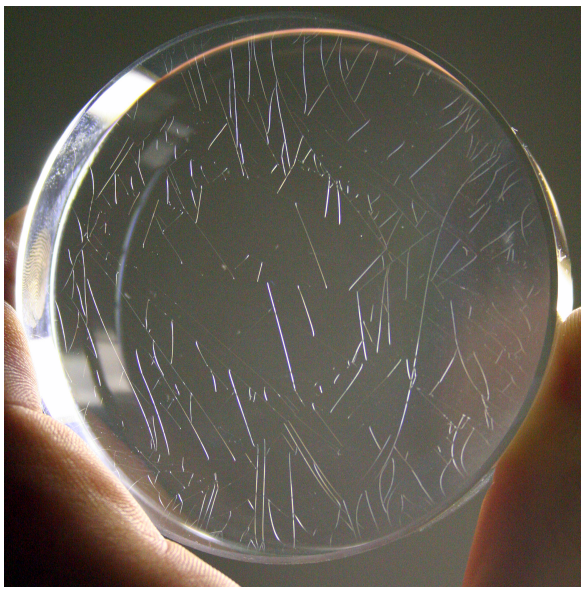

Figure 3.10: Image of cracks which appeared through the tantala coating during the annealing process.

In order to prevent the second coating from similar cracking, the silica coated sample was annealed at the lower temperature of 400 °C. Mechanical loss measurements for these two samples and for two uncoated control substrates were taken. One control sample was annealed at 600 °C to aid the analysis of the tantala coated sample and the other annealed at 400 °C to match the annealing process of the silica coated sample.

Loss measurements were made of four resonant modes for each of the samples. ANSYS® illustrations of each of these resonant mode shapes measured on all the 76.2 mm diameter by 25.4 mm thick fused silica substrates measured throughout this chapter are shown in figure 3.11. The measured mechanical losses for these four samples are shown in figure 3.12.

The 4.85 μm thick tantala coating was modelled in ANSYS® using the material properties detailed in table 3.1, and the ratio of strain energy stored in the coating for each resonant mode determined using the convergence method described in section 3.7. The converged energy ratios for each resonant mode are presented in column 2 of table 3.5. Using the mechanical losses measured for the tantala coated substrate and the corresponding control substrate losses (since $\phi(\omega_0)_{\text{control}} = \phi(\omega_0)_{\text{substrate}}$), the coating loss can be calculated for each resonant mode using equation 3.11 and is shown in table 3.5.

Frequency (Hz)	**Energy Ratio** ($\times 10^{-4}$)	$\phi(\omega_0)_{\text{coated}}$ ($\times 10^{-7}$)	$\phi(\omega_0)_{\text{substrate}}$ ($\times 10^{-8}$)	$\phi(\omega_0)_{\text{coating}}$ ($\times 10^{-3}$)
20221	0.967	7.86 ± 0.06	2.16 ± 0.14	0.79 ± 0.01
28457	1.040	12.56 ± 0.06	4.52 ± 0.08	1.16 ± 0.01
47402	0.355	5.33 ± 0.75	3.60 ± 0.13	1.40 ± 0.21
73521	0.741	9.92 ± 0.47	6.02 ± 0.04	1.26 ± 0.06

Table 3.5: Calculation of the coating loss of a 4.85 μm thick coating of tantala sputtered onto a 76.2 mm diameter by 25.4 mm thick silica substrate.

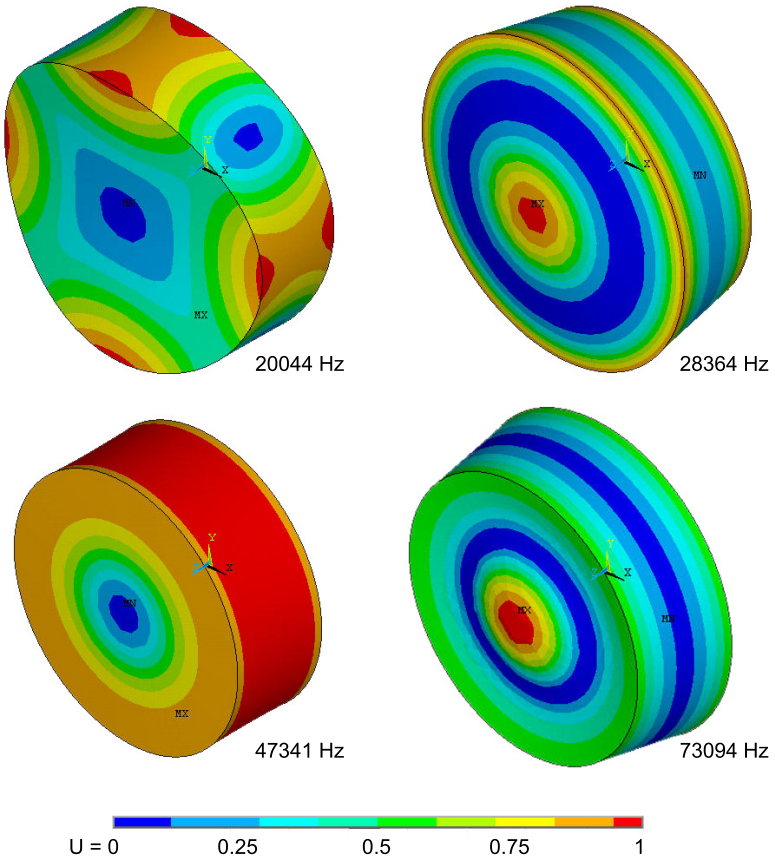

Figure 3.11: ANSYS® illustrations of the four resonant mode shapes and calculated frequencies measured on the 76.2 mm diameter by 25.4 mm thick silica substrates where the relative displacements U $= \sqrt{x^2 + y^2 + z^2}$ are plotted in normalised, dimensionless units.

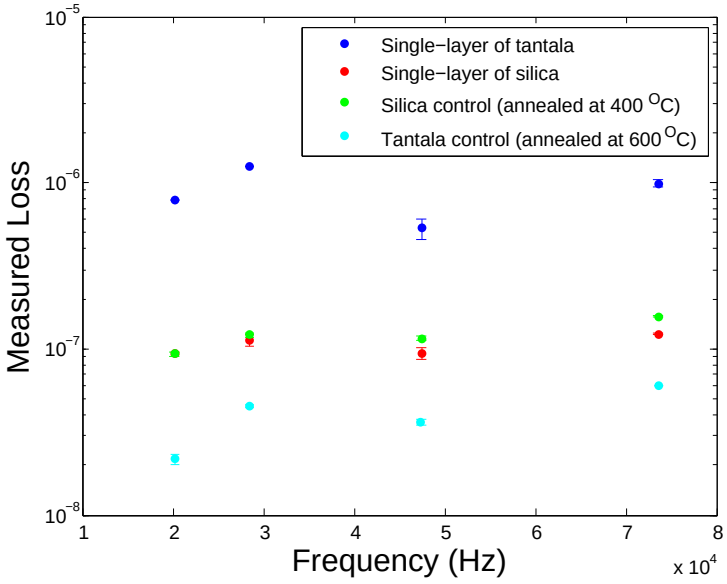

Figure 3.12: Measured mechanical losses of fused silica substrates coated with single layers of silica and tantala and of their corresponding uncoated control samples.

The thermoelastic loss associated with the tantala coating can then be calculated for each resonant mode of the coating using equation 2.28. Equation 3.13 is then be used to calculate $\phi(\omega_0)_{\text{residual}}$ for each of the resonant modes, as shown in table 3.6[2].

Frequency (Hz)	$\phi(\omega_0)_{\text{coating}}$ ($\times 10^{-3}$)	$\phi(\omega_0)_{\text{thermo-elastic}}$ ($\times 10^{-5}$)	$\frac{E_{\text{coating}_{\text{vol change}}}}{E_{\text{coating}_{\text{total}}}}$	$\phi(\omega_0)_{\text{residual}}$ ($\times 10^{-3}$)
20221	0.79 ± 0.01	9.22	0.042	0.79
28457	1.16 ± 0.01	8.45	0.506	1.12
47402	1.40 ± 0.21	7.27	0.509	1.36
73521	1.26 ± 0.06	6.26	0.441	1.23

Table 3.6: Calculation of the residual coating loss of a 4.85 μm single layer of tantala sputtered onto a 76.2 mm diameter by 25.4 mm thick silica substrate.

[2]The ratios for the volume change were calculated by D. Crooks.

The individual residual losses for the tantala coating are averaged and presented in table 3.7.

Sample	ϕ_0 $(\times 10^{-4})$
Silica	-0.6 ± 0.3
Tantala	11.2 ± 1.2

Table 3.7: Residual losses for layers of coating material applied to fused silica substrates.

A similar analysis was also undertaken for the silica coating, as shown in table 3.8, and the average residual loss for this coating is also shown in table 3.7.

Frequency (Hz)	**Energy Ratio** $(\times 10^{-4})$	$\phi_{\mathbf{coated}}$ $(\times 10^{-7})$	$\phi_{\mathbf{substrate}}$ $(\times 10^{-7})$	$\phi_{\mathbf{coating}}$ $(\times 10^{-4})$
20221	4.71	0.94 ± 0.02	0.93 ± 0.03	0.01 ± 0.08
28457	5.06	1.12 ± 0.09	1.21 ± 0.05	-0.16 ± 0.20
47402	1.73	0.94 ± 0.08	1.16 ± 0.02	-1.32 ± 0.48
73521	3.61	1.23 ± 0.02	1.57 ± 0.01	-0.94 ± 0.06

Table 3.8: Calculation of the coating loss of a 4.59 μm single layer of silica sputtered onto a 76.2 mm diameter by 25.4 mm thick silica substrate.

The data in table 3.7 suggests the residual loss of the single layer of silica coating is significantly lower than that of the tantala coating. However, the small cracks on the tantala coating which formed during the 600 °C annealing process could have introduced excess losses, making the loss larger than determined in the earlier analysis of multi-layer coatings in section 3.8.

The difference between the single-layer coating and multi-layer coating loss values for silica can possibly be attributed to the fact that although the control sample used in the analysis had been annealed to the same temperature as the silica coated mass, it had not been annealed at the same time as the coated sample. This is clearly indicated in figure 3.12, and table 3.8, since three of the resonant modes of the silica

coated substrate had losses slightly lower than the corresponding losses measured on the uncoated control sample which yielded negative coating losses. Reanalysis with a pair of silica coated and control masses, annealed together at the same time, may bring this residual loss nearer to that obtained from the multi-layer analysis. Moreover, a single 4.59 μm layer of silica may not have the same structure as the much thinner 183 nm thicknesses of silica used in a multi-layer coating.

Having determined that the tantala layers are the dominant source of loss in these dielectric coatings, the next stage of research has concentrated on improving the mechanical loss without degrading the required low optical absorption. Jean-Marie Mackowski from LMA suggested adding titania as a dopant to the tantala layers of a multi-layer silica/tantala coating.

Firstly, it has a high Young's Modulus of 290 GPa [2], which is twice that of tantala. The atomic radius of the titanium atoms is 144.8 pm which is almost identical to the 143 pm atomic radius of tantalum [139], which allows for dense packing in the matrix of tantala and oxygen. Finally, the TiO_2/Ta_2O_5 alloy has a relatively high melting point, which is indicative of a stable amorphous structure. Experiments on a coating with $\sim$ 3% titania (TiO_2) introduced to the tantala component of a silica/tantala coating showed the mechanical loss of the tantala was reduced by 47% [140].

Following this reduction in the mechanical loss, LMA then produced a third single-layer coated sample, this time with a single 4.73 μm thick layer of tantala doped with $\sim$ 3% titania, denoted 'Formula 1' by the manufacturers. The measured losses of this sample are shown in figure 3.13 along with the losses measured for the single layer of undoped tantala for comparison. As cracks had appeared on that sample after the 600 °C annealing process, the doped tantala sample was annealed at the lower temperature of 400 °C and as a result a different control sample was needed for the analysis.

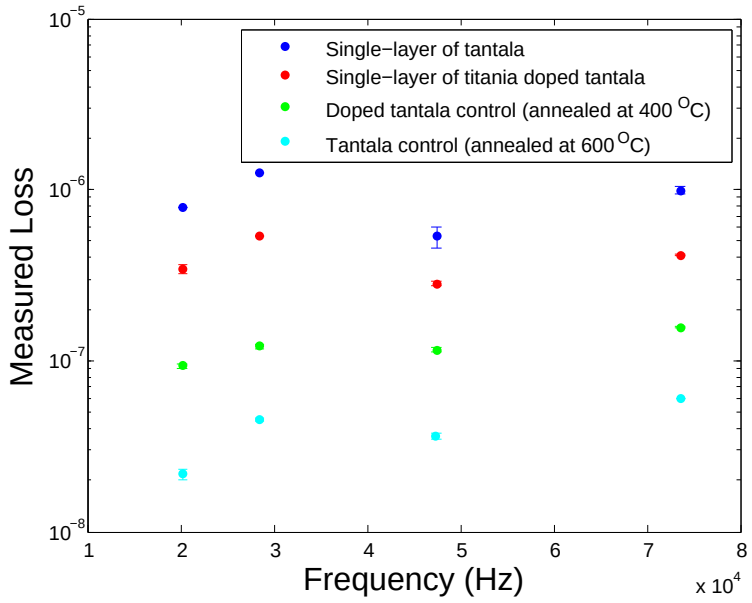

Figure 3.13: Measured mechanical losses of single layers of doped and undoped tantala compared to their corresponding uncoated control samples.

Analysis of this doped tantala yielded a residual coating loss of $(3.5 \pm 0.4) \times 10^{-4}$ which is lower than the tantala losses calculated from both the multi-layer and single layer samples. This provided some suggestion that doping the tantala with titania reduced the residual coating loss, however, it was clear that considerable further investigation was needed.

Unfortunately, LMA was only able to provide an approximate percentage of titania dopant in this coating, but for later coatings more accurate measurements of the titania were made, as discussed in section 3.10.

3.10 Investigations into the Effects of Doping Tantala with TiO_2

Given the reduction, seen in section 3.9, in mechanical loss of the single layer tantala coating doped with $\sim 3\%$ titania, studies were needed to investigate the effect of doping in multi-layer coatings. LMA produced a series of multi-layer tantala-silica coatings with differing percentages of titania introduced to the Ta_2O_5 component. Each coating consisted of 30 alternating quarter wavelength layers of Ta_2O_5 and SiO_2 and all were annealed at 600 °C.

Each different coating was given a name to identify it; 'Formula 1', 'Formula 2', etc. and sputtered onto two different thicknesses of fused silica substrate. The larger coin shaped samples were 76.2 mm diameter by 25.4 mm thick and were tested by the author in the University of Glasgow, whereas the thinner 76.2 mm diameter by 2.54 mm disc shaped coated samples were tested at the Massachusetts Institute of Technology. These thinner discs were suspended with a welded silica suspension and mechanical loss measurements were made using a birefringence readout, detailed in [114]. Mechanical loss measurements were also made on the 76.2 mm diameter by 25.4 mm thick coated substrates at the University of Glasgow and are presented in figure 3.14.

All these silica substrates were coated using ion beam deposition. Two different coating chambers were used to produce the various TiO_2-doped silica/tantala coatings, one with a smaller chamber and one larger, as indicated by column 3 of table 3.10. Apart from the different sizes of the coating chamber, which should not affect the loss of a coating, the ion sources for the ion beam deposition process were different. The smaller chamber has a Kaufman source which has a gridded broad beam ion source with a heated cathode filament to provide a source of electrons [141] whereas the larger chamber has two Radio Frequency ion sources which use inductively-coupled discharge instead of a hot cathode. The tungsten filament in the smaller coater also heated the target as well as the substrate.

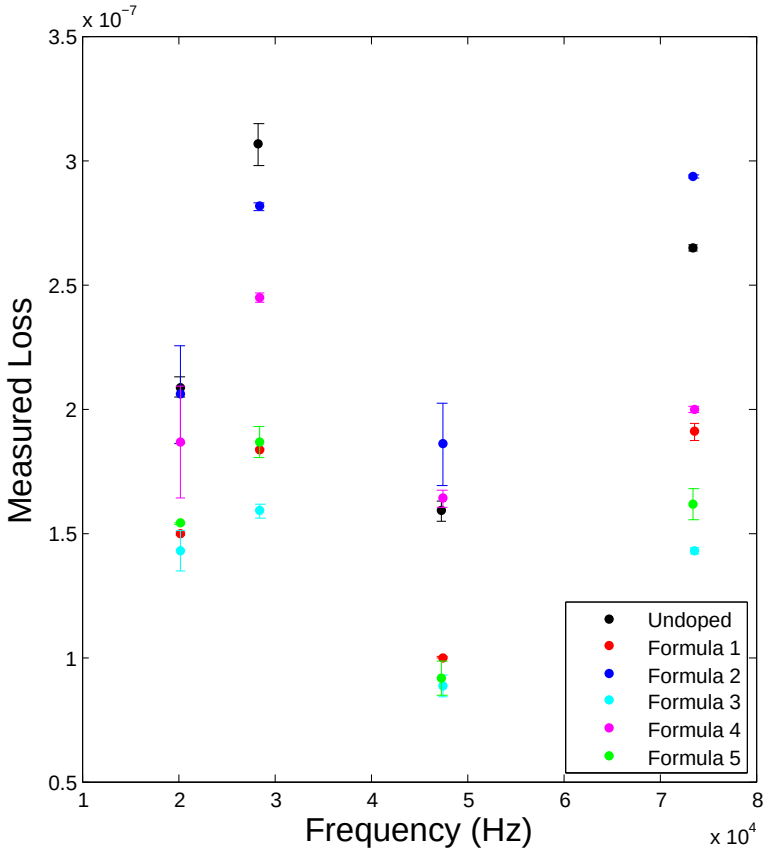

Figure 3.14: Measured mechanical losses of multi-layer tantala/silica coated samples with differing percentages of titania dopant introduced to the tantala component.

Originally the coating vendor was able to provide only an approximate value for the amount of TiO_2 in the Ta_2O_5 layers. Consequently studies were made at the University of Glasgow on some of the samples using Electron Energy Loss Spectroscopy, *EELS*, [142] to produce a definitive composition of these coatings. An EELS image of the TiO_2 content within a doped silica/tantala coating is shown in figure 3.15. In this image the light layers show the doped Ta_2O_5 layers. The brighter the pixel, the more TiO_2 is present.

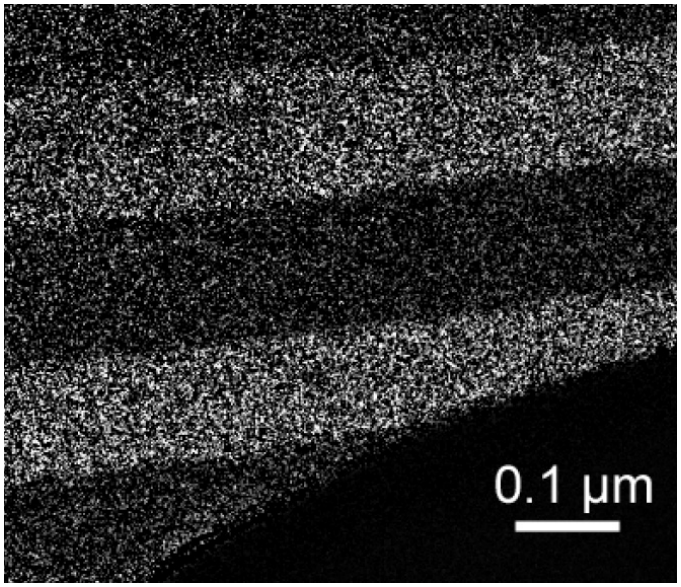

Figure 3.15: EELS image of the TiO_2 content within a doped silica/tantala coating.

LMA was then able to estimate the percentage of titania in each coating from its refractive index. This was done by comparing the refractive index of the TiO_2-doped Ta_2O_5 with pure Ta_2O_5 and TiO_2. The TiO_2 concentration was then evaluated by assuming a linear relationship between the TiO_2 concentration and the refractive index. This interpolation had to be made separately for each coating chamber. The results of this interpolation by the coating vendor and of the *EELS* analysis are presented in table 3.9. It is clear that the results from the two different techniques are broadly consistent.

Coating	$\%TiO_2$ from Refractive Index	$\%TiO_2$ from EELS
T/S	0	–
F1-T/S	6 ± 0.6	8.5 ± 1.2
F2-T/S	13 ± 1	20.8 ± 4.4
F3-T/S	24 ± 2	22.5 ± 2.9
F4-T/S	54.5 ± 5	54 ± 5
F5-T/S	14.5 ± 1	–

Table 3.9: Concentration of TiO_2 in the Ta_2O_5 layers of the coatings, as measured by the change in refractive index and by electron energy loss spectroscopy.

From the measured losses in figure 3.14, together with the loss measurements from MIT and the information provided by the coating manufacturer on the composition of these coatings, the residual coating losses for all the different 'Formula' coatings, and an undoped 30 layer silica/tantala coating were calculated, as presented in table 3.10.

Coating	$\phi_{\mathbf{residual}}(\times 10^{-4})$	Coater
T/S	3.0 ± 0.2	Smaller
F1-T/S	2.7 ± 0.3	Smaller
F2-T/S	1.9 ± 0.1	Smaller
F3-T/S	1.7 ± 0.1	Smaller
F4-T/S	2.1 ± 0.1	Larger
F5-T/S	2.0 ± 0.2	Larger

Table 3.10: Calculated residual losses for the different doped silica/tantala coated test substrates.

The data in these two tables can then be combined to produce a plot of the residual losses of the different tantala/silica coating as a function of TiO_2 concentration in the Ta_2O_5, as shown in figure 3.16. It is seen that, in general, adding $\sim 15\%$ TiO_2 to the Ta_2O_5 reduces the mechanical loss by approximately 15% to 40%, but that increased concentration of TiO_2 does not lead to significant further improvement.

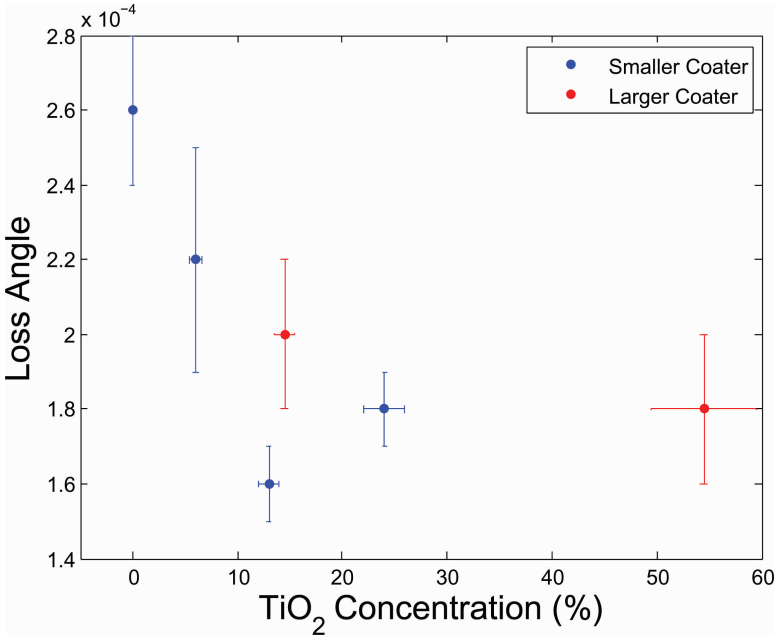

Figure 3.16: Residual losses of TiO_2-doped tantala/silica coating as a function of TiO_2 concentration in the Ta_2O_5.

While Formula 2 and Formula 5 had nominally identical amounts of TiO_2 dopant, they were deposited in different coating chambers. The residual losses of these two coatings were similar, suggesting that the use of a different coating chamber has no significant effect on the coating losses.

Low optical absorption is essential to create Fabry-Perot cavities of high finesse in interferometric gravitational wave detectors. The optical absorption of the standard tantala/silica coating measured here was found to be 0.9 ± 0.2 ppm whereas the 'Formula 4' coating with 54% TiO_2 had a larger absorption of 2.5 ± 0.5 ppm [143]. However, for coatings with relatively low concentrations of titania the optical absorption appears to increase only slightly, with the optical absorption of the 'Formula 3' coating measured as 1.1 ± 0.1 ppm [143]. This may be problematic in an advanced interferometer, but further research into improvements in coating techniques, and using a minimal amount of titania might alleviate the problem.

The reduction of nearly 40% of the residual loss from the coating results in an improvement in thermal noise, which in turn could translate into a greater astronomical reach for advanced interferometric gravitational wave detectors.

3.11 Investigations into the Losses Associated with Coatings Supplied by CSIRO

A parallel study of the mechanical loss of coatings produced by Australia's national science agency, the Commonwealth Scientific and Industrial Research Organisation (CSIRO), [144] is underway.

3.11.1 Thirty Layer Tantala/Silica Coating

CSIRO produced first a 30 layer un-doped tantala/silica coating on a 76.2 mm diameter by 25.4 mm tall silica substrate, using Argon, Ar, as the sputtering gas so that a comparison of identical coatings produced by the two different vendors, LMA and CSIRO, could be effected. This coated substrate was annealed at the lower temperature of 350 °C, whereas the LMA sample was annealed at 600 °C.

Loss measurements of this sample were made, denoted by 'Ar sputtered T/S' in figure 3.17 and the residual loss calculated to be $(4.2 \pm 0.1) \times 10^{-4}$ which is slightly higher than the loss of $(3.0 \pm 0.2) \times 10^{-4}$, presented earlier in table 3.4, for the similar LMA sample. The lower temperature used to anneal the CSIRO coating could account for the increased levels of residual loss from this sample.

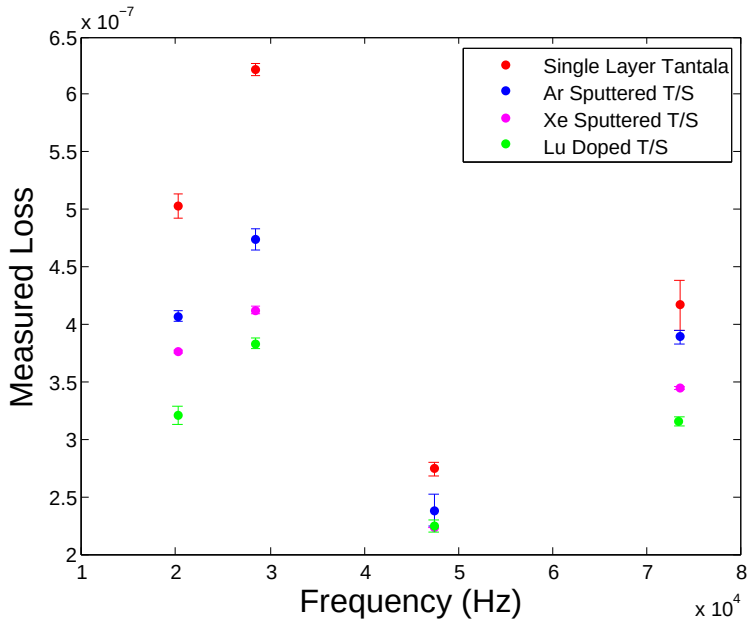

Figure 3.17: Measured mechanical losses of four coated samples of fused silica produced by CSIRO.

3.11.2 Tantala/Silica Coatings Produced Using Xenon Sputtering Ions

The properties of ion-beam sputtered coatings are influenced by the presence of high-velocity neutral forms of the sputtering gas which are reflected with residual momentum from colliding with the sputtering target and can bombard the coating being grown. Some films contain as much as 5% of sputter gas implanted into them [145]. The introduction of these atoms may increase the internal stresses of thin film coatings. The residual energy of these particles can constitute a significant fraction of the energy supplied by the ion-beam system.

The scale of the residual energy is dependent on the relative masses of the sputter gas and the sputter target. A light sputter gas is more likely to be reflected from a heavier sputter target. Consequently, a more matched, heavier sputter gas relative to the sputter target is more effective since a greater fraction of the momentum is transferred from the sputter gas to the target.

Argon is used frequently as the sputter gas in ion-beam deposition systems because it is cheaper than Krypton or Xenon. However, the atomic weight of Argon is 39.95 [146] which is much smaller than 180.94 for Tantalum [146]. A larger sputter gas such as Krypton (atomic weight 83.80) or Xenon (atomic weight 131.29) [146] would be a much better choice with the heavier Tantalum sputter target.

CSIRO produced a second 30 layer un-doped tantala/coated sample which was identical to the previous sample but the sputtering targets were bombarded with Xenon ions instead of Argon ions. This was produced to establish if the larger Xenon ions would produce a lower loss coating, since a smaller percentage of neutral sputtering gas should enter the coating. From the loss measurements, denoted 'Xe sputtered T/S' in figure 3.17, a loss of $(3.5 \pm 0.1) \times 10^{-4}$ was determined, which is a very slight improvement on that from the Argon sputtered sample. This suggests that the use of a heavier sputtering ion may improve the residual loss of tantala/silica coatings by $\sim 15\%$. However, this loss is still not as low as that for the tantala/silica sample produced by LMA.

3.11.3 Mechanical Loss Measurements of a Single Layer of Tantala

As discussed in section 3.8, it is thought that the dominant source of loss in these multi-layer coatings comes from the tantala within the coating. To continue this investigation CSIRO also produced a sample coated with a single 4.65 μm layer of tantala. Loss measurements were made on this sample which yielded a residual loss of tantala of $(3.8 \pm 0.1) \times 10^{-4}$, slightly lower than the earlier calculation of the loss of tantala from multi-layer coatings, in table 3.4, of $(4.4 \pm 0.2) \times 10^{-4}$.

This may, however, be attributed to the lack of an exactly matched control substrate, because the tantala coated sample had been annealed to 290 °C whereas the nearest control had been annealed to 350 °C. Reanalysis with a more suitable control may bring this residual loss closer to the extracted values.

3.11.4 Lutetium Doped Tantala/Silica Coatings

As with the studies of improving the mechanical losses of coating produced by LMA, detailed in section 3.10, investigations have also begun using samples produced by CSIRO. In Ta_2O_5 there are two electrons associated with each oxygen vacancy in the matrix of Ta and O. Based on studies of crystalline Ta_2O_5 it is possible that amorphous Ta_2O_5 has a tendency to form with oxygen vacancies [147, 148, 149, 150]. If this is the case, one way to fill the vacancies may be to dope the coating with an ion which will bind the two free electrons per vacancy. One dopant which could do so is lutetium.

Preliminary investigations have begun after CSIRO produced a tantala/silica coating in which the tantala layers were doped with lutetium. X-ray Photoelectron Spectroscopy [151] measurements by CSIRO determined there was $\sim 3\%$ lutetium in the tantala layers of the coating [145]. Using the losses measured on this sample, shown in figure 3.17, a coating loss of $(3.8 \pm 0.2) \times 10^{-4}$ was determined. This was a slight improvement of $\sim 10\%$ on the loss of the undoped tantala, but not to the extent of the 40% seen in some of the titania doped samples from LMA. Research in Glasgow and MIT will continue to reduce the loss of the tantala layers in the coatings with lutetium and other possible dopants.

3.11.5 Improving the Mechanical Loss and Reducing the Absorption of High-Index Coating Layers

One of the best performing doped tantala coatings manufactured by the coating vendor LMA was the 'Formula 5' coating where the tantala layers were doped with $\sim 15\%$ titania [143]. CSIRO then produced a nominally identical coated substrate so that a direct comparison between coatings produced by the two coating vendors could be made. A schematic of this coating is shown in figure 3.18.

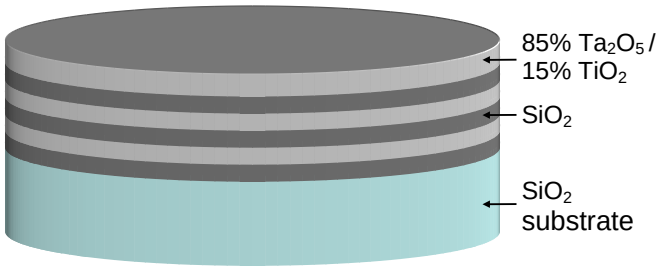

Figure 3.18: Schematic of the tantala/titania // silica multi-layer dielectric coating produced by CSIRO.

Doping the tantala with titania increases the Young's modulus of the layers. This also increases the refractive index of these layers resulting in *less* layers being needed to achieve a highly reflective coating [152].

Measurements were made on a 30 $\lambda/4$ layer coating comprising of 50% titania and 50% silica high index material and silica low index material sputtered onto a 76.2 mm diameter by 2.54 mm thick disc at MIT. This was manufactured because the Young's Modulus of these high refractive index layers would be similar to that of the low refractive silica layers making it well matched acoustically with the silica substrate, thus improving thermal noise. It also has been demonstrated that the optical absorption of such a coating matches the Advanced LIGO requirement of 0.5 ppm [153]. MIT calculated a promising residual loss of $(3.1 \pm 0.2) \times 10^{-4}$ for this coating [153].

To further match the properties of the coating with the silica substrates, CSIRO then manufactured a 30 $\lambda/4$ layers coating with a mixture of 65% of silica and 35% titania to produce the high refractive index layers, as represented in figure 3.19. This coating was sputtered onto a 76.2 mm diameter by 25.4 mm thick coin, the mechanical losses of which were measured at the University of Glasgow. However, such a multi-layer coating would require *more* layers to achieve the high reflectivity required in Advanced LIGO.

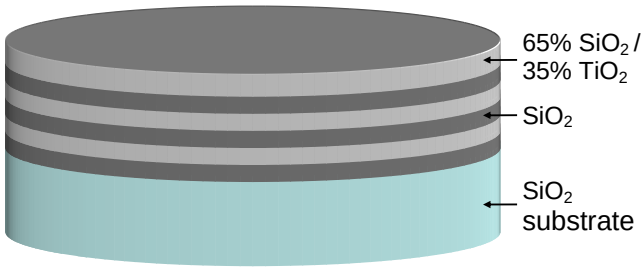

Figure 3.19: Schematic of the silica/titania // silica multi-layer dielectric coating produced by CSIRO.

To provide information on the effect of doping the tantala layers of a coating with silica, a third substrate was coated with 30 $\lambda/4$ layers of material with silica as the low refractive index layers and a mixture of 65% tantala and 35% silica as the high refractive index material. A schematic of this third coating is shown in figure 3.20.

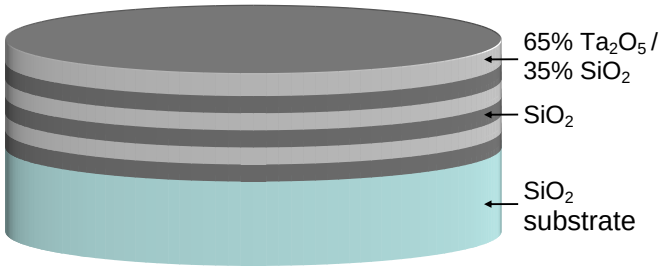

Figure 3.20: Schematic of the tantala/silica // silica multi-layer dielectric coating produced by CSIRO.

The mechanical losses of these three 76.2 mm diameter by 25.4 mm thick samples were measured and are presented below in figure 3.21 along with the measured losses for the standard 30 $\lambda/4$ layer tantala/silica coating produced by CSIRO for comparison.

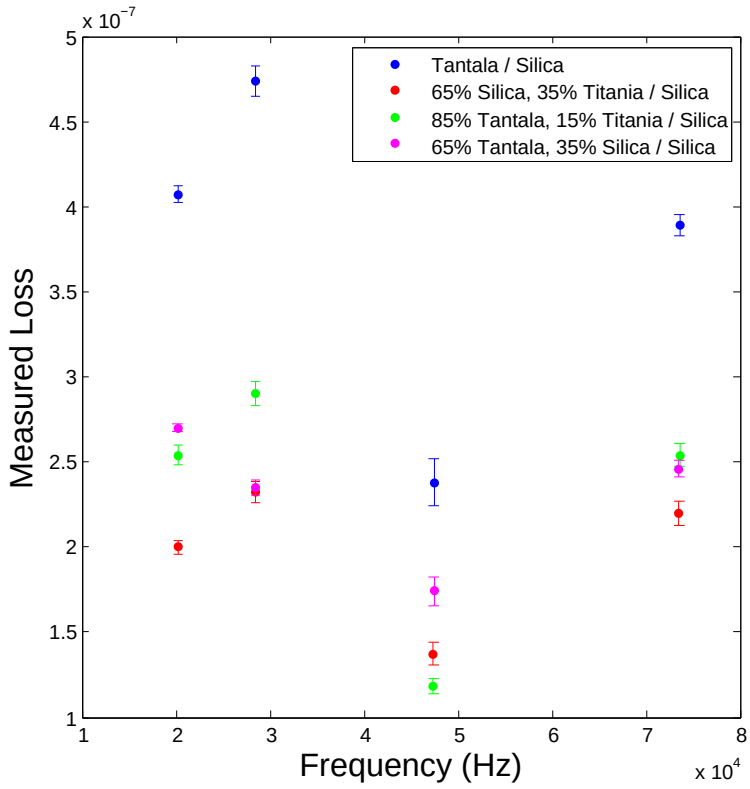

Figure 3.21: Measured mechanical losses of three different 30 layer coated fused silica substrates produced by CSIRO.

3.11.6 Finite Element Analysis of CSIRO Coatings

In order to determine the residual loss of these three coatings it was necessery to calculate the fraction of energy stored in the different coatings at each of the resonance modes measured. Before running finite element models in ANSYS®, the material properties of the coatings needed to be established.

Material	Y **(GPa)**	ν	ρ **(kgm^{-3})**
Silica	72	0.17	2200
Tantala	140	0.23	6850
Titania	290	0.28	4260

Table 3.11: Table of the material properties used in calculating the effective material properties of the high index layers. All values come from [2] except the density of titania which is taken from [3]

Using the material properties stated in table 3.11, it was possible to calculate the effective Young's Modulus of the different mixed-composition high index layers using

$$Y_{\text{eff}} = \frac{Y_{\text{a}} Y_{\text{b}}}{t_{\text{b}} Y_{\text{a}} + t_{\text{a}} Y_{\text{b}}} \tag{3.18}$$

where Y_{a} and Y_{b} are the Young's Modulus of materials a and b which form the high-index layer comprising of fractions t_{a} and t_{b} respectively. From equation 3.16 the Poisson's ratio may be found using

$$\nu_{\text{eff}} = \frac{h_1}{h_1 + h_2}\nu_1 + \frac{h_2}{h_1 + h_2}\nu_2. \tag{3.19}$$

Coating	$Y_{\textbf{eff}}$ **(GPa)**	$\nu_{\textbf{eff}}$	$\rho_{\textbf{eff}}$ **(kgm^{-3})**
85% Ta / 15% Ti	152	0.25	6462
65% Si / 35% Ti	98	0.24	2921
65% Ta / 35% Si	105	0.21	5223

Table 3.12: Calculated effective material properties of the high index layers.

CSIRO was able to provide information about the overall thickness of different coatings, as well as the average thicknesses of the high and low index layers [154].

Coating	t_{hi} (nm)	t_{low} (nm)	$t_{coating}$ (μm)
Ta/Ti // Si	127	187	4.70
Si/Ti // Si	191	129	4.80
Ta/Si // Si	145	174	4.78

Table 3.13: CSIRO measured thicknesses of individual layers and the overall coating thickness.

From the values in tables 3.12 and 3.13, it was possible to determine the effective properties of the different multi-layer coatings from equations 3.14, 3.15 and 3.16.

Coating	Y_{eff} (GPa)	ν_{eff}	ρ_{eff} (kgm^{-3})
85% Ta / 15% Ti // Si	104	0.21	3922
65% Si / 35% Ti // Si	87	0.21	2631
65% Ta / 35% Si // Si	87	0.19	3572

Table 3.14: Calculated effective material properties of multi-layer coatings.

Using these values, models of the appropriate coating thickness were run in ANSYS® and the fraction of energy stored in each of the coatings determined.

30 Layer Titania-Tantala / Silica Coating

Several models of increasing numbers of nodes of the 4.70 μm thick titania-tantala/silica coating on a silica substrate were run and the fraction of energy stored in the coating plotted against increasing number of nodes, as shown in figure 3.22. The converged energy ratios for each of the resonant modes can then be used in conjunction with the experimentally measured results to determine the residual coating loss of the sample.

The fractions of energy determined from this graph agree to within 1% of the values determined by D. Crooks for use in the analysis of the nominally identical coating produced by LMA.

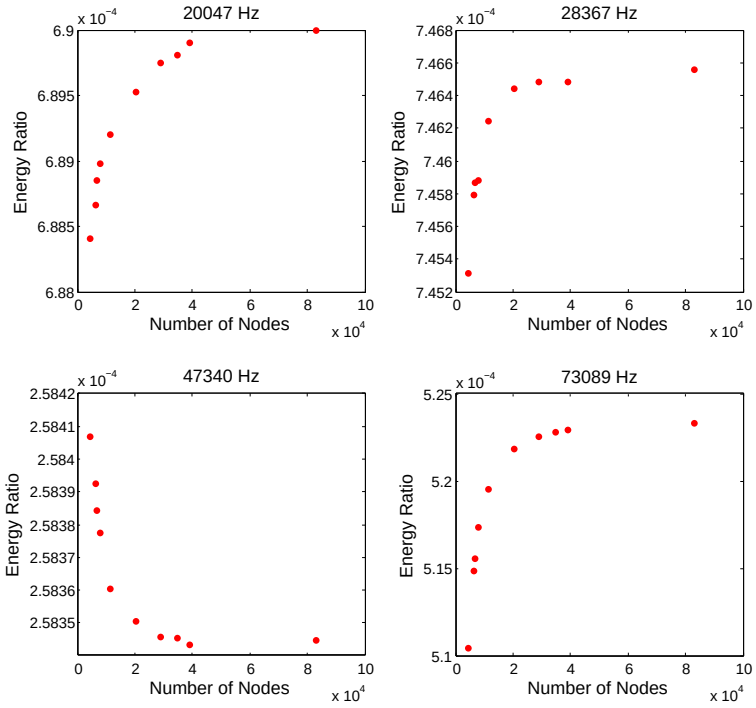

Figure 3.22: Convergence of ratio of energy stored in a 15% titania 85% tantala/silica coating on a 76.2 mm diameter by 25.4 mm tall silica substrate.

30 Layer Silica-Tantala / Silica Coating

A similar finite element analysis was undertaken for a 4.78 μm silica-tantala / silica coating and the convergence of the fraction of energy stored in this coating is shown in figure 3.23.

30 Layer Silica-Titania / Silica Coating

Similarly, for a 4.80 μm thick silica-titania / silica coating finite element models were run and the convergence of the fraction of energy stored in such a coating is presented in figure 3.24.

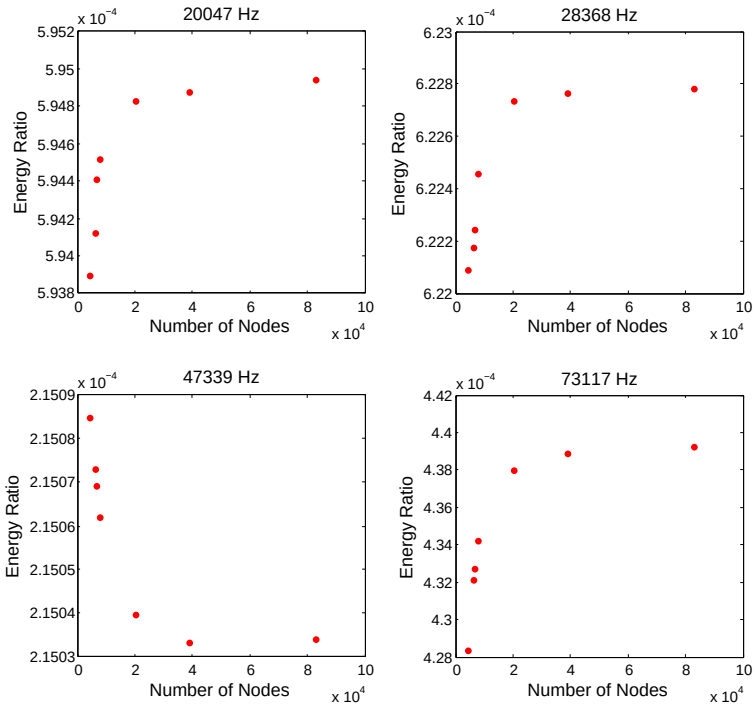

Figure 3.23: Convergence of ratio of energy stored in a 65% tantala 35% silica/silica coating on a 76.2 mm diameter by 25.4 mm tall silica substrate.

3.11.7 Residual Coating Loss of CSIRO Multi-Layer Coatings

These three samples from CSIRO were annealed at 500 °C over a period of 24 hours, however there was no uncoated control sample which had gone through the same annealing process, so the nearest control sample used in this analysis was one which was annealed by LMA at 450 °C.

Using this control, and the energy ratios determined in 3.22, the residual loss of the titania doped tantala sample was determined to be $(2.4\pm0.2)\times10^{-4}$ which is slightly higher than the $(2.0\pm0.2)\times10^{-4}$ loss of the identical LMA sample. It does however, show a $\sim$ 40% improvement of residual loss compared to the $(4.2 \pm 0.1) \times 10^{-4}$ measured on the CSIRO produced thirty layer tantala/silica coating which is similar to the improvement found from the nominally identical LMA titania doped sample.

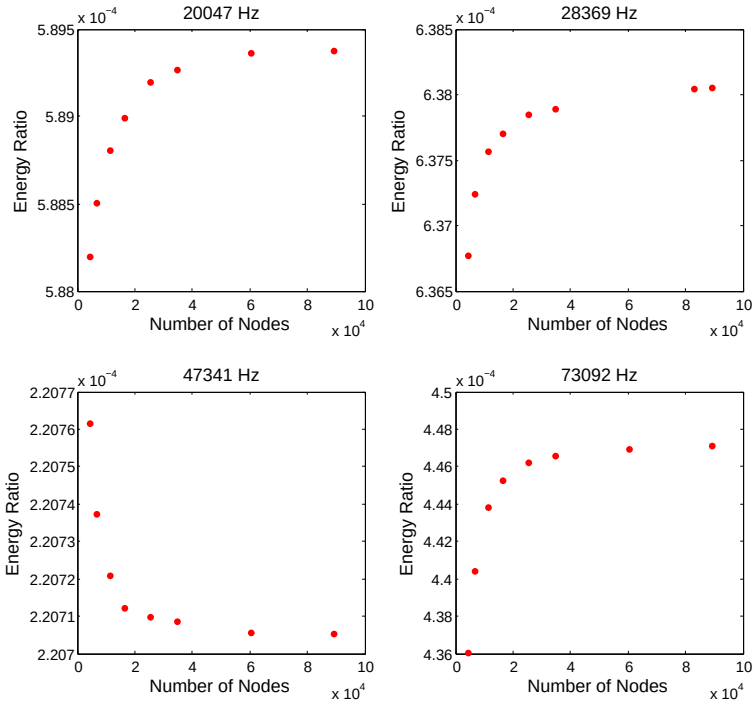

Figure 3.24: Convergence of ratio of energy stored in a 35% titania 65% silica/silica coating on a 76.2 mm diameter by 25.4 mm tall silica substrate.

This slight increase in residual loss could partly be attributed to the slightly different control sample used, but when a comparison between the measured losses is made it is clear that the losses of the resonant modes are all higher for the CSIRO sample as shown in figure 3.25. It appears that the coating produced by CSIRO is more lossy than the coating produced by LMA, which is a repeat of the result found earlier in this section for the standard tantala/silica coatings. Again it is unknown why there is a difference between identical coatings produced by different coating vendors.

The loss of the sample coated with 65% tantala and 35% silica as the high refractive index material was calculated to be $(2.5 \pm 0.4) \times 10^{-4}$ which is also $\sim 40\%$ lower than the residual loss determined for a standard tantala/silica coating. This result suggests that doping the tantala with silica may equally reduce the residual losses of a multi-layer coating.

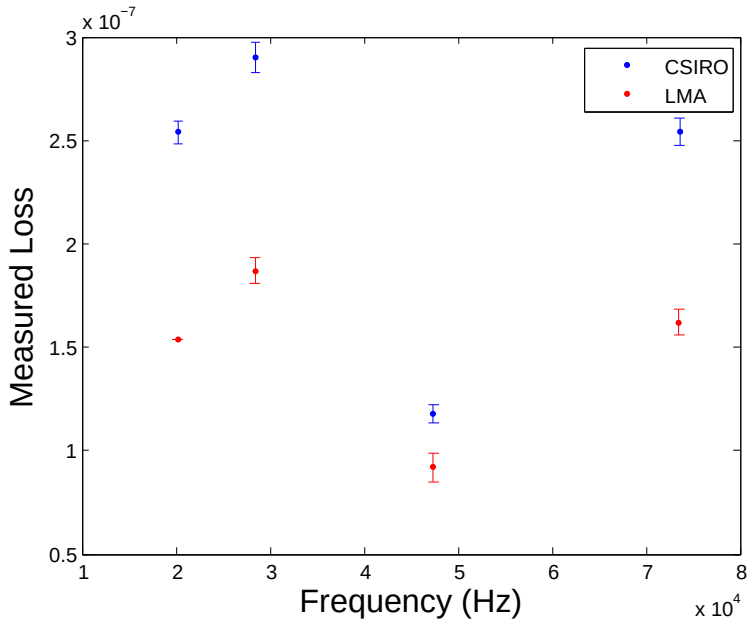

Figure 3.25: Measured mechanical losses of two identical 15% doped titania tantala/silica coated samples produced by two different coating vendors CSIRO and LMA.

The residual loss of the 35% titania 65% silica/silica coating was determined to be $(1.7 \pm 0.4) \times 10^{-4}$. This loss is greater than the loss of a single layer of silica, showing that the addition of titania is a source of mechanical dissipation. However, the magnitude of the dissipation appears to be less than that of tantala.

3.12 Conclusion

Highly reflective dielectric multi-layer coatings are necessary for all interferometric gravitational wave detectors. The introduction, however, of such coatings produces a significant noise source which significantly limits the sensitivities of these detectors. Studies show that the tantala component of the layers is the source of the majority of the loss within these coatings and that doping them with titania reduces this loss by up to 40% as shown by the measurements presented from samples produced by both vendors.

Early investigations of other dopants and different processes to produce such coatings also suggest that improvements can be implemented. However a reduction in the loss of nearly 40% already indicated a great improvement in thermal noise, which translates into a greater astronomical reach for advanced interferometers.

Chapter 4

Measurements of Mechanical Loss of Hydroxide Catalysis Bonds

4.1 Introduction

Friction between the fused silica mirror substrates and their suspension fibres in the test mass suspensions of interferometric gravitational wave detectors can lead to increased levels of thermal noise [104]. In the laboratory, this friction is reduced by lubricating the silk suspension loops and the test mass surface around the line of contact [125]. Whilst this is appropriate for measurements of the dissipation of the internal resonant modes of the samples tested in the laboratory environment, this is not suitable for the suspensions of an interferometric gravitational wave detector, as it would degrade the thermal noise of the pendulum modes of the suspensions. Instead, low mechanical loss jointing techniques are required to attach the suspension fibres to the test masses.

The process of hydroxide-catalysis bonding has been studied for use in the construction of low-loss fused silica suspensions and is currently implemented in the suspensions of the GEO600 detector [155]. Fused silica 'ears' are attached to flats on the barrels of the detector test masses, onto which fused silica suspension fibres

are welded. An illustration of a variant of this quasi-monolithic suspension is shown in figure 4.1 [87].

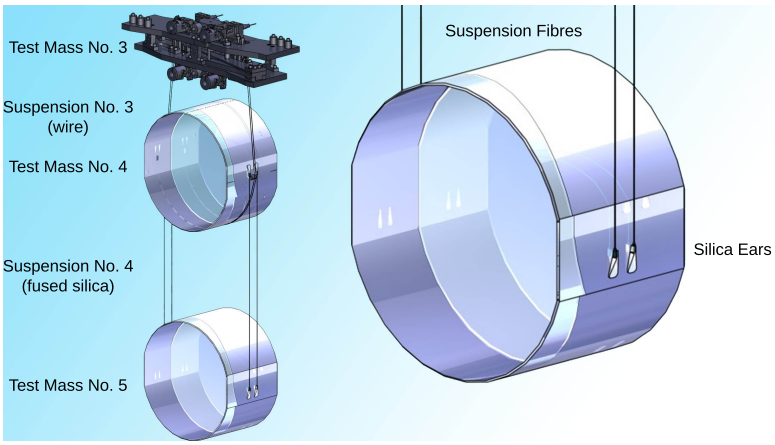

Figure 4.1: Conceptual design for the monolithic final stage suspension for the input and end test masses of the Advanced LIGO detectors . The test mass will be suspended using ears bonded to flats on the barrel of the mass with silica ribbons welded to the ears.

The technique of hydroxide catalysis bonding of fused silica components was developed at Stanford University by D. H. Gwo [156] and subsequently patented [157] for use in the construction of telescopes for the Gravity Probe B experiment [158].

Enhancements to this hydroxide catalysis bonding technique have been made at the University of Glasgow [4, 159, 160, 161]. Consequently, the currently operating GEO600 detector utilises quasi-monolithic fused silica test mass suspensions constructed using hydroxide catalysis bonds [77]. Current plans to upgrade the LIGO instruments to form an 'Advanced LIGO' detector system incorporate this technique [67]. It may also be used in the plans to upgrade the VIRGO detector. It is thus important to characterise the mechanical loss of the bonds and its significance for thermal noise.

Preliminary experiments on loss were carried out by Elliffe and Sneddon [160, 104] but it was felt these had to be extended and this was the aim of the work described in this chapter.

However, before discussing the experiment a description of the hydroxide catalysis process is needed.

4.2 The Chemistry of Hydroxide-Catalysis Bonds

Hydroxide-catalysis bonding is used to join oxide materials. Two surfaces, typically having a global flatness of $\lambda/10$ (where $\lambda = 633$nm), can be bonded using a very small volume of aqueous sodium or potassium hydroxide solution, commonly referred to as the *bonding solution*. The bonding solution is placed on one of the two surfaces to be bonded and the second surface is then gently placed on top. This solution enables a series of chemical processes, detailed in this section, which results in the formation of a silicate gel which then solidifies, over a period of weeks, to form a very thin, but strong and rigid, bond between the pieces being joined.

4.2.1 Hydration of the Silica Surface

The surface of silica is normally hydrophilic and attracts hydroxide ions (OH^-) to fill any open bonds of the silica [162]. This process is called hydration and when the silica is fully hydrated a large number of silanol groups (Si-OH) are formed on the surface [163]. Any contamination of the silica surface inhibits hydration so it is essential that before any bonding is performed, the silica surfaces are thoroughly cleaned to ensure maximum hydration. This process is detailed in [164].

4.2.2 Etching of the Silica Surface

Placing a concentrated aqueous hydroxide solution onto the surface of the silica causes etching. The additional OH^- ions form weak bonds with the silicon atoms on the substrate surface thus weakening the original lattice bond. This increases the number of liberated silicate molecules $Si(OH)_5^-$ which break away and become

available in solution. The hydration and etching process are described by equation 4.1 [162].

$$SiO_2 + OH^- + 2H_2O \rightarrow Si(OH)_5^- \tag{4.1}$$

4.2.3 Dehydration and Polymerisation

While the $Si(OH)_5^-$ ions are being released from the silica into the bonding solution, the overall number of active hydroxide ions in the solution is being correspondingly reduced. This means that the pH of the bonding solution decreases and that once the pH of the solution falls below 11, the silicate ions dissociate [162] to form $Si(OH)_4$ as described in 4.2.

$$Si(OH)_5^- \rightarrow Si(OH)_4 + OH^- \tag{4.2}$$

The $Si(OH)_4$ molecules then start to combine and polymerise to form siloxane polymer chains [162] and to dehydrate as represented by 4.3.

$$2Si(OH)_4 \rightarrow (OH)_3SiOSi(OH)_3 + H_2O \tag{4.3}$$

At the interface of the two surfaces, the siloxane chains start to form a rigid bond while the water evaporates or migrates into the bulk of the material. As the dehydration process continues, the siloxane chains intertwine and tangle rapidly forming a 3-D network which joins the two surfaces.

If the initial pH of the alkaline bonding solution is increased then the amount of time required for the silicate ions to become dissociated increases. This then increases the time required for the bond to set. Measurements have also shown that the maximum bond strength is achieved after it is left to cure at room temperature for approximately four weeks [165].

4.3 Measurements of Mechanical Loss of Hydroxide Catalysis Bonds

Despite the near monolithic properties of bonded pieces of silica, the hydroxide catalysis bonds introduce some mechanical loss. Quantifying the magnitude of such losses introduced by this bond is essential for determining the levels of thermal noise in bonded suspensions intended for use in interferometric gravitational wave detectors. As detailed in [104, 160, 4] investigations were made to determine the intrinsic loss factor of hydroxide catalysis bonds. In those studies measurements were made of the mechanical loss of bonds between three samples bonded with varying geometries and surface areas. For two of the samples the bonds were between two pieces of fused silica, and in the third a fused silica piece was attached to a sapphire substrate.

The first pair of fused silica samples bonded together were of equal size. They were both cylinders of 65 mm diameter and 70 mm long. The mechanical losses of each cylinder were measured separately before bonding. The lowest measured loss value obtained for the 40050 Hz fundamental longitudinal resonant mode of either cylinder was then used as a measure for the *substrate* loss. Thereafter the pair were bonded, left to cure and the mechanical loss of the fundamental longitudinal mode measured. The test mass was suspended by a silk loop and placed under vacuum. The resonant modes of these samples were excited electrostatically and the resulting displacements of the front face sensed interferometrically.

Assuming all other losses in the system are negligible, and letting the measured loss factors of the unbonded substrate and bonded sample be $\phi_{\text{substrate}}$ and ϕ_{bonded} respectively, we may write the following equation for each mode of the sample [104, 160]:

$$\phi_{\text{bonded}} = \left(\frac{E_{\text{substrate}}}{E_{\text{total}}}\right)\phi_{\text{substrate}} + \left(\frac{E_{\text{bond}}}{E_{\text{total}}}\right)\phi_{\text{bond}} \tag{4.4}$$

where $\frac{E_{\text{bond}}}{E_{\text{total}}}$ is the ratio of strain energy stored in the bond material, E_{bond}, to the

total strain energy stored in the substrate and the bond, E_{total}. $\frac{E_{\text{substrate}}}{E_{\text{total}}}$ is the ratio of energy stored in the substrate components, $E_{\text{substrate}}$, alone. The strain energy of the substrate is much greater than the strain energy stored in the bond, $E_{\text{total}} \simeq E_{\text{substrate}}$, thus the mechanical loss of the bonded sample is expressed by equation 4.5:

$$\phi_{\text{bonded}} \simeq \phi_{\text{substrate}} + \left(\frac{E_{\text{bond}}}{E_{\text{total}}}\right)\phi_{\text{bond}}. \tag{4.5}$$

In certain cases the ratio of strain energy in the bond to the total strain energy of a bonded sample of length L can be found analytically, if the thickness, b, and Young's Modulus of the bond layer are known. It can be shown that for the fundamental longitudinal mode [160]:

$$\frac{E_{\text{bond}}}{E_{\text{total}}} = \frac{2b}{L}\frac{Y_{\text{substrate}}}{Y_{\text{bond}}}. \tag{4.6}$$

In the previous investigations, Atomic Force Microscope (AFM) measurements were made of a sample bonded using the equivalent concentration and volume of bonding solution of the samples being investigated. The average bond thickness was determined to be (81 ± 4) nm and studies of a 1 μm thick bond determined that the Young's Modulus of the bond was 11% of the Young's Modulus of fused silica [160, 4].

Parameter	**Value**
ϕ_{bonded}	$(3.7 \pm 0.1) \times 10^{-6}$
$\phi_{\text{substrate}}$	$(7.1 \pm 0.1) \times 10^{-7}$
b (m)	$(81 \pm 4) \times 10^{-9}$
L (m)	0.14
$Y_{\text{substrate}}$ (GPa)	72
Y_{bond} (GPa)	7.9

Table 4.1: Parameters used in calculations by Sneddon et al of the bond loss for a 65 mm diameter by 140 mm long bonded fused silica cylinder [4].

The parameters presented in table 4.1 can be substituted into equation 4.5 and 4.6 to yield the bond loss of the 20411 Hz resonant mode of the bonded sample of 0.28 ± 0.04.

There were, however, aspects of this experiment which were not optimised. Firstly, since the two samples bonded together were the same size, the suspension loop coincided with the edge of the bond region and the chamfers of the test masses. This could have introduced excess loss in the measurement of the mechanical loss of the 20411 Hz resonant mode of the bonded sample.

Furthermore, $\phi_{\text{substrate}}$ was determined by measuring the mechanical loss of a 65 mm diameter by 70 mm long cylinder of a mode shape of a similar type to that measured for the bonded composite mass. However, despite being of a similar shape, these modes were of different frequencies - 40050 Hz and 20411 Hz respectively.

Recent studies have shown that the mechanical loss of silica can be a function of frequency and surface to volume ratio of sample studied, thus the mechanical loss of a mode of the 70 mm long mass may differ from that of an equivalent mode shape of a 140 mm long sample.

4.4 Semi-Empirical Model of Mechanical Losses in Silica

There are two companies which are capable of producing fused silica samples in the sizes and quality required for use in the network of interferometric gravitational wave detectors. The first vendor is Corning [166], who provided mirror substrates for the end mirrors and recycling mirror on the LIGO detectors, and Heraeus [167], who provided fused silica optics for the LIGO input mirrors and beam splitters as well as the fused silica optics for the GEO600 and VIRGO detectors. Each supplier offers a number of different optical grades of fused silica which have differing specifications for absorbtion and homogeneity. As discussed in section 3.1, these optical and

mechanical properties are of significant importance for interferometric gravitational wave detectors.

Measurements by Numata et al. [105] suggest that fused silica substrates produced by Heraeus have a lower mechanical loss than that of fused silica substrates produced by Corning. They also suggest that the various grades of Heraeus fused silica have different mechanical losses, with Suprasil-311 and Suprasil-312 both having the lowest mechanical loss, whereas the differing grades of fused silica produced by Corning all have similar mechanical losses.

Considerable studies have been made by other authors of the different types, sizes and aspect ratios of fused silica samples and their mechanical properties in relation to their use as optics in gravitational wave detectors [168, 169, 170, 171, 172]. A semi-empirical model has been developed by Penn et al. for the mechanical loss in fused silica [173]. This model contains terms representing the losses which are associated with the bulk of a silica sample, losses associated with the surface of the sample and thermoelastic loss

$$\phi\left(f, \frac{V}{S}\right) = \phi_{\text{bulk}} + \phi_{\text{surface}} + \phi_{\text{thermoelastic}}. \tag{4.7}$$

In this model, the loss of a sample depends both on frequency, f, and the sample volume to surface ratio, $\left(\frac{V}{S}\right)$, such that the mechanical loss of a fused silica sample, $\phi\left(f, \frac{V}{S}\right)$ is expressed as

$$\phi\left(f, \frac{V}{S}\right) = C_1 f^{C^2} + C_3 \left(\frac{V}{S}\right)^{-1} + C_4 \phi_{\text{th}} \tag{4.8}$$

where V is the volume of the sample in mm^3, S is the surface area in mm^2 and ϕ_{th}, the thermoelastic loss, is calculated from the material properties of fused silica [173]. The coefficients C_1, C_2, C_3 and C_4 are constants related to the specific type of fused silica studied.

The surface loss term for bulk samples is associated with damage from the abrasive polishing undertaken to obtain the desired flatness. In high quality fused silica the

bulk loss term is associated with the strained Si-O-Si bonds, where a minimum of energy at two different bond angles exists. This forms an asymmetric double-well potential so that when a strain is applied there is a redistribution of bond angles which results in a source of mechanical dissipation [174]. For the bulk samples measured in this chapter, the frequencies at which the mechanical loss is measured (15-80 kHz) lie well away from the peak of thermoelastic loss, therefore this term may be assumed to be negligible.

The coefficients which have been found to describe best the loss mechanism in Heraeus Suprasil-312 fused silica are [173]

$$C_1 = (0.76 \pm 0.02) \times 10^{-11} \quad (4.9)$$

$$C_2 = (0.77 \pm 0.02) \quad (4.10)$$

$$C_3 = (6.5 \pm 0.2) \times 10^{-9}. \quad (4.11)$$

However, the samples used throughout this chapter are cylinders of Heraeus Suprasil-311 fused silica. Suprasil-311 is manufactured identically to the Suprasil-312 type but with the addition of one more annealing cycle in order to increase the homogeneity of the refractive index. Numata investigated the mechanical losses of these two types of fused silica and found their losses to be identical within experimental error [105]. Consequently, the same coefficients were used originally in the comparison of the measured losses of the Heraeus Suprasil-311 fused silica samples and the predictions of the empirical model.

65 mm Diameter by 70 mm Long Fused Silica Cylinders

Loss measurements were made of two 65 mm diameter by 70 mm long fused silica cylinders. The loss values for each of the resonant modes were measured for at least three ringdowns of the same suspension. Samples were suspended several times to mimimise, as much as possible, the measurements being limited by the effects of suspension losses as described in section 3.4. For each suspension the length and amount of grease used to lubricate the suspension loop varied, resulting in a large

variation between the measured losses of each resonant mode with each changing suspension, as shown in table 4.2. For example, the measured mechanical loss of the 37998 Hz mode is $\sim$ 6 times higher in the seventh suspension compared with measured mechanical loss of the same mode during the second suspension.

Suspension	**Measured Mechanical Loss** ($\times 10^{-8}$)				
Number	**32308 Hz**	**36996 Hz**	**37998 Hz**	**39873 Hz**	**42901 Hz**
1	-	4.61	3.13	4.00	-
2	-	**3.04**	**2.44**	3.87	4.29
3	11.03	4.05	3.52	3.62	6.18
4	**3.60**	3.88	2.50	9.34	**3.34**
5	4.05	3.80	3.07	4.79	4.03
6	5.78	3.48	3.72	**3.08**	5.92
7	4.34	7.35	12.61	3.46	4.70
8	4.42	3.87	3.16	3.67	4.29
9	3.69	5.60	2.67	3.13	4.59
10	6.59	6.99	6.70	3.25	4.77

Table 4.2: Measured mechanical losses of the first five resonant modes of a 65 mm diameter by 70 mm thick Heraeus Suprasil-311 fused silica sample number 1 for ten different suspensions. The lowest measured mechanical loss for each resonant mode is highlighted in **bold**. The error in each measurement is estimated to be 5%.

Each sample was suspended ten times. The lowest average measured mechanical loss for each of the resonant modes of the fused silica cylinder were then plotted in figure 4.2 and compared with the losses predicted by the empirical model. The standard error in the measured loss values is observed to be between 5 and 10%.

It can be seen in figure 4.2 that some of the lowest measured loss values lie close to the empirical model. It is also clear that several loss values lie significantly above the empirical model. This is likely to be due to the measurements being limited by suspension losses.

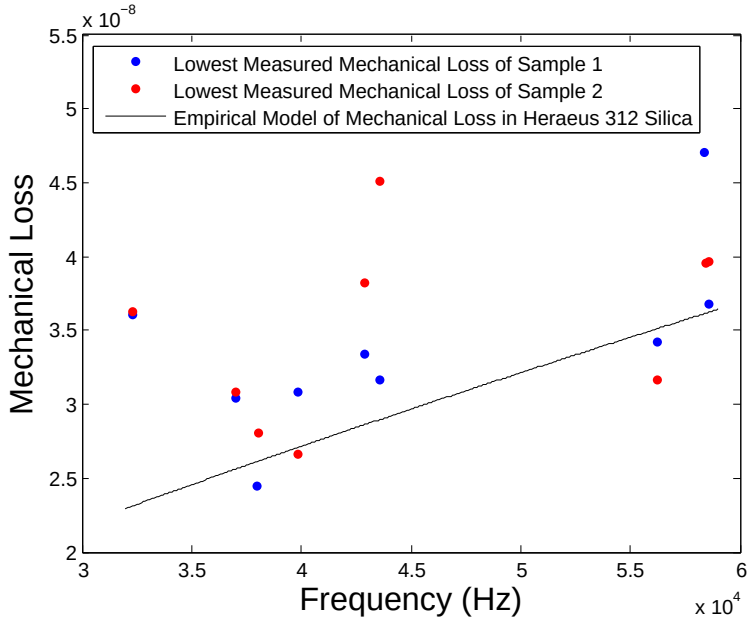

Figure 4.2: Lowest measured mechanical losses of resonant modes of two 65 mm diameter by 70 mm long Heraeus Suprasil-311 fused silica cylinders compared with the losses predicted by the empirical model.

More detailed analysis of the resonant modes measured can be made by looking at the shape of each resonant mode with finite element analysis. This provides more clues as to the source of the excess loss in some of these measurements.

Figure 4.3 shows the summed displacements U where $U = \sqrt{x^2 + y^2 + x^2}$ of two excited resonant modes whose minimum measured losses both lie *above* the empirical model. The minimum displacements within each resonant mode is indicated by the colour blue, and the maximum displacement is indicated by red. There is considerable motion observed in both these resonant mode shapes around the centre of the barrel where the thread forming the suspension loop lies. This could lead to excess *stick-slip* loss because the thread rubs against the barrel of the mass as the resonant mode rings down, resulting in a higher measured mechanical loss.

The resonant mode shapes of two of the modes whose measured mechanical losses lie close to the empirical model are represented in figure 4.4. The relative displacements around the centre of the barrel of these two modes are significantly lower than those

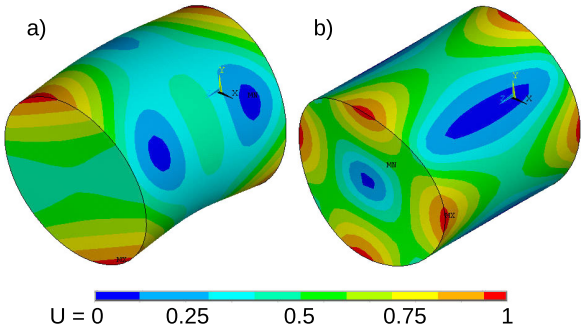

Figure 4.3: Finite element representation of the 32308 Hz and 36998 Hz resonant mode shapes for a 65 mm diameter by 70 mm long fused silica substrate where the relative displacements U = $\sqrt{x^2 + y^2 + z^2}$ are plotted in normalised, dimensionless units.

of the 32308 Hz and 36998 Hz resonant mode shapes. This is consistent with the hypothesis that, for resonant modes with significant motion around the barrel of the sample being suspended, they may be suspension limited.

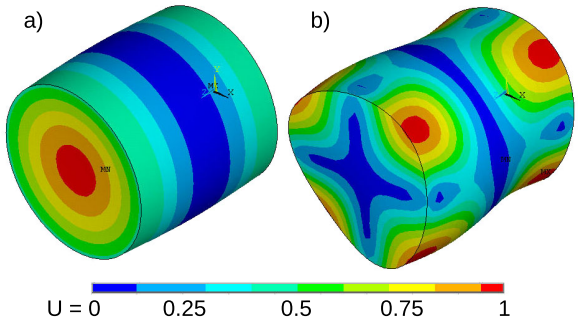

Figure 4.4: Finite element representation of the 39873 Hz and 56204 Hz resonant mode shapes for a 65 mm diameter by 70 mm long fused silica substrate where the relative displacements U = $\sqrt{x^2 + y^2 + z^2}$ are plotted in normalised, dimensionless units.

65 mm Diameter by 50 mm Long Fused Silica Cylinders

As a further check on the empirical model, two 65 mm diameter by 50 mm thick Heraeus Suprasil-311 fused silica substrates had their mechanical losses measured

and these are presented in figure 4.5. These follow a similar pattern to the slightly larger 70 mm thick samples with the measured mechanical loss of resonant modes with a larger amount of motion at the suspension region being higher than that of modes with little motion around the suspension contact area.

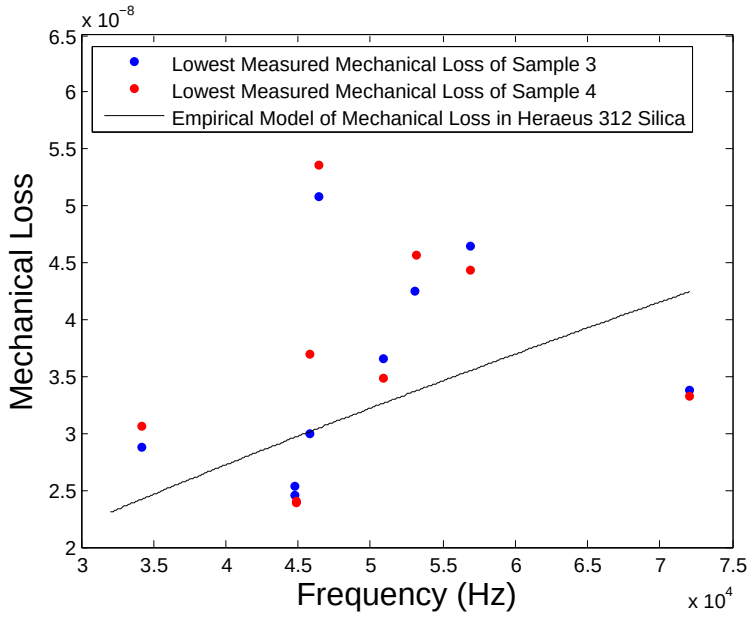

Figure 4.5: Lowest measured mechanical losses of resonant modes of two 65 mm diameter by 50 mm long Heraeus Suprasil-311 fused silica cylinders compared with the losses predicted by the empirical model.

It is clear, however, that measured mechanical losses of the 44801 Hz and 72048 Hz resonant modes on both fused silica samples lie *below* the empirical model. This pattern was repeated for the measured mechanical losses of these modes on both the 50 mm thick samples. Figure 4.6 shows that both these resonant modes have areas of little motion around the suspension area suggesting that it is the bulk loss which has been measured, since there should be less interaction with the suspension loop for those types of resonant mode. This suggests that the coefficients being used in the empirical model are not quite correct for the Heraeus Suprasil-311 type of fused silica.

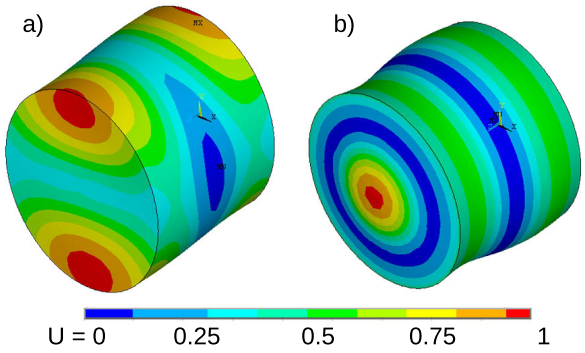

Figure 4.6: Finite element representation of the 44801 Hz and 72048 Hz resonant mode shapes for a 65 mm diameter by 50 mm long fused silica substrate where the relative displacements U = $\sqrt{x^2 + y^2 + z^2}$ are plotted in normalised, dimensionless units.

Fitting the Empirical Model to Heraeus Suprasil-311

The coefficient C_2 corresponds to the power-law of relaxation in fused silica due to thermally activated transitions [174], which is a property inherent to silica glass. Consequently, this coefficient is unlikely to change between the two different types of fused silica.

The surface loss of fused silica samples will be dependent on the surface polish. The final polishing of the four Heraeus Suprasil-311 cylinders measured in this section was specified to be identical. It is also likely to be similar to the Suprasil-312 samples tested to produce the semi-empirical model because they would be polished to a similar level before loss measurements were made. Therefore C_3 is also likely to remain the same for the two types of Suprasil fused silica.

This means that the only component of loss which may be expected to change between the different types of silica will be that of the bulk loss. This indicates that adjusting the value of C_1 should result in the semi-empirical model matching better the lowest measured mechanical losses of the four Suprasil-311 fused silica cylinders.

The eight resonant modes with the lowest measured mechanical losses from the four Heraeus Suprasil-311 samples were fitted to the empirical model. From a least squares fit, it was found that $C_1 = 0.63 \times 10^{-11}$ which corresponds to a reduction of $\sim 17\%$ in the bulk loss of Suprasil-311 compared to Suprasil-312. This is entirely feasible, because the extra annealing cycle performed in the production of the Suprasil-312 could potentially result in a reduction of the bulk loss.

The new empirical model for Heraeus Suprasil-311 fused silica was then plotted with the eight lowest measured mechanical losses and the original Suprasil-312 model for comparison, as shown in figure 4.7.

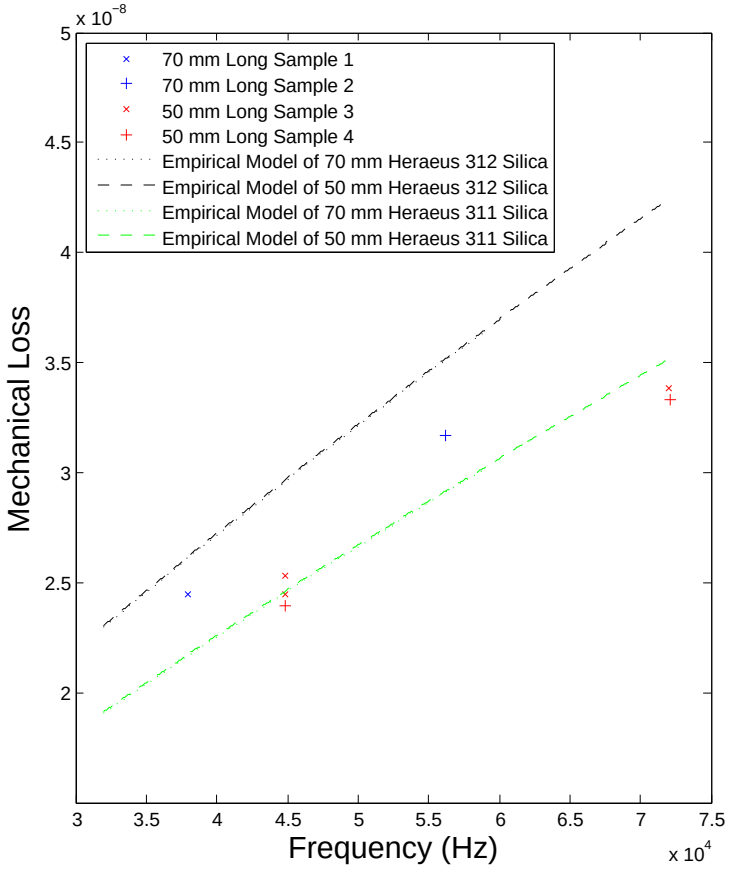

Figure 4.7: Empirical model fitted for Heraeus Suprasil-311 compared with the original Suprasil-312 Model and the eight lowest measured mechanical losses from the Heraeus Suprasil-311 fused silica cylinders.

It is clear from this figure that the new semi-empirical model fits the lowest mechanical loss of these two different aspect ratios of fused silica cylinders much better.

4.5 Hydroxide-Catalysis Bonding of Fused Silica Cylinders

As discussed in section 4.3, in an attempt to quantify the bond loss of a hydroxide-catalysis bond produced over a large area (~ 32 cm^2), two identical 65 mm diameter by 70 mm long fused silica cylinders were previously bonded together to make a 65 mm diameter by 140 mm long cylinder, an image of which can be seen in figure 4.8a. However, as both masses were of identical length, the chamfers of the cylinders, and the bond region itself, coincided with the suspension loop introducing potentially excess loss into the mechanical loss measurements.

This experiment was repeated here using non-identical fused silica cylinders so that the bond region is offset from the suspension loop. One mass was a 65 mm diameter by 70 mm long fused silica cylinder (sample 1 from section 4.4) and the other was a 65 mm diameter and 50 mm long fused silica cylinder (sample 3 from section 4.4) and they were hydroxide-catalysis bonded together to form a 120 mm long fused silica cylinder, as shown in figure 4.8b [1].

The bond was made between two flat faces on the end of the cylinders. The cylinders had small chamfers around their front faces making these faces 64 mm in diameter, so the area bonded is ~ 32.2 cm^2. The bonding solution used is the same bonding formula proposed for Advanced LIGO [175] which itself is based on the procedures used in the formation of bonds in the GEO600 detector [78]. It consists of commercially available NaOH $\sim 14\%$, SiO2 $\sim 27\%$ by weight (diluted 1:6 in de-ionised water). The sample was bonded by placing 12 μl of bonding solution on the cleaned

[1] Sample 1 was chosen over sample 2 as the measured mechanical losses of sample 1 were lower than sample 2. Sample 3 was used because sample 4 was used in another experiment which is not detailed in this thesis.

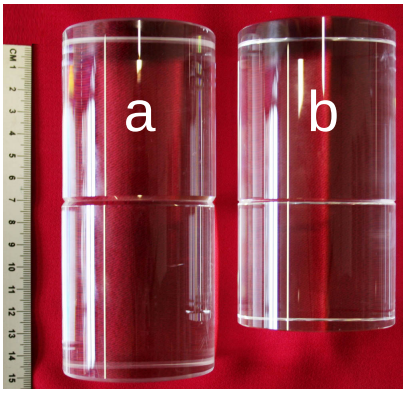

Figure 4.8: Image of the two bonded masses comprising of a) two identical 65 mm diameter by 70 mm long silica samples studied previously and of b) 65 mm diameter by 50 mm and 70 mm long silica samples studied in this thesis.

face of one of the masses and positioning the corresponding face of the second mass in contact with the solution. It was then left to cure for a period of five months, when, on inspection, the sample appeared to have successfully bonded with only a few small bubbles and one small area in the centre which appeared to contain a tiny amount of contamination. It was thought that these imperfections were not significant enough to affect the bond and the corresponding loss measurements.

4.6 Scanning Electron Microscope Measurements of the Thickness of Hydroxide Catalysis Bonds

In order to calculate the ratio of the strain energy stored in the bond region to the total strain energy in the bonded sample it is essential to establish the thickness of the bonded region. At the same time as the 50 mm and 70 mm long fused silica samples were being bonded, a second pair of samples was bonded together to produce a nominally identical bond which could be studied without damaging the full scale sample. The two samples which were bonded to create this *witness* bond were 25.4 mm diameter by 5 mm long fused silica samples, bonded using 2 μl of bonding solution. The bonding area of this smaller pair of samples is a sixth of the

area of the bond of the larger sample, so to keep the volumes of bonding solution identical one sixth of the bonding solution was used.

A third bonded sample was produced from two 25.4 mm diameter by 5 mm long cylinders, polished by General Optics [176] to $\frac{\lambda}{10}$ flatness, and bonded together with the same concentration but using one tenth of the volume of the bonding solution: 0.2 μl. This volume was just sufficient to fill the bonded area, and after this the bond was left to set and cure.

A cross-section $\sim$ 3 mm thick was cut from the one inch diameter witness bonds using a silicon carbide blade mounted on a Logitech Model 15 Saw [177]. The slices were sawn in such a way that the bond lies perpendicular to the cut face, as shown in figure 4.9. In these samples the bond region lies horizontally across the centres of each of the slices and runs through the sample. It is highlighted by the dotted red line.

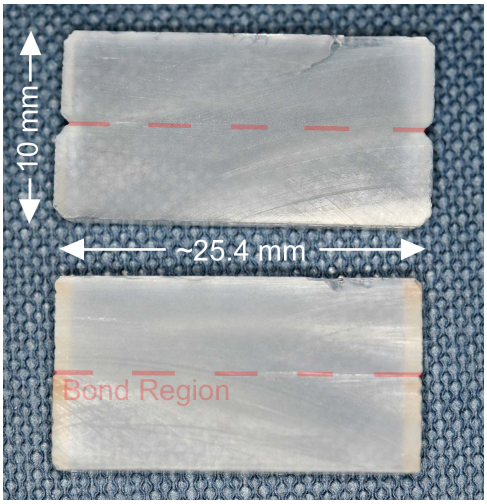

Figure 4.9: Image of two cross-sections cut from the 0.2 μl (top) and 2 μl (bottom) 1 inch diameter hydroxide-catalysis bonded samples.

The samples were then mounted inside a Hitachi TM-1000 Tabletop Electron Microscope [178] and images of the bond region were captured. In figure 4.10, the region where the bond lies in the cross-section of the 2 μl bonded sample can be seen clearly running horizontally across the 1,500$\times$ magnification image. However, when

viewed using the maximum magnification of the electron microscope (10,000×) it is impossible to distinguish exactly where the bond area is from the rough surface created by the sawing of this cross-section.

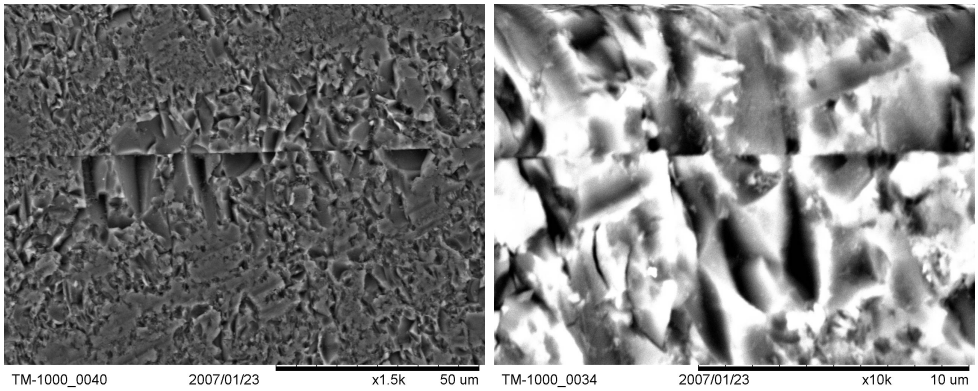

Figure 4.10: 1,500× and 10,000× magnified Scanning Electron Microscope images of an *unpolished* cross-section of the 2 μl hydroxide-catalysis bonded sample, taken using a Hitachi TM-1000.

To enable measurements of the bond thickness to be taken from this sample it was necessary for the surface to be polished to remove the rough surface created by the sawing process. The slice cut from the 2 μl bonded sample was polished for three hours on a Logitech Precision Polishing Machine [179] with SF-1 colloidal silica polishing compound. After this, visual inspection showed that the newly polished face of the cross-section sample was clear, instead of the scratched opaque colour it had been before the polishing commenced, and no longer had visible scratches.

The sample was cleaned and studied for a second time with the table-top scanning electron microscope. This greatly enhanced the surface of the cross-section, and the bond region can be identified clearly in figure 4.11.

Using the maximum magnification of the microscope, measurements of the bond thickness were taken at several points on the bond region of the polished sample. This indicated a bond thickness of (83 ± 7) nm, which is consistent with the (81 ± 4) nm nm measured in the original experiment [160, 4]. However, the mea-

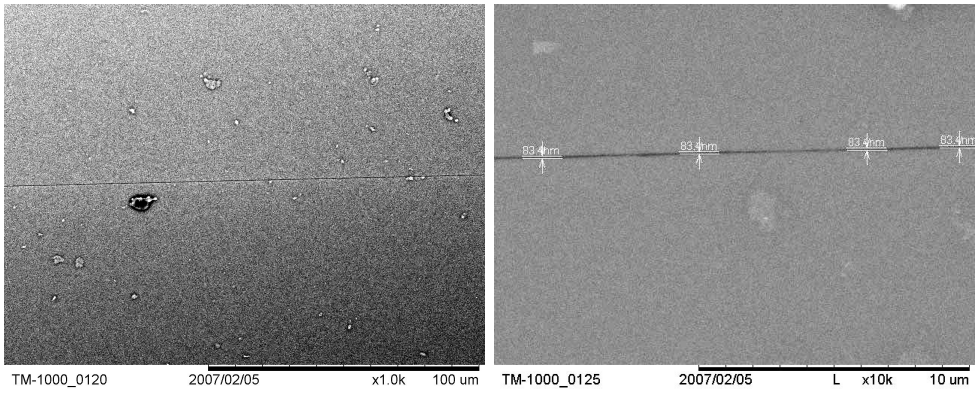

Figure 4.11: 1,000× and 10,000× magnified Scanning Electron Microscope images of *polished* cross-section of the 2 μl hydroxide-catalysis bonded sample, taken with a Hitachi TM-1000.

surement tool of the software which controls the microscope increases in 27.8 nm steps, therefore the 83 nm is of questionable accuracy.

In an attempt to increase the resolution of the measurement tool, the sample was rotated $\sim 45°$ so that two measurements were taken perpendicular to each other in the same area. This provided thickness measurements in the x and y directions of 111 nm, as shown in figure 4.12, which, when combined, yielded a bond thickness of (79 ± 5) nm.

It was then decided to measure the thickness of the bond using a more powerful FEI Nova 200 Dualbeam FIB system Scanning Electron Microscope [180] at the Kelvin Nanocharacterisation Centre [181]. On the first attempt to image the bond using this microscope the silica sample charged up electrostatically so much under the 15 kV accelerating voltage of the electron beam that the surface of the sample could not be imaged. To dissipate any charge build-up on the surface of the silica the sample was removed, sputtered with a few nanometers of gold, remounted inside the electron microscope with copper tape and re-imaged using a lower accelerating voltage of 5 kV.

The second scanning electron microscope has a much greater magnification and imaging resolution. Viewing at 120,088× magnification produced a clearer picture

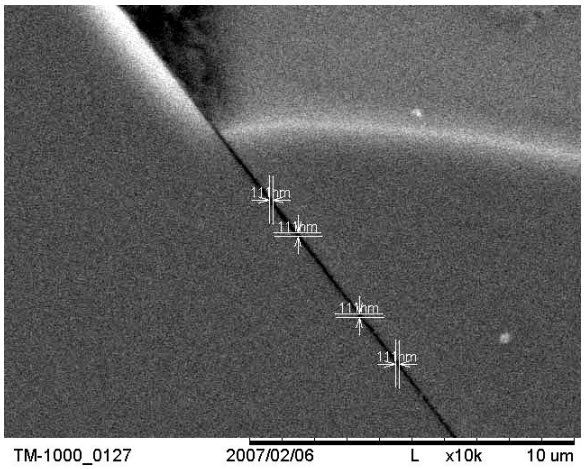

Figure 4.12: 10,000× magnified Scanning Electron Microscope image of polished cross-section of the 2 μl hydroxide-catalysis bonded sample rotated 45°, taken with a Hitachi TM-1000.

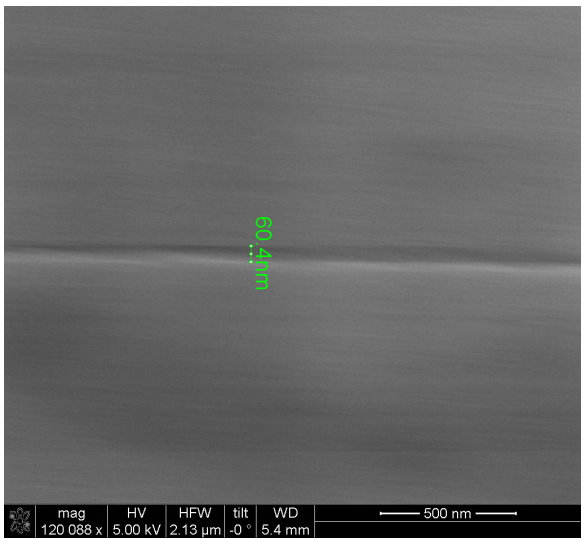

Figure 4.13: 120,088× magnified Scanning Electron Microscope image of polished cross-section of the 2 μl hydroxide-catalysis bonded sample, taken with a FEI Nova 200 Dualbeam FIB system.

of an area of the bond region, as visible in figure 4.13. Measurement of this region indicated a bond thickness of (60.4 ± 2.0) nm. After this was completed, the copper tape which was earthing the sample became unstuck and detached itself from the sample. Consequently, the silica sample charged up, as the charge could not be dissipated, making further measurements impossible.

A cross-section of the 0.2 μl bonded sample was cut and polished using exactly the same processes. Bond thickness measurements were made of this sample using the scanning electron microscope. Measurements of three areas across the cross-section of the sample determined the thickness of the hydroxide catalysis bond to be (80.9 ± 2.0) nm, (81.2 ± 2.0) nm and (80.1 ± 2.0) nm, as indicated in figure 4.14.

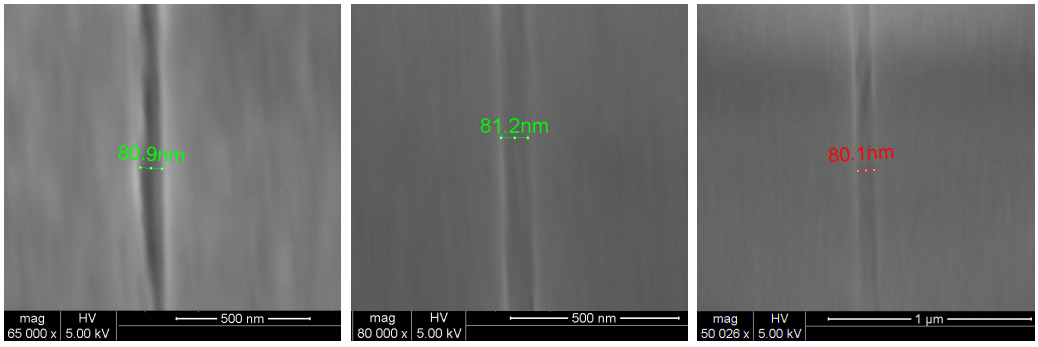

Figure 4.14: 65,000×, 80,000× and 50,026× magnified Scanning Electron Microscope images taken across a polished cross-section of the 0.2 μl hydroxide-catalysis bonded sample, using a FEI Nova 200 Dualbeam FIB system.

4.7 Atomic Force Microscope Measurements of the Thickness of Hydroxide Catalysis Bonds

Atomic force microscope measurements of the bond thickness were then taken of the sample bonded with 2 μl of bonding solution. This was done with the atomic force microscope set to *tapping mode* [182] and taking surface profiles of 2 μm × 2 μm regions containing the bond region, as shown in the right-hand-side of figure 4.15.

The graph on the left-hand-side shows the profile of the surface indicated by the black line in the image. It is clear that in between the two red markers on this line there is a distinct dip in the height across the profile which corresponds with the darker bond region. The thickness of the bond can then be determined by measuring the width of this dip. The cross-section sample was mounted in the atomic force microscope in such a way that the bond region did not run exactly vertically from top to bottom of the profile image, so after correcting for the $\sim 5°$ angle the bond was determined to be 101.2 nm thick.

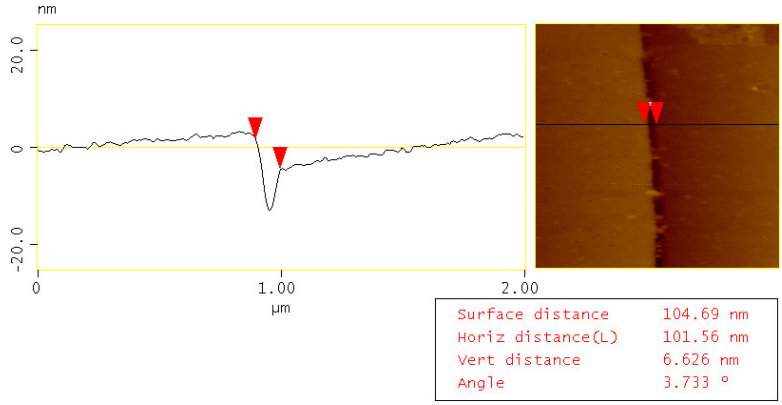

Figure 4.15: Atomic Force Microscope image of the polished cross-section of the 2 μl hydroxide-catalysis bonded sample.

However, on closer inspection of the profile image, it is obvious that the red markers do not coincide exactly with the darker region of the bond area. It was then suggested that the dip in the surface profile could have been created by the abrasive nature of the polishing process. The silicon carbide and aluminium oxide grits used in the various stages of the polishing process, detailed in Appendix A, as well as polishing the scratched face of the cross-section sample could have ground down the hydroxide catalysis bond but at a much greater rate. This is because the bond is much softer than the fused silica, as discussed in section 4.3, since the Young's Modulus of the bond is $\sim 11\%$ of that of fused silica. Grit in this newly hollowed out bond region would then erode and curve the edges of the silica pieces where the bond was originally, accounting for the curved profile at the two red markers. This erosion was not obvious when the samples were viewed from directly above by the

two scanning electron microscopes. It is thought not to have affected the thickness measurements taken by them, since the hydroxide-catalysis bond region could be determined easily because it appeared to be a different shade of grey from the fused silica surroundings.

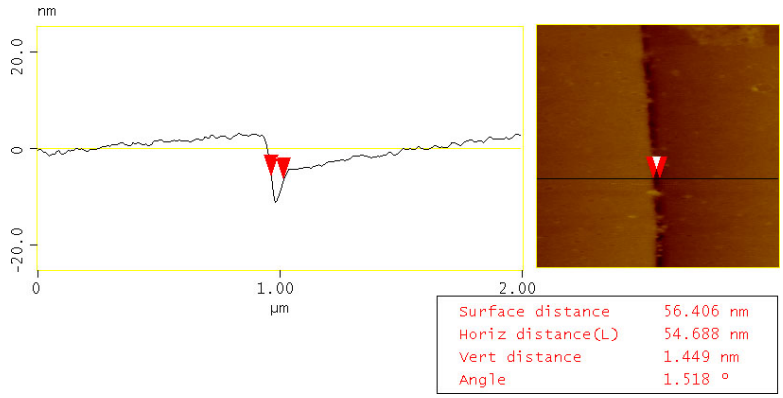

Figure 4.16: Reanalysed Atomic Force Microscope image of the polished cross-section of the 2 μl hydroxide-catalysis bonded sample.

Reanalysis of this profile was made by measuring the thickness of the dark region on the image of the bond area, as indicated in figure 4.16. This determined a bond thickness of 54.5 nm, which is approximately 10% thinner than the 60.4 nm thickness measured using the higher powered Scanning Electron Microscope.

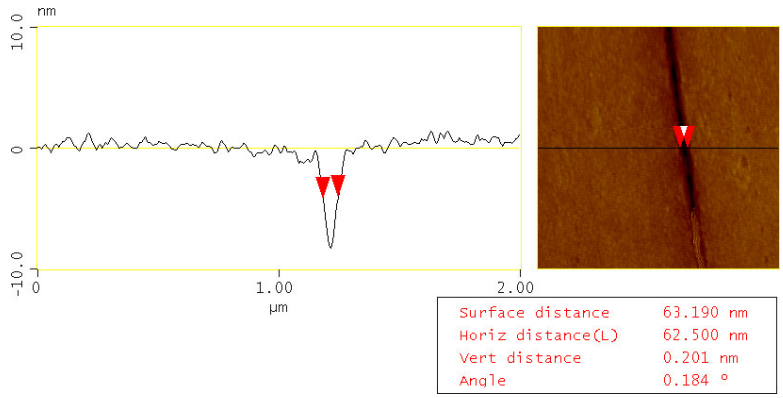

Figure 4.17: Second Atomic Force Microscope image of the polished cross-section of the 2 μl hydroxide-catalysis bonded sample.

A second area on this bonded cross-section was imaged, as shown in figure 4.17, and measurement of the dark bond region in the surface profile yields a slightly thicker bond thickness of 61.6 nm, which again is in agreement with the thickness measured using the scanning electron microscope. The two fused silica pieces which were bonded together to make this sample were *recycled* from another experiment. Consequently, the bonding surfaces may not have been precisely $\frac{\lambda}{10}$ flat so it is possible that the thickness of the bond may vary slightly through the cross-section. Combining these reanalysed measurements of the bond gives an average bond thickness of (58.0 ± 3.5) nm which agrees with the measurements taken on this sample using the scanning electron microscope.

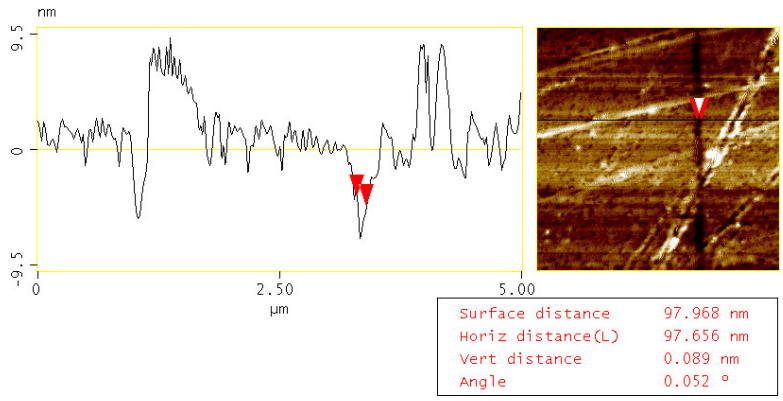

Figure 4.18: Atomic Force Microscope image of the polished cross-section of the 0.2 μl hydroxide-catalysis bonded sample.

Atomic Force Microscope measurements were also made on the cross-section cut from the 0.2 μl hydroxide-catalysis bonded sample. Imaging of two regions on this sample, presented in figures 4.18 and 4.19, determined the bond thicknesses to be 97.4 nm and 97.1 nm, which combine to give a thickness of (97.3 ± 0.1) nm. This is slightly higher than the 80.7 nm average thickness measured using the scanning electron microscope. The combined error in the thickness measurements of this sample is approximately 35$\times$ less than the combined error obtained from the thickness measurements of the 2 μl bonded sample. This could be because the two faces on the fused silica samples which were bonded together to make the 0.2 μl bonded sample were polished to $\frac{\lambda}{10}$ flatness which could have produced a much more consistent

bond thickness throughout the cross-section.

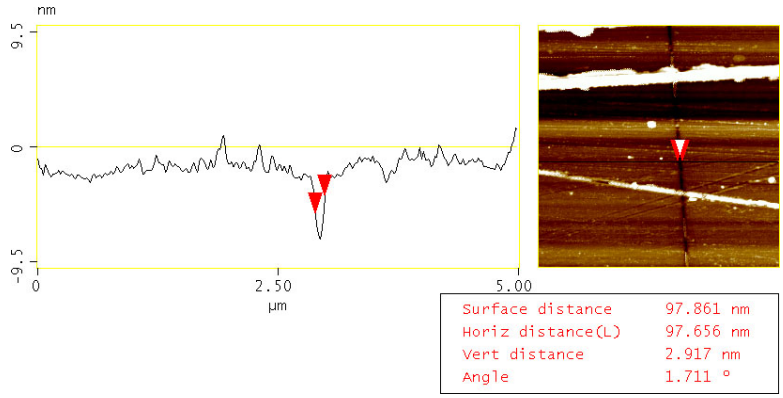

Figure 4.19: Second Atomic Force Microscope image of the polished cross-section of the 0.2 μl hydroxide-catalysis bonded sample.

4.8 Transmission Electron Microscope Measurements of the Thickness of Hydroxide Catalysis Bonds

The technique of Transmission Electron Microscopy can be used to image specimens which are a few microns thick because an electron beam can transit through these thinner samples, and show clearly different materials from their differing transmissions. A 1 μm thick electron transmissive slice was prepared from the 2 μl bonded sample using Focussed Ion-Beam milling, on the FEI Nova 200 Dualbeam FIB system Scanning Electron Microscope [180] at the Kelvin Nanocharacterisation Centre [181]. The gallium ions of the highly concentrated and focused beam were used to mill out a $\sim$ 10 μm cubic volume from the bond region. This slice could then be *lifted out* by positioning an aluminium tip next to it and attaching them through sputtering the contact area with platinum and lifting away the sample to be imaged under the transmission electron microscope. The ion-beam was then used to thin down the centre of the milled region to make it wedge-shaped where the top of the

wedge is 1 μm thick, as shown in figure 4.20. The bond region can be seen running vertically down the centre of this image, with the aluminium tip on the right hand side of the image.

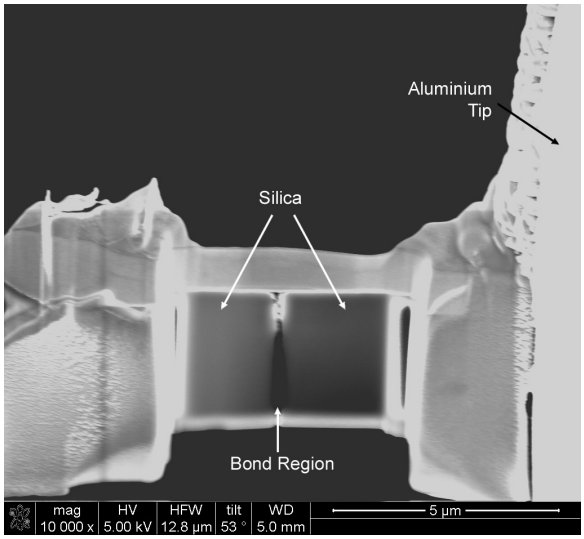

Figure 4.20: $10,000\times$ Scanning Electron Microscope image of a slice of the 2 μl hydroxide-catalysis bonded sample fabricated using Focus Ion-Beam milling.

This sample was then transferred into a FEI Tecnai T20 Transmission Electron Microscope [183] and the thinned out bond region imaged, as shown in figure 4.21. This gave a bond thickness measurement of (65 ± 5) nm, which is in agreement with the thickness determined using the scanning electron and atomic force microscopy. The Transmission Electron Microscope yielded the clearest image of the bond and consequently the thickness of the bond in the sample is taken to be (65 ± 5) nm throughout the analysis in the remainder of this chapter.

The image on the left hand side of figure 4.21 suggests that the bond gets thinner at the bottom, but this is thought to be due to the manufacturing process of the TEM sample. The silicate bond is softer than the surrounding silica, so it is possible that the gallium ions mill this region away at a higher rate. Subsequently, the tip of the wedge could be milled away completely as the bond area is so thin. With the sample mounted so that the bond runs vertically, it is possible that the weight of the lump of silica still attached to the left hand side of the TEM sample, visible in

figure 4.20, could cause the sample to sag in the middle, making the bond appear thinner at the bottom. This is less likely to affect the thickness nearer the top of the sample, as the wedge is much thicker and less likely to bend, consequently the bond thickness measurement was taken across this area, which is indicated by the black box.

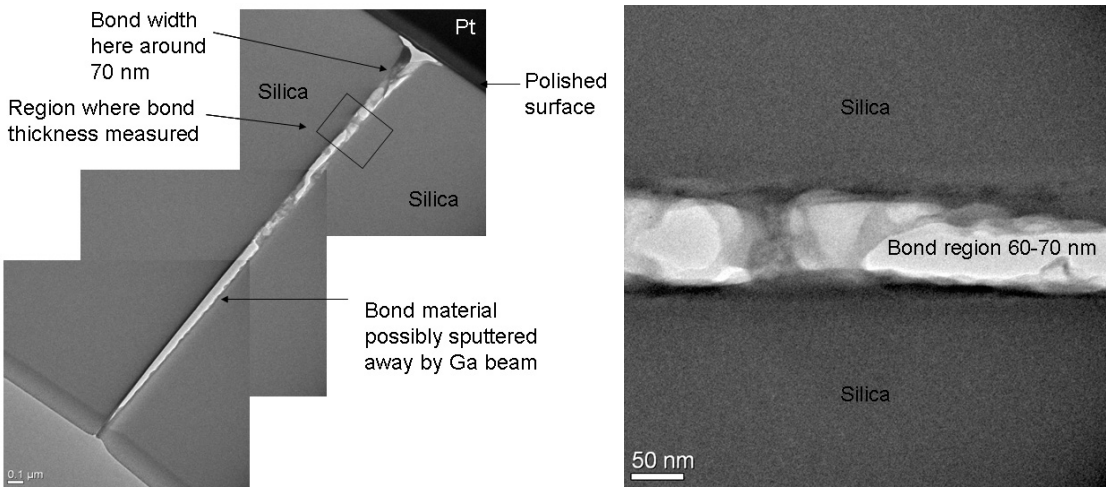

Figure 4.21: Transmission Electron Microscope images of focus ion-beam milled section of the 2 μl hydroxide-catalysis bonded sample.

Further evidence of the effect of milling of the bond region is clear in the image of a different sample. Figure 4.22 shows a transmission electron microscope image of a bond made, using the same bonding solution, but of an advanced LIGO ear [184] bonded to a $\frac{\lambda}{10}$ silica flat. It is clear in this image that the focussed ion-beam milling process has worn away all the bond material from the edge of the sample, thus creating a void. The thickness of this bond is measured to be (34 ± 5) nm.

4.9 Finite Element Analysis of Hydroxide-Catalysis Bonds

The ratio of strain energy stored in the bond region to the total strain energy of the bonded sample as a whole was previously calculated analytically using equation

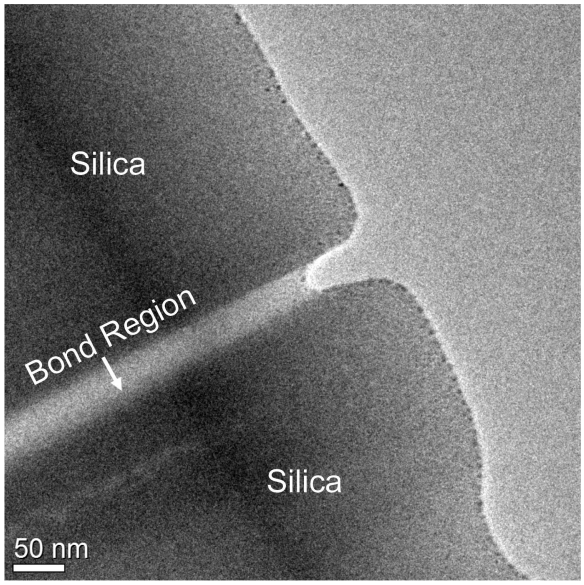

Figure 4.22: Transmission Electron Microscope image of polished cross-section of an *Advanced LIGO ear* bonded using 0.7 μl of hydroxide-catalysis bonding solution.

4.6 [160] for the *fundamental longitudinal* (2, n=0) resonant mode, where the numbering denotes the symmetry classification of the modes, following the paper by G. MacMahon [133]. However, it is also possible to evaluate the ratio for this resonant mode, and others, using finite element analysis. The ratio was calculated in two ways.

4.9.1 Finite Element Analysis of Strain Energy stored in Hydroxide-Catalysis Bonded Fused Silica Samples Modelled Using Beam Elements

As described in section 4.8, the thickness of the bond layer in the bonded sample found using the transmission electron microscope was $\sim$ 65 nm. This thickness is much less than the 32.2 cm^2 bond area which makes the aspect ratio difficult for the bond region to be accurately *meshed* in the ANSYS® finite element package [132]. Instead, the 65 mm diameter by 50 mm long and 65 mm diameter by 70 mm long fused silica cylinders were modelled using *3 node 189 beam elements* [185] with a

series of hydroxide-catalysis bonds of different thicknesses varying from 1×10^{-4} m to 1×10^{-7} m.

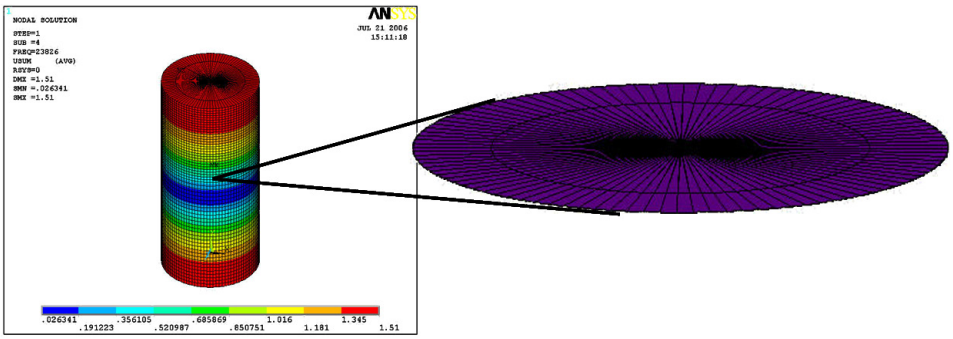

Figure 4.23: Finite element representation of the 23826 Hz resonant mode of the 65 mm diameter by 120 mm long bonded silica mass, and isolated bond region.

The strain energy of the entire bonded mass was calculated for each resonant mode in the finite element analysis before isolating the bond region, as illustrated in figure 4.23, and outputting the strain energy in this region only.

The strain energy ratio $\frac{E_{\text{bond}}}{E_{\text{total}}}$ for four resonant modes was calculated for each of the thicknesses modelled (1×10^{-4} m , 5×10^{-5} m $\ldots$ 1×10^{-7} m) and plotted in figure 4.24.

A linear fit of this data allows the extrapolation of the energy ratio for bond thicknesses below 1×10^{-7} m. Scanning electron microscopy of the *witness* bonded sample determined the thickness of the bond, and therefore of the full-scale bond, to be (65 ± 5) nm. By multiplying the gradient of each of the linear fits with this thickness the ratio of strain energy stored in the bond region to the total strain energy can be calculated, as presented in table 4.3.

This technique of determining the energy ratio, is not too processor intensive and each model can be run in only a few seconds. However, this technique, for an unknown reason, does not identify *all* the resonant modes for the bonded silica.

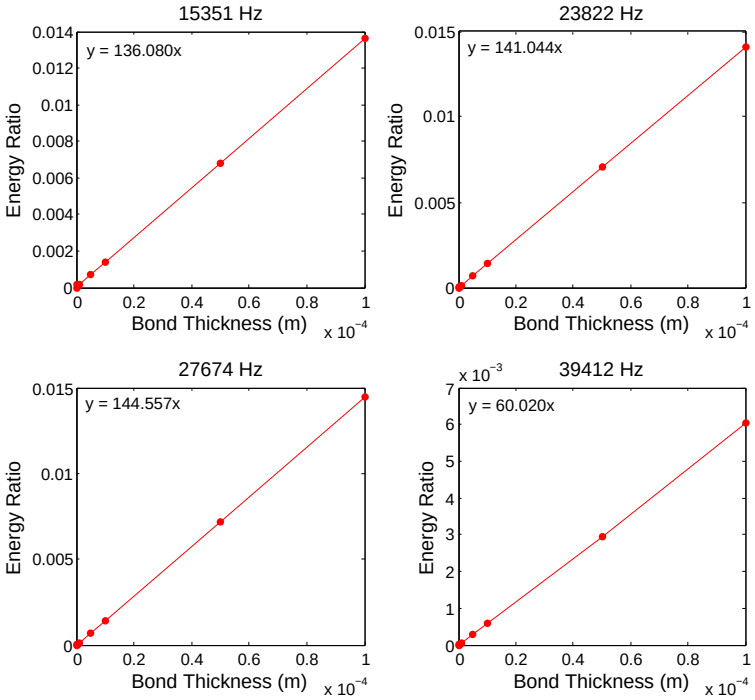

Figure 4.24: Ratio of Energy Stored in varying bond thicknesses on the 65 mm diameter by 120 mm long bonded fused silica sample for four of the resonant modes, modelled using *3 Node 189 Beam Elements*.

Frequency (Hz)	Gradient	Energy Ratio ($\times 10^{-6}$)
15195	136.08	8.85 ± 0.68
23826	141.04	9.17 ± 0.71
27255	144.56	9.40 ± 0.72
40267	60.02	3.90 ± 0.30

Table 4.3: Ratio of strain energy stored in the (65 ± 5) nm bond region of four resonant modes of the 65 mm diameter by 120 mm long bonded Heraeus Suprasil-311 fused silica cylinder, modelled using *3 Node 189 Beam Elements*.

4.9.2 Finite Element Analysis of Strain Energy stored in Hydroxide-Catalysis Bonded Fused Silica Samples Modelled Using Solid Elements

The bonded silica cylinder was modelled instead using *20 Node 95 Solid Elements* [186]. As before, it is not possible to model a bond $\sim$ 65 nm thick so a series of models was run with decreasing thicknesses of bonds. The maximum number of nodes available with the ANSYS® Academic Teaching Advanced v. 11.0 licence to create the elements in the model is only 256,000. This meant that the thinnest bond which could be modelled between the two cylinders was 0.2 mm. A series of models was run between 0.5 mm and 0.2 mm, and the ratio of strain energies stored in each resonant mode for each bond thickness determined. This technique is detailed in Appendix C and in a tutorial created by the author [187].

Using the same computing power, each model takes several hours to run, but this technique identifies all of the resonant modes for the bonded sample, including the four found using the previous technique. They are shown in figure 4.25. The bond area in the modelled cylinder is indicated in each of the resonant mode illustrations by the black band which runs around the barrel.

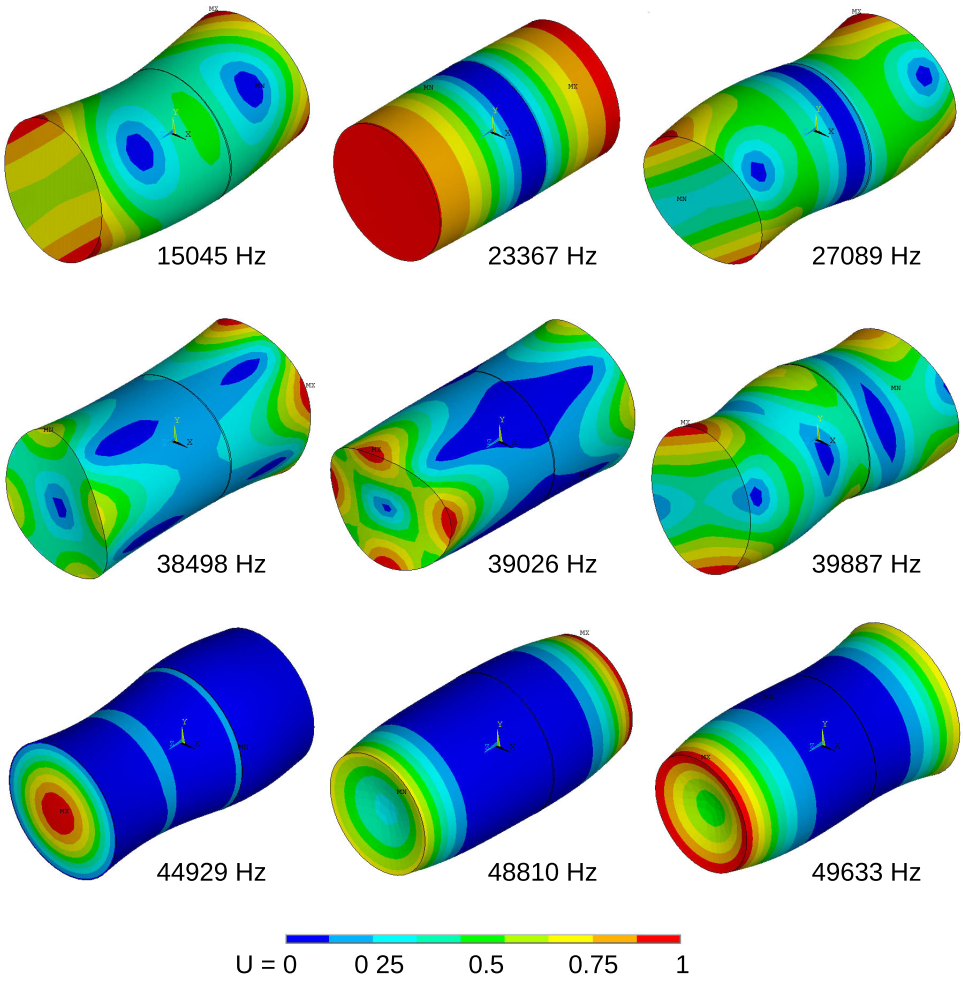

Figure 4.25: ANSYS® illustrations of nine resonant mode shapes of the 65 mm diameter by 120 mm long bonded fused silica substrates where the relative displacements $\mathrm{U} = \sqrt{x^2 + y^2 + z^2}$ are plotted in normalised, dimensionless units.

Seven different models were run with varying bond thicknesses, and the energy ratios for nine of the resonant modes determined and plotted against thicknesses for each individual frequency in figure 4.26.

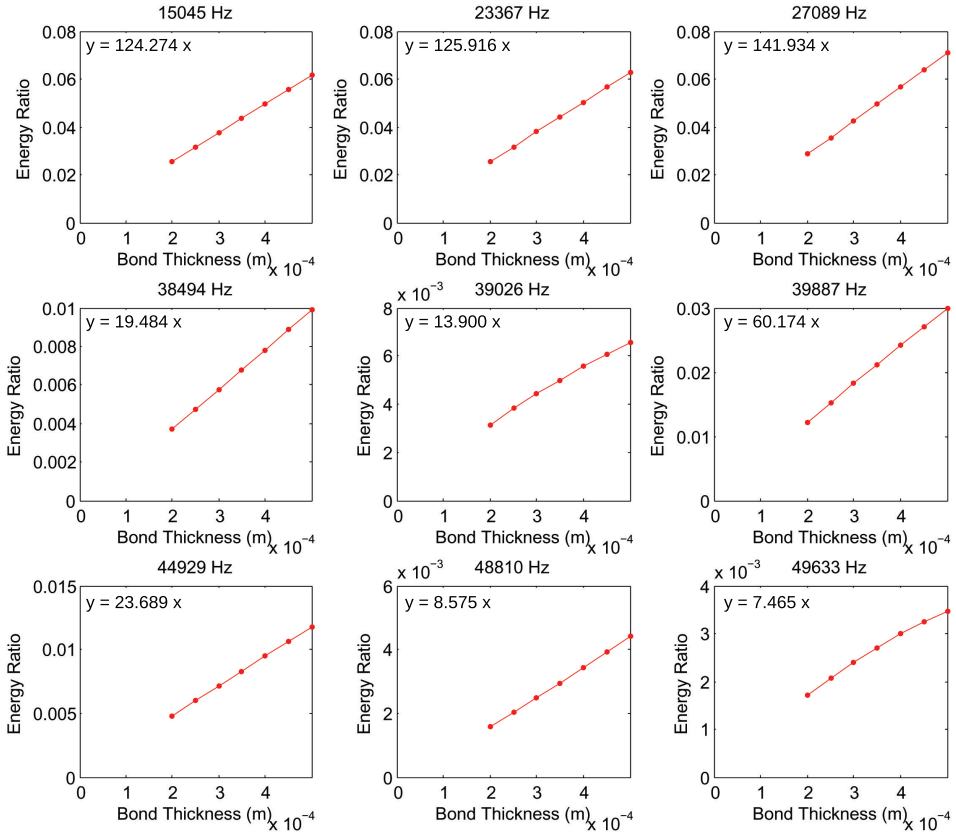

Figure 4.26: Ratio of Energy Stored in varying bond thicknesses on the 65 mm diameter by 120 mm long bonded fused silica sample for nine of the resonant modes, modelled using *20 Node 95 Solid Elements*.

Using the gradient of each of the linear fits, the ratio of strain energy stored in the (65 ± 5) nm hydroxide-catalysis bond between the two fused silica cylinders can be calculated for each resonant mode. These energy ratios are detailed in table 4.4.

The four energy ratios for the bond between the two cylinders determined from models created using *beam* elements are in reasonable agreement with the corresponding energy ratios found by modeling the bonded mass with *solid* elements.

Frequency (Hz)	**Gradient**	**Energy Ratio** ($\times 10^{-6}$)
15045	124.274	8.08 ± 0.62
23367	125.916	8.18 ± 0.63
27089	141.964	9.23 ± 0.71
38498	19.484	1.27 ± 0.10
39026	13.900	0.90 ± 0.07
39887	60.174	3.91 ± 0.30
44929	23.689	1.54 ± 0.12
48810	8.575	0.56 ± 0.04
49633	7.465	0.49 ± 0.04

Table 4.4: Ratio of strain energy stored in the (65 ± 5) nm bond region of nine resonant modes of the 65 mm diameter by 120 mm long bonded Heraeus Suprasil-311 fused silica cylinder, modelled using *20 Node 95 Solid Elements*.

It can be seen in table 4.5 that the modelled resonant frequencies from both techniques are in reasonable agreement with those found experimentally on the bonded mass. The modelled resonant frequencies determined using the solid element models are slightly below the experimentally found resonant frequencies, Despite this, the ratios found using this technique, presented in table 4.4, will be used in section 4.11 for the calculation of the bond loss for each of these modes. This is because the second technique finds the strain energy stored in the bond region for *all* the experimentally measured resonant modes of the cylinder.

4.10 Measurement of the Bond Loss of Two Masses Hydroxide-Catalysis Bonded Together

Mechanical loss measurements were then made of nine resonant modes of both the 65 mm diameter by 120 mm long bonded fused silica cylinder and a 65 mm diameter by 120 mm long substrate Heraeus Suprasil-311 fused silica cylinder, forming a control

Beam Element Modelled Freq (Hz)	Solid Element Modelled Freq (Hz)	Experimentally Measured Freq (Hz)
15195	15045	15280
23826	23367	23756
27255	27089	27605
-	38498	38866
-	39026	39399
40267	39887	40385
-	44929	45389
-	48810	49002
-	49633	49838

Table 4.5: Comparison of experimentally measured and modelled resonant frequencies of the 65 mm diameter by 120 mm long bonded Heraeus Suprasil-311 fused silica cylinder.

sample for the bond loss analysis. The resonant frequencies and the mode shapes of all these modes were found using finite element analysis, a selection of which is shown in figure 4.25.

The samples were suspended by a loop of lightly greased silk thread, placed in a vacuum tank and pumped out to $\sim 10^{-5}$ mbar. The mechanical loss of each resonant mode was measured several times before repeating the process for different suspension lengths. This was done to mimimise any excess suspension loss. The lowest average measured mechanical loss of each of the resonant modes of the bonded and substrate cylinders are plotted in figure 4.27 and compared with the losses predicted by the adjusted empirical model for Heraeus Suprasil-311.

It is evident from this plot that the measured mechanical losses of the 120 mm long bonded cylinder are much higher than the losses measured of the 120 mm long monolithic cylinder. For all four of the 65 mm diameter by 70 mm long and 65 mm diameter by 50 mm long Heraeus Suprasil-311 fused silica samples some of the

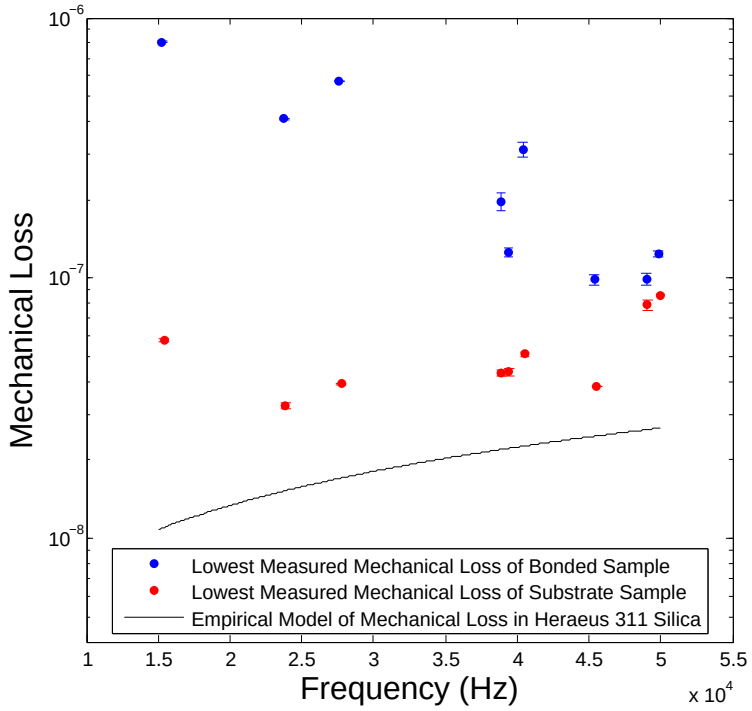

Figure 4.27: Lowest measured mechanical losses of resonant modes of the 65 mm diameter by 120 mm long bonded and substrate Heraeus Suprasil-311 fused silica cylinders compared with the losses predicted by the Suprasil-311 empirical model.

measured mechanical losses of resonant modes coincided with, or even bettered, the losses predicted by the empirical model. However, all the measured mechanical losses of resonant modes of the 65 mm diameter by 120 mm long Heraeus Suprasil-311 samples follow a trend similar to the line of the empirical model in figure 4.27, but, this time, the measured points lie approximately a factor of two and a half times above the model.

There are several possible reasons for this difference, but the exact cause is as yet unknown. Firstly, the 120 mm long fused silica cylinders weigh approximately twice as much as the 50 mm and 70 mm long fused silica cylinders and therefore it was necessary to suspend the larger cylinders with a slightly *thicker* silk suspension loop. However, as discussed earlier in section 4.4, suspension losses introduced potentially by this different silk thread should be minimised for resonant modes with little, or no, motion in the area where the suspension loop lies. Two such resonant modes are the 23822 Hz and 27674 Hz resonant modes, shown in figure 4.25, but their measured mechanical losses are higher than the predicted losses. Therefore it is unlikely that this is the cause of the difference.

Secondly, the most likely cause for the discrepancy, is that the 120 mm long fused silica cylinder came from a different batch of Heraeus Suprasil-311 since it was manufactured and bought nearly three years after the original 50 mm and 70 mm long fused silica cylinders were produced. It is possible that this different batch produces a slightly higher mechanical loss. Mechanical loss measurements on a 50 mm and 70 mm cylinder which were purchased from the same batch of Heraeus Suprasil-311 fused silica as the 120 mm cylinder will provide more information about this possible cause.

However, as discussed later in section 4.11, the difference between the measured mechanical loss of the substrate sample and the values predicted by the empirical model does not make a significant difference to the calculated values for the bond loss.

4.11 Calculation of Bond Loss Between Two Silica Test Masses

From the measurements taken throughout this chapter it is possible to calculate the bond loss for all nine of the resonant modes of the fused silica cylinder measured, constructed by bonding two 65 mm diameter by 50 mm long and 65 mm diameter by 70 mm long Heraeus Suprasil-311 cylinders. As discussed in section 4.3, the bond loss ϕ_{bond} of a singular resonant mode can be determined using equation 4.5, which can be rearranged to give:

$$\phi_{\text{bond}} = \left(\frac{E_{\text{bond}}}{E_{\text{total}}}\right)^{-1} \times \left(\phi_{\text{bonded}} - \phi_{\text{substrate}}\right). \tag{4.12}$$

The measured mechanical losses of the nine resonant modes which were studied by finite element analysis and modelled using *solid elements* are presented in table 4.6 for the bonded mass and in table 4.7 for the substrate mass.

Frequency (Hz)	$\phi_{\textbf{bonded}}(\times 10^{-7})$
15280	8.06 ± 0.06
23756	4.09 ± 0.03
27605	5.70 ± 0.06
38866	1.98 ± 0.16
39399	1.25 ± 0.05
40385	1.25 ± 0.05
45839	3.12 ± 0.19
49002	0.99 ± 0.05
49838	1.24 ± 0.04

Table 4.6: Lowest measured mechanical losses of nine resonant modes of the 65 mm diameter by 120 mm long bonded Heraeus Suprasil-311 fused silica cylinder.

Frequency (Hz)	$\phi_{\mathbf{substrate}}(\times 10^{-8})$
15421	5.79 ± 0.06
23888	3.23 ± 0.09
27742	3.92 ± 0.04
38911	4.34 ± 0.12
39425	4.36 ± 0.16
40543	5.10 ± 0.09
45537	3.84 ± 0.02
49084	7.87 ± 0.37
49954	8.57 ± 0.05

Table 4.7: Lowest measured mechanical losses of nine resonant modes of the 65 mm diameter by 120 mm long substrate Heraeus Suprasil-311 fused silica cylinder.

This data, together with the corresponding energy ratios determined for a 65 nm bond thickness modelled using *solid elements*, can then be substituted into equation 4.12 to calculate the bond loss for the individual resonant modes. These losses are presented in table 4.8.

A value for the overall bond loss was determined by averaging the bond losses from each of the individual resonant modes. This yields an average bond loss for the 65 nm thick bond between the 50 mm and 70 mm long cylinders of 0.07 ± 0.01 which is four times lower than the 0.28 ± 0.04 bond loss of the fundamental longitudinal mode found by Elliffe and Sneddon [160, 104] with the identical masses.

In figure 4.27 it was shown that the measured mechanical losses of the 65 mm diameter by 120 mm long fused silica substrate lie approximately a factor of two above the predicted losses of the empirical model for Heraeus Suprasil-311. The bond losses of each of the resonant modes were recalculated using the mechanical losses predicted by the empirical model for such a fused silica test mass. These theoretical losses are presented in table 4.9 along with the corresponding bond losses for each resonant mode calculated using them. Averaging these individual losses gives a

Frequency (Hz)	$\phi_{\mathbf{bond}}$
15351	0.093 ± 0.007
23822	0.046 ± 0.004
27674	0.058 ± 0.004
38889	0.122 ± 0.016
39412	0.091 ± 0.009
40464	0.067 ± 0.007
45463	0.039 ± 0.004
49043	0.036 ± 0.012
49896	0.080 ± 0.010

Table 4.8: Bond losses of nine resonant modes of the 65 mm diameter by 120 mm long bonded Heraeus Suprasil-311 fused silica cylinder calculated using the measured mechanical losses of the 120 mm long substrate cylinder.

higher overall bond loss of 0.10 ± 0.01 which is approximately a factor of three lower than the previous experiment.

The errors in both cases are similar because the largest source of error comes from the Energy Ratio calculation, as there is an error of $\sim 10\%$ in the measurement of the bond thickness.

4.12 Conclusions

The measurement of the bond loss of hydroxide-catalysis bonds is crucial in determining the size of bonds which may be used in producing monolithic fused silica suspensions in the next generation of gravitational wave detectors. Scanning Electron, Transmission Electron and Atomic Force Microscopy techniques are useful techniques to measure the thickness of bonds formed using different volumes and concentrations of bonding solution. A summary of the bond thicknesses determined using these techniques is presented in table 4.10.

Frequency (Hz)	$\phi_{\text{substrate}}(\times 10^{-8})$	ϕ_{bond}
15351	1.33 ± 0.03	0.098 ± 0.007
23822	1.84 ± 0.05	0.048 ± 0.004
27674	2.06 ± 0.05	0.060 ± 0.004
38889	2.65 ± 0.07	0.139 ± 0.015
39412	2.68 ± 0.07	0.114 ± 0.009
40464	2.74 ± 0.07	0.074 ± 0.007
45463	2.99 ± 0.08	0.048 ± 0.004
49043	3.16 ± 0.08	0.130 ± 0.010
49896	3.20 ± 0.08	0.202 ± 0.010

Table 4.9: Bond losses of nine resonant modes of the 65 mm diameter by 120 mm long bonded Heraeus Suprasil-311 fused silica cylinder calculated using the theoretical mechanical losses of the 120 mm long substrate cylinder from the Suprasil-311 empirical model.

Sample	Vol (μl)	Area (cm^2)	SEM (nm)	TEM (nm)	AFM (nm)
1	2	5.07	60.4 ± 2.0	65 ± 5	58.0 ± 3.5
2	0.2	5.07	80.7 ± 1.1	-	97.3 ± 0.1
3	0.7	1.77	-	34 ± 5	-

Table 4.10: Summary table of all the bond thicknesses measured throughout chapter 4 using different measurement techniques for 1) 2 μl one inch bonded *witness* sample, 2) 0.2 μl one inch bonded sample and 3) Advanced LIGO ear.

The thickness of bonds appears not to be related directly to the volume of bonding solution used to make the bond. The bonds created in samples 1 and 2 were made over identical areas, but with different volumes of bonding solution yet the sample with less bonding solution was found to be thicker than the one with ten times as much solution. Samples 1 and 3 were bonded such that the bonds were identical except for the surface area of the bond but the thickness of these two bonds was not the same. This might suggest that the thickness of bonds may be determined by the flatness of the surfaces being bonded. Future experiments may clarify this situation.

Measurements of the mechanical loss of a 65 mm diameter by 120 mm long fused silica cylinder, bonded using non-identical masses, suggest that the bond loss could be as much as 4 times lower than previous experiments suggested. Thus the levels of thermal noise associated with hydroxide-catalysis bonds are likely to be lower than previously calculated.

The empirical model for fused silica agrees with the losses measured in the laboratory of some resonant modes. It also suggests that some of the mechanical loss measurements may be limited by factors such as suspension losses, instead of intrinsic losses. Loss measurements on the longer 120 mm long fused silica cylinder all lie above the model, but could be due to this sample being produced and polished at a different time from the original samples.

Chapter 5

Measurements of Mechanical Loss of Sapphire Substrates

5.1 Introduction

Fused silica is the material of choice for use as the test mass mirror substrates in the LIGO [60], GEO600 [77], VIRGO [80] and TAMA300 [83] interferometric gravitational wave detectors operating currently. It was chosen because it can be manufactured specifically to have low optical and mechanical losses and is available in the large pieces required. However, the mechanical loss of fused silica will set a limit on the thermal noise performance of future gravitational wave detectors. In order to improve the sensitivities of these detectors different materials with lower losses are necessary.

One such candidate material for detectors using transmissive optics is sapphire (Al_2O_3). The relevant properties of sapphire have been studied for a number of years. The Braginsky group in Moscow State University, Russia, measured mechanical losses as low as 3×10^{-9} [125] on samples grown using the horizontal orientated crystallisation process [188]. Unfortunately, samples produced using this technique are not able to be manufactured in sufficient size, and of the optical quality required,

for use in a gravitational wave detector.

Instead, samples must be grown using the Heat Exchanger Method (HEM) [189]. In 1999 the laboratory in Glasgow measured losses of 3.9×10^{-9} [190] on such a HEMEX sapphire sample, fabricated by Crystal Systems [191]. HEMEX is the name given to the highest optical grade of sapphire which this supplier produces. Loss measurements were then made by the author and S. Reid on this 30 mm diameter by 100 mm long HEMEX cylinder, which had a 10 mm wide flat polished along its length, by General Optics [176], in the intervening period [104]. Figure 5.1 shows two 25 minute long ring-downs of the 53611 Hz resonant mode. The average loss of this resonant mode was found to be $(4.61 \pm 0.03) \times 10^{-9}$.

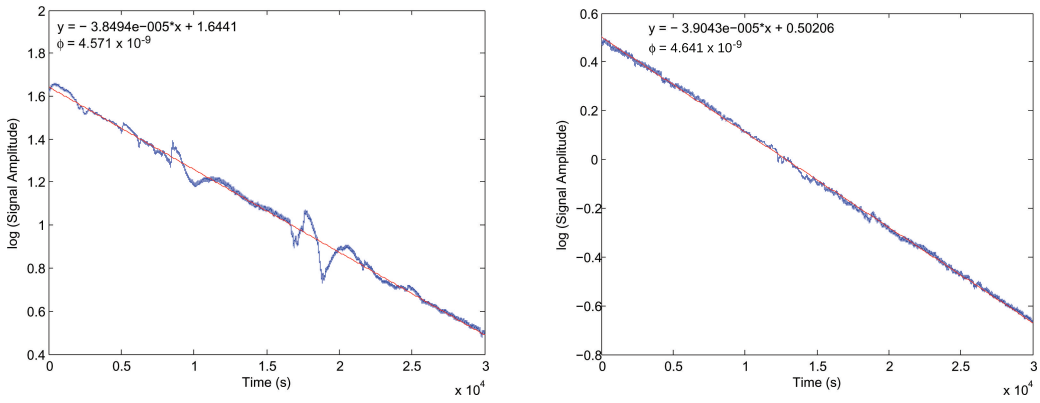

Figure 5.1: Two 25 minute long ring-downs of the 53611 Hz resonant mode of a 30 mm diameter by 100 mm long HEMEX sapphire sample.

The combination of various measurements indicating the low mechanical losses of sapphire samples resulted in the gravitational wave communities around the world becoming more interested in sapphire as a candidate for a mirror substrate in gravitational wave detectors, particularly as part of a study evaluating both fused silica and sapphire as possible test mass materials for use in the Advanced LIGO detector system [129]. The decision making process was not simple, since both materials met the design sensitivity goal for Advanced LIGO of $\sim$ 200 Mpc range for binary neutron star systems and both materials had advantages and disadvantages.

At frequencies below 100 Hz silica has a lower level of thermal noise than sapphire,

meaning that if it were used in an interferometric detector, this would make it more sensitive to *low* frequency sources, for example high-mass black hole binaries [192]. The performance and properties of fused silica were better characterised, especially with regard to the ability to have suitable optical coatings applied to them, as discussed in Chapter 3, and the joining of the lower-stage optics using the hydroxide-catalysis bonding detailed in Chapter 4.

Sapphire, on the other hand, has lower thermal noise levels at *higher* frequencies which, if it were used instead of fused silica as an interferometric gravitational wave detector optic, may lead to higher sensitivities in the frequency band where Low Mass X-Ray Binaries may emit gravitational waves [192]. The higher thermal conductivity of sapphire [112] would also enable increased levels of laser power to circulate within the interferometer without the mirrors distorting due to the greater thermal load. Unfortunately, sapphire exhibits higher levels of both homogeneous and inhomogeneous optical loss [129] and observations have also noted a larger amount of optical scattering than with silica [193].

The decision of the Advanced LIGO down-select working group to choose silica as the material of choice was made due to the better understanding of the properties of silica and the coatings required to be applied to the test masses. Despite this, sapphire still remains of considerable interest as it is the material of choice for the planned LCGT detector in Japan [69] and the AIGO detector in Australia [194]. Consequently, studies of the mechanical losses of sapphire samples and the coatings which may be applied to them, remain of considerable interest.

5.2 The Anisotropic Properties of Sapphire

Sapphire has a $\bar{3}$m *hexagonal (rhombohedral)* crystallographic system. This means that a sapphire crystal has 3-fold rotation-inversion and mirror symmetry. Sapphire has three main crystallographic axes: the c-axis denoted by the (0001) Miller-Bravais Index, the m-axis indicated by the $(10\bar{1}0)$ Miller-Bravias Index and the a-axis which

corresponds to the $(11\bar{2}0)$ Miller-Bravias Index [1]. There are two other sets of crystal axes, n-axis and r-axis and all five axes are shown in figure 5.2.

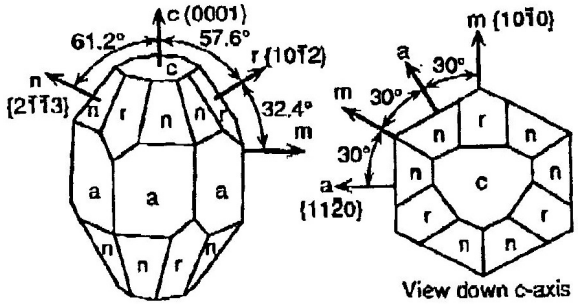

Figure 5.2: Diagram of the crystal axes of sapphire. Figure taken from *Factors that influence mechanical failure of sapphire at high temperatures* [1].

5.2.1 Stiffness Constants of *c*-Axis Sapphire

The stiffness matrix [**c**] for a *trigonal* crystal class (which is a subset of the hexagonal class) is defined as [195]:

$$[\mathbf{c}] = \begin{bmatrix} c_{11} & c_{12} & c_{13} & c_{14} & 0 & 0 \\ c_{12} & c_{11} & c_{13} & -c_{14} & 0 & 0 \\ c_{13} & c_{13} & c_{33} & 0 & 0 & 0 \\ c_{14} & -c_{14} & 0 & c_{44} & 0 & 0 \\ 0 & 0 & 0 & 0 & c_{44} & c_{14} \\ 0 & 0 & 0 & 0 & c_{14} & \frac{1}{2}(c_{11} - c_{12}) \end{bmatrix}. \tag{5.1}$$

The material properties of sapphire are defined, by convention, relative to the c-axis. The values for the c-axis *stiffness* matrix can be calculated from the *compliance* s_{ij}

constants [195] (where each value has units m^2/N):

$$\begin{aligned} s_{11} &= 2.38 \times 10^{-12} \\ s_{12} &= -0.70 \times 10^{-12} \\ s_{13} &= -0.38 \times 10^{-12} \\ s_{14} &= 0.49 \times 10^{-12} \\ s_{33} &= 2.20 \times 10^{-12} \\ s_{44} &= 7.05 \times 10^{-12}. \end{aligned} \tag{5.2}$$

The trigonal conversion between compliance and stiffness constants is defined in [195] as:

$$\begin{aligned} s &= s_{33}(s_{11} + s_{12}) - 2s_{13}^2 \\ s' &= s_{44}(s_{11} - s_{12}) - 2s_{14}^2 \\ c_{13} &= -\tfrac{s_{13}}{s} \\ c_{14} &= -\tfrac{s_{14}}{s'} \\ c_{33} &= \tfrac{s_{11}+s_{12}}{s} \\ c_{44} &= \tfrac{s_{11}-s_{12}}{s'} \\ c_{11} + c_{12} &= \tfrac{s_{33}}{s} \\ c_{11} - c_{12} &= \tfrac{s_{44}}{s'} \end{aligned} \tag{5.3}$$

These equations can be solved to give the c-axis stiffness matrix. Each entry in the following matrix has units $\times 10^{11}$ kg/ms^2.

$$[\mathbf{c}_{c\text{-axis}}] = \begin{bmatrix} 4.889 & 1.568 & 1.115 & -0.231 & 0 & 0 \\ 1.568 & 4.889 & 1.115 & 0.231 & 0 & 0 \\ 1.115 & 1.115 & 4.931 & 0 & 0 & 0 \\ -0.231 & 0.231 & 0 & 1.451 & 0 & 0 \\ 0 & 0 & 0 & 0 & 1.451 & -0.231 \\ 0 & 0 & 0 & 0 & -0.231 & 1.660 \end{bmatrix} \tag{5.4}$$

Sapphire samples fabricated by the heat-exchanger method are grown more easily along the m and a-axes. This means that is it is possible to produce larger diameter cylindrical samples which have their axes in these directions. As the crystal structure

of sapphire is anisotropic, the mechanical properties are different along each of the axes, and it is important to calculate the different properties, particulary of the m and a-axes.

5.3 Bond Matrix Transformations

A technique developed by W. L. Bond, and detailed in B. A. Auld [195], enables the *stiffness* matrix transformation of $[\mathbf{c}]$ to $[\mathbf{c}']$ by equation 5.5 to calculate the elastic properties in the other crystal axes of sapphire.

$$[\mathbf{c}'] = [\mathbf{M}][\mathbf{c}][\tilde{\mathbf{M}}] \tag{5.5}$$

The Bond *stress* transformation Matrix $[\tilde{\mathbf{M}}]$ is the transpose of $[\mathbf{M}]$, which itself is defined as

$$[\mathbf{M}] = \begin{bmatrix} a_{xx}^2 & a_{xy}^2 & a_{xz}^2 & 2a_{xy}a_{xz} & 2a_{xz}a_{xx} & 2a_{xx}a_{xy} \\ a_{yx}^2 & a_{yy}^2 & a_{yz}^2 & 2a_{yy}a_{yz} & 2a_{yz}a_{yx} & 2a_{yx}a_{yy} \\ a_{zx}^2 & a_{zy}^2 & a_{zz}^2 & 2a_{zy}a_{zz} & 2a_{zz}a_{zx} & 2a_{zx}a_{zy} \\ a_{yx}a_{zx} & a_{yy}a_{zy} & a_{yz}a_{zz} & a_{yy}a_{zz} + a_{yz}a_{zy} & a_{yx}a_{zz} + a_{yz}a_{zx} & a_{yy}a_{zx} + a_{yx}a_{zy} \\ a_{zx}a_{xx} & a_{zy}a_{xy} & a_{zz}a_{xz} & a_{xy}a_{zz} + a_{xz}a_{zy} & a_{xz}a_{zx} + a_{xx}a_{zz} & a_{xx}a_{zy} + a_{xy}a_{zx} \\ a_{xx}a_{yx} & a_{xy}a_{yy} & a_{xz}a_{yz} & a_{xy}a_{yz} + a_{xz}a_{yy} & a_{xz}a_{yx} + a_{xx}a_{yz} & a_{xx}a_{yy} + a_{xy}a_{yx} \end{bmatrix} \tag{5.6}$$

Matrix $[\mathbf{a}]$, shown in equation 5.7, is the transformation tensor, and it is used to transform the first set of 3-dimensional cartesian coordinates into a second set. This matrix can be used to describe rotations about an axis (detailed in section 6.2), reflections about a plane, stresses applied to planes (both of which are not detailed in this thesis) and the permutation of axes.

$$[\mathbf{a}] = \begin{bmatrix} a_{xx} & a_{xy} & a_{xz} \\ a_{yx} & a_{yy} & a_{yz} \\ a_{zx} & a_{zy} & a_{zz} \end{bmatrix} \tag{5.7}$$

If we use the cartesian coordinate system to describe the relative orientations of the three main crystal axes of sapphire, then the c-axis lies along the z-axis since its

Miller-Bravais Index is (0001) and the m-axis along the x-axis as its Miller-Bravais Index is $(10\bar{1}0)$, as shown in figure 5.3. Due to the trigonal nature of sapphire the m-axis repeats itself every 60° in the xy-plane, as seen in figure 5.2. The Miller-Bravais Index of the a-axis is $(11\bar{2}0)$ which corresponds to it lying in the same xy-plane as the m-axis lying at 30° from it. Again, due to the nature of the sapphire crystal the a-axis repeats every 60°. This means that the a-axis may correspond to the y-axis in a cartesian coordinate system.

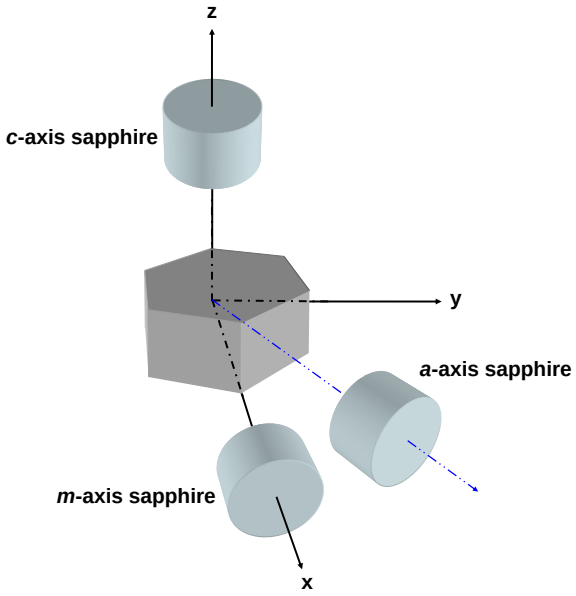

Figure 5.3: Simplified illustration of the crystal axes of sapphire and the orientation of c-axis sapphire cut with its cylindrical axis parallel to the z-axis, m-axis sapphire cut with its cylindrical axis parallel to the x-axis and a-axis sapphire cut so that its cylindrical axis lies 30° from the m-axis in the same xy-plane.

Large sapphire crystals are produced more easily in the m and a crystal orientations. In order to model these different orientations of sapphire in ANSYS® it is necessary to transform the elastic properties from the c-axis to both the m and a-axes, i.e. so that their axes point in the z-direction after their respective transformations.

To correctly transform the stiffness matrix to these different axes it is necessary to permutate the axis so that the z-axis is transformed into either the x-axis (for m-axis sapphire) or the y-axis (for a-axis sapphire).

5.3.1 *c*-axis to *m*-axis Bond Matrix Transformation

The transformation from c to m-axis involves a permutation in order that the axes are transformed, as represented in figure 5.4 into:

$$\begin{aligned} x\text{-axis} &\rightarrow y\text{-axis} \\ y\text{-axis} &\rightarrow z\text{-axis} \\ z\text{-axis} &\rightarrow x\text{-axis} \end{aligned} \tag{5.8}$$

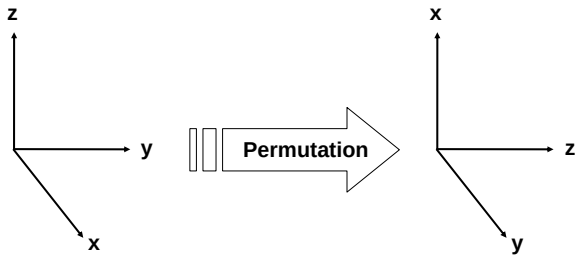

Figure 5.4: Illustration of the *permutation* of axes from c-axis sapphire to m-axis sapphire.

which is not the same as a 90° rotation around the y-axis, indicated in figure 5.5, where the transformation of axes yields:

$$\begin{aligned} x\text{-axis} &\rightarrow -z\text{-axis} \\ y\text{-axis} &\rightarrow y\text{-axis} \\ z\text{-axis} &\rightarrow x\text{-axis.} \end{aligned} \tag{5.9}$$

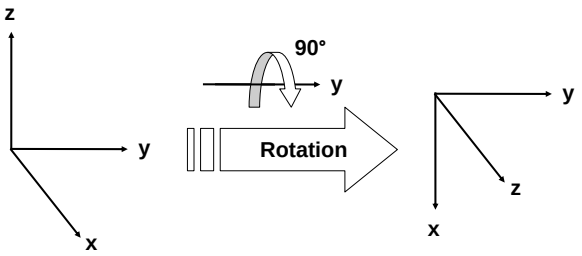

Figure 5.5: Illustration of the 90° *rotation* of axes about the y-axis from c-axis sapphire to m-axis sapphire.

In both these cases, the z-axis is transformed so that it now points in the direction of the original x-axis (ie in line with the m-axis), but the original x and y-axes are rotated differently.

Therefore the [**a**] to transform from c-axis sapphire to m-axis sapphire is:

$$[\mathbf{a}] = \begin{bmatrix} a_{xx} & a_{xy} & a_{xz} \\ a_{yx} & a_{yy} & a_{yz} \\ a_{zx} & a_{zy} & a_{zz} \end{bmatrix} = \begin{bmatrix} 0 & 0 & 1 \\ 1 & 0 & 0 \\ 0 & 1 & 0 \end{bmatrix}. \tag{5.10}$$

This yields a bond stress transformation [**M**] of the following form:

$$[\mathbf{M}] = \begin{bmatrix} 0 & 0 & 1 & 0 & 0 & 0 \\ 1 & 0 & 0 & 0 & 0 & 0 \\ 0 & 1 & 0 & 0 & 0 & 0 \\ 0 & 0 & 0 & 0 & 0 & 1 \\ 0 & 0 & 0 & 1 & 0 & 0 \\ 0 & 0 & 0 & 0 & 1 & 0 \end{bmatrix}. \tag{5.11}$$

Substituting this into equation 5.5, the Bond stiffness matrix for m-axis sapphire can then be calculated from [$\mathbf{c}_{c\text{-axis}}$] where each entry in the following matrix has units $\times 10^{11}$ kg/ms^2:

$$[\mathbf{c}_{m\text{-axis}}] = \begin{bmatrix} 4.931 & 1.115 & 1.115 & 0 & 0 & 0 \\ 1.115 & 4.889 & 1.568 & 0 & -0.231 & 0 \\ 1.115 & 1.568 & 4.889 & 0 & 0.231 & 0 \\ 0 & 0 & 0 & 1.660 & 0 & -0.231 \\ 0 & -0.231 & 0.231 & 0 & 1.451 & 0 \\ 0 & 0 & 0 & -0.231 & 0 & 1.451 \end{bmatrix}. \tag{5.12}$$

5.3.2 *m*-axis to *a*-axis Bond Matrix Transformation

To calculate the stiffness matrix for a-axis sapphire the same permutation which was applied to the c-axis stiffness matrix can be used to transform the m-axis stiffness

matrix continuing the permutation such that:

$$\begin{array}{ccccc} x\text{-axis} & \rightarrow & y\text{-axis} & \rightarrow & z\text{-axis} \\ y\text{-axis} & \rightarrow & z\text{-axis} & \rightarrow & x\text{-axis} \\ z\text{-axis} & \rightarrow & x\text{-axis} & \rightarrow & y\text{-axis}. \end{array} \tag{5.13}$$

Substituting the same bond stress transformation into equation 5.5, the Bond stiffness matrix for a-axis sapphire can then be calculated from $[\mathbf{c}_{m\text{-axis}}]$:

$$[\mathbf{c}_{a\text{-axis}}] = \begin{bmatrix} 4.889 & 1.115 & 1.568 & 0 & 0 & 0.231 \\ 1.115 & 4.931 & 1.115 & 0 & 0 & 0 \\ 1.568 & 1.115 & 4.889 & 0 & 0 & -0.231 \\ 0 & 0 & 0 & 1.451 & -0.231 & 0 \\ 0 & 0 & 0 & -0.231 & 1.660 & 0 \\ 0.231 & 0 & -0.231 & 0 & 0 & 1.451 \end{bmatrix} \tag{5.14}$$

where each entry in equation 5.14 has units $\times 10^{11}$ kg/ms^2.

5.4 Cyclic Permutation of Elastic Properties

It was suggested that the stiffness matrix could be rotated directly toward the different axes using a *cyclic permutation* of the indexes of each c_{ij} entry in the matrix [196]. This method eliminates the need to calculate [**a**], [**M**] and [$\bar{\mathbf{M}}$] before finally calculating [**c**']. The stiffness matrix for a trigonal system is:

$$[\mathbf{c}] = \begin{bmatrix} c_{11} & c_{12} & c_{13} & c_{14} & 0 & 0 \\ c_{12} & c_{11} & c_{13} & -c_{14} & 0 & 0 \\ c_{13} & c_{13} & c_{33} & 0 & 0 & 0 \\ c_{14} & -c_{14} & 0 & c_{44} & 0 & 0 \\ 0 & 0 & 0 & 0 & c_{44} & c_{14} \\ 0 & 0 & 0 & 0 & c_{14} & \frac{1}{2}(c_{11} - c_{12}) \end{bmatrix} \tag{5.15}$$

as stated earlier in equation 5.1. To rotate the system using this technique, there must be two separate cycles. The first one converts the first three indexes in the

order $1 \rightarrow 2 \rightarrow 3 \rightarrow 1$, and the second converts the remaining three indexes so that $4 \rightarrow 5 \rightarrow 6 \rightarrow 4$. For example, in the trigonal system, the c_{33} entry of the original matrix becomes c_{11} and the c_{44} entry is transformed into $\frac{1}{2}(c_{11} - c_{12})$ in the second matrix etc ...

For one permutation equation 5.15 becomes:

$$[\mathbf{c}'] = \begin{bmatrix} c_{33} & c_{13} & c_{13} & 0 & 0 & 0 \\ c_{13} & c_{11} & c_{12} & 0 & c_{14} & 0 \\ c_{13} & c_{12} & c_{11} & 0 & -c_{14} & 0 \\ 0 & 0 & 0 & \frac{1}{2}(c_{11} - c_{12}) & 0 & c_{14} \\ 0 & c_{14} & -c_{14} & 0 & c_{44} & 0 \\ 0 & 0 & 0 & c_{14} & 0 & c_{44} \end{bmatrix}. \tag{5.16}$$

which gives an m-axis stiffness matrix of:

$$[\mathbf{c}_{m\text{-axis}}] = \begin{bmatrix} 4.931 & 1.115 & 1.115 & 0 & 0 & 0 \\ 1.115 & 4.889 & 1.568 & 0 & -0.231 & 0 \\ 1.115 & 1.568 & 4.889 & 0 & 0.231 & 0 \\ 0 & 0 & 0 & 1.660 & 0 & -0.231 \\ 0 & -0.231 & 0.231 & 0 & 1.451 & 0 \\ 0 & 0 & 0 & -0.231 & 0 & 1.451 \end{bmatrix}. \tag{5.17}$$

where each entry in this matrix has units $\times\ 10^{11}$ kg/ms^2. Inspection shows that matrix is identical to the stiffness matrix calculated using the Bond transformation to m-axis in equation 5.12.

Similarly, performing the cyclic permutation on equation 5.16 produces the stiffness matrix for a-axis sapphire:

$$[\mathbf{c}''] = \begin{bmatrix} c_{11} & c_{13} & c_{12} & 0 & 0 & -c_{14} \\ c_{13} & c_{33} & c_{13} & 0 & 0 & 0 \\ c_{12} & c_{13} & c_{11} & 0 & 0 & c_{14} \\ 0 & 0 & 0 & c_{44} & c_{14} & 0 \\ 0 & 0 & 0 & c_{14} & \frac{1}{2}(c_{11} - c_{12}) & 0 \\ -c_{14} & 0 & c_{14} & 0 & 0 & c_{44} \end{bmatrix} \tag{5.18}$$

which again gives the same values as already found in 5.14. Each entry in the following matrix has units $\times 10^{11}$ kg/ms^2.

$$[\mathbf{c}_{a\text{-axis}}] = \begin{bmatrix} 4.889 & 1.115 & 1.568 & 0 & 0 & 0.231 \\ 1.115 & 4.931 & 1.115 & 0 & 0 & 0 \\ 1.568 & 1.115 & 4.889 & 0 & 0 & -0.231 \\ 0 & 0 & 0 & 1.451 & -0.231 & 0 \\ 0 & 0 & 0 & -0.231 & 1.660 & 0 \\ 0.231 & 0 & -0.231 & 0 & 0 & 1.451 \end{bmatrix} \tag{5.19}$$

Consequently, the stiffness matrices for all three of the axes of sapphire can be used in the finite element modelling of sapphire test samples in ANSYS®.

5.5 Finite Element Analysis of Sapphire in ANSYS®

Anisotropic materials can be modelled in ANSYS® by entering the density of sapphire (3980 kg/m^3), the appropriate stiffness matrix (ANSYS® MAIN MENU → PREPROCESSOR → MATERIAL PROPERTIES → MATERIAL MODELS → STRUCTURAL → LINER → ELASTIC → ANISOTROPIC) and creating a model of the sample to be analysed.

It is possible to model the m and a-axes of sapphire in two different ways. The first technique is to model the sapphire sample using the stiffness matrices found utilising the transformations described in sections 5.3 and 5.4. The second method is to enter the c-axis stiffness matrix expressed in equation 5.12 into ANSYS® and to rotate the workplane (WORKPLANE → OFFSET WP BY INCREMENTS ... → DEGREES → XY, YZ, ZX ANGLES) so that the cylindrical axis of the sample being modelled corresponds with the correct axis of sapphire.

5.5.1 Finite Element Analysis of *m*-axis Sapphire

Finite element models were constructed to determine the resonant mode frequencies of a 76.2 mm diameter by 29.6 mm long *m*-axis sapphire cylinder. Two separate models were run, the first using the *m*-axis elastic stiffness properties, the results of which are plotted in the second column of table 5.1.

Mode Number	***m*-axis Modelled Frequency (Hz)**	**Rotated *c*-axis Modelled Frequency (Hz)**	**Measured Frequency (Hz)**
1	36920	36920	35679
3	54169	54170	54855
7	68482	68483	68629
10	81723	81725	82987
12	87159	87161	87275

Table 5.1: Comparison of experimentally measured and modelled resonant frequencies of a 76.2 mm diameter by 29.6 mm long *m*-axis sapphire substrate. The sample was modelled in two ways: firstly, by entering the *m*-axis elastic properties directly into ANSYS® and secondly, by entering the *c*-axis elastic properties and rotating the mass so that it points in the direction of *m*-axis sapphire.

The second model was run by entering the *c*-axis elastic properties of sapphire and then rotating the cylindrical axis in ANSYS® so that it corresponded with the *m*-axis (WORKPLANE → OFFSET WP BY INCREMENTS . . . → DEGREES → XY, YZ, ZX ANGLES → 0, 90, 0 → OK). The resonant frequencies found using this technique, shown in column three of table 5.1, match the resonant frequencies found by the model using the *m*-axis properties.

These modelled frequencies are then compared with the experimentally measured resonant mode frequencies. The precise reason for the discrepancy of ~ 1 kHz in two of the predicted frequencies is unknown. It could be that the sample was not grown exactly along the *m*-axis. It was also noted that the sample was not quite perfectly right-cylindrical since there was a slight wedge on one of the faces, giving a height

at one end of the wedge of 0.0290 m and at the other 0.0302 m [111]. This wedge shape could account for some of the difference, because the sample was modelled using the average thickness of 0.0296 m.

5.5.2 Finite Element Analysis of *a*-axis Sapphire

Similarly for *a*-axis sapphire, it is possible to model the resonant modes of a 76.2 mm diameter by 25.4 mm long right-cylindrical sample using the two different modelling techniques. The results from modelling the sample using the *a*-axis stiffness matrix are presented in column 2 of table 5.2. The second model was run using the *c*-axis properties, but with the cylinder drawn so that its axis corresponded with the *a*-axis (WORKPLANE → OFFSET WP BY INCREMENTS . . . → DEGREES → XY, YZ, ZX ANGLES → 0, 0, 90 → OK). Again, the results shown in column 3 agreed with the model run using the *a*-axis properties.

Mode Number	***a*-axis Modelled Frequency (Hz)**	**Rotated *c*-axis Modelled Frequency (Hz)**	**Measured Frequency (Hz)**
1	32416	32417	32573
2	35960	35961	36022
3	50562	50562	50640
6	64243	64243	64134
11	86220	86223	86135
12	86321	86322	86704

Table 5.2: Comparison of experimentally measured and modelled resonant frequencies of a 76.2 mm diameter by 25.4 mm long *a*-axis sapphire substrate. The sample was modelled in two ways: firstly, by entering the *m*-axis elastic properties directly into ANSYS® and secondly by entering the *c*-axis elastic properties and rotating the mass so that it points in the direction of *a*-axis sapphire.

The resonant mode frequencies were then measured for a 76.2 mm diameter by 25.4 mm long a-axis sapphire cylinder and compared with the modelled frequencies. The modelled frequencies are in very good agreement with the experimentally measured frequencies and the first five resonant modes agree within 150 Hz. The final resonant mode is still within agreement but the modelled frequency is $\sim$ 400 Hz below the measured frequency. ANSYS® illustrations of the six experimentally measured resonance modes are shown in figure 5.6.

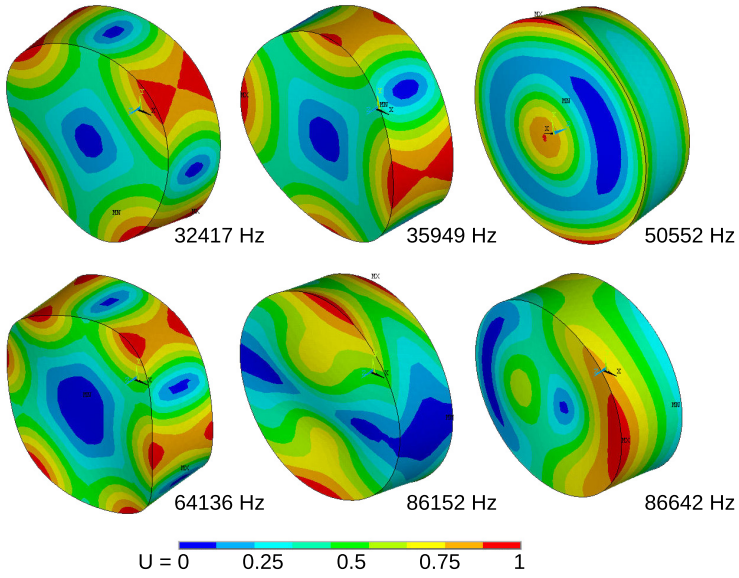

Figure 5.6: ANSYS® illustrations of the six resonant mode shapes measured on the 76.2 mm diameter by 25.4 mm thick a-axis sapphire substrates where the relative displacements U = $\sqrt{x^2 + y^2 + z^2}$ are plotted in normalised, dimensionless units.

The results produced in this section show that is it possible to model accurately samples produced along the different crystal axes of sapphire. Each of the three different techniques of generating sapphire models: using bond transformations, cyclic permutations and rotating cylindrical axes in the finite element element package yield the same results, giving confidence in each of the methods described in this chapter.

5.6 Investigations into the Effect of Surface Polish on the Mechanical Loss of Sapphire

Before coatings can be applied to sapphire substrates they must be polished. This can be done relatively straightforwardly by polishing companies to a *standard* inspection polish with a surface roughness of several nanometers. However, for the real mirrors used in gravitational wave detectors a more expensive and complex *super-polish* is required to achieve a sub-angstrom surface roughness [197]. Three 76.2 mm diameter by 25.4 mm long a-axis sapphire samples were tested to determine if there was any difference in the mechanical losses of resonance modes for masses polished using these differing techniques. Two of the samples were standard polished while the third was super-polished.

The abrasive polishing compounds used in the final stage of the standard polish have been shown, in measurements for the Gravity Probe B experiment, to leave a ~ 1 μm thick sub-surface damaged layer [198]. The additional chemo-mechanical final step of the super-polish should reduce this damage, but it has been observed that despite the improved surface roughness obtained using this technique, the process leaves surface build-ups of polishing compound and surface particles after polishing [199]. Although this helps to create a smoother surface in order to achieve a higher optical figure, this amorphous, contaminated surface layer may also affect the surfaces losses of the super-polished sample.

Figure 5.7 shows that, for four of the five resonant modes for which there was comparable data, the measured mechanical losses of the resonant modes of the super-polished sample are lower than those of the standard polished samples. This suggests that the improved surface roughness of the super-polished sample results in a lower mechanical loss.

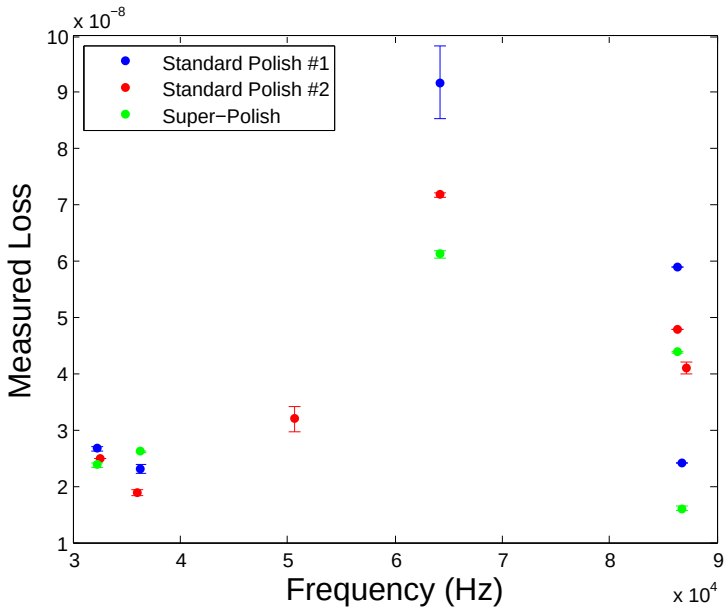

Figure 5.7: Measured mechanical losses of two standard polished and one super-polished uncoated 76.2 mm diameter by 25.4 mm long a-axis sapphire substrates.

This can be quantified by expressing the total measured mechanical loss ϕ_{total} in terms of a bulk loss and surface loss components such that,

$$\phi_{\text{total}} = \frac{E_{\text{bulk}}}{E_{\text{total}}}\,\phi_{\text{bulk}} + \frac{E_{\text{surface}}}{E_{\text{total}}}\,\phi_{\text{surface}} \tag{5.20}$$

where ϕ_{bulk} is the bulk loss of the substrate, ϕ_{surface} is the loss associated with the surfaces of the sample, E_{total} is the total energy which is stored in the sample, E_{bulk} is the energy stored in the bulk of the substrate and E_{surface} is the energy stored in a thin layer of the surface. The surface layers, damaged by the polishing processes, are all very thin, then $E_{\text{total}} \approx E_{\text{bulk}}$ and equation 5.20 becomes

$$\phi_{\text{total}} \simeq \phi_{\text{bulk}} + \frac{E_{\text{surface}}}{E_{\text{bulk}}}\,\phi_{\text{surface}}. \tag{5.21}$$

The thickness of the damaged layer resulting from the polishing process is typically of the order of 1 μm. Finite element models were then run in ANSYS® to estimate the ratio of energy stored in the surface layer to the bulk strain energy for each resonant mode. A variety of models was run with decreasing surface thicknesses down to 1.7 mm which enabled the extrapolation of the energy ratios for a surface

thickness of 1 μm, $\frac{E_{1\mu\text{m surface}}}{E_{\text{bulk}}}$ to be made. The results of the fractional energies stored in each of the resonant modes measured of the sapphire samples are presented in figure 5.8.

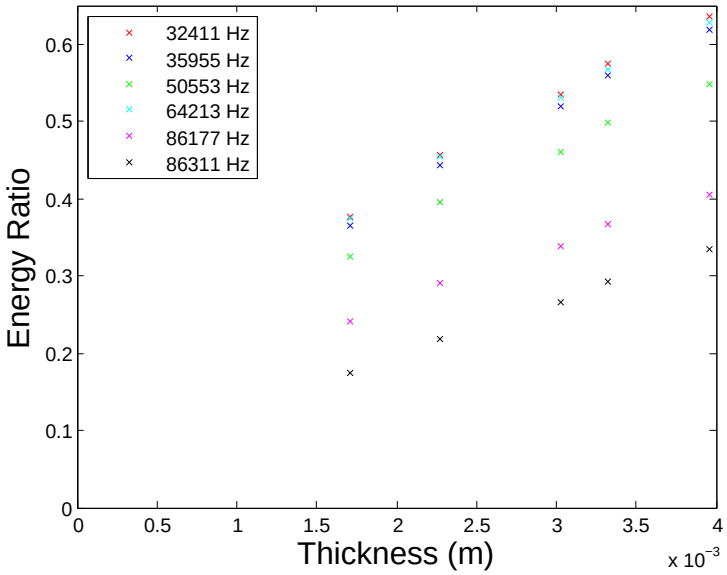

Figure 5.8: Ratio of energy stored in the surface to energy stored in the bulk for each resonant mode of the sapphire samples studied with varying thicknesses of surface layer.

The bulk loss of the samples is thought to be much lower than the term associated with the surface loss. Therefore equation 5.20 can be approximated to

$$\phi_{\text{total}} \approx \frac{E_{\text{surface}}}{E_{\text{bulk}}}\,\phi_{\text{surface}} \tag{5.22}$$

$$= \frac{E_{1\mu\text{m surface}}}{E_{\text{bulk}}}\,t\,\phi_{\text{surface}} \tag{5.23}$$

where t is the surface thickness in μm. For the different polishing techniques the thicknesses of the damaged layer and the surface losses, ϕ_{surface}, are unknown. However from equation 5.23, the product of both the thickness and loss of the surface, $t \times \phi_{\text{surface}}$, it is possible to observe if there is a noticeable difference between the products for the two polishing techniques.

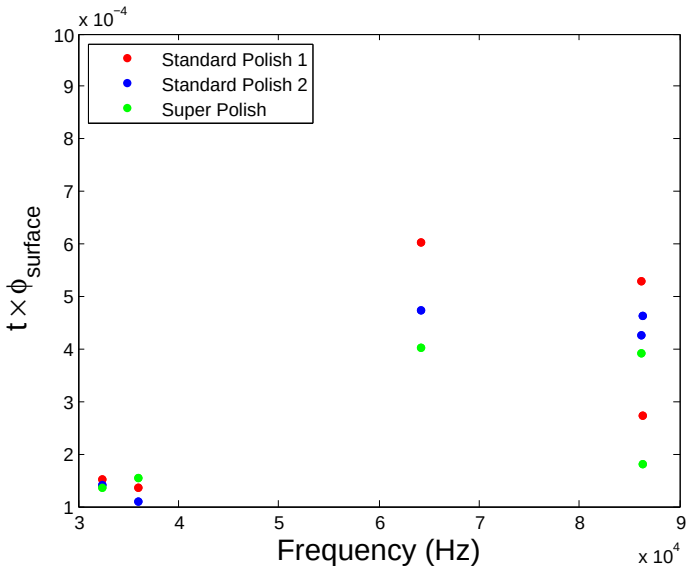

Figure 5.9: $t \times \phi_{\text{surface}}$ for each resonant mode of the three a-axis sapphire samples studied.

Figure 5.9 shows the values of $t \times \phi_{\text{surface}}$ for each resonant mode of the three samples. It can be seen that the values of $t \times \phi_{\text{surface}}$ for the super-polished sample are on average 25% lower than those calculated for the standard polished samples.

If mechanical loss measurements are limited by surface losses then for each sample $t \times \phi_{\text{surface}}$ should be constant for each resonant mode. However, these values are not constant which suggests there is another factor affecting mechanical loss measurements, ϕ_{other}. Therefore equation 5.21 should be expressed as

$$\phi_{\text{total}} = \phi_{\text{bulk}} + \frac{E_{\text{surface}}}{E_{\text{bulk}}}\, \phi_{\text{surface}} + \phi_{\text{other}}. \tag{5.24}$$

which can be approximated as

$$\phi_{\text{total}} \approx \frac{E_{1\mu\text{m surface}}}{E_{\text{bulk}}}\, t\, \phi_{\text{surface}} + \phi_{\text{other}}. \tag{5.25}$$

It is still possible though to estimate the reduction in surface loss of the super-polished sapphire substrate compared to the standard polished samples. For each individual resonant mode $\frac{E_{1\mu\text{m surface}}}{E_{\text{bulk}}}$ and ϕ_{other} can assumed to be the same between test substrates. Therefore if the thickness of the damaged layer created by

the two polishing techniques is the same then

$$\phi_{\text{total}_1} - \phi_{\text{total}_2} = \frac{E_{1\mu\text{m surface}}}{E_{\text{bulk}}}\, t(\phi_{\text{surface}_1} - \phi_{\text{surface}_2}). \tag{5.26}$$

For each of the standard polished substrates it is possible to then calculate

$$t\left(\phi_{\text{surface}_{\text{standard}}} - \phi_{\text{surface}_{\text{super-polish}}}\right)$$

for each resonant mode, as shown in figure 5.10.

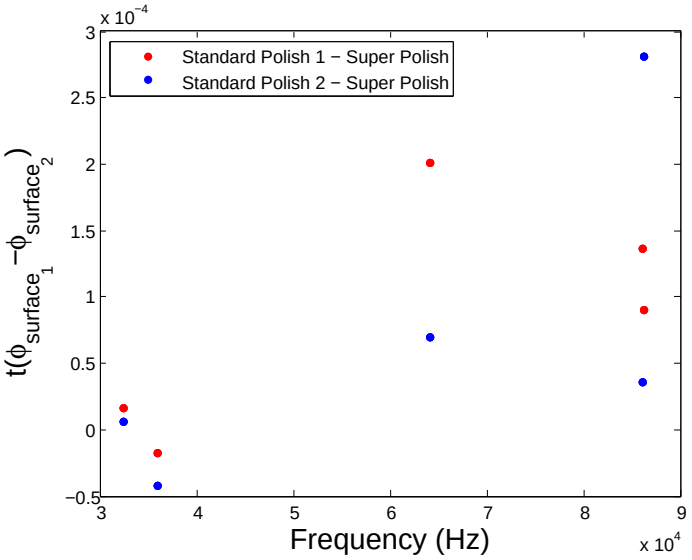

Figure 5.10: $t(\phi_{\text{surface}_1} - \phi_{\text{surface}_2})$ for each resonant mode of the standard polish samples and the super polished sample.

From this figure, if the thickness of the damaged layer is the same for both the standard polished samples and the super-polished sample then the surface loss of the super-polished sample is on average less than that of the standard polished samples.

This suggests that the dissipation of a contaminated smoother surface resulting from a super-polish is less than the dissipation resulting from micro-cracks remaining on the surface from the abrasive standard polish. However, it is clear from the non constant difference in the surface losses that there must be some other factor also affecting the mechanical loss measurements.

For both the standard polished samples the energy ratios and surfaces losses should be the same, therefore the measured mechanical losses of each of the resonant modes on each of the standard polished samples should be identical to within experimental error. The measured losses on the first two resonant modes of the two standard polished samples are reasonably similar. However, the measured losses of the 64 kHz and 86.2 kHz resonant modes of the second standard polished sample are both *lower* than the first sample, whereas the measured loss of the 86.7 kHz resonant mode is instead a factor of two *higher*.

Since one set of loss values is not consistently above or below the other sample, this suggests that there is some other factor outwith the samples which affects the measured loss values. Furthermore, because loss values as low as $(4.61 \pm 0.03) \times 10^{-9}$ have been measured by the author in sapphire samples of different aspect ratio, this suggests that the intrinsic mechanical loss factors of the samples have not been measured here.

Inspection of the resonant mode shapes, shown in figure 5.6, shows that there is considerable motion around the centre of the barrel where the thread forming the suspension loop lies. This could lead to excess slip-stick loss because the thread rubs against the barrel of the mass while the resonant mode rings down, resulting in a higher measured mechanical loss. It is thought that suspension losses could then be limiting the mechanical loss measurements in some of the resonant modes of these samples.

5.7 Reduction of Suspension Loss Through the Introduction of a Nodal Support

To reduce the effect of such suspension losses investigations were made into different techniques of holding test substrates for mechanical loss measurements. Several classifications of mode shape have areas of little or no displacement while they resonate. By suspending a test substrate at these positions of minimum displacement for particular resonant mode shapes the suspension losses should be reduced.

From figure 5.6 it can be observed that for the 32417 Hz, 35949 Hz and 64316 Hz resonant modes for *a*-axis sapphire there are nodes of minimum displacement in the centre of the front and back faces of the substrate. If a test substrate was supported between these two points then coupling between the substrate and the support structure should be minimised.

Numata et al. at the University of Tokyo adopted a nodal support technique where the samples were supported, with their cylindrical axis aligned vertically, at the centre of their flat faces by two small ruby balls [105]. This orientation of support would not be ideal for placing inside the mechanical loss measurement apparatus at the University of Glasgow because the viewports used for interferometric sensing of the motion of the flat faces of the test substrates while they resonate are positioned on the side of the vacuum tanks.

Therefore, to test the feasibility of creating a nodal support where the test substrates were mounted with their cylindrical axis aligned horizontally E. Chalkley and J. Faller at the University of Glasgow created a simple nodal support comprised of two adapted optics mounts, shown in figure 5.11. Housings were manufactured to hold two ruby balls and attached to the optics mounts which could be adjusted to hold in place a 76.2 mm diameter by 25.4 mm thick *a*-axis sapphire cylinder. Ruby balls were chosen to make contact with the sapphire because they are of a similar hardness.

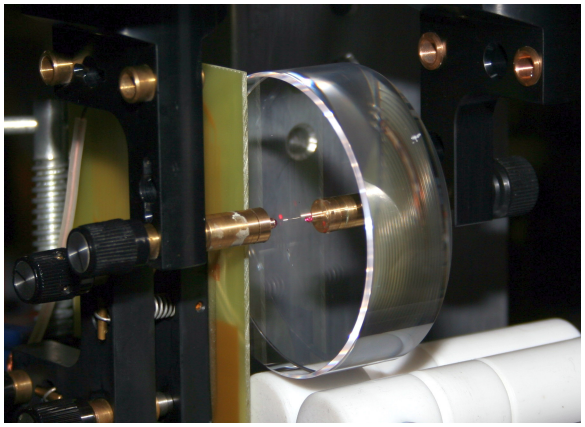

Figure 5.11: Nodal support created using adapted optics mounts to hold a 76.2 mm diameter by 25.4 mm thick a-axis sapphire substrate.

Using this apparatus it was possible to mount the sapphire substrate horizontally to find and excite the resonant modes which had no displacement at the contact points. The mechanical losses measured using this apparatus were however only of the order 10^{-6}, which is two orders of magnitude greater than the evaluated upper limit of the support loss of the Japanese nodal support [105]. Having found that is was possible to suspend a sapphire cylinder in this orientation, an improved, more rigid, nodal support was designed and manufactured to improve the mechanical loss measurements. An image of this nodal support is shown in figure 5.12.

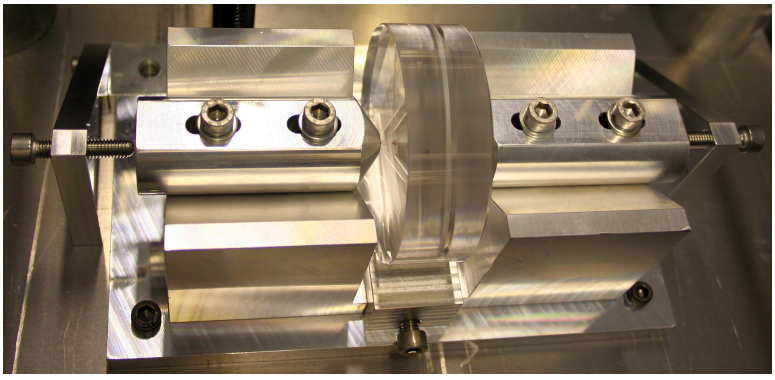

Figure 5.12: Image of the nodal support used for the mechanical loss measurements of a 76.2 mm diameter by 25.4 mm thick a-axis sapphire substrate.

As with the first nodal support the sapphire substrate was clamped between two ruby balls, a close-up image of which is shown in figure 5.13, held in larger aluminium rods which were bolted perpendicular to the holding force for extra stiffness.

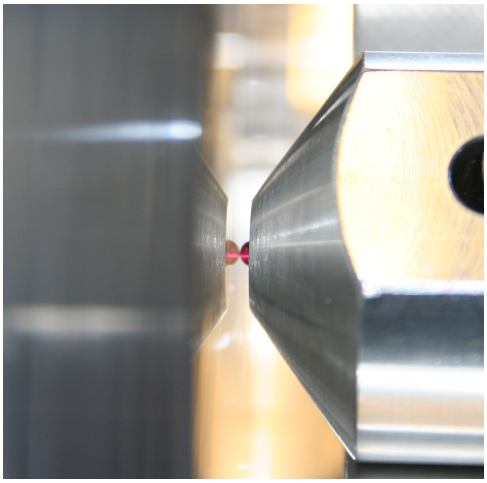

Figure 5.13: Close-up image of the 2 mm diameter ruby ball contacting the flat face of a suspended sapphire substrate.

Mechanical loss measurements were then made of a 76.2 mm diameter by 25.4 mm thick *a*-axis sapphire substrate and compared with the best mechanical loss measurements obtained using a silk thread suspension loop. The tension between the ruby balls holding the sapphire and the substrate itself is adjustable using two screws, visible on both the left and right-hand side of figure 5.12. As with silk thread loops, several '*suspensions*' of different tensions were made with the nodal support. The lowest measured mechanical losses are shown in figure 5.14.

From figure 5.14 it can be seen that for the first two resonant modes the mechanical losses measured using the nodal support are over an order of magnitude higher than the mechanical losses measured on the same resonant modes using a silk suspension loop.

Possible reasons for the measured mechanical losses of the first three resonant modes using the nodal support being higher than those measured using suspension loops are that the sapphire substrates were not quite centred in the support, the support itself is not rigid enough at lower frequencies or these resonant modes couple into a

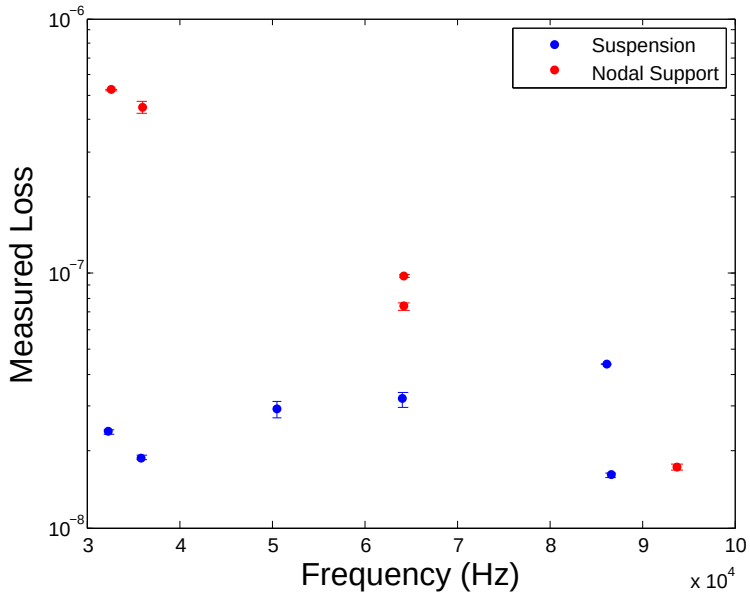

Figure 5.14: Comparison of lowest mechanical losses measured on a-axis sapphire using a silk suspension sling and a nodal support.

resonance of the support.

However, the mechanical losses measured using the nodal support appear to improve at higher frequencies with the lowest mechanical loss measured of 1.72×10^{-8} at 94 kHz. This is comparable to the lowest measured suspension loop loss of 1.61×10^{-8} at 86 kHz. This indicates that a nodal support is capable of measuring low mechanical losses, but improvements are needed to the nodal support to lower the measured mechanical losses at lower frequencies.

It can be seen in figure 5.15 that, after all the mechanical loss measurements were made of this sapphire sample, small scratches had been formed on the faces of the substrate at the two contact points with the nodal support. Refinements will need to be made to the clamping mechanism of the nodal support to ensure that scratches are not produced on future samples.

The Young's Modulus of the multilayer silica/tantala coatings of the type used in an interferometric gravitational wave detectors is $\sim 1 \times 10^{11}$ Pa which is a factor of four less than the $\sim 4 \times 10^{11}$ Pa of sapphire and of the ruby ball contacts of the

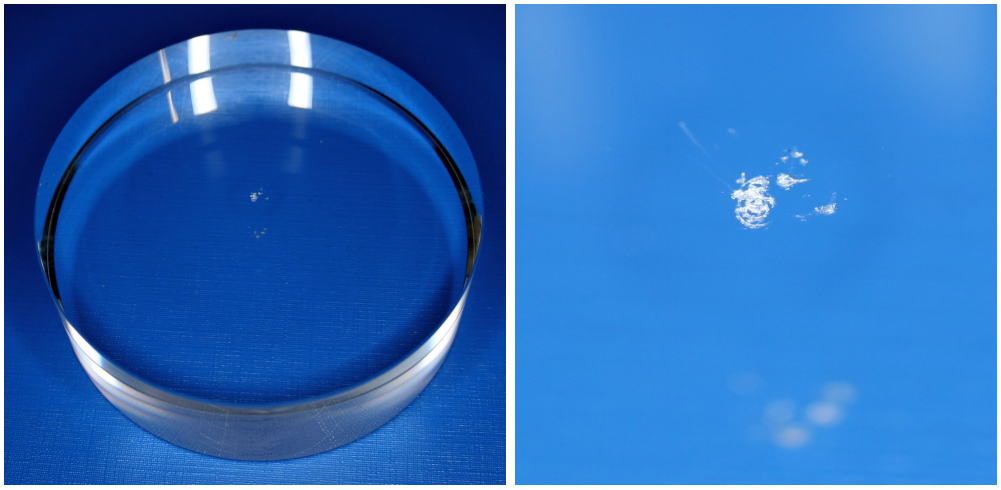

Figure 5.15: Sapphire substrate after being suspended in the nodal support (left) close-up image of the scratches (right).

nodal support. The mechanical loss measurements of silica/tantala coatings applied to sapphire substrates detailed in the following sections were measured using only silk suspension loops to prevent them from being scratched since these coatings are softer than the ruby balls.

5.8 Measurements of the Coating Loss of Tantala/Silica Coated *a*-axis Sapphire Substrates

A study of the effects of applying coatings to sapphire substrates has begun at the University of Glasgow. At the same time as LMA produced a series of titania doped tantala/silica coatings applied to fused silica substrates, as detailed in section 3.10, a selection of identical coatings was produced on *a*-axis sapphire substrates. Five different 'Formula' thirty layer tantala/silica coatings were produced with differing percentages of titania introduced to the tantala layers. The percentages of dopant present in the tantala layers of these coatings are the same as those produced on fused silica substrates. The percentages of titania present in the coatings were estimated by LMA, the coating vendor, and are the same as those presented in table 3.9. These coatings were applied to 76.2 mm diameter by 25.4 mm thick cylindrical substrates

and annealed to 600 °C. The measured mechanical losses of all these samples are presented in figure 5.16.

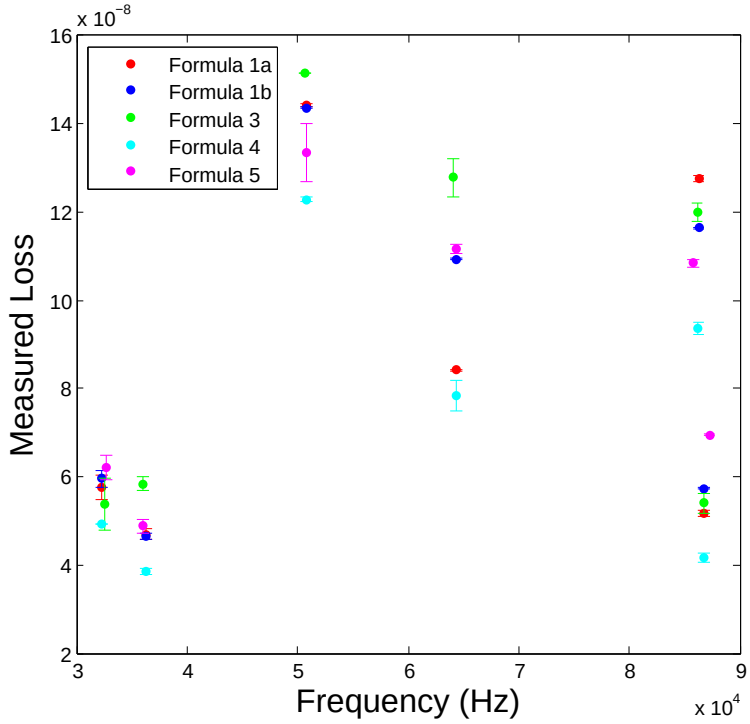

Figure 5.16: Measured mechanical losses of 76.2 mm diameter by 25.4 mm long *a*-axis sapphire substrates coated with multi-layer tantala/silica coatings of differing percentages of titania dopant introduced to the tantala component.

Two identical 'Formula 1' coatings were produced by LMA. The first was applied to a standard polished sapphire substrate, denoted 'Formula 1a' in figure 5.16, and the second sputtered onto a super-polished substrate labelled 'Formula 1b'. The thickness and composition of all these coatings are taken to be identical to their equivalent coatings applied to fused silica substrates.

The loss for each of the coatings can be calculated once the fraction of energy stored in the coating is established. This was done in ANSYS® as described in section 3.7.2 using the a-axis sapphire elastic stiffness properties from equation 5.14. To approximate an infinite point model six models were run with an increasing number of nodes, as shown in figure 5.17, and a converged value for each energy ratio calculated.

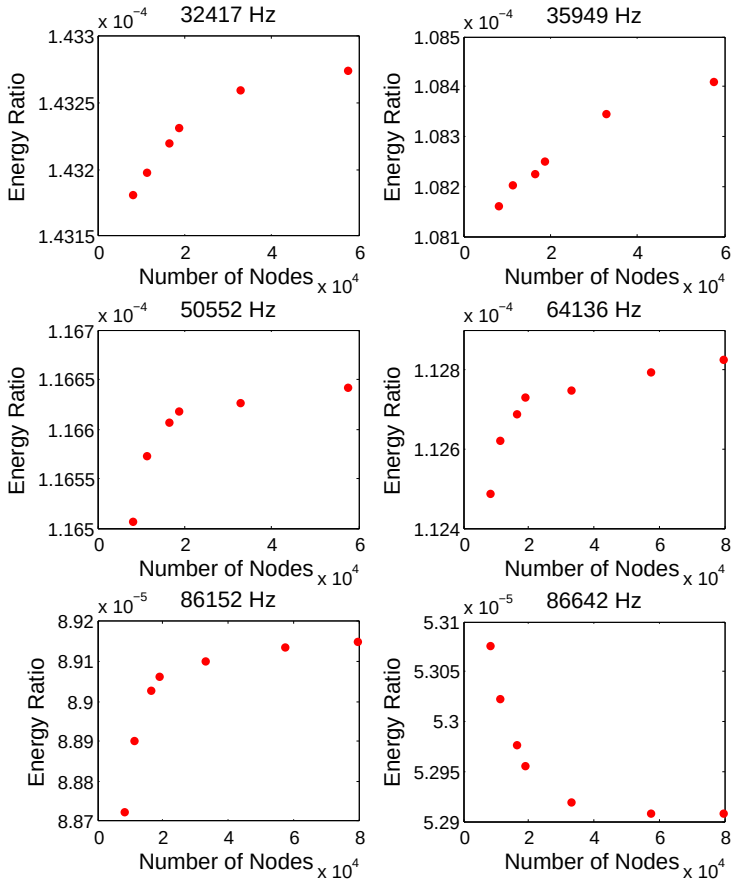

Figure 5.17: Convergence of Ratio of Energy Stored in a 30 layer silica/tantala coating on a 76.2 mm diameter by 25.4 mm long *a*-axis sapphire substrate.

These energy ratios were then substituted into equation 3.11 to calculate $\phi(\omega_0)_{\text{coating}}$. To eliminate the effects of suspension losses as much as possible the lowest measured mechanical losses from figure 5.7 were used for $\phi(\omega_0)_{\text{substrate}}$ of each resonant mode as it was thought this would represent more accurately the effective bulk substrate losses. The coating loss for each resonant mode of the different coatings was then calculated and is shown in figure 5.18.

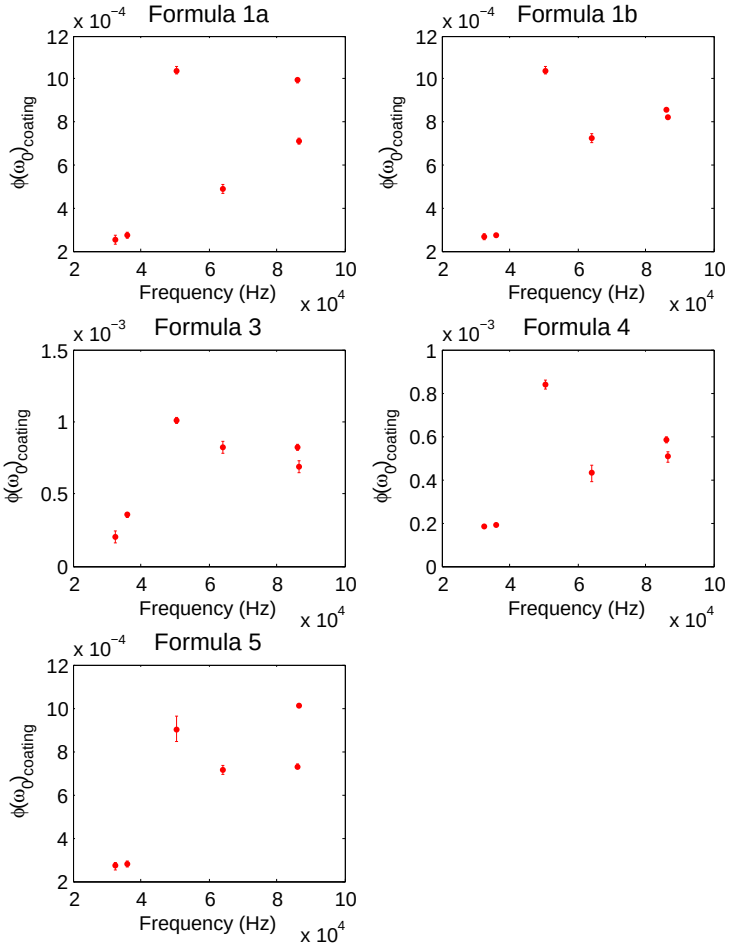

Figure 5.18: Plot of the calculated coating loss of each resonant mode for each of the five 76.2 mm diameter by 25.4 mm long *a*-axis sapphire substrates coated with multi-layer tantala/silica coatings of differing percentages of titania dopant introduced to the tantala component.

The ratio of energy in the coating associated with the change in volume of the coating during the motion of each resonant mode was estimated by D. Crooks [200]. These were then substituted into equation 3.13, together with the loss attributable to

coating thermoelastic dissipation, calculated using equation 2.28, to find the residual coating losses of each individual resonant mode and are shown in figure 5.19.

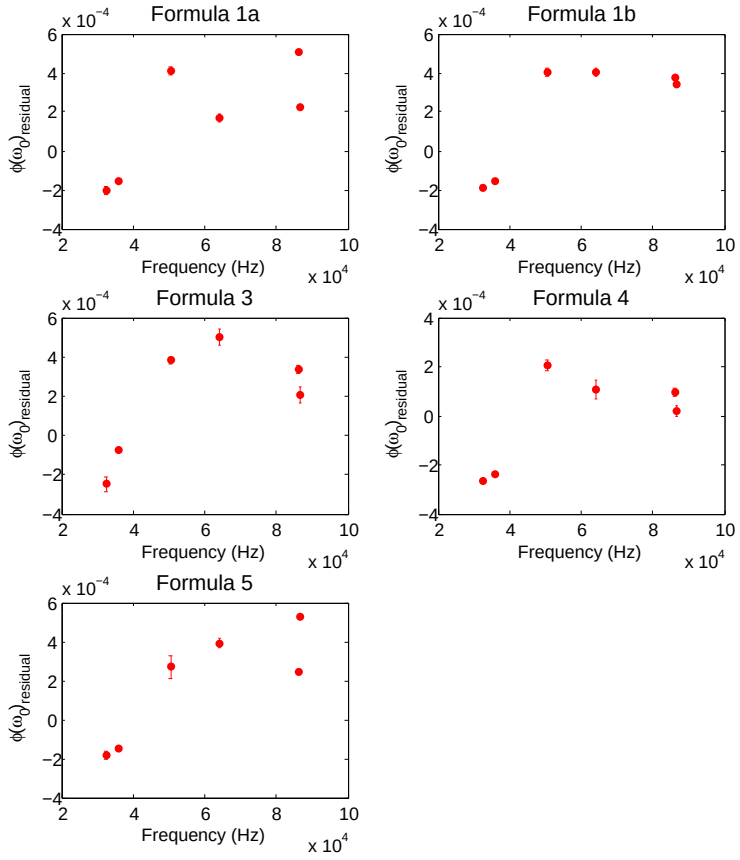

Figure 5.19: Plot of the calculated residual loss of each resonant mode for each of the five 76.2 mm diameter by 25.4 mm long *a*-axis sapphire substrates coated with multi-layer tantala/silica coatings of differing percentages of titania dopant introduced to the tantala component.

It is clear from figure 5.19 that the residual coating losses for the first two resonant modes of each coated sample are negative. One explanation for this was that the minimum loss factor had not been obtained for these resonant modes for the measurements of the uncoated substrate samples. It is thought that, as discussed in section 5.6, suspension losses may be limiting these loss factors to the $\sim 2 \times 10^{-8}$ measured in the laboratory.

In an attempt to calculate an overall residual loss of each of the coatings, the first two individual losses were excluded as they were unrealistic. Averaging the remaining four individual losses gives the residual losses as shown in table 5.3.

Coating	$\phi(\omega_0)_{\mathbf{residual}}$ $(\times 10^{-4})$
Formula 1a	3.3 ± 0.3
Formula 1b	3.8 ± 0.3
Formula 3	3.6 ± 0.7
Formula 4	1.1 ± 0.5
Formula 5	3.6 ± 0.6

Table 5.3: Calculated residual losses for the different 'Formula' coatings applied to *a*-axis sapphire substrates.

These residual losses can then be plotted against the estimated percentages of dopant present in the tantala layers of the coating given by LMA the coating vendor in table 3.9, as shown in figure 5.20.

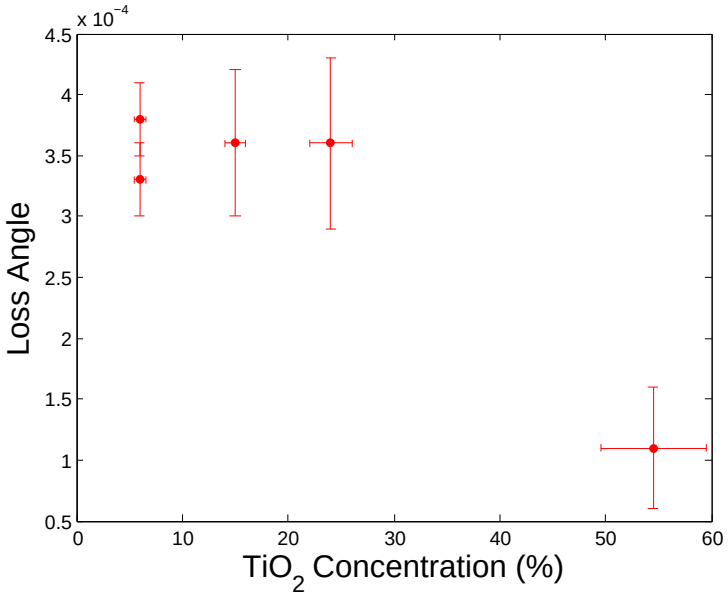

Figure 5.20: Residual losses of TiO_2-doped tantala/silica coatings applied to *a*-axis sapphire substrates as a function of TiO_2 concentration in the Ta_2O_5.

From figure 5.20, it can be seen that for low percentages of titania dopant there is no apparent difference in the residual loss of the tantala/silica coatings. However, without an undoped tantala/silica coating for comparison it is impossible to determine whether there is any reduction in the residual loss of the coating due to the addition of titania.

For the two 'Formula 1' coatings produced on standard polished and super-polished sapphire substrates their residual losses agree within experimental error. This shows that the residual losses of the samples tested with a standard inspection polish do not differ from the losses of a super-polished sample. The figure also shows a reduction of almost 70% in the residual loss of the 'Formula 4' sample doped with $\sim 50\%$ titania compared to the lower percentages of dopant, suggesting that higher percentages of dopant may reduce the residual loss of tantala/silica coatings.

The residual losses of the doped tantala/silica coatings are broadly all higher than the equivalent coating sputtered onto a fused silica substrate. At this point it is unclear whether this is in any way related to the use of a different substrate material, or other factors such as suspension losses limiting measurements.

Further experiments are needed to verify these results as it is thought that suspension losses may be limiting some of the loss measurements. In addition, studies of an undoped 30 layer silica/tantala coating produced by LMA are desirable to quantify the reduction in loss due to the doping when coatings are applied to sapphire substrate compared to the results found for coatings applied to fused silica substrates.

5.9 Conclusion

Mechanical loss measurements on a HEMEX sapphire substrate show that losses as low as $(4.61 \pm 0.03) \times 10^{-9}$ are possible. However, great care must be taken when measuring the mechanical loss of 76.2 mm diameter by 25.4 mm thick sapphire substrates so that other factors such as suspension losses are not limiting the mechanical loss measurements.

Results presented in this chapter indicate that it is possible to measure the mechanical loss of some resonant mode shapes by using a nodal support instead of a silk suspension loop. Mechanical losses as low as 1.72×10^{-8} on a resonant mode at 94 kHz have been measured which is comparable to the lowest mechanical losses measured using a silk suspension loop. Alterations need to be made to this support to improve the measurable mechanical losses of lower frequency resonant modes.

There is some suggestion that the addition of $\sim 50\%$ titania to the tantala layers of a thirty layer tantala/silica coating may reduce the residual loss of coatings. However, an undoped tantala/silica coating needs to be produced on a sapphire substrate to allow a comparison of all the doped coatings to be made.

In this chapter it has been shown that it is possible to create finite element analysis models of the different orientations of sapphire sample in ANSYS®. Future finite element models should also improve our estimates of the volume change of the coating as they resonate. Research into this is beginning at the University of Glasgow while this thesis is being written. Once completed it should be possible to create a script which, when the material and physical properties of the substrate and a coating applied to it are entered into the finite element package, models will be able to determine automatically the resonant mode frequencies, resonant mode shapes, the strain energy in these modes and the change in volume of these resonances.

Chapter 6

Measurements of Mechanical Loss of Silicon Substrates

6.1 Silicon as a Mirror Substrate

High laser power (several hundreds of kilowatts) may be necessary to obtain improved shot-noise limited sensitivity in the future generation of gravitational wave detectors. At these levels of laser power thermally induced deformations of the interferometer optics can be significant. The Advanced LIGO detector which is planned to start observations in 2013 [86] will operate with ~ 830 kW of laser power stored in the cavities of the interferometer arms which is expected to result in distortions of the fused silica mirror substrates and the coatings applied to them to a level that requires active thermal compensation. A combination of CO_2 laser based and radiative heating elements is proposed to correct these effects [201].

If the laser power incident on the silica mirrors were to be increased even more, the corresponding thermal deformation of these mirrors would be so great that it would be difficult to compensate. The magnitude of the thermally induced deformation is proportional to $\frac{\alpha}{\kappa}$ where α is the coefficient of thermal expansion and κ the thermal conductivity of the material [124]. Using a material in which this ratio is minimised,

it is then possible to improve the tolerance of the substrate to thermally induced deformations and consequently enable the use of even greater laser powers increasing the shot-noise performance of interferometric gravitational wave detectors utilizing this material. The study of materials which have both a low mechanical loss and ratio $\frac{\alpha}{\kappa}$ is of interest to the gravitational wave community.

One such material is silicon [202, 203]. The average thermal conductivity of silicon at room temperature (145 $\mathrm{Wm^{-1}K}$) [204] is two orders of magnitude greater than fused silica (1.4 $\mathrm{Wm^{-1}K}$) [2], but it also has a larger coefficient of thermal expansion (2.54×10^{-6} $\mathrm{K^{-1}}$) [205] than fused silica (5.5×10^{-7} $\mathrm{K^{-1}}$) [2]. Despite this bigger coefficient of thermal expansion, the ratio $\frac{\alpha}{\kappa}$ is ~ 22 times lower in silicon, meaning that expansion effects from the absorption of laser power can be tolerated more easily.

Unfortunately, silicon is opaque to the 1.064 μm of the Nd:YAG laser light used in interferometric gravitational wave detectors. One way of avoiding this difficulty would be to construct a detector using diffractive optics [206] to form an all-reflective layout.

Silicon is widely available in the large sizes required for use as a mirror substrate in a gravitational wave detector, and research suggests that it can be produced to have a low mechanical loss. It also has interesting thermo-mechanical properties when cooled, which are detailed later in chapter 7. Studies of the mechanical loss factor of silicon samples of different aspect ratios and crystal orientations have been carried out by the author in the laboratory at the University of Glasgow.

6.2 Crystal Orientation of Silicon

Silicon, unlike sapphire, has an m3m *cubic* crystallographic system. This means that a silicon crystal has three fold rotational symmetry and two axes of mirror symmetry.

6.2.1 Stiffness Constants of (100) Silicon

The stiffness matrix for a *cubic* crystal class is defined as [195]:

$$[\mathbf{c}] = \begin{bmatrix} c_{11} & c_{12} & c_{12} & 0 & 0 & 0 \\ c_{12} & c_{11} & c_{12} & 0 & 0 & 0 \\ c_{12} & c_{12} & c_{11} & 0 & 0 & 0 \\ 0 & 0 & 0 & c_{44} & 0 & 0 \\ 0 & 0 & 0 & 0 & c_{44} & 0 \\ 0 & 0 & 0 & 0 & 0 & c_{44} \end{bmatrix} \tag{6.1}$$

The material properties of silicon are defined, by convention, relative to the (100) direction, indicated parallel to the x-axis in figure 6.1. The *stiffness* c_{ij} constants are stated to be

$$\begin{aligned} c_{11} &= 1.657 \times 10^{11} \\ c_{12} &= 0.639 \times 10^{11} \\ c_{44} &= 0.7956 \times 10^{11} \end{aligned} \tag{6.2}$$

where each value has units $\mathrm{N/m^2}$ [195]. These entities can be substituted into equation 6.1 to give the stiffness matrix for silicon in the (100) direction $[\mathbf{c}_{(100)}]$. Each entry in the following matrix has units $\times 10^{11}$ $\mathrm{kg/ms^2}$.

$$[\mathbf{c}_{(100)}] = \begin{bmatrix} 1.657 & 0.639 & 0.639 & 0 & 0 & 0 \\ 0.639 & 1.657 & 0.639 & 0 & 0 & 0 \\ 0.639 & 0.639 & 1.657 & 0 & 0 & 0 \\ 0 & 0 & 0 & 0.7956 & 0 & 0 \\ 0 & 0 & 0 & 0 & 0.7956 & 0 \\ 0 & 0 & 0 & 0 & 0 & 0.7956 \end{bmatrix} \tag{6.3}$$

The orientation of the crystal axis with respect to the cylindrical axis of a sample may be of importance for loss measurements in a number of ways. Firstly, a similar elastic distortion (ie a similar mode shape) of samples cut along different axes will involve different combinations of elastic constants and thus may result in a different intrinsic loss for the samples.

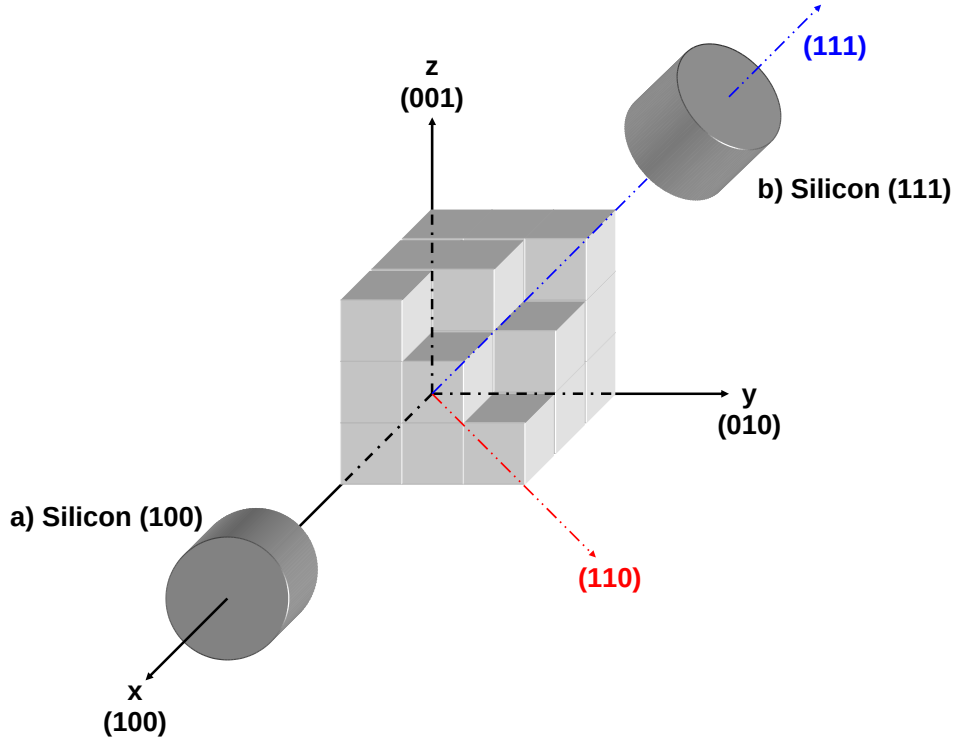

Figure 6.1: Illustration of the crystal axes of silicon and the orientation of a) silicon cut with its cylindrical axis parallel to the (100) axis and b) silicon cut with its cylindrical axis parallel to the (111) direction.

Since the crystal structure of silicon is anisotropic, it is important to calculate the different mechanical properties along the different orientations of the crystal axes. Investigations in this thesis concentrate on samples manufactured specifically so that their cylindrical axes are parallel to either the (100) crystal axis of silicon, shown in figure 6.1a, or parallel to the (111) axis, see figure 6.1b.

6.3 Bond Transformations of Silicon

Using the technique of bond transformation described in section 5.3, it is possible to determine the elastic properties in the different orientations of silicon. To calculate the stiffness matrix for silicon (111) it is necessary to *rotate* the elastic properties from the silicon (100) direction to the (110) direction and then to the (111) direction.

To perform a transformation by *rotating* the original axes in a clockwise direction through an angle ξ_x about the x-axis, the transformation tensor matrix $[\mathbf{a}]$ becomes:

$$[\mathbf{a}] = \begin{bmatrix} a_{xx} & a_{xy} & a_{xz} \\ a_{yx} & a_{yy} & a_{yz} \\ a_{zx} & a_{zy} & a_{zz} \end{bmatrix} = \begin{bmatrix} 1 & 0 & 0 \\ 0 & \cos\xi_x & \sin\xi_x \\ 0 & -\sin\xi_x & \cos\xi_x \end{bmatrix} \tag{6.4}$$

which gives a Bond *stress* transformation matrix of:

$$[\mathbf{M}_x] = \begin{bmatrix} 1 & 0 & 0 & 0 & 0 & 0 \\ 0 & \cos^2\xi_x & \sin^2\xi_x & \sin 2\xi_x & 0 & 0 \\ 0 & \sin^2\xi_x & \cos^2\xi_x & -\sin 2\xi_x & 0 & 0 \\ 0 & -\frac{\sin 2\xi_x}{2} & \frac{\sin 2\xi_x}{2} & \cos 2\xi_x & 0 & 0 \\ 0 & 0 & 0 & 0 & \cos\xi_x & -\sin\xi_x \\ 0 & 0 & 0 & 0 & \sin\xi_x & \cos\xi_x \end{bmatrix}. \tag{6.5}$$

Similarly, for a rotation through an angle ξ_y and ξ_z about the y and z-axes respectively, the corresponding Bond stress transformations can be calculated and are shown in equations 6.6 and 6.7.

$$[\mathbf{M}_y] = \begin{bmatrix} \cos^2\xi_y & 0 & \sin^2\xi_y & 0 & -\sin 2\xi_y & 0 \\ 0 & 1 & 0 & 0 & 0 & 0 \\ \sin^2\xi_y & 0 & \cos^2\xi_y & 0 & \sin 2\xi_y & 0 \\ 0 & 0 & 0 & \cos\xi_y & 0 & \sin\xi_y \\ \frac{\sin 2\xi_y}{2} & 0 & -\frac{\sin 2\xi_y}{2} & 0 & \cos 2\xi_y & 0 \\ 0 & 0 & 0 & -\sin\xi_y & 0 & \cos\xi_y \end{bmatrix} \tag{6.6}$$

$$[\mathbf{M}_z] = \begin{bmatrix} \cos^2\xi_z & \sin^2\xi_z & 0 & 0 & 0 & \sin 2\xi_z \\ \sin^2\xi_z & \cos^2\xi_z & 0 & 0 & 0 & -\sin 2\xi_z \\ 0 & 0 & 1 & 0 & 0 & 0 \\ 0 & 0 & 0 & \cos\xi_z & -\sin\xi_z & 0 \\ 0 & 0 & 0 & \sin\xi_z & \cos\xi_z & 0 \\ -\frac{\sin 2\xi_z}{2} & \frac{\sin 2\xi_z}{2} & 0 & 0 & 0 & \cos 2\xi_z \end{bmatrix} \tag{6.7}$$

6.3.1 Silicon (100) to Silicon (110) Bond Matrix Transformation

To achieve the transformation from the (100) orientation to the (110) direction it is necessary to apply a 45° rotation about the z-axis (shown in figure 6.1). Substituting $\xi_z = 45°$ into equation 6.7 yields a Bond stress transformation matrix $[\mathbf{M}_z]$ of:

$$[\mathbf{M}_z] = \begin{bmatrix} \frac{1}{2} & \frac{1}{2} & 0 & 0 & 0 & 1 \\ \frac{1}{2} & \frac{1}{2} & 0 & 0 & 0 & -1 \\ 0 & 0 & 1 & 0 & 0 & 0 \\ 0 & 0 & 0 & \frac{1}{2}\sqrt{2} & -\frac{1}{2}\sqrt{2} & 0 \\ 0 & 0 & 0 & \frac{1}{2}\sqrt{2} & \frac{1}{2}\sqrt{2} & 0 \\ -\frac{1}{2} & \frac{1}{2} & 0 & 0 & 0 & 0 \end{bmatrix} \tag{6.8}$$

which when substituted into $[\mathbf{c}'] = [\mathbf{M}_z][\mathbf{c}][\tilde{\mathbf{M}}_z]$ gives

$$[\mathbf{c}'] = \begin{bmatrix} c'_{11} & c'_{12} & c_{12} & 0 & 0 & 0 \\ c'_{12} & c'_{11} & c_{12} & 0 & 0 & 0 \\ c_{12} & c_{12} & c_{11} & 0 & 0 & 0 \\ 0 & 0 & 0 & c_{44} & 0 & 0 \\ 0 & 0 & 0 & 0 & c_{44} & 0 \\ 0 & 0 & 0 & 0 & 0 & \frac{c_{11}-c_{12}}{2} \end{bmatrix} \tag{6.9}$$

where

$$c'_{11} = \frac{c_{11} + c_{12} + 2c_{44}}{2} \tag{6.10}$$

$$c'_{12} = \frac{c_{11} + c_{12} - 2c_{44}}{2}. \tag{6.11}$$

Substituting the stiffness constants from equation 6.2 into $[\mathbf{c}']$ gives the stiffness matrix for silicon (110) of

$$[\mathbf{c}_{(110)}] = \begin{bmatrix} 1.944 & 0.352 & 0.639 & 0 & 0 & 0 \\ 0.352 & 1.944 & 0.639 & 0 & 0 & 0 \\ 0.639 & 0.639 & 1.657 & 0 & 0 & 0 \\ 0 & 0 & 0 & 0.7956 & 0 & 0 \\ 0 & 0 & 0 & 0 & 0.7956 & 0 \\ 0 & 0 & 0 & 0 & 0 & 0.509 \end{bmatrix} \tag{6.12}$$

where each entry in the above matrix has units $\times 10^{11}$ kg/ms^2.

6.3.2 Silicon (110) to Silicon (111) Bond Matrix Transformation

To transform the elastic properties from the (110) direction to the (111) direction (i.e., to line up with the body diagonal of the cube elements, see figure 6.1) requires a rotation of $\xi_y = \cos^{-1}\left(\frac{1}{\sqrt{3}}\right)$ determined from figure 6.2.

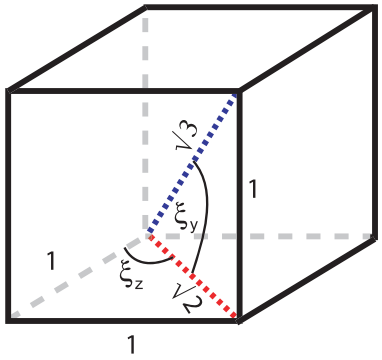

Figure 6.2: Representation of the length of the body diagonal in a cubic crystal.

Substituting $\cos\xi_y = \frac{1}{\sqrt{3}}$ and $\sin\xi_y = \sqrt{\frac{2}{3}}$ into equation 6.6 gives a bond stress transformation matrix $[\mathbf{M}_y]$ of

$$[\mathbf{M}_y] = \begin{bmatrix} \frac{1}{3} & 0 & \frac{2}{3} & 0 & -\frac{2}{3}\sqrt{2} & 0 \\ 0 & 1 & 0 & 0 & 0 & 0 \\ \frac{2}{3} & 0 & \frac{1}{3} & 0 & \frac{2}{3}\sqrt{2} & 0 \\ 0 & 0 & 0 & \frac{1}{3}\sqrt{3} & 0 & \frac{1}{3}\sqrt{6} \\ \frac{1}{3}\sqrt{2} & 0 & -\frac{1}{3}\sqrt{2} & 0 & -\frac{1}{3} & 0 \\ 0 & 0 & 0 & -\frac{1}{3}\sqrt{6} & 0 & \frac{1}{3}\sqrt{3} \end{bmatrix} \tag{6.13}$$

since

$$\begin{aligned} \sin 2\xi_y &= 2\sin\xi_y\cos\xi_y &&= \tfrac{2}{3}\sqrt{2} \\ \cos 2\xi_y &= \cos^2\xi_y - 1 &&= -\tfrac{1}{3} \end{aligned} \tag{6.14}$$

which when substituted into $[\mathbf{c}''] = [\mathbf{M}_y][\mathbf{c}'][\tilde{\mathbf{M}}_y]$ gives

$$[\mathbf{c}''] = \begin{bmatrix} c''_{11} & c''_{12} & c''_{13} & 0 & c''_{15} & 0 \\ c''_{12} & c''_{11} & c''_{13} & 0 & -c''_{15} & 0 \\ c''_{13} & c''_{13} & c''_{33} & 0 & 0 & 0 \\ 0 & 0 & 0 & c''_{44} & 0 & -c''_{15} \\ c''_{15} & -c''_{15} & 0 & 0 & c''_{44} & 0 \\ 0 & 0 & 0 & -c''_{15} & 0 & c''_{66} \end{bmatrix} \tag{6.15}$$

where

$$c''_{11} = \frac{c_{11} + c_{12} + 2c_{44}}{2} \tag{6.16}$$

$$c''_{12} = \frac{c_{11} + 5c_{12} - 2c_{44}}{6} \tag{6.17}$$

$$c''_{13} = \frac{c_{11} + 2c_{12} - 2c_{44}}{3} \tag{6.18}$$

$$c''_{15} = \frac{c_{12} - c_{11} + 2c_{44}}{3\sqrt{2}} \tag{6.19}$$

$$c''_{33} = \frac{c_{11} + 2c_{12} + 4c_{44}}{3} \tag{6.20}$$

$$c''_{44} = \frac{c_{11} - c_{12} + c_{44}}{3} \tag{6.21}$$

$$c''_{66} = \frac{c_{11} - c_{12} + 4c_{44}}{6}. \tag{6.22}$$

Substituting the stiffness constants from equation 6.2 gives the stiffness matrix for silicon (111) of

$$[\mathbf{c}_{(111)}] = \begin{bmatrix} 1.944 & 0.543 & 0.448 & 0 & 0.135 & 0 \\ 0.543 & 1.944 & 0.448 & 0 & -0.135 & 0 \\ 0.448 & 0.448 & 2.039 & 0 & 0 & 0 \\ 0 & 0 & 0 & 0.605 & 0 & -0.135 \\ 0.135 & -0.135 & 0 & 0 & 0.605 & 0 \\ 0 & 0 & 0 & -0.135 & 0 & 0.700 \end{bmatrix} \tag{6.23}$$

where each entry in the above matrix has units $\times 10^{11}$ kg/ms^2.

6.4 Finite Element Analysis of Silicon in ANSYS®

It is possible to model all the silicon samples tested in the remainder of this chapter in ANSYS® and to compare the modelled resonant frequencies with those measured experimentally. Silicon (100) and (111) samples can be modelled in ANSYS® by entering the density of silicon (2330 kg/m^3), the appropriate stiffness matrix (detailed in section 5.5) and creating a model of the sample to be analysed using *aniso solid 64* element types (ANSYS® MAIN MENU → PREPROCESSOR → ELEMENT TYPE → ADD/EDIT/DELETE → ADD . . . → SOLID → ANISO 64 → OK).

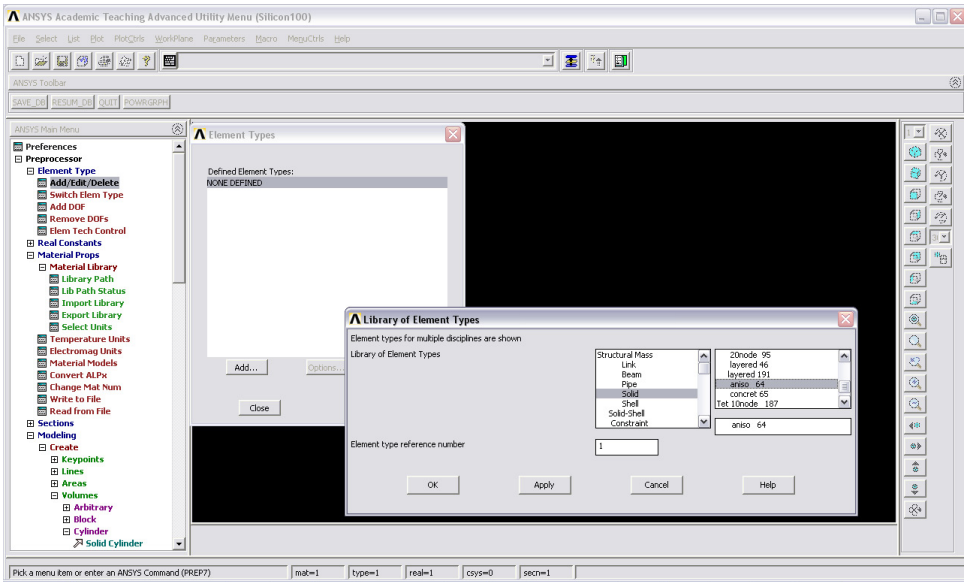

Figure 6.3: Inputting *aniso solid 64* element types into ANSYS®.

6.4.1 Finite element analysis of 98 mm diameter by 100 mm long silicon (100) cylinders

The first sample to be modelled is a 98 mm diameter by 100 mm long silicon (100) cylinder. This was modelled as described above, and the frequencies found were compared to those measured experimentally in the laboratory. They are shown in table 6.1. It can be seen that these modelled frequencies agree on average to within 60 Hz of the resonant frequencies measured on the test mass.

The reason for this small difference could result from the density of the sample not matching exactly the textbook density of 2330 kg/m^3. Also, it is possible that the sample was not grown precisely along the (100) axis. However, the frequencies are sufficiently accurate to measure the resonant frequencies experimentally. The mode shapes and the strain energy stored in them are not likely to change significantly with small changes in the density.

The resonant mode shapes of all these resonant modes were then modelled in ANSYS® and are illustrated in figure 6.4.

Mode Number	Modelled Frequency (Hz)	Measured Frequency (Hz)
2	30529	30593
4	31629	31551
5	34811	34858
6	35593	35528
7	37481	37526
9	39966	39956
11	41262	41256
13	45419	45398
19	53993	53902
22	56319	56190
25	57704	57621

Table 6.1: Comparison of experimentally measured and modelled resonant frequencies of a 98 mm diameter by 100 mm long silicon (100) substrate.

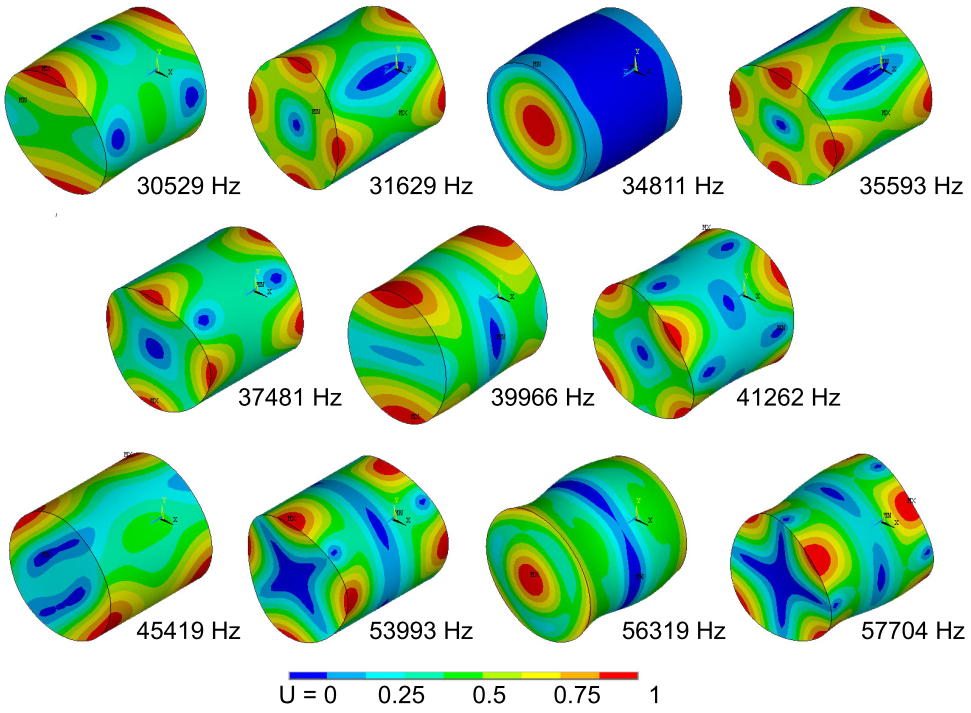

Figure 6.4: ANSYS® illustrations of the resonant mode shapes measured on the 98 mm diameter by 100 mm long silicon (100) substrates where the relative displacements U = $\sqrt{x^2 + y^2 + z^2}$ are plotted in normalised, dimensionless units.

6.4.2 Finite element analysis of 98 mm diameter by 100 mm long silicon (111) cylinders

The second sample modelled in ANSYS® was a 98 mm diameter by 100 mm long silicon (111) cylinder. This was modelled using the stiffness constants given in equation 6.23 and then compared to those measured experimentally in the laboratory. Table 6.2 shows that the modelled frequencies agree on average to within 340 Hz (0.8%) of those measured on the test mass.

Mode Number	Modelled Frequency (Hz)	Measured Frequency (Hz)
2	32209	32936
3	33308	33536
4	33752	33717
6	35449	35549
10	43123	43195
12	44591	44437
13	45001	46078
14	46940	47260
19	52089	52374
20	52878	52676
22	54102	53987
26	58540	58552
27	59870	58783

Table 6.2: Comparison of experimentally measured and modelled resonant frequencies of a 98 mm diameter by 100 mm long silicon (111) substrate.

The resonant mode shapes of all these resonant modes are shown in figure 6.5.

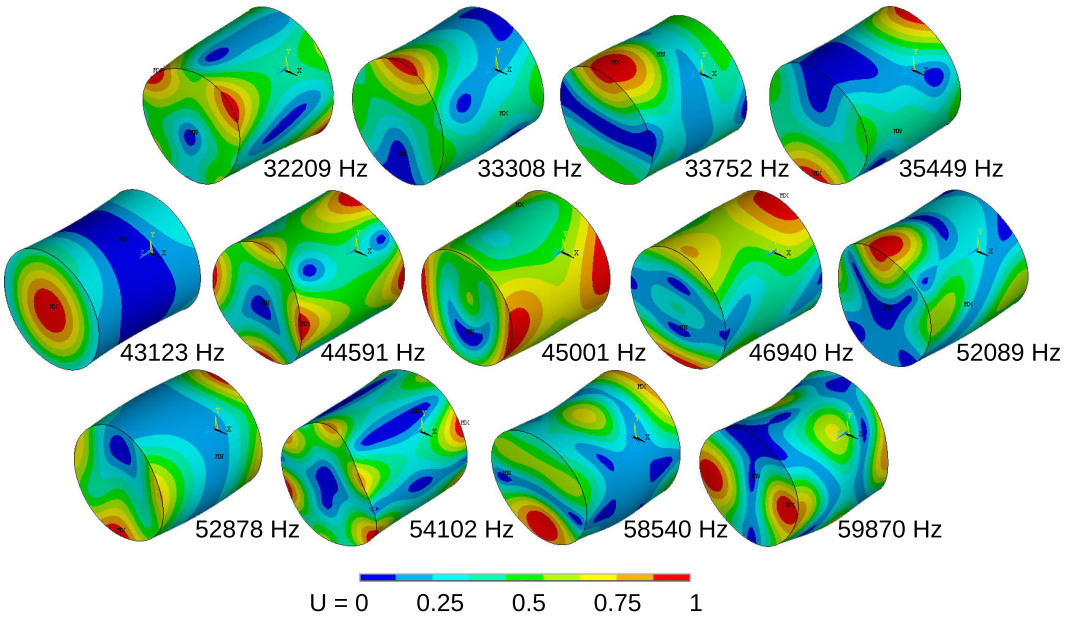

Figure 6.5: ANSYS® illustrations of the resonant mode shapes measured on the 98 mm diameter by 100 mm long silicon (111) substrates where the relative displacements U = $\sqrt{x^2 + y^2 + z^2}$ are plotted in normalised, dimensionless units.

6.5 Measurements of Mechanical Loss in Silicon Cylinders

To begin the investigations into the suitability of silicon for use in an interferometric gravitational wave detector, measurements of the mechanical losses of eight different single-crystal silicon test substrates have been made. As before for the silica and sapphire samples, the mechanical loss factors for each resonant mode of the silicon samples were measured using the experimental apparatus described in section 3.4. Each sample was suspended inside a vacuum tank using a loop of very lightly greased silk thread. The minimum loss measurements were then taken for each of the resonant modes over, on average, ten different suspensions. For each suspension at least three loss measurements were taken for each individual resonant mode and then averaged. A picture of a suspended silicon cylinder is shown in figure 6.6.

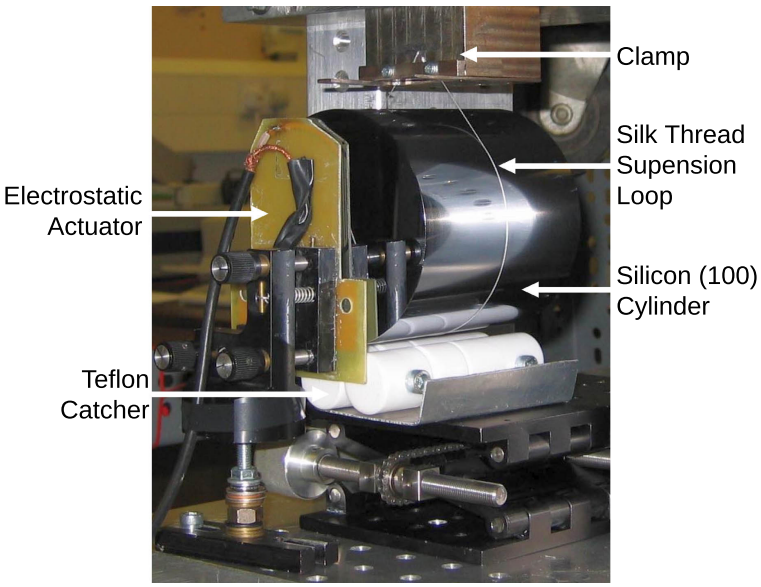

Figure 6.6: Image of silicon (100) cylinder suspended using a loop of silk thread.

The mechanical losses measured on two large 98 mm diameter by 100 mm long silicon cylinders are presented in figure 6.8. The first cylinder was cut along the (100) axis, as shown in figure 6.1a, and was undoped with resistivity $\sim$ 7000 Ωcm, whereas the second sample was cut so that its cylindrical axis points in the (111) direction as shown in figure 6.1b, and was boron doped (with resistivity $\sim$ 20 Ωcm).

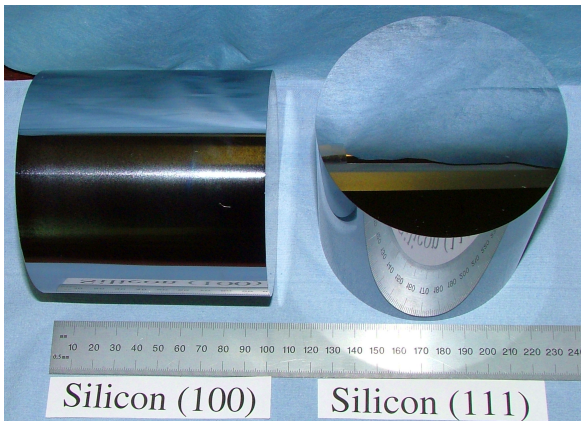

Figure 6.7: Image of the 98 mm diameter by 100 mm long silicon (100) and (111) cylinders.

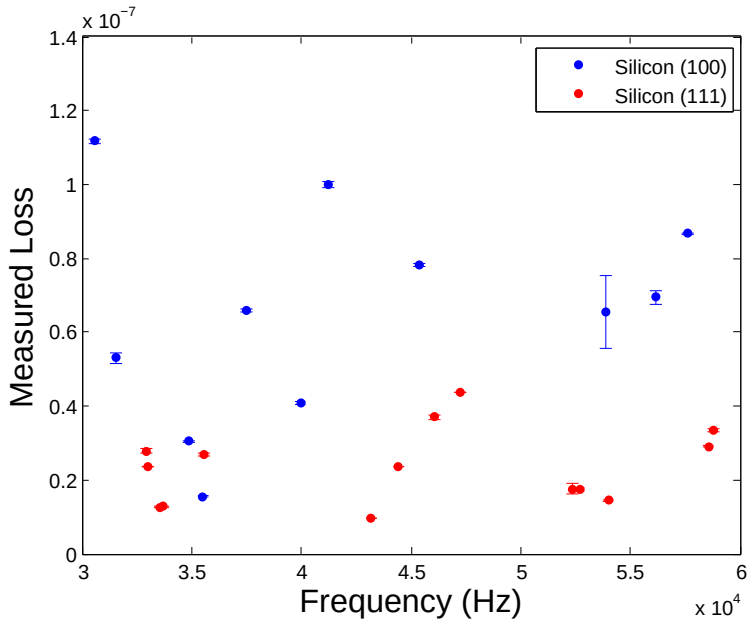

Figure 6.8: Lowest measured mechanical losses of resonant modes of the 98 mm diameter by 100 mm long Silicon (100) and (111) cylinders.

Figure 6.8 shows that the (111) orientated silicon cylinder yielded the lower mechanical losses of the two samples as low as $(9.6 \pm 0.1) \times 10^{-9}$ for the 43195 Hz resonant mode. This is comparable with the lowest mechanical losses measured for other materials, for example, sapphire where losses of $(4.61 \pm 0.03) \times 10^{-9}$ were measured by the author in chapter 5. The lowest mechanical loss measured for the (100) orientated sample was a factor of three higher at $(3.05 \pm 0.03) \times 10^{-8}$ for the resonant mode at 34858 Hz.

From the finite element analysis in ANSYS® it can be observed from figures 6.4 and 6.5 that the lowest measured mechanical losses on each of the silicon cylinders both came from their respective *fundamental longitudinal* (n=0, 4) resonant modes [133]. Such resonant modes, as discussed in section 4.4, have very little motion corresponding to the suspension loop around the barrel, and therefore it is likely that these measured mechanical losses are a true representation of the mechanical loss of the material. It is unclear, however, from these two samples whether it is the crystal cut or the presence of dopant which results in the improved mechanical losses of the (111) orientated silicon.

6.6 Measurements of Mechanical Loss in Silicon Coins

Two *coin* shaped silicon samples 76.2 mm diameter by 25.4 mm long, with the (100) axis pointing along the cylindrical axis of the sample and one 76 mm by 28.4 mm long *coin* cut so that its cylindrical axis was parallel to the (111) direction were produced by Prolog Semicor Ltd [207] and their faces were polished to have a global flatness of $\frac{\lambda}{10}$ by Spanoptic [208]. All three samples were boron doped with resistivity in the range $1 - 10\ \Omega$cm.

Finite element models were then constructed of the (100) and (111) orientated coin shaped silicon samples in ANSYS®. The resonant mode shapes measured experimentally on the 76.2 mm diameter by 25.4 mm long silicon (100) substrates are shown in figure 6.9. The modelled frequencies were $\sim 4\%$ above the measured resonant frequencies on both the (100) orientated coins and the resonant frequencies of both the samples tested agreed to within 0.05%. The difference between the modelled and measured resonant frequencies may be attributed to the samples having possibly a different density from the 2330 kg/m^3 used in the finite element analysis, or not being cut precisely enough along the (100) crystal axis.

Finite element models were also run of the 76 mm diameter by 28.4 mm long silicon (111) substrate, and the resonant mode shapes of this sample are indicated in figure 6.10. The modelled frequencies this time were less than 1.6% below the experimentally measured resonant frequencies. This suggests that the density of this sample is similar to the density used in the finite element analysis and that the sample is close to being cut along the (111) axis.

Mechanical loss measurements were made of all three samples and are presented in figure 6.11.

Inspection of this figure shows again that the mechanical losses of the (111) orientated silicon coin are lower than the (100) coins with losses as low as $(8.51 \pm 0.02) \times$

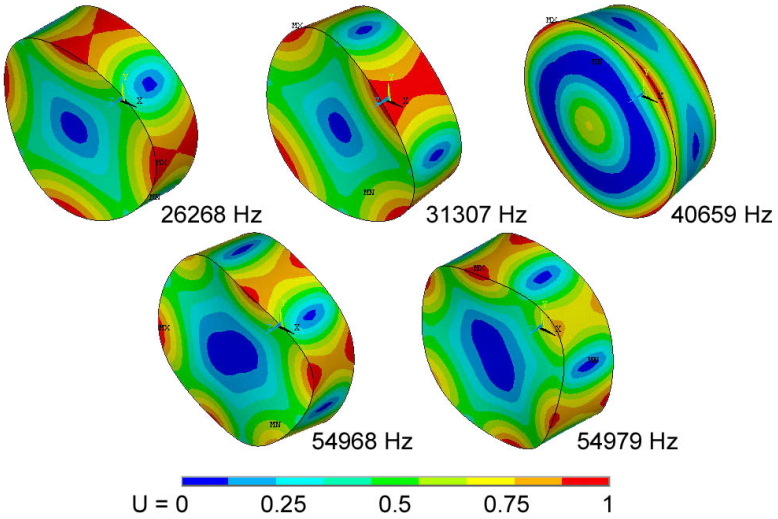

Figure 6.9: ANSYS® illustrations of the five resonant mode shapes measured on the 76.2 mm diameter by 25.4 mm long silicon (100) substrates where the relative displacements U = $\sqrt{x^2 + y^2 + z^2}$ are plotted in normalised, dimensionless units.

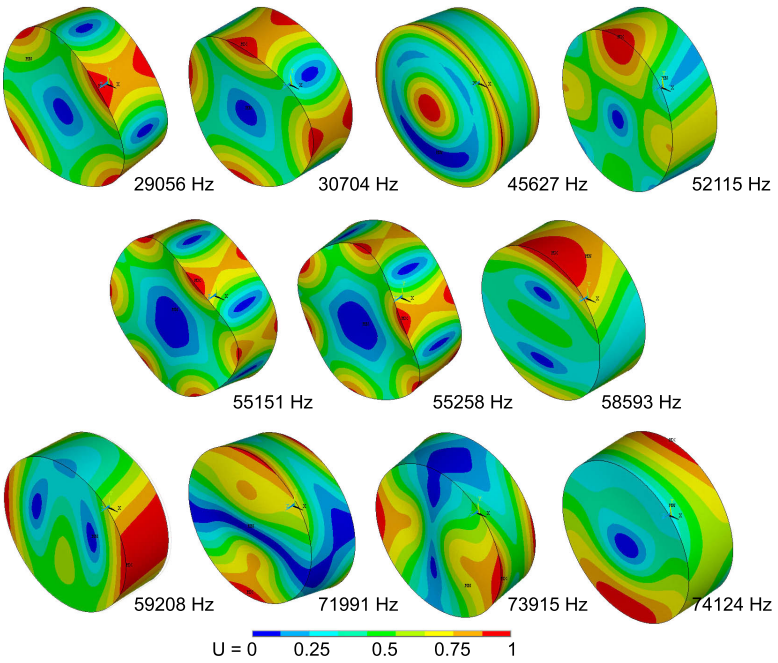

Figure 6.10: ANSYS® illustrations of the resonant mode shapes measured on the 76 mm diameter by 28.4 mm long silicon (111) substrates where the relative displacements U = $\sqrt{x^2 + y^2 + z^2}$ are plotted in normalised, dimensionless units.

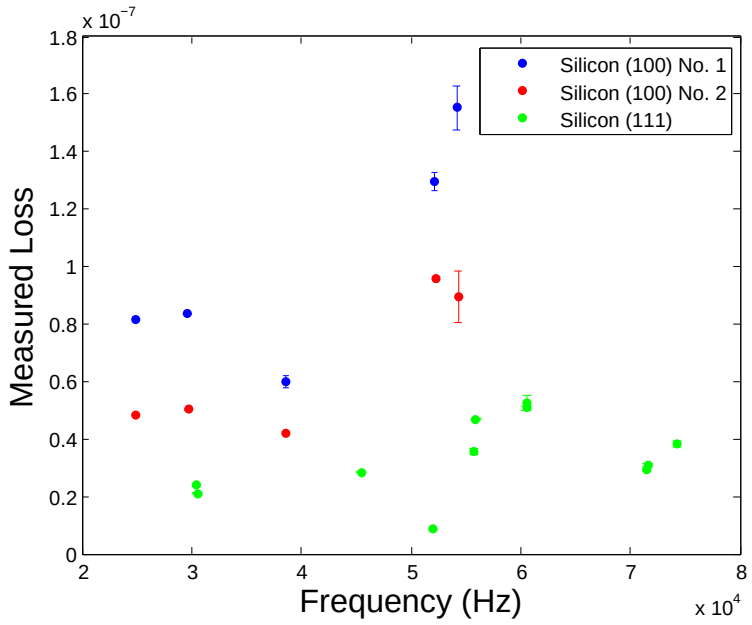

Figure 6.11: Lowest measured mechanical losses of resonant modes of the 76.2 mm diameter by 25.4 mm long Silicon (100) coins and 76 mm diameter by 28.4 mm long Silicon (111) coin.

10^{-9} measured on the 51975 Hz resonant mode. This is comparable to the lowest mechanical loss measured on the (111) orientated 98 mm diameter by 100 mm long silicon (111) cylinder detailed in section 6.5. The mechanical losses of both the (100) coins are all higher, with the lowest loss measured being $(4.21 \pm 0.01) \times 10^{-8}$ on the 38596 Hz resonant mode. Again this is comparable with the lowest losses measured on the (100) orientated silicon cylinder.

All three samples had nominally the same levels of boron dopant. The difference in the measured mechanical losses of the different orientations therefore suggests that, at these levels of measured loss, it is the crystal cut of the silicon which determines the levels of mechanical loss rather than the level, or type, of doping.

It still remains unclear why the mechanical losses of the two (100) orientated silicon samples are not similar. Extensive measurements were made on the Silicon (100) No. 1 sample, but the measured mechanical losses remained approximately a factor of two above the second sample. Both these samples were purchased from the

same vendor, at the same time, with identical specifications and polished together at Spanoptic. This pattern is repeated for the pair of Silicon (100) *rods*, detailed in section 6.7, both purchased and polished at the same time as the coins. One possibility is that although both samples were bought at the same time they came from different batches of silicon.

6.7 Measurements of Mechanical Loss in Silicon Rods

Mechanical loss measurements were taken of two 53 mm diameter by 150 mm long silicon (100) *rods* and of a 51 mm by 153 mm long silicon (111) rod. All three samples were again boron doped, provided by Prolog Semicor Ltd. and polished to have a global flatness of $\frac{\lambda}{4}$ by Spanoptic [208].

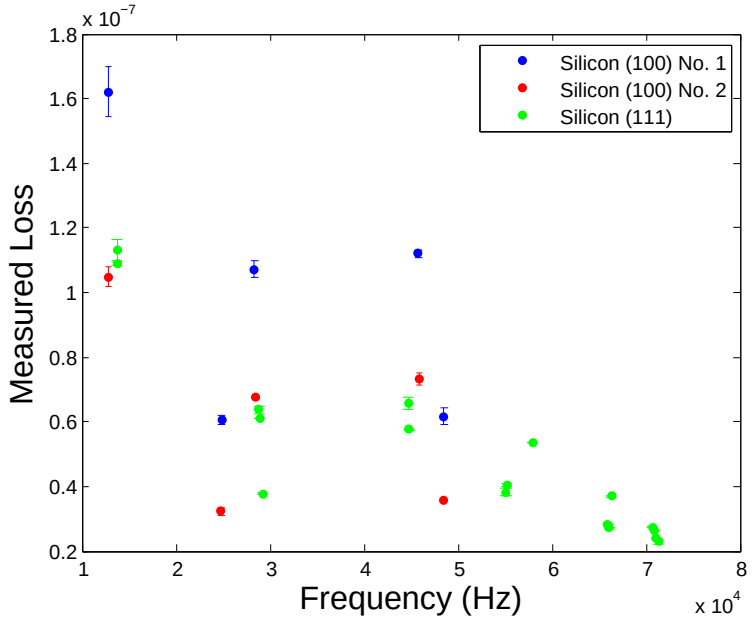

Figure 6.12: Lowest measured mechanical losses of resonant modes of the 50 mm diameter by 150 mm long Silicon (100) rods and 51 mm diameter by 153 mm long Silicon (111) rods.

Unlike the loss measurements recorded on the silicon *cylinders* and *coins*, there appears to be no obvious difference in the mechanical losses of the two different orientations of silicon rod. The lowest mechanical loss measured on the (100) orientated test substrates was $(3.22 \pm 0.10) \times 10^{-8}$ on the *fundamental longitudinal* (n=0, 2) [133] resonant mode at 24834 Hz. The mechanical losses of the silicon (111) sample, shown in figure 6.12, appear to improve with frequency, with the lowest measured mechanical loss measured being $(2.28 \pm 0.08) \times 10^{-8}$ on the *clover 4* (n=2, 16) [133] resonant mode at 71298 Hz.

This is only slightly better than the lowest mechanical loss measured on the silicon (100) rod, while the mechanical loss of the *fundamental longitudinal* (n=0, 2) resonant mode at 29248 Hz of the silicon (111) sample was measured to be $(3.77 \pm 0.03) \times 10^{-8}$ which is slightly higher than the loss measured on the identical mode on the (100) orientated sample.

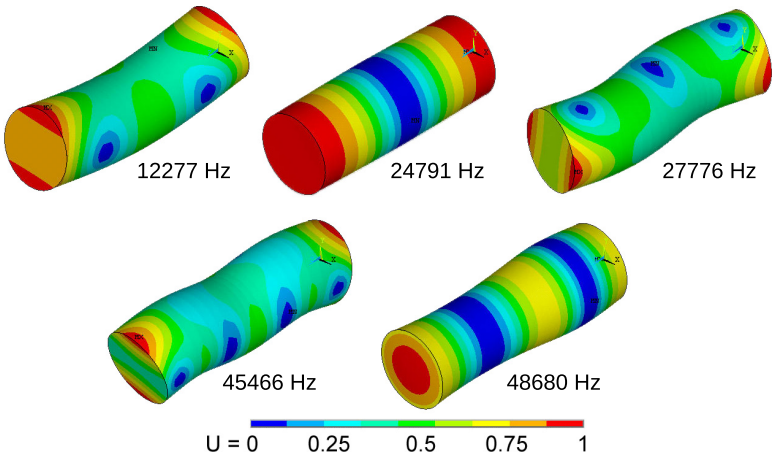

Figure 6.13: ANSYS® illustrations of the five resonant mode shapes measured on the 50 mm diameter by 150 mm long silicon (100) substrates where the relative displacements U = $\sqrt{x^2 + y^2 + z^2}$ are plotted in normalised, dimensionless units.

It appears that suspension losses may be limiting many of the mechanical loss measurements made on all three rod-shaped samples. Four of the five resonant modes measured of the silicon (100) rod shown in the ANSYS® representations in figure 6.13 appear to have motion which corresponds with the suspension loop used to suspend this mass. Friction losses from the motion of these resonant modes against

the silk thread could have lead to the higher mechanical losses. The 24791 Hz resonant mode has no motion around the suspension which could explain the lower mechanical loss measurements at this frequency.

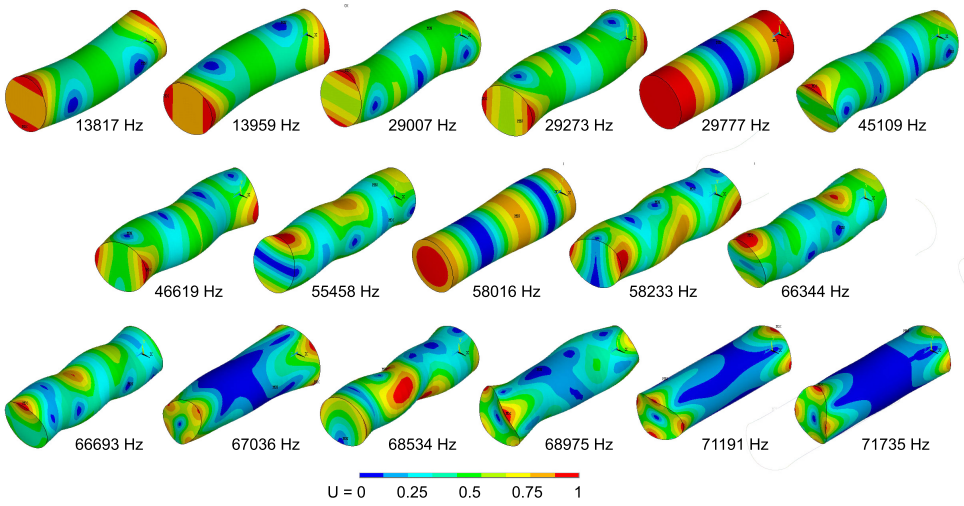

Figure 6.14: ANSYS® illustrations of the five resonant mode shapes measured on the 51 mm diameter by 153 mm long silicon (111) substrates where the relative displacements $\mathrm{U} = \sqrt{x^2 + y^2 + z^2}$ are plotted in normalised, dimensionless units.

Similarly, it can be observed in figure 6.14 that the majority of the first resonant mode frequencies for the (111) orientated silicon rod have motion at points which correspond to the contact points of the suspension. This could account for the higher mechanical losses measured on these modes. The resonant modes at $68 - 71$ kHz all have very little motion in the suspension area and all have lower mechanical losses. These losses may be more representative of the losses of silicon rods cut along the (111) direction. Clearly, further measurements need to be made on higher frequency modes on the (100) orientated samples for a more direct comparison. To improve the loss measurements on all the lower frequency modes it is necessary to devise other methods of supporting the samples for loss measurements. Unfortunately, a nodal support for the rods similar to the one discussed in section 5.7, would restrict the loss measurements on the same suspension-limited resonant modes due to the motion of the faces of these modes.

6.8 Rotation of Silicon Within a Suspension

In addition to the differing cuts of silicon samples, the anisotropic crystal properties of silicon also introduce an extra factor which must be taken into account when optimising the suspension of a sample. Some of the results presented in this thesis suggest that the suspensions upon which the test masses are hung may limit some of the mechanical loss factors measured. Silica is isotropic which means for whatever orientation the sample is suspended, the resonant mode shapes would be the same in relation to the suspension.

Silicon is anisotropic so its resonant modes orientations are fixed to the crystal structure. Consequently, if the mass is rotated in its suspension, the mode shape would rotate with it. This means that for a resonant mode with varied degrees of motion around the middle of the mass the slip-stick loss between the mass and thread will change with rotation. This indicates that, for an anisotropic mass, as well as an optimum suspension material, suspension length, and amount of grease there may also be an optimum orientation within the suspension which minimises the measured mechanical losses.

To test this, the (100) silicon cylinder was suspended at an arbitrary starting position, which was indicated by applying a small pen mark to the side of the sample. The mechanical losses for a resonant mode which should change with rotation, clover 4 (n=2, 16) [133], and the fundamental longitudinal mode (n=0, 2) [133] which should not change were measured. This was recorded and the mass was rotated every 30 degrees and re-tested until a complete rotation had been measured.

From figure 6.15 it is clear that there is a small degree of variation of the mechanical loss for the fundamental longitudinal resonant mode, pictured on the bottom left. This variation can be attributed to the rotation process of the test sample, which was done by hand, and could have resulted in the cylinder not sitting exactly as it was in the suspension loop. There also is a significant variation of the mechanical loss when the clover 4 mode, pictured on the top left, was rotated. This agrees with

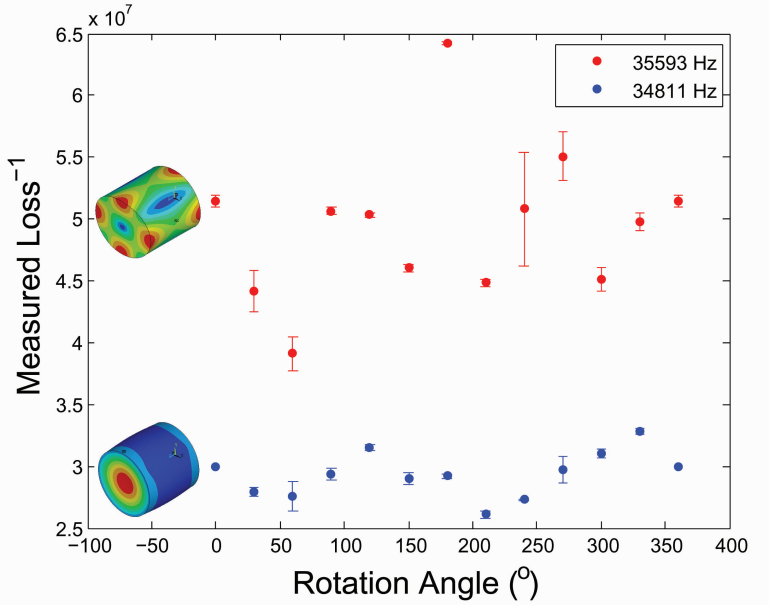

Figure 6.15: Variation of 1/Mechanical loss with rotation of a (100) silicon cylinder in its suspension, for fundamental longitudinal and clover 4 mode shapes.

the suggestion that, for anisotropic materials, the orientation in which test masses are hung is important.

There appears to be a pattern in the mechanical losses of the clover 4 mode, because the measured loss seems to peak every 90° with a minimum mechanical loss measured of $(1.56 \pm 0.01) \times 10^{-8}$ at 180°. This appears to correlate with the clover 4 mode shape which has four fold symmetry around its axis. However, it is unclear why the peaks are not all of similar level of mechanical loss.

Since the start point was chosen arbitrarily, further work needs to be undertaken to establish whether the improvements in mechanical loss coincide with the areas of least motion around the middle of the mass lining up with the points where the suspension breaks off from the mass or with the suspension loop itself.

6.9 Conclusions

The mechanical losses presented in figures 6.8, 6.11 and 6.12 for the three different aspect ratios of (100) orientated silicon are slightly above the typical loss values measured for high grades of fused silica samples, such as those measured on Heraeus Suprasil-311 in Section 4.4.

The lowest measured mechanical losses on the (111) orientated silicon cylinders and coins, down to 8.51×10^{-9} are comparable with the lowest mechanical losses measured on other materials such as the 4.61×10^{-9} measured on a HEMEX sapphire in section 5.1.

The loss values for the smaller doped (100) samples in section 6.6 and 6.7 are comparable with those of the larger undoped (100) orientated cylinder in section 6.5. This suggests that the crystal orientation is affecting the measured values of mechanical loss, rather than the level or type of doping at the levels of loss measured here, however levels of doping may still be an important factor for the mechanical loss of either orientation of silicon, particularly at low temperature [209]. Doping can also alter the levels of thermoelastic dissipation and the distortion of the mirror under thermal loads by altering the thermal conductivity of silicon [204]. Further investigations should increase the understanding of these parameters and how they would affect the sensitivity of an interferometer comprising of silicon optics.

The results presented in this chapter also suggest that the orientation of silicon, and other anisotropic materials, within the suspension may also affect the measurable mechanical loss of the material. Care must therefore be taken in the positioning of an anisotropic substrate in suspensions because the orientation of the mass may yield a low mechanical loss for some resonant mode shapes and high mechanical losses for others at the same time.

Chapter 7

Silicon as a Mirror Substrate for Third Generation Detectors

7.1 Challenges for Future Gravitational Wave Detectors

As discussed in section 1.5.3, the high frequency sensitivity of interferometric gravitational wave detectors is limited by photoelectron shot noise and section 6.1 details the significant interest in silicon as a future test mass substrate from a thermal loading point of view. In chapter 6 it has been shown that, at room temperature, silicon can have a level of intrinsic dissipation similar to that of sapphire, which also makes it an interesting choice for study as a potential test mass substrate material.

It is predicted that in the frequency band of interest for ground-based gravitational wave detectors using crystalline optics a significant source of thermal noise will be present in the form of thermoelastic noise [70]. Therefore, in order to improve the sensitivity of detectors a further reduction in the level of thermal noise from the test masses and their suspensions is necessary. One technique for achieving this is cooling.

Fused silica is not a suitable candidate material for cooling as it exhibits a broad dissipation peak at $\sim$ 40 K [125]. Sapphire and silicon are, however, both good candidate materials to use in a cryogenic gravitational wave detector. Research in Japan is being undertaken on the development of transmissive Fabry-Perot layout interferometers utilising cooled sapphire test masses and suspension fibres [69, 210]. Investigations in the US and Europe are underway on developing the use of silicon at low temperatures [211, 212, 213, 164].

The spectral density for thermoelastic noise resulting from thermodynamical fluctuations of temperature can be expressed as [70]

$$S_{TD}(\omega) \approx \frac{8}{\sqrt{2\pi}}\alpha^2(1+\sigma)^2\frac{a^2\kappa T^2}{\rho C r_0^3 \omega^3}. \tag{7.1}$$

The level of thermoelastic dissipation in silicon, at room temperature, is expected to be broadly comparable to that of sapphire. The thermoelastic loss in silicon has a noteworthy characteristic in that, with cooling, it may reduce significantly at two temperatures thus possibly allowing improved detector sensitivities.

The dissipation resulting from the thermoelastic loss varies with the thermal coefficient of expansion, α, squared. In silicon, this coefficient is particularly interesting as there are two temperatures, $\sim$ 125 K and $\sim$ 18 K, where α is zero [205]. This means that the thermoelastic noise tends to zero at these temperatures. Studies of intrinsic dissipation resulting from defects or dislocations in the crystal structure suggest that there are two peaks in this noise at temperatures similar to where the thermal coefficient of expansion is zero [202].

It is relevant therefore to investigate the temperature dependence of the mechanical loss in silicon samples and their potential use as suspension element and test mass substrates.

7.1.1 Mechanical Loss in Silicon Flexures

Mechanical loss measurements have been made at the University of Glasgow on single crystal cantilevers. They were fabricated from a silicon wafer and cut to be $34 - 57$ mm long and 10 mm. A hydroxide chemical etch was applied to thin them to ~ 92 μm. One end of each of the cantilevers was masked from the etch in order to keep a thick end as a clamping block. The cantilevers were fastened to a stainless steel clamp, illustrated in figure 7.1, which was placed within the experimental chamber of a small cryostat and pumped out to 3×10^{-6} mbar.

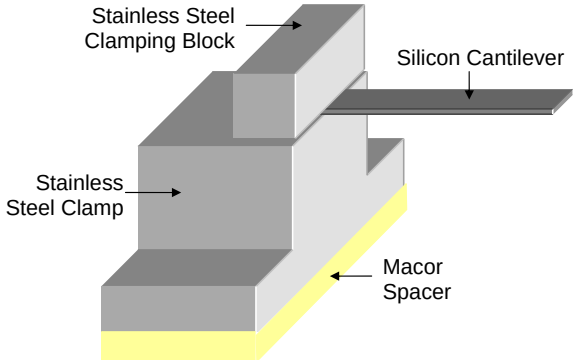

Figure 7.1: Illustration of stainless steel clamp used to hold silicon flexures.

The clamp was placed on a macor spacer to insulate it thermally from the liquid nitrogen cooled bottom plate of the chamber. A temperature control system was set up with a resistive heater and a temperature sensor enabling a steady temperature of the silicon flexure. This allowed several ringdowns to be made of each resonant mode at each temperature, and also a series of measurements to be taken at regular temperature intervals. The mechanical loss of the flexure resonant modes was taken by exciting the sample with an electrostatic actuator and the ringdowns of the resonances recorded using an external photodiode to sense the light from an illuminating laser beam reflected off the surface of the silicon.

Results showed that the mechanical loss decreased with decreasing temperature and that at room temperature the dissipation strongly on the level of thermoelastic dissipation in the sample. At lower temperatures other loss mechanisms became

dominant because the measured mechanical loss was 4.4×10^{-7} which is an order of magnitude higher than the bulk losses presented in Chapter 6. There was however no distinct 125 K peak in dissipation. Other indistinct peaks were observed but they were occurring due possibly to coupling between the sample and the clamping structure. For a diagram of the cryostat used in this experiment and a detailed analysis of the measurements made on these samples see [213] and [164].

7.1.2 Mechanical Loss in Bulk Silicon

Measurements in chapter 6 suggest that the bulk loss of silicon is significantly lower at room temperature than the measured mechanical losses of the cantilevers. D. F. McGuigan et al. made loss measurements over a range of temperatures on a single crystal silicon substrate, 106 mm in diameter, 229 mm in length and orientated in the (111) direction, as described in section 6.2 [202]. They measured a mechanical loss of 5×10^{-8} at $\sim$ 300 K on the fundamental longitudinal resonant mode of this sample which decreased by two orders of magnitude to 5×10^{-10} at 3.5 K. They observed two maxima of mechanical loss at 13 K and 115 K where the loss increased to 1×10^{-7}. This increase was attributed to impurities and mechanical imperfections in the crystal. Recently, R. Nawrodt et al. at the Friedrich-Schiller-Universität in Jena showed that the mechanical loss of a 76 mm diameter by 24 mm thick silicon sample also decreased by almost two orders of magnitude from 5×10^{-6} at $\sim$ 300 K to under 1×10^{-8} at $\sim$ 4.2 K [214].

To extend the University of Glasgow's study at low temperatures to include bulk silicon samples, a stainless steel cryostat with a 30 cm diameter by 40 cm high experimental chamber was constructed by AS Scientific LTD [215], as shown in figure 7.2. This cryostat is in the process of being commissioned at the University of Glasgow.

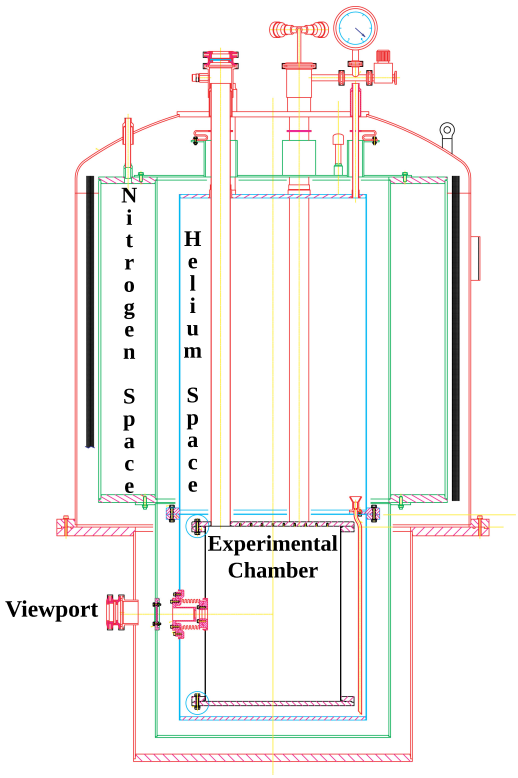

Figure 7.2: Schematic of the Large Cryostat constructed by AS Scientific LTD.

This has been designed specifically so that the test masses can be suspended in the chamber. The bulk samples are suspended from a silk thread loop held by a stainless steel clamp, as shown in figure 7.3. An aluminium catcher is placed underneath the bulk sample to prevent the mass from falling should the suspension loop slip or break during cooling. An interferometer, similar to the one detailed in section 3.4, is used to sense the motion of the sample's front face through a sapphire viewport in the side of the experimental chamber, as shown in figure 7.2.

It is essential to first check that, when the cryostat is cooled with liquid nitrogen, the suspended silicon test substrate is also cooled. With the experimental chamber evacuated to $\sim 10^{-6}$ mbar, the only direct contact the sample has with the surrounding experimental chamber is through the clamped silk thread suspension loop. The stainless steel clamp used to hold the suspension loop is attached directly to the top plate of the experimental chamber enabling it to cool easily to the same temperature as the liquid nitrogen cooled surroundings. Therefore, for the sample

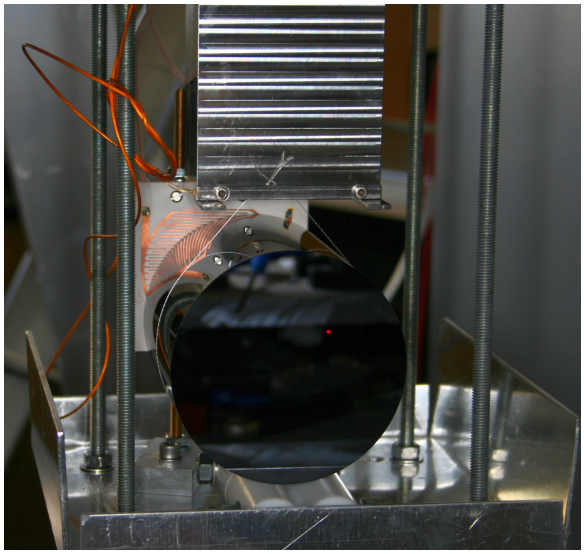

Figure 7.3: Silicon (111) Cylinder suspended in experimental chamber of the Large Cryostat.

to cool, the heat must be lost from the sample to the clamp via the silk thread loop.

A temperature cycle has been made with a temperature sensor attached to the front face of the silicon test mass with a small amount of cryogenic compatible grease. The helium and nitrogen spaces were then filled with a total of 88 litres of liquid nitrogen and the temperature of the silicon test mass recorded over a period of several days. In figure 7.4 it can be seen that after a period of 24 hours the sample had cooled to 80 K. The temperature of this suspended test substrate stayed constant for another 24 hours. It then took another week for the sample to heat back up to room temperature. This would be long enough for a series of cryogenic mechanical loss measurements to be made.

In this study of the temperature dependency of mechanical dissipation in silicon it is essential to have an accurate temperature measurement of the sample. However, a temperature sensor cannot be attached to the test mass during mechanical loss measurements, since the value of the mechanical loss would be increased by the sensor. Furthermore, the temperature of the sample may differ from the temperature measured by a temperature sensor positioned on the clamp or cold plate.

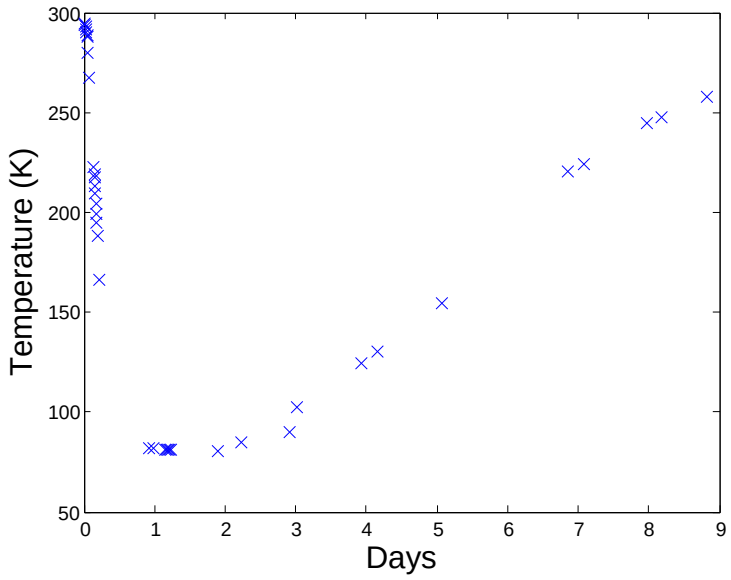

Figure 7.4: Cooling curve of silicon (111) cylinder after the addition of 88 l of liquid nitrogen to the cryostat.

Preliminary measurements of the resonant frequency of the fundamental longitudinal resonant mode indicated that the frequency had shifted from 43195 Hz at 293 K to 43335 Hz at 140 K. Therefore since the resonant frequency of the sample in the cryostat will change with temperature, this characteristic can therefore be utilised as a *thermometer* for the test mass. This enables the temperature to be determined by the shift in the resonant frequency of the fundamental longitudinal resonant mode. By taking another set of readings with a temperature sensor mounted on the sample, the change in resonant frequency can be recorded, introducing a technique of determining the temperature of the suspended silicon substrate with the sensor removed.

The commissioning of the cryostat is ongoing, and once this *thermometer* is calibrated mechanical loss measurements of the silicon substrates presented in Chapter 6 will be undertaken.

7.2 Conclusions

Studies show that the measured mechanical loss of both silicon flexures and bulk samples of single crystal silicon decreases generally as the samples are cooled to cryogenic temperatures. The mechanical loss can increase by several orders of magnitude at some temperatures, partly attributed to impurities and imperfections in the samples, but great care must be taken to ensure that there is no excess loss introduced from the sample coupling with the clamping mechanism.

It is planned that the proposed Einstein Telescope detector, ET, will operate with its test masses at cryogenic temperatures [91]. The study of thermal noise is an important factor in the decision making process for the choice of test mass substrates, coatings and suspension material in advanced cryogenic detectors. Experiments at the University of Glasgow on silicon flexures and bulk single crystal substrates are continuing.

Chapter 8

Conclusions

As the current generation of gravitational wave detectors which are in operation around the world reach their targeted design sensitivities, it enhances the possibility of the first successful detections of gravitational waves emitted from astronomical sources. To increase the use of these detectors for gravitational wave astronomy, research and development is continuing to reduce further the various sources of noise which limit the sensitivities of the current detectors.

The introduction of low-loss fused silica suspension technology from GEO600 to the longer baseline detectors will reduce thermal displacement noise. In addition to this, the implementation of higher laser powers together with the necessary thermal compensation schemes, and other technical advances, will enable the second generation of gravitational wave detectors to be ten times more sensitive. In order to allow large-scale astronomical observations of gravitational waves, further research and development is essential to develop an even more sensitive third generation of detectors.

The study of material and coating losses is providing information for decisions relevant to the upgrades of the mirrored test masses for advanced gravitational wave detectors. Finite element analysis is a useful instrument in the modelling of test mass materials and, together with the experimental measurement of the mechanical

loss, provides valuable information about the performance of coatings.

Experimental measurements on silica samples coated with single layers of tantala and silica are broadly consistent with earlier calculations from multi-layer coatings which suggested that the intrinsic coating loss was dominated by loss associated with the tantala coating. It has been shown that doping the tantala with titania reduces this loss by up to 40%, a result shown by the measurements presented from samples produced by both LMA and CSIRO. Investigations have also shown that other dopants such as Lutetium and different manufacturing processes used to produce the coatings can also reduce the intrinsic loss of multi-layer coatings.

Another factor which can increase the levels of thermal noise in an interferometric gravitational wave detector is the technique used to suspend the test masses. Hydroxide-catalysis bonding is used as a low mechanical loss jointing technique to construct quasi-monolithic fused silica test mass suspensions. Results presented suggest that the bond loss could be as much as four times lower than previous experiments suggested making this method even more attractive for future instruments. Measurements also show that the thickness of these bonds is ~ 65 nm.

Loss measurements made on suprasil-311 fused silica cylinders suggested that the losses of some of the resonant modes were lower than the semi-empirical model developed for the similar suprasil-312 variety. Adjusting the coefficient of the bulk loss term of this model enabled a better fit for different aspect ratios of suprasil-311 fused silica. Results also show that the loss measurement apparatus is capable of obtaining low-loss values with losses of $\phi_{\text{silica}} = 2.4 \times 10^{-8}$, $\phi_{\text{sapphire}} = 4.6 \times 10^{-9}$ and $\phi_{\text{silicon}} = 8.5 \times 10^{-9}$ reached. Analysis shows that care has to be taken to ensure that these measurements are not limited by other sources of loss such as suspension losses, especially in anisotropic materials like sapphire and silicon. The lowest mechanical loss recorded on a coin shaped sapphire substrate measured using a nodal support is comparable to the lowest mechanical losses measured using a suspension loop.

The importance of the magnitude of losses associated with any suspension technique, for materials such as sapphire, is evident in the analysis of coated sapphire substrates, while there is an indication that doping the tantala layers of a tantala/silica coating with $\sim 50\%$ titania may reduce the residual coating losses. The influence of suspension losses on the results is an area that requires further study.

Furthermore, the research presented here highlights the benefit of switching to an all-reflective optical layout for third generation interferometric gravitational wave detectors using silicon optics. Silicon's low mechanical loss make it a suitable material for use in future detectors. Mechanical loss measurements on (111) orientated silicon cylinders are comparable to the lowest mechanical losses measured on HEMEX sapphire. Research suggests that the crystal orientation rather than the level or type of doping is the definitive factor in establishing the levels of mechanical loss, for the magnitude of loss seen here.

The research presented in this thesis expands on previous work carried out in the field of gravitational waves. It emphasises the great care which is needed in the selection, manufacturing and measurement techniques of test mass materials for use in interferometric gradational wave detectors. A number of materials meet the low mechanical loss specifications for a test mass substrate, but the effect of applying multi-layer dielectric coatings to them must also be taken into account. The effects of the introduction of these coatings is reasonably well understood on silica substrates, but requires further study in the case of sapphire. Research to clarify this will continue at the University of Glasgow in collaboration with other research groups.

A new field of gravitational wave astronomy is opening up with the possibility of the first direct detections of gravitational waves approaching. The development of second and third generation detectors will help with these observations, increasing our knowledge and understanding of the universe.

Appendix A

Process for the polishing of cross-sections

Cross-sections of fused silica, sapphire or silicon samples are polished using a Logitech PM5 Precision Polishing Machine [179], shown in figure A.1. The samples are mounted onto a polishing jig and then polished with increasingly finer grits of polish until a flat, smooth and scratch free surface is achieved. The process takes several hours to complete and comprises several stages detailed in this Appendix.

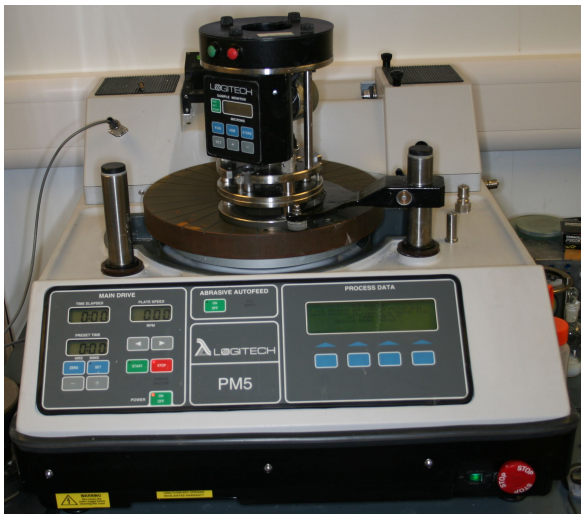

Figure A.1: Image of the Logitech PM5 Precision Polishing Machine.

A.1 Stage 1 - Mounting the Sample

Before polishing it is essential that the sample to be polished is firmly mounted to the polishing jig. This is achieved by bonding the sample to the mount with wax. The wax is placed between the sample and mount and melted by being heated over a hotplate, as shown in figure A.2.

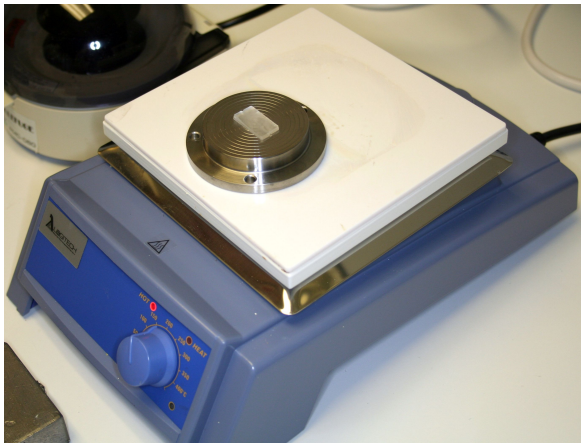

Figure A.2: Fused silica cross-section and sample mount are heated to 150 °C on hotplate.

The hot sample and mount are then placed on a lead block to cool down. After cooling the wax has set and the sample is held firm, as seen in figure A.3.

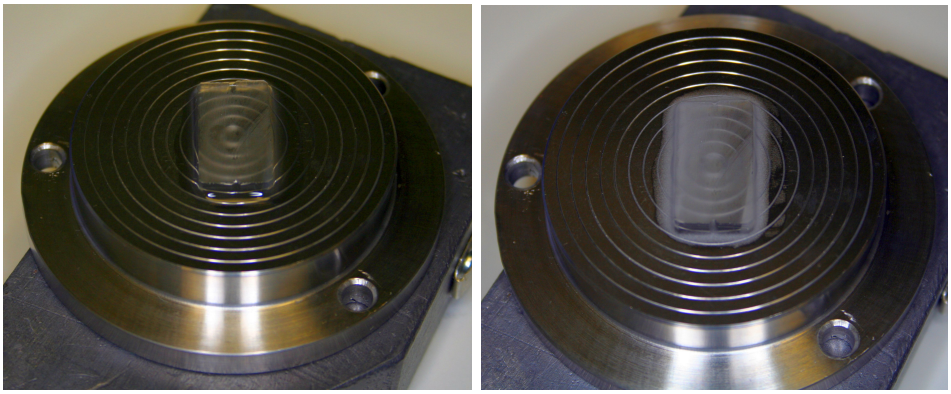

Figure A.3: Hot waxed sample (left) placed on lead block and left to cool until wax has set (right).

The sample and mount can then be attached to the polishing jig, visible in figure A.4.

Figure A.4: Sample jig (left) and an image from above of the mounted sample in the jig (right).

A.2 Stage 2 - Polishing with 600 grit Silicon Carbide Powder

The first polishing stage is to polish the sample with 600 grit silicon carbide powder. The silicon carbide solution is prepared by mixing a spatula of powder into ~ 50 mm of water in a small beaker.

A small volume of polishing liquid is dripped onto the grooved steel polishing plate to make it moist. The polisher is set to operate at 40 rpm and the arm holding the polishing jig set to sweep, as seen in figure A.5. Samples are then polished for ~ 30 min until all scratches from sawing, or any other manufacturing process, have been removed. In order to keep the polishing plate moist during all the different polishing stages more polishing solution will need to be added at regular intervals.

To obtain a smooth finished polish a series of finer polishing stages is needed. Each of these stages requires the use of a smaller grit size. It is essential to have no trace of the grit from the completed stage in the following stage as the polish will not be effective. Therefore, for each stage a different polishing plate is used and the sample jig and all apparatus are thoroughly scrubbed and cleaned to remove any left over

Figure A.5: Grooved steel polishing plate (left) and polisher set-up (right) for Stage 2 of polishing.

grit.

A.3 Stage 3 - Polishing with 9 μm Aluminium Oxide Powder

The second polishing stage is undertaken with 9 μm aluminium oxide powder. One litre of polishing solution is made up with approximately one part in ten of Al_2O_3 powder to water. This solution is then poured into the automatic feeder barrel labelled for 9 μm Al_2O_3 use only. The feed is adjusted so that it drips roughly once a second onto the flat steel plate used in this polishing stage, shown in figure A.6.

The sample is polished for $\sim$ 1 hour until the sample is less opaque.

A.4 Stage 4 - Polishing with 3 μm Aluminium Oxide Powder

The next stage of polishing uses 3 μm aluminium oxide powder. This polishing solution is made up in the same way as detailed in stage 3. The sample is then

Figure A.6: Flat steel polishing plate (left) and polisher set-up (right) for Stage 3 of polishing.

polished for $\sim$ 2 hours on a honeycomb patterned polytron plate, shown in figure A.7 until it starts to become shiny.

Figure A.7: Polytron polishing plate (left) and polisher set-up (right) for Stage 4 of polishing.

A.5 Stage 5 - Final Polish with Syton

To obtain a smooth, flat and shiny finish the sample is polished using a chemical polish *Syton*. A small quantity of Syton is manually dripped onto a porous expanded polyurethane plate, shown in figure A.8 and the sample is polished for $40-60$ mins until any remaining opacity is removed. Regular drips of polishing solution are needed to keep the plate moist.

Figure A.8: Expanded polyurethane polishing plate (left) and polisher set-up (right) for Stage 5 of polishing.

Once this stage is complete it is essential that everything is thoroughly cleaned as the Syton crystallizes when it dries out. To prevent the polishing plate being damaged by this crystallisation it needs to be rinsed under a tap for 30 mins to ensure all the Syton is washed away.

A.6 Stage 6 - Removing Sample from the Polishing Mount

When the sample is suitably polished it is necessary to detach it from the polishing mount. The mount is heated up on the hot plate until the wax softens enough for the sample to be carefully removed. Once the sample has cooled, the sample needs to be cleaned with acetone to remove any traces of wax.

A.7 Stage 7 - Cleaning Sample and Polisher Post-Polishing

It is important that all traces of polishing compounds are removed from the newly polished sample, so that they do not interfere with any bonding processes or high-

magnification imaging which may be made of the sample. The sample is thoroughly rinsed, cleaned with sodium bicarbonate and placed in an ultrasonic bath for $\sim$ 15 mins.

It is important that all apparatus is cleaned after use and carefully stored to prevent damage to the polishing plates.

Appendix B

Finite Element Analysis of the strain energy stored in hydroxide-catalysis bonded fused silica samples using beam elements

Summary

- Tutorial presents a technique of modelling the strain energy stored in a hydroxide-catalysis bond between two fused silica cylinders using beam elements
- Typically bond is ~65 nm thick, which is difficult to be modelled accurately in ANSYS®
- The ratio of strain energy in the bond region can be extracted for each resonant mode by running a series of models with 1×10^{-4} to 1×10^{-7} m and plotting the energy ratios against bond thickness for each resonant mode
- NOTE: This tutorial is designed for a person with some general knowledge of ANSYS®

Case Study

- 2 Fused Silica Cylinders
  - First 65 mm diameter by 70 mm long
  - Second 65 mm diameter by 50 mm long
- Material Properties
  - Young's Modulus: 72 GPa
  - Density: 2202 kg/m^3
  - Poisson's Ratio: 0.17
- Hydroxide-Catalysis Bond between two faces
  - ~65 nm thick bond
  - Covering entire 32.2 cm^2 area of face
- Material Properties
  - Young's Modulus: 7.9 GPa
  - Density: 2202 kg/m^3
  - Poisson's Ratio: 0.17

Case Study

- Use Finite Element to:
- Model 1×10^{-4} m thick Hydroxide-Catalysis bond between the two cylinders
- Apply the properties of the bond
- Find the resonant frequencies of the cylinder
- Plot the mode shapes of these resonances
- Extract the ratio of strain energy stored in the bond region to the total energy in the entire bonded mass

Creating the Model

- Create 4 Keypoints
  - At points:
  - (0, 0)
  - (0, 0.070)
    - 70 mm mass
  - (0, 0.0701)
    - 1×10^{-4} m bond region
  - (0, 0.1201)
    - 50 mm mass
  - ANSYS Main Menu
    > Preprocessor
    > Modelling
    > Create
    > Keypoints
    > On Working Plane
- Create 3 Lines
  - ANSYS Main Menu
    > Preprocessor
    > Modelling
    > Create
    > Lines
    > Straight Lines
  - NOTE: Pick keypoint 1 and then keypoint 2 to create the first line
  - Repeat for 2, 3 and 3, 4

Define Material Properties

- Silica
  - ANSYS Main Menu
    > Preprocessor
    > Material Models
    > Material Model Number 1
    > Structural
    > Linear
    > Elastic
    > Isotropic
      - EX: 7.2E10
      - PRXY: 0.17
    > OK
    > Structural
    > Density
      - Density: 2202
    > OK
- Hydroxide-Catalysis Bond
  - ANSYS Main Menu
    > Preprocessor
    > Material Models
    > Material
    > New Model…
    > Material Model Number 2
    > Structural
    > Linear
    > Elastic
    > Isotropic
      - EX: 7.9E9
      - PRXY: 0.17
    > OK
    > Structural
    > Density
      - Density: 2202
    > OK

Creating the Model

- Define Element Type
  - ANSYS Main Menu
    > Preprosessor
    > Element Type
    > Add/Edit/Delete
    > Add
    > Beam 3node 189
    > OK

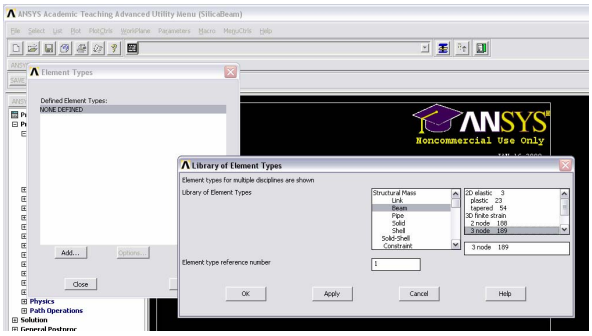

Defining the Three Beam Sections

- ANSYS Main Menu
  > Preprocessor
  > Sections
  > Beam
  > Common Sections
  - ID: 1
  - Name: Cylinder
  - Sub-Type: Circle
  - R: 0.0325 m
  - N: 100

  > OK

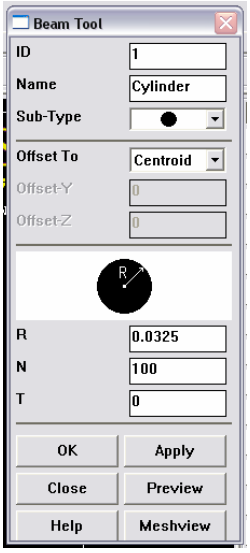

Meshing the Model

- ANSYS Main Menu
  > Preprocessor
  > Meshing
  > MeshTool
  Element Attributes
  > Lines
  > Set
  Pick Line 1
  - > Apply
    MAT: 1
    > Apply

  Pick Line 2 (may need to zoom in)
  - > Apply
    MAT: 2
    > Apply

  Pick Line 3
  - > Apply
    MAT: 1
    > OK

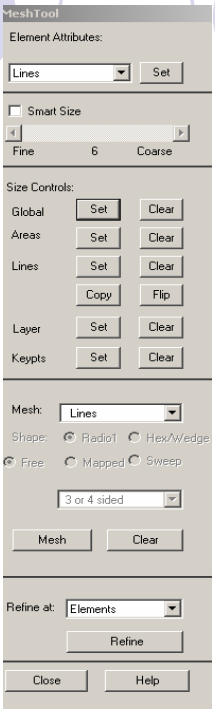

Meshing the Model

- ANSYS Main Menu
  > Preprocessor
  > Meshing
  > MeshTool
  Size Controls
  > Global
  > Set
  NDIV : 10
  - NOTE: NDIV sets the number of divisions per segment. The Beam is divided into 3 line segments so 30 elements will be produced
  > OK

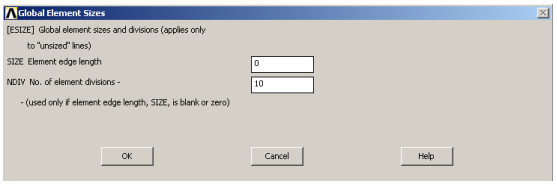

- MeshTool
  > Mesh
  > Pick All
  - - NOTE: If the structure does not show the next command is needed
- ANSYS Command Prompt
  /ESHAPE, 1 [Enter]
  EPLOT [Enter]

Running a Modal Analysis

- Set type of analysis to modal
  - ANSYS Main Menu
    > Solution
    > Analysis Type
    > New Analysis
    > Type of Analysis
    - Modal
    > OK

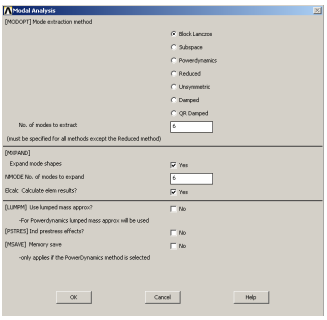

- Set analysis options
  - ANSYS Main Menu
  - > Solution
  - > Analysis Type
  - > Analysis Options
  - > No. of modes to extract
    - 25
    - NOTE: This depends on how many modes you wish to find
  - > Expand mode shapes
    - Yes
  - > No. of modes to expand
    - 25
  - > Calulate elem results?
    - Yes
  - > OK

Running a Modal Analysis

- Specify range of frequencies to be analysed
  - Start Frequency
    1000 Hz
    NOTE: This is to eliminate displacement modes
  - End Frequency
    100000 Hz
    NOTE: This is the upper limit of experimental measurements
- Save the Database
  - SAVE_DB
- Run the Analysis
  - ANSYS Main Menu
    > Solution
    > Solve
    > Current LS
    > OK
  - Warning Message
    > OK

Calculating Total Strain Energy

- Create Strain Energy Table
  - ANSYS Main Menu
    > General Postproc
    > Element Table
    > Define Table
    > Add
    - Energy
    - Strain Energy SENE

    > OK
- List Strain Energy Element Table
  - ANSYS Main Menu
    > General Postproc
    > Element Table
    > List Elem Table
    - SENE

    > OK

Calculating Total Strain Energy

- Sum total strain energy by adding individual strain energies from table
  - ANSYS Main Menu
    > General Postproc
    > Element Table
    > Sum of Each Item
    > OK
- Note total strain energy in Excel or MATLAB
- For the remaining resonant modes
  - Select Results by Pick
  - Plot Nodal Solution
  - Define Element Table
    - Update
      - NOTE: For each picked set of results the element table must be updated.
  - List Element Table
  - Sum of Each Item
  - Take note of each total strain energy

Calculating Strain Energy in Bond

- Select only volumes that lie in the bond region
  - Select
    > Entities
    > Volumes
    > By Attributes
    > Material num
    - 2
    > Apply
    > Plot
- Select only elements that lie in the bond region
  - Select
    > Entities
    > Elements
    > Attached to
    > Volumes
    > From Full
    > Apply
    > Plot
    > OK

Calculating Stain Energy in Bond

- Select Results by Pick
- Define Element Table
  - Update
  - NOTE: For each picked set of results the element table must be updated
- List Element Table
- Sum of Each Item
- Take note of each total strain energy
- The Ratio of strain energy stored in the bond region to the total strain energy in the sample can be calculated

Appendix C

Finite Element Analysis of the strain energy stored in hydroxide-catalysis bonded fused silica samples using solid elements

Summary

- Tutorial presents one way to model the strain energy stored in a hydroxide-catalysis bond between two fused silica cylinders
- Typically bond is ~65 nm thick, which is too thin to be modelled in Finite Element Analysis
- Instead, we can extract the energy ratio by running a series of models with 0.2 – 0.5 mm thick bonds and plot the energy ratios against bond thickness for each resonant mode

Case Study

- 2 Fused Silica Cylinders
  - First 65 mm diameter by 70 mm long
  - Second 65 mm diameter by 50 mm long
- Material Properties
  - Young's Modulus: 72 GPa
  - Density: 2202 kg/m^3
  - Poisson's Ratio: 0.17

- Hydroxide-Catalysis Bond between two faces
  - ~65 nm thick bond
  - Covering entire 32.2 cm^2 area of face
- Material Properties
  - Young's Modulus: 7.9 GPa
  - Density: 2202 kg/m^3
  - Poisson's Ratio: 0.17

Case Study

- Use Finite Element to:
  - Model 0.005 m thick Hydroxide-Catalysis bond between the two cylinders
  - Apply the properties of the bond
  - Find the resonant frequencies of the cylinder
  - Plot the mode shapes of these resonances
  - Extract the ratio of strain energy stored in the bond region to the total energy in the entire bonded mass

Creating the Model

- Open ANSYS
- Create New Jobname
  - i.e. Bond0005mm
- Select Structural GUI
  - ANSYS Main Menu
    > Preferences
    > Structural
    > OK

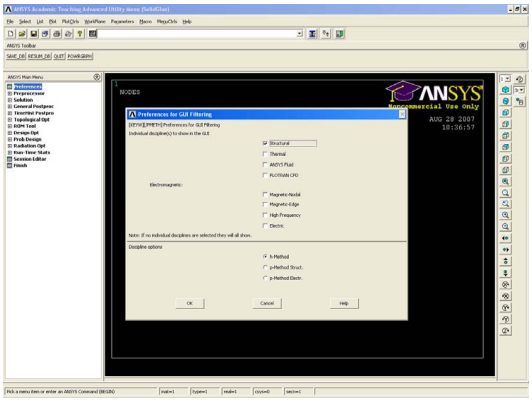

Creating the Model

- Define Element Type
  - ANSYS Main Menu
    > Preprosessor
    > Element Type
    > Add/Edit/Delete
    > Add
    > Solid Brick 20node 95
    > OK

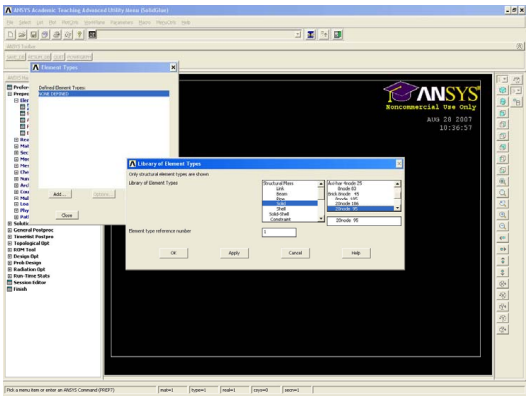

Creating the Model

- Create First Cylinder
  - 65 mm diameter
  - 70 mm long
  - ANSYS Main Menu
    > Preprocessor
    > Modelling
    > Create
    > Volumes
    > Cylinder
    > Solid Cylinder
      - Radius: 0.065/2
      - Depth: 0.07
        - NOTE: Units are in metres

    > Apply

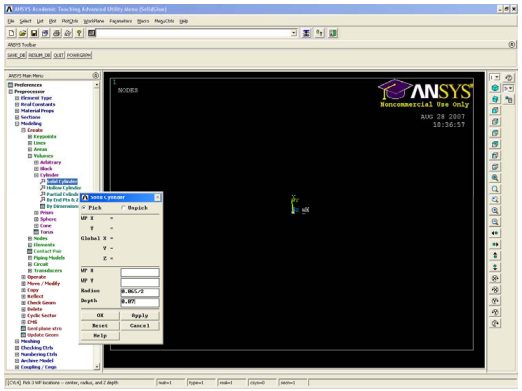

Creating the Model

- Create Bond Region
  - 65 mm diameter
  - 0.5 mm long
  - ANSYS Main Menu
    > Preprocessor
    > Modelling
    > Create
    > Volumes
    > Cylinder
    > Solid Cylinder
    - Radius: 0.065/2
    - Depth: -0.0005
      - NOTE: Negative Depth

    > OK

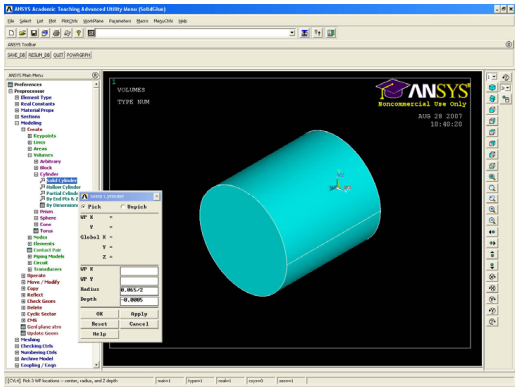

Creating the Model

- Offset workplane by thickness of the bond so that front face of second silica cylinder lines up with bond
  - Workplane
    > Offset WP by increments…
    > Element Type
    > X, Y, Z Offsets: 0, 0, -0.0005
    > OK

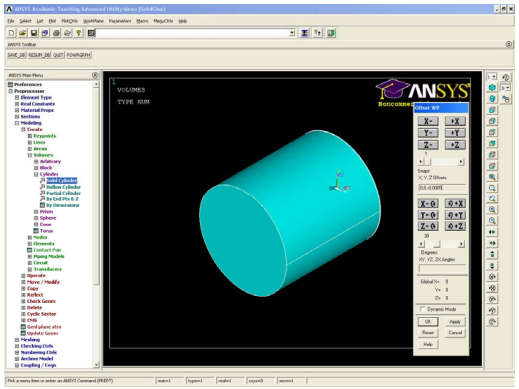

Creating the Model

- Create Second Cylinder
  - 65 mm diameter
  - 50 mm long
  - ANSYS Main Menu
    > Preprocessor
    > Modelling
    > Create
    > Volumes
    > Cylinder
    > Solid Cylinder
      - Radius: 0.065/2
      - Depth: -0.05
        - NOTE: Still Negative

    > OK

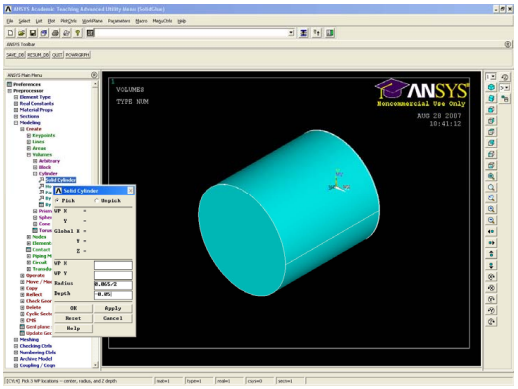

Creating the Model

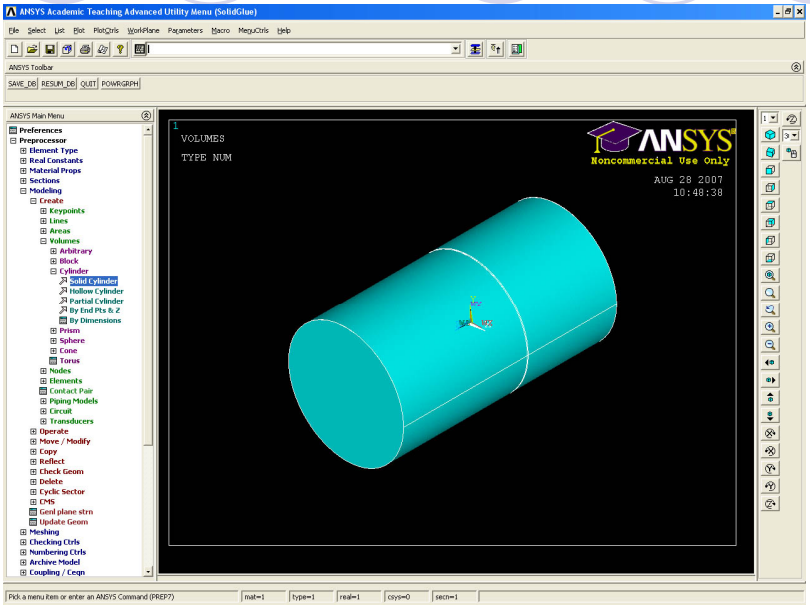

Creating the Model

- So far the three cylinders are in contact, but not attached
- Must glue the surfaces together
- Select Right View and Zoom in on bond region

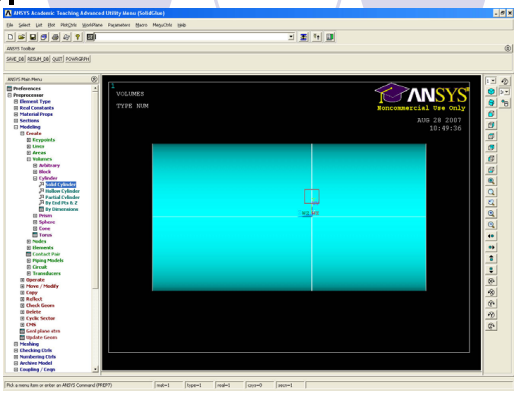

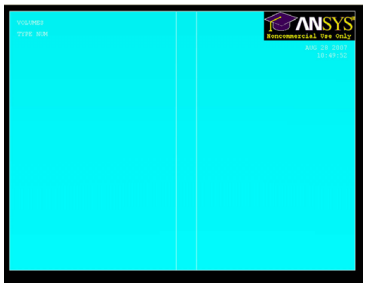

Creating the Model

- Glue First Cylinder to Bond
  - ANSYS Main Menu
    > Preprocessor
    > Modelling
    > Operate
    > Booleans
    > Glue
    > Volumes
    - Select First Cylinder
    - Select Bond Region

    > APPLY

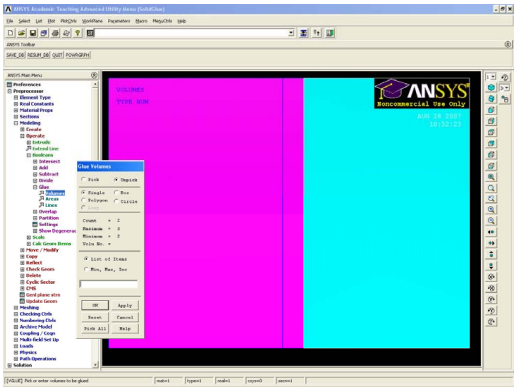

Creating the Model

- Glue Second Cylinder to Bond
  - ANSYS Main Menu
    > Preprocessor
    > Modelling
    > Operate
    > Booleans
    > Glue
    > Volumes
    - Select Second Cylinder
    - Select Bond Region

    > OK

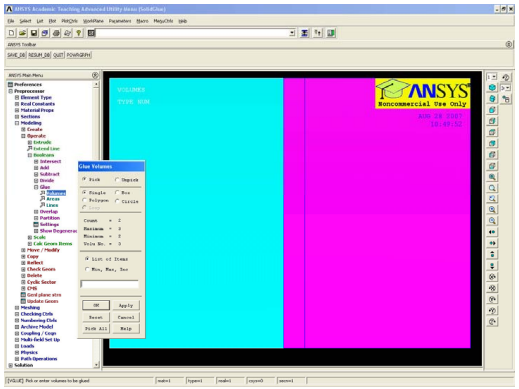

Define Material Properties

- Properties detailed in Case Study Slide
- Silica
  - ANSYS Main Menu
    > Preprocessor
    > Material Models
    > Material Model Number 1
    > Structural
    > Linear
    > Elastic
    > Isotropic
    - EX: 7.2E10
    - PRXY: 0.17

    > OK
    > Structural
    > Density
    - Density: 2202

    > OK

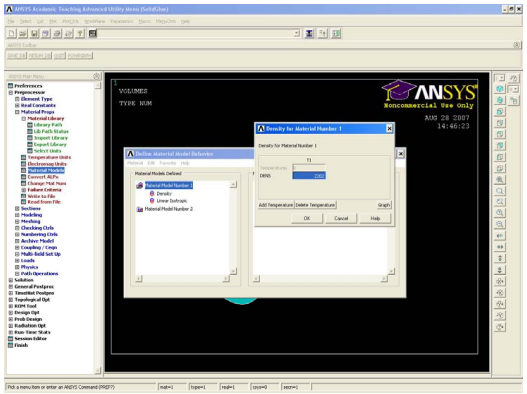

Define Material Properties

- Hydroxide-Catalysis Bond
  - ANSYS Main Menu
    > Preprocessor
    > Material Models
    > Material
    > New Model…
    > Material Model Number 2
    > Structural
    > Linear
    > Elastic
    > Isotropic
      - EX: 7.9E9
      - PRXY: 0.17

    > OK
    > Structural
    > Density
      - Density: 2202

    > OK

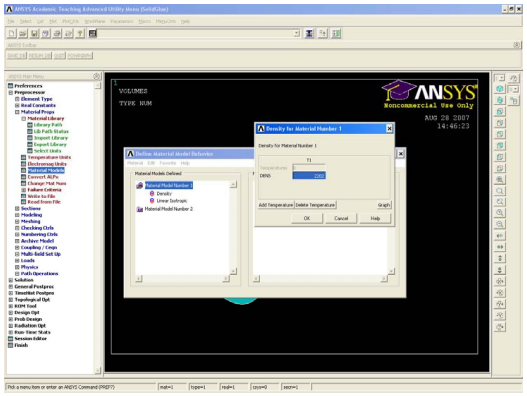

Meshing the Model

- Define Hydroxide-Catalysis Bond Mesh
  - ANSYS Main Menu
    > Preprocessor
    > Meshing
    > Mesh Tool
    > Element Attributes:
    > Global
    > Set
    > Material Number
      - MAT: 2

    > OK

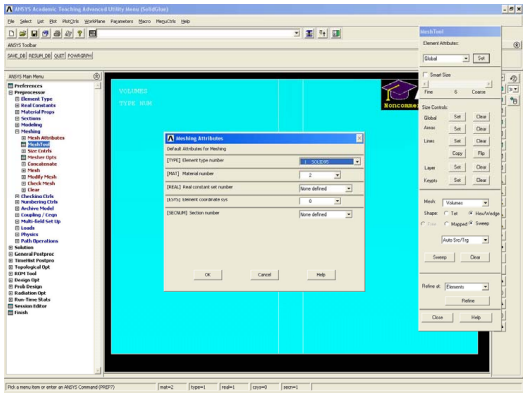

Meshing the Model

- Set element length to be ten times the modelled bond thickness
  - NOTE: Too small an element length will create mesh with more nodes than the licence permits
  - ANSYS Main Menu
    > Preprocessor
    > Meshing
    > Mesh Tool
    > Size Controls:
    > Global
    > Set
    > Element Length
    - SIZE: 0.005

    > OK

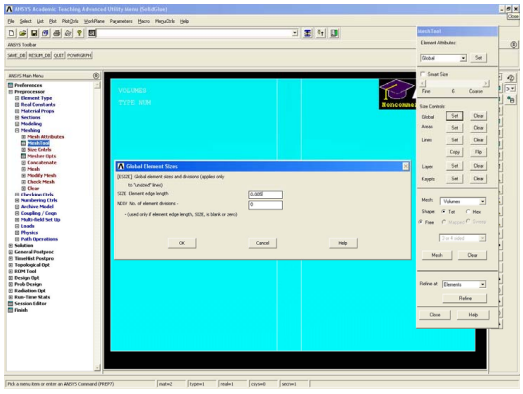

Meshing the Model

- Mesh the Bond
  - ANSYS Main Menu
    > Preprocessor
    > Meshing
    > Mesh Tool
    > Mesh:
    - Volumes

    > Shape:
    - Hex/Wedge
    - Sweep

    > Select Bond Region
    > OK

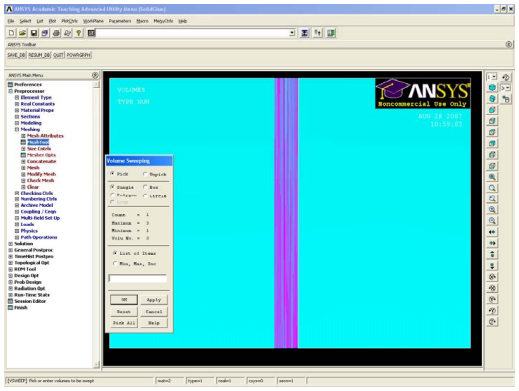

Meshing the Model

- Define Silica Cylinder Mesh
  - ANSYS Main Menu
    > Preprocessor
    > Meshing
    > Mesh Tool
    > Element Attributes:
    > Global
    > Set
    > Material Number
      - MAT: 1

    > OK

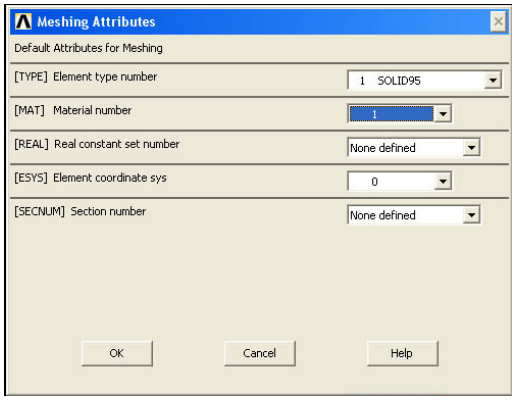

Meshing the Model

- Remove the set element length
  - NOTE: The mesh will automatically map to match the mesh on the faces of the bond
  - ANSYS Main Menu
    > Preprocessor
    > Meshing
    > Mesh Tool
    > Size Controls:
    > Global
    > Set
    > Element Length
      - SIZE: 0

    > OK

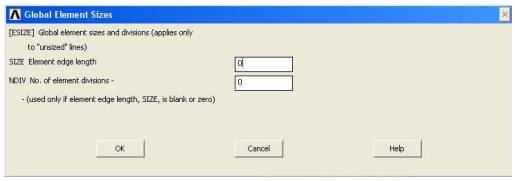

Meshing the Model

- Mesh the Cylinders
  - ANSYS Main Menu
    > Preprocessor
    > Meshing
    > Mesh Tool
    > Mesh:
    - Volumes
    > Shape:
    - Hex/Wedge
    - Sweep
    > Select Both Cylinders
    > OK

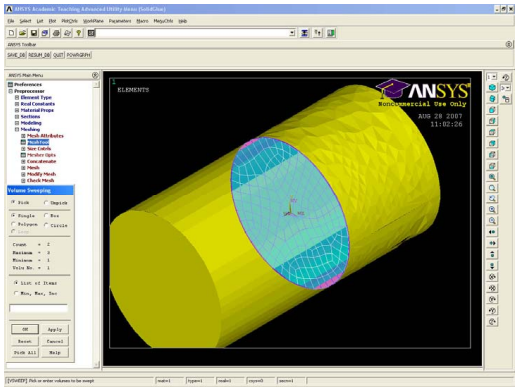

Meshing the Model

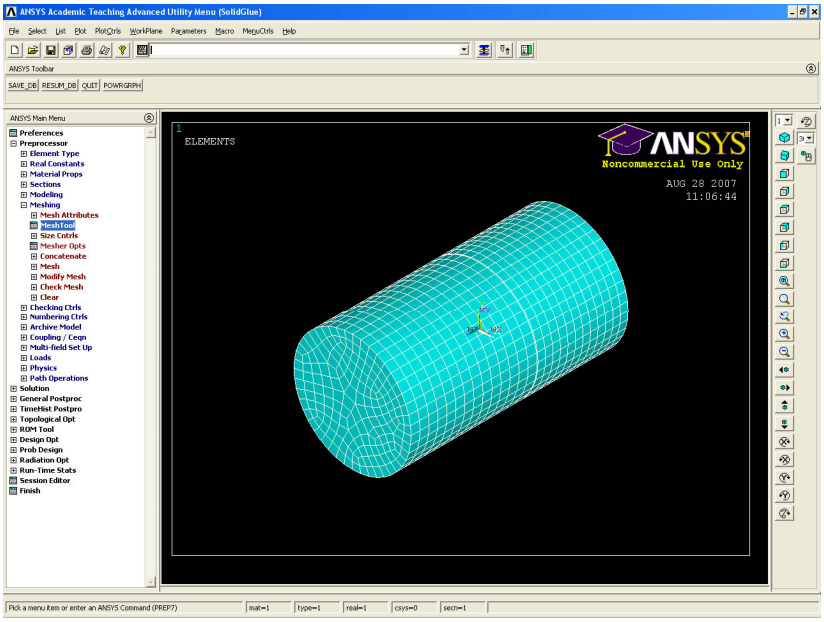

Running a Modal Analysis

- Set type of analysis to modal
  - ANSYS Main Menu
    > Solution
    > Analysis Type
    > New Analysis
    > Type of Analysis
    - Modal

    > OK

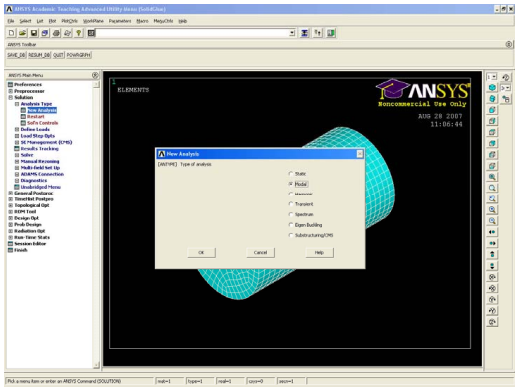

Running a Modal Analysis

- Set analysis options
  - ANSYS Main Menu
    > Solution
    > Analysis Type
    > Analysis Options
    > No. of modes to extract
    - 25
      - NOTE: This depends on how many modes you wish to find

    > Expand mode shapes
    - Yes

    > No. of modes to expand
    - 25

    > Calulate elem results?
    - Yes

    > OK

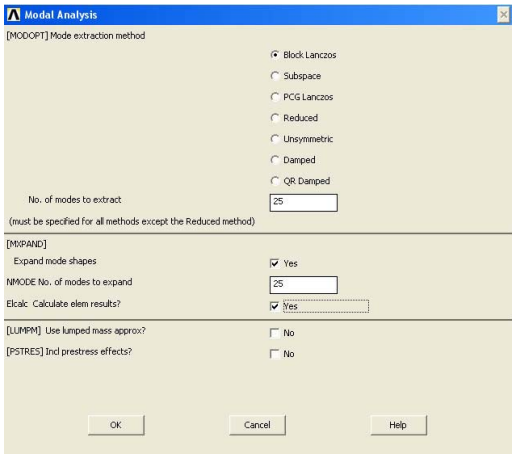

Running a Modal Analysis

- Specify range of frequencies to be analysed
  - Start Frequency
    - 1000 Hz
      - NOTE: This is to eliminate displacement modes
  - End Frequency
    - 100000 Hz
      - NOTE: This is the upper limit of experimental measurements

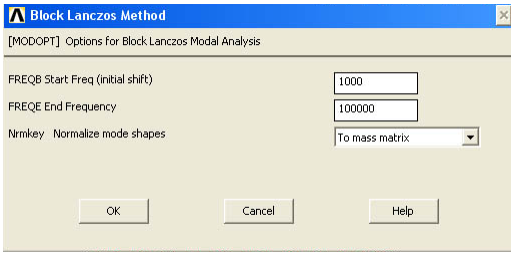

Running a Modal Analysis

- Save the Database
  - SAVE_DB
- Run the Analysis
  - ANSYS Main Menu
    > Solution
    > Solve
    > Current LS
    > OK
  - Warning Message
    > OK

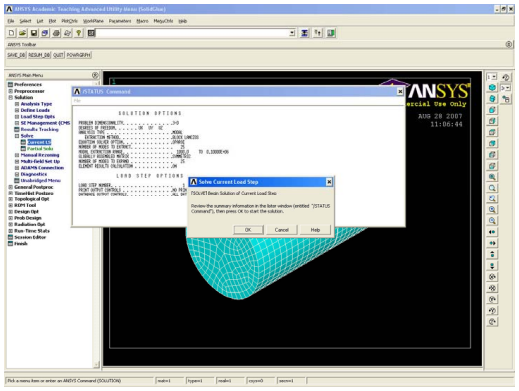

Have a Cup of Coffee

Listing Resonant Mode Frequencies

- To generate a list of resonant mode frequencies
  - ANSYS Main Menu > General Postproc > Results Summary

SET,LIST Command

File

***** INDEX OF DATA SETS ON RESULTS FILE *****

SET	TIME/FREQ	LOAD STEP	SUBSTEP	CUMULATIVE
1	14740.	1	1	1
2	14740.	1	2	2
3	15037.	1	3	3
4	22917.	1	4	4
5	26520.	1	5	5
6	26520.	1	6	6
7	30769.	1	7	7
8	38372.	1	8	8
9	38372.	1	9	9
10	38954.	1	10	10
11	38954.	1	11	11
12	39483.	1	12	12
13	39483.	1	13	13
14	40027.	1	14	14
15	40027.	1	15	15
16	42807.	1	16	16
17	42807.	1	17	17
18	44658.	1	18	18
19	44658.	1	19	19
20	44693.	1	20	20
21	45745.	1	21	21
22	48731.	1	22	22
23	48741.	1	23	23
24	48741.	1	24	24
25	49572.	1	25	25

Picking Resonant Mode Frequencies

- The element results for each individual resonant mode can be selected
  - ANSYS Main Menu
    > General Postproc
    > Read Results
    > By Pick
  - Select result you wish to load
    > Read
    > Close

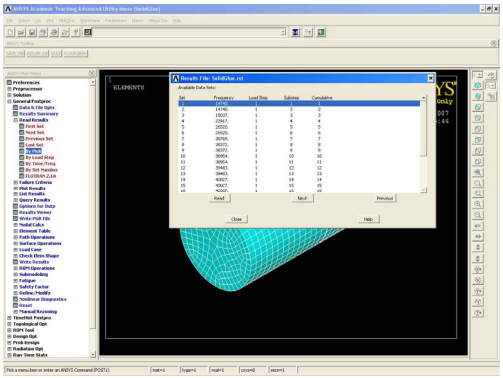

Plotting Resonant Mode Shapes

- Each resonant mode picked can be plotted
  - ANSYS Main Menu
    > General Postproc
    > Plot Results
    > Contour Plot
    > Nodal Solu
    - Nodal Solution
    - DOF Solution
    - Displacement vector sum

    > OK

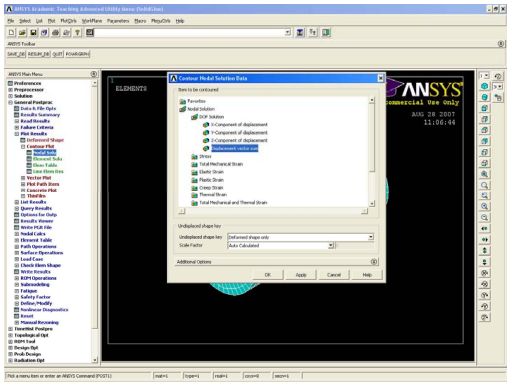

Plotting Resonant Mode Shapes

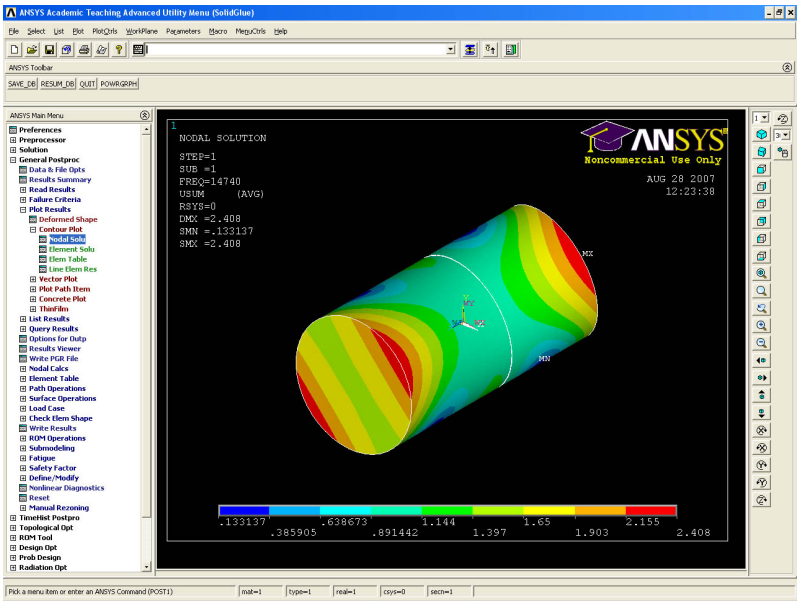

Calculating Total Strain Energy

- Create Strain Energy Table
  - ANSYS Main Menu
    > General Postproc
    > Element Table
    > Define Table
    > Add
    - Energy
    - Strain Energy SENE

    > OK

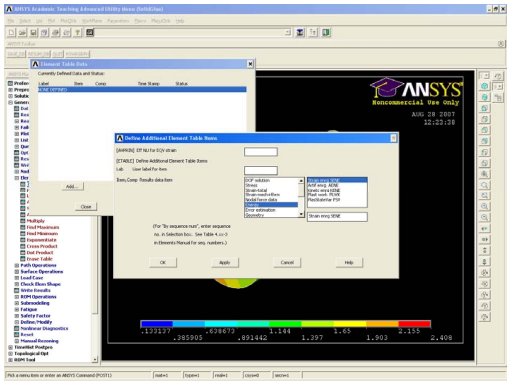

Calculating Total Strain Energy

- List Strain Energy Element Table
  - ANSYS Main Menu
    > General Postproc
    > Element Table
    > List Elem Table
    - SENE

    > OK

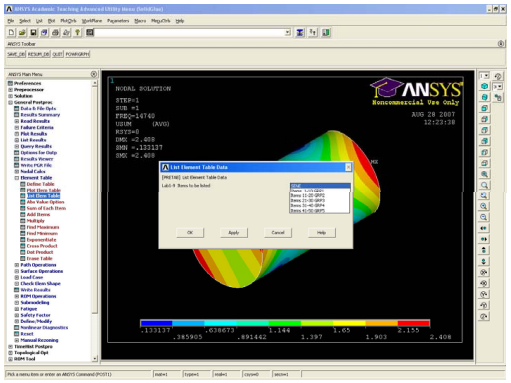

Calculating Total Strain Energy

- Sum total strain energy by adding individual strain energies from table
  - ANSYS Main Menu
    > General Postproc
    > Element Table
    > Sum of Each Item
    > OK
- Note total strain energy in Excel or MATLAB

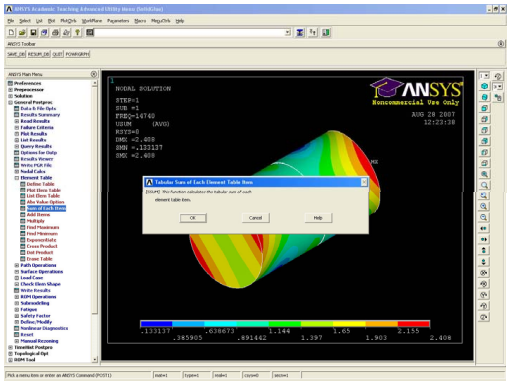

Calculating Total Strain Energy

- For the remaining resonant modes
  - Select Results by Pick
  - Plot Nodal Solution
  - Define Element Table
    - Update
      - NOTE: For each picked set of results the element table must be updated.
  - List Element Table
  - Sum of Each Item
  - Take note of each total strain energy

Calculating Strain Energy in Bond

- Select only elements that lie in the bond region
  - Select
    > Entities
    > Volumes
    > By Attributes
    > Material num
    - 2
    > Apply
    > Plot

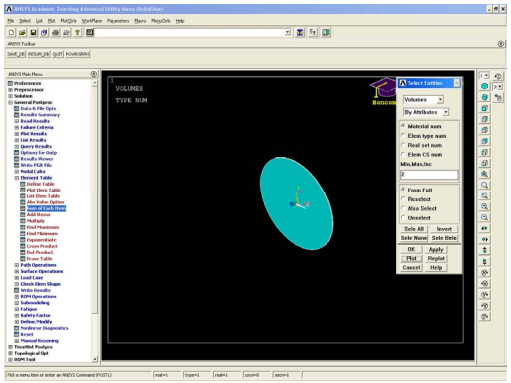

Calculating Strain Energy in Bond

- Select only elements that lie in the bond region
  - Select
    > Entities
    > Elements
    > Attached to
    > Volumes
    > From Full
    > Apply
    > Plot
    > OK

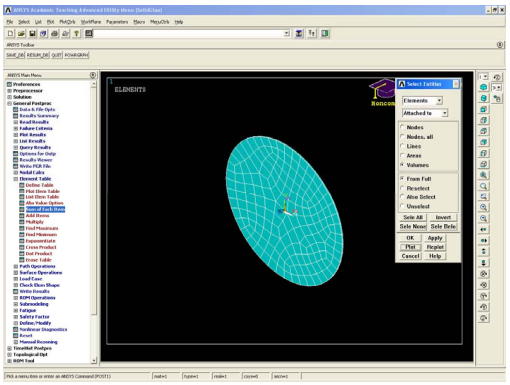

Calculating Strain Energy in Bond

- Select Results by Pick
- Define Element Table
  - Update
    - NOTE: For each picked set of results the element table must be updated.
- List Element Table
- Sum of Each Item
- Take note of each total strain energy

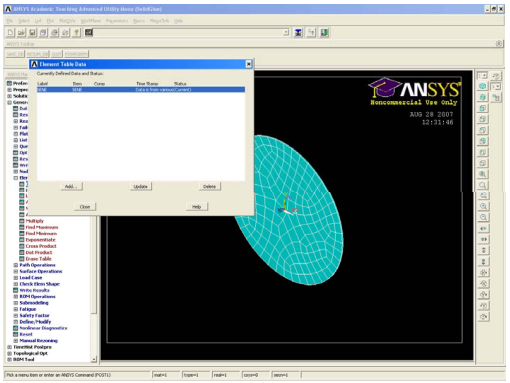

Calculating Energy Ratios

- The Ratio of strain energy stored in the bond region to the total strain energy in the sample can be calculated by: $\frac{\text{Strain Energy}_{\text{bond}}}{\text{Strain Energy}_{\text{total}}}$
- For this model the first five energy ratios should be:

	Frequency	Total Strain	Bond Strain	Ratio
1	14740	4.29E+09	2.64E+08	6.16E-02
2	14740	4.29E+09	2.64E+08	6.16E-02
3	15037	4.46E+09	3.07E+08	6.88E-02
4	22917	1.04E+10	6.49E+08	6.26E-02
5	26520	1.39E+10	9.84E+08	7.08E-02

Calculating Energy Ratio

- Repeat Model for different bond thicknesses
  - 0.00045 m
  - 0.00040 m
  - 0.00035 m
  - 0.00030 m
  - 0.00025 m
  - 0.00020 m
- Plot Energy Ratio v Thickness for each mode
- Calculate Energy Ratio for 65 nm

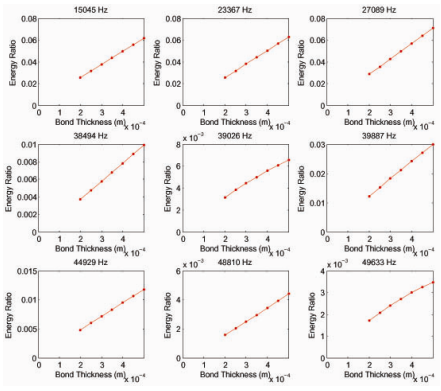

Bibliography

[1] D. C. Harris, F. Schmid, D. R. Black, E. Savrun, and H. E. Bates. Factors that influence mechanical failure of sapphire at high temperatures. In R. W. Tustison, editor, *Proc. SPIE Vol. 3060, p. 226-235, Window and Dome Technologies and Materials V, Randal W. Tustison; Ed.*, volume 3060 of *Presented at the Society of Photo-Optical Instrumentation Engineers (SPIE) Conference*, pages 226–235, 1997.

[2] V. B. Braginsky and S. P. Vyatchanin. Thermodynamical fluctuations in optical mirror coatings. *Physics Letters A*, 312:244–255, 2003.

[3] Shanti R. Rao. *Mirror Thermal Noise in Interferometric Gravitational Wave Detectors*. PhD thesis, California Institute of Technology, 2003.

[4] P. H. Sneddon, S. Bull, G. Cagnoli, D. R. M. Crooks, E. J. Elliffe, J. E. Faller, M. M. Fejer, J. Hough, and S. Rowan. The intrinsic mechanical loss factor of hydroxy-catalysis bonds for use in the mirror suspensions of gravitational wave detectors. *Classical and Quantum Gravity*, 20:5025–5037, 2003.

[5] A. Einstein. *Annalen der Physik*, 49:769, 1916.

[6] J. Weber. Detection and generation of gravitational waves. *Phys. Rev.*, 117(1):306–313, 1960.

[7] J. Weber. *General relativity and gravitational waves*. Interscience Tracts on Physics and Astronomy, New York: Interscience, 1961.

[8] R.A. Hulse and J. H. Taylor. Discovery of a pulsar in a binary system. *Astrophys. J.*, 195:51–53, 1975.

[9] J. H. Taylor, R. A. Hulse, L. A. Fowler, G. E. Gullahorn, and J. M. Rankin. Further observations of the binary pulsar PSR 1913+16. *Astrophys. J.*, 206:53–58, 1976.

[10] J. H. Taylor and J. M. Weisberg. A new test of general relativity: Gravitational radiation and the binary pulsar PSR 1913+16. *Astrophys. J.*, 253:908–920, 1982.

[11] J. H. Taylor and J. M. Weisberg. Further experimental test of relativistic gravity using the binary pulsar PSR 1913+16. *Astrophys. J.*, 345:434–450, 1989.

[12] The Nobel Prize in Physics 1993 http://nobelprize.org/nobel_prizes/physics/laureates/1993/.

[13] H. Hertz. *Annalen der Physik*, 33:983–1000, 1887.

[14] J. C. Maxwell. On physical lines of force. *Philosopical Magazine*, XXIII:85–95, 1862.

[15] J. C. Maxwell. A dynamical theory of the electromagnetic field. *Roy. Soc. Proc.*, XIII:531–536, 1864.

[16] P. R. Saulson. *Fundamentals of Interferometric Gravitational Wave Detectors*. World Scientific, 1994.

[17] B. F. Schutz. Determining the Hubble Constant from gravitational wave observations. *Nature*, 323:310 – 311, 1986.

[18] K. Thorne. Science section of LIGO-II proposal http://www.ligo.caltech.edu/docs/p/p000024-00.pdf, 2000.

[19] B. F. Schutz. Gravitational-wave sources. *Classical and Quantum Gravity*, 1996.

[20] E. Muller *et. al.* Toward gravitational wave signals from realistic core collapse supernova models. *The Astrophysical Journal*, 603(1):221–230, 2004.

[21] A. Hewish, S. J. Bell, J. D. H. Pilkington, P. F. Scott, and R. A. Collins. Observation of a rapidly pulsating radio source. *Nature*, 217:709–713, 1968.

[22] E. Flanagan. Astrophysical Sources of Gravitational Radiation and Prospects for Their Detection. In N. Dadhich and J. Narlikar, editors, *Gravitation and Relativity: At the Turn of the Millennium*, page 177, 1998.

[23] B. Abbott *et. al.* Upper limits on gravitational wave emission from 78 radio pulsars. *Phys. Rev. D*, 2007.

[24] J. L. Friedman and B. F. Schutz. Secular instability of rotating Newtonian stars. *Astrophysical Journal,*, 1978.

[25] R. V. Wagoner. Gravitational radiation from accreting neutron stars. *Astrophysical Journal,*, 1984.

[26] B.F. Schutz J. Ehlers H. Welling I.F. Corbett J. Hough, H. Walther and V. Kose *et. al.*. Proposal for a joint German-British interferometric gravitational wave detector. Max-Planck Institut für Quantenoptik Report, 1989.

[27] J. Weber. Gravitational-wave-detector events. *Phys. Rev. Lett.*, 20(23):1307–1308, 1968.

[28] J. Weber. Evidence for discovery of gravitational radiation. *Phys. Rev. Lett.*, 22(24):1320–1324, 1969.

[29] M. Lee, D. Gretz, S. Steppel, and J. Weber. Gravitational-radiation-detector observations in 1973 and 1974. *Phys. Rev. D*, 14(4):893–906, 1976.

[30] D. H. Douglass, R. Q. Gram, J. A. Tyson, and R. W. Lee. Two-detector-coincidence search for bursts of gravitational radiation. *Physical Review Letters*, 1975.

[31] H. Billing, P. Kafka, K. Maischberger, F. Meyer, and W. Winkler. Results of the Munich-Frascati gravitational-wave experiment. *Nuovo Cimento Lettere*, 1975.

[32] R. W. P. Drever, J. Hough, R. Bland, and G. W. Lessnoff. Search for short bursts of gravitational radiation. *Nature*, 1973.

[33] V. B. Braginskii, A. B. Manukin, E. I. Popov, V. N. Rudenko, and A. A. Khorev. Search for Gravitational Radiation of Extraterrestrial Origin. *Soviet Journal of Experimental and Theoretical Physics Letters*, 1972.

[34] H. Hirakawa and K. Narihara. Search for gravitational radiation at 145 HZ. *Physical Review Letters*, 1975.

[35] H. Hirakawa and K. Narihara. Search for Gravitational Radiation at 145 Hz. *Physical Review Letters*, 1975.

[36] J. L. Levine. Early Gravity-Wave Detection Experiments, 1960-1975. *Physics in Perspective*, 6:42–75, 2004.

[37] L. Baggio, M. Bonaldi, M. Cerdonio, L. Conti, V. C. Visconti, P. Falferi, P. L. Fortini, V. Martinucci, R. Mezzena, A. Ortolan, G. A. Prodi, L. Taffarello, G. Vedovato, S. Vitale, and J. P. Zendri. Resonant Detectors for Gravitational Waves. *Advances in Space Research*, 25:1171–1176, 2000.

[38] M. Cerdonio, M. Bonaldi, D. Carlesso, E. Cavallini, S. Caruso, A. Colombo, P. Falferi, G. Fontana, P. L. Fortini, R. Mezzena, A. Ortolan, G. A. Prodi, L. Taffarello, G. Vedovato, S. Vitale, and J. P. Zendri. The ultracryogenic gravitational-wave detector AURIGA . *Classical and Quantum Gravity*, 14:1491–1494, 1997.

[39] A. Vinante and the AURIGA Collaboration. Present performance and future upgrades of the AURIGA capacitive readout. *Classical and Quantum Gravity*, 23:103, 2006.

[40] P. Astone, M. Bassan, P. Bonifazi, P. Carelli, M. G. Castellano, G. Cavallari, E. Coccia, C. Cosmelli, S. D'Antonio, V. Fafone, G. Federici, Y. Minenkov,

G. Modestino, I. Modena, A. Moleti, G. Pizzella, G. V. Pallottino, L. Quintieri, A. Rocchi, F. Ronga, R. Terenzi, G. Torrioli, and M. Visco. The EXPLORER gravitational wave antenna: recent improvements and performances. *Classical and Quantum Gravity*, 2002.

[41] P. Astone, R. Ballantini, D. Babusci, M. Bassan, P. Carelli, G. Cavallari, F. Cavanna, A. Chincarini, E. Coccia, C. Cosmelli, S. D'Antonio, F. Dubath, V. Fafone, S. Foffa, G. Gemme, G. Giordano, M. Maggiore, A. Marini, Y. Minenkov, I. Modena, G. Modestino, A. Moleti, G. P. Murtas, A. Pai, O. Palamara, G. V. Pallottino, R. Parodi, G. Piano Mortari, G. Pizzella, L. Quintieri, A. Rocchi, F. Ronga, R. Sturani, R. Terenzi, G. Torrioli, R. Vaccarone, G. Vandoni, and M. Visco. Status report on the EXPLORER and NAUTILUS detectors and the present science run. *Classical and Quantum Gravity*, 23:57, 2006.

[42] P. Astone, D. Babusci, M. Bassan, P. Bonifazi, E. Coccia, S. D'Antonio, V. Fafone, G. Giordano, A. Marini, Y. Minenkov, I. Modena, G. Modestino, A. Moleti, G. V. Pallottino, G. Pizzella, L. Quintieri, A. Rocchi, F. Ronga, R. Terenzi, and M. Visco. The next science run of the gravitational wave detector NAUTILUS. *Classical and Quantum Gravity*, 19:1911–1917, 2002.

[43] L. Gottardi, A. de Waard, A. Usenko, G. Frossati, M. Podt, J. Flokstra, M. Bassan, V. Fafone, Y. Minenkov, and A. Rocchi. Sensitivity of the spherical gravitational wave detector MiniGRAIL operating at 5 K. *ArXiv e-prints*, 705, 2007.

[44] O. D. Aguiar, L. A. Andrade, J. J. Barroso, F. Bortoli, L. A. Carneiro, P. J. Castro, C. A. Costa, K. M. F. Costa, J. C. N. de Araujo, A. U. de Lucena, W. de Paula, E. C. de Rey Neto, S. T. de Souza, A. C. Fauth, C. Frajuca, G. Frossati, S. R. Furtado, N. S. Magalhães, R. M. Marinho, Jr., J. L. Melo, O. D. Miranda, N. F. Oliveira, Jr., K. L. Ribeiro, C. Stellati, W. F. Velloso, Jr., and J. Weber. The Brazilian gravitational wave detector Mario Schenberg: status report. *Classical and Quantum Gravity*, 23:239, 2006.

[45] M. Bonaldi, M. Cerdonio, L. Conti, P. Falferi, P. Leaci, S. Odorizzi, G. A. Prodi, M. Saraceni, E. Serra, and J. P. Zendri. Principles of wide bandwidth acoustic detectors and the single-mass dual detector. *Phys. Rev. D*, 2006.

[46] M. Bonaldi, M. Cerdonio, L. Conti, G. A. Prodi, L. Taffarello, and J. P. Zendri. Wide bandwidth dual acoustic gravitational wave detectors. *Classical and Quantum Gravity*, 2004.

[47] M. E. Gertenshtein and V. I. Pustovoit. On the detection of low frequency gravitational waves. *Soviet Physical Journal of Experimental and Theoretical Physics*, 16:433435, 1963. English translation.

[48] R. L. Forward. Wideband laser-interferometer gravitational-radiation experiment. *Phys. Rev. D*, 1978.

[49] D. Dewey, P. S. Linsay, J. Livas, R. Weiss, and D. H. Shoemaker. The MIT Prototype Gravitational Wave Detector: A Status Report. In *Bulletin of the American Astronomical Society*, volume 16 of *Bulletin of the American Astronomical Society*, 1984.

[50] R. Weiss. Electromagnetically coupled broadband gravitational antenna http://www.ligo.caltech.edu/docs/p/p720002-01/p720002-01.pdf. Quart. Progress, 1972.

[51] W. Winkler. A Michelson Interferometer Using Delay Lines. In D. G. Blair, editor, *The Detection of Gravitational Waves*, page 269, 1991.

[52] Max-Planck-Institut für Quantenoptik http://www.mpq.mpg.de/mpq.html.

[53] D. Shoemaker, R. Schilling, L. Schnupp, W. Winkler, K. Maischberger, and A. Rüdiger. Noise behavior of the Garching 30-meter prototype gravitational-wave detector. *Phys. Rev. D*, 1988.

[54] R. W. P. Drever. Fabry-Perot Cavity Gravity-Wave Detectors. In D. G. Blair, editor, *The Detection of Gravitational Waves*, page 306, 1991.

[55] B. W. Barr *et. al.* Silica research in Glasgow. *Classical and Quantum Gravity*, 19:1655–1662, 2002.

[56] A. Weinstein. Status and future of the Caltech 40 m lab http://www.ligo.caltech.edu/∼cit40m/docs/40mfuture_070129.pdf, 2007.

[57] W. A. Edelstein, J. Hough, J. R. Pugh, and W. Martin. Limits to the measurement of displacement in an interferometric gravitational radiation detector. *Journal of Physics E Scientific Instruments*, 11:710–712, 1978.

[58] J. Hough and S. Rowan. Laser interferometry for the detection of gravitational waves. *Journal of Optics A: Pure and Applied Optics*, 7:S257–S264, 2005.

[59] J. Hough. Prospects for gravitational wave detection with laser interferometer detectors. In D.G. Blair and M.J. Buckingham, editors, *The Fifth Marcel Grossmann Meeting on recent developments in theoretical and experimental general relativity, gravitation and relativistic field theories, Part A*, pages 265–282, Singapore; River Edge, U.S.A., 1989. World Scientific.

[60] A. Abramovici, W. E. Althouse, R. W. P. Drever, Y. Gursel, S. Kawamura, F. J. Raab, D. Shoemaker, L. Sievers, R. E. Spero, and K. S. Thorne. LIGO - The Laser Interferometer Gravitational-Wave Observatory. *Science*, 256:325–333, 1992.

[61] S. W. Ballmer. *LIGO interferometer operating at design sensitivity with application to gravitational radiometry.* PhD thesis, Massachusetts Institute of Technology, United States – Massachusetts, 2006.

[62] Brian J. Meers. Recycling in laser-interferometric gravitational-wave detectors. *Phys. Rev. D*, 38(8):2317–2326, 1988.

[63] C. M. Caves. Quantum-mechanical noise in an interferometer. *Phys. Rev. D*, 1981.

[64] V. B. Braginsky and F. Y. Khalily. Nonlinear meter for the gravitational wave antenna. *Physics Letters A*, 1996.

[65] V. B. Braginsky, M. L. Gorodetsky, and F. Y. Khalili. Optical bars in gravitational wave antennas. *Physics Letters A*, 1997.

[66] J. Hough, S. Rowan, and B. S. Sathyaprakash. The search for gravitational waves. *Journal of Physics B Atomic Molecular Physics*, 38:497–+, May 2005.

[67] N. A. Robertson, G. Cagnoli, D. R. M. Crooks, E. Elliffe, J. E. Faller, P. Fritschel, S. Goßler, A. Grant, A. Heptonstall, J. Hough, H. Lück, R. Mittleman, M. Perreur-Lloyd, M. V. Plissi, S. Rowan, D. H. Shoemaker, P. H. Sneddon, K. A. Strain, C. I. Torrie, H. Ward, and P. Willems. Quadruple suspension design for Advanced LIGO. *Classical and Quantum Gravity*, 19:4043–4058, 2002.

[68] P. R. Saulson. Terrestrial gravitational noise on a gravitational wave antenna. *Phys. Rev. D*, 1984.

[69] K. Kuroda and the LCGT Collaboration. The status of LCGT. *Classical and Quantum Gravity*, 23:215, 2006.

[70] V. B. Braginsky, M. L. Gorodetsky, and S. P. Vyatchanin. Thermo-refractive noise in gravitational wave antennae. *Physics Letters A*, 271:303–307, 2000.

[71] GEO600 sensitivity curves http://www.geo600.uni-hannover.de/geocurves/.

[72] R. G. Beausoleil, E. K. Gustafson, M. M. Fejer, E. D'Ambrosio, W. Kells, and J. Camp. Model of thermal wave-front distortion in interferometric gravitational- wave detectors. I. Thermal focusing. *Journal of the Optical Society of America B Optical Physics*, 2003.

[73] R. Lawrence, D. Ottaway, M. Zucker, and P. Fritschel. Active correction of thermal lensing through external radiative thermal actuation. *Optics Letters*, 2004.

[74] G. González. Suspensions thermal noise in the LIGO gravitational wave detector. *Classical and Quantum Gravity*, 17:4409–4435, 2000.

[75] B. C. Barish. The Laser Interferometer Gravitational-Wave Observatory LIGO. *Advances in Space Research*, 25:1165–1169, 2000.

[76] LIGO laboratory homepage for interferometer sensitivities http://www.ligo.caltech.edu/∼jzweizig/distribution/lsc_data/.

[77] B. Wilke *et. al.* The GEO 600 gravitational wave detector . *Classical and Quantum Gravity*, 19:1377–1387, 2002.

[78] J. R. Smith, G. Cagnoli, D. R. M. Crooks, M. M. Fejer, S. Goßler, H. Lück, S. Rowan, J. Hough, and K. Danzmann. Mechanical quality factor measurements of monolithically suspended fused silica test masses of the GEO 600 gravitational wave detector. *Classical and Quantum Gravity*, 2004.

[79] F. Acernese *et. al.* The status of VIRGO. *Classical and Quantum Gravity*, 23:63, 2006.

[80] F. Acernese *et. al.* The VIRGO interferometric gravitational antenna. *Optics and Lasers in Engineering*, 45:478–487, 2007.

[81] S. Braccini *et. al.* Measurement of the seismic attenuation performance of the VIRGO Superattenuator. *Astroparticle Physics*, 23:557–565, 2005.

[82] General status of the VIRGO interferometer http://wwwcascina.virgo.infn.it/monitoringweb/general/.

[83] D. Tatsumi, R. Takahashi, K. Arai, N. Nakagawa, K. Agatsuma, T. Yamazaki, M. Fukushima, M.-K. Fujimoto, A. Takamori, A. Bertolini, V. Sannibale, R. DeSalvo, S. Marka, M. Ando, K. Tsubono, T. Akutsu, K. Yamamoto, H. Ishitsuka, T. Uchiyama, S. Miyoki, M. Ohashi, K. Kuroda, N. Awaya, N. Kanda, A. Araya, S. Telada, T. Tomaru, T. Haruyama, A. Yamamoto, N. Sato, T. Suzuki, and T. Shintomi. Current status of Japanese detectors. *ArXiv e-prints*, 704, 2007.

[84] S. J. Waldman and the LIGO Science Collaboration. Status of LIGO at the start of the fifth science run. *Classical and Quantum Gravity*, 2006.

[85] S. Waldman R. Adhikari, P. Fritschel. Enhanced LIGO http://www.ligo.caltech.edu/docs/t/t060156-01.pdf. Technical Note, 2006.

[86] Advanced LIGO http://www.ligo.caltech.edu/advligo/.

[87] G. Cagnoli, H. Armandula, C. A. Cantley, D. R. M. Crooks, A. Cumming, E. Elliffe, M. M. Fejer, A. M. Gretarsson, G. M. Harry, A. Heptonstall, J. Hough, R. Jones, J. M. Mackowski, I. Martin, P. Murray, S. D. Penn, M. Perreur-Lloyd, S. Reid, R. Route, S. Rowan, N. A. Robertson, P. H. Sneddon, and K. A. Strain. Silica suspension and coating developments for Advanced LIGO. *Journal of Physics: Conference Series*, 32:386–392, 2006.

[88] Advanced VIRGO http://wwwcascina.virgo.infn.it/advirgo/.

[89] B. Willke *et. al.* The GEO-HF project. *Classical and Quantum Gravity*, 23:207, 2006.

[90] R. Schnabel, J. Harms, K. A. Strain, and K. Danzmann. Squeezed light for the interferometric detection of high-frequency gravitational waves. *Classical and Quantum Gravity*, 21:1045, 2004.

[91] H. Lueck. Plans for E.T. (Einstein Telescope). presentation at the AMALDI 7 conference, 2007.

[92] G. C. Cagnoli. R&D on thermal noise in Europe: the Strega Project. *Journal of Physics Conference Series*, 2006.

[93] European Space Agency ESA-SCI (2000) 11. Laser Interferometer Space Antenna: A cornerstone mission for the observation of gravitational waves. System and Technology report, 2000.

[94] Laser Interferometer Space Antenna http://lisa.nasa.gov/gallery/lisa-waves.html.

[95] B. Jancovici. *Statistical Physics and Thermodynamics.* McGrawHill Book Company Limited, 1973.

[96] R. Brown. A brief account of microscopical observations made in the months of June, July and August, 1827, on the particles contained in the pollen of plants; and on the general existence of active molecules in organic and inorganic bodies. *Edinburgh new Philosophical Journal*, pages 358–371, 1828.

[97] A. Einstein. Über die von der molekularkinetischen Theorie der Wärme geforderte Bewegung von in ruhenden Flüssigkeiten suspendierten Teilchen. *Annalen der Physik*, 17:549, 1905.

[98] A. Einstein. *Investigations on the theory of the* B*rownian movement.* Dover, 1956.

[99] H. B. Callen and T. A. Welton. Irreversibility and Generalized Noise. *Physical Review*, 83:34–40, 1951.

[100] H. B. Callen and R. F. Greene. On a Theorem of Irreversible Thermodynamics. *Physical Review*, 86:702–710, 1952.

[101] Y. L. Huang and Peter R. Saulson. Dissipation mechanisms in pendulums and their implications for gravitational wave interferometers. *Review of Scientific Instruments*, 69(2):544–553, 1998.

[102] B.S. Berry A.S. Nowick. *Anelastic Relaxation in Crystalline Solids,.* Academic Press, New York and London, 1972.

[103] P. R. Saulson. Thermal noise in mechanical experiments. *Phys. Rev. D*, 42:2437–2445, 1990.

[104] P. H. Sneddon. *Investigations of Internal Mechanical Loss Factors of Test Mass Materials for Interferometric Gravitational Wave Detectors.* PhD Thesis, University of Glasgow, 2001.

[105] K. Numata, S. Otsuka, M. Ando, and K. Tsubono. Intrinsic losses in various kinds of fused silica . *Classical and Quantum Gravity*, 19:1697–1702, 2002.

[106] D. Busby P. Willems. Report to the April 25th 2003 Core Optics Down-select committee meeting, http://www.ligo.caltech.edu/docs/t/t030087-00.pdf.

[107] S. Penn. Lowering mechanical loss in fused silica optics with annealing, http://www.ligo.caltech.edu/docs/g/g040160-00/g040160-00.ppt.

[108] K. Yamamoto. *Study of the thermal noise caise by inhomogeneously distributed loss*. PhD thesis, University of Tokyo, 2000.

[109] Y. Levin. Internal thermal noise in the LIGO test masses: A direct approach. *Phys. Rev. D*, 57:659–663, 1998.

[110] Y. T. Liu and K. S. Thorne. Thermoelastic noise and homogeneous thermal noise in finite sized gravitational-wave test masses. *Phys. Rev. D*, 2000.

[111] D. R. M. Crooks. *Mechanical Loss and its Significance in Test Mass Mirrors of Gravitational Wave Detectors*. PhD thesis, University of Glasgow, 2003.

[112] V. B. Braginsky, M. L. Gorodetsky, and S. P. Vyatchanin. Thermodynamical fluctuations and photo-thermal shot noise in gravitational wave antennae. *Physics Letters A*, 1999.

[113] N. Nakagawa, E. K. Gustafson, P. T. Beyersdorf, and M. M. Fejer. Estimating the off resonance thermal noise in mirrors, Fabry-Perot interferometers, and delay lines: The half infinite mirror with uniform loss. *Phys. Rev. D*, 2002.

[114] S. D. Penn, P. H. Sneddon, H. Armandula, J. C. Betzwieser, G. Cagnoli, J. Camp, D. R. M. Crooks, M. M. Fejer, A. M. Gretarsson, G. M. Harry, J. Hough, S. E. Kittelberger, M. J. Mortonson, R. Route, S. Rowan, and C. C. Vassiliou. Mechanical loss in tantala/silica dielectric mirror coatings. *Classical and Quantum Gravity*, 20:2917–2928, 2003.

[115] G. M. Harry, A. M. Gretarsson, P. R. Saulson, S. E. Kittelberger, S. D. Penn, W. J. Startin, S. Rowan, M. M. Fejer, D. R. M. Crooks, G. Cagnoli, J. Hough, and N. Nakagawa. Thermal noise in interferometric gravitational wave detectors due to dielectric optical coatings. *Classical and Quantum Gravity*, 2002.

[116] G. M. Harry, H. Armandula, E. Black, D. R. M. Crooks, G. Cagnoli, J. Hough, P. Murray, S. Reid, S. Rowan, P. Sneddon, M. M. Fejer, R. Route, and S. D. Penn. Thermal noise from optical coatings in gravitational wave detectors. *Applied Optics*, 2006.

[117] M. M. Fejer, S. Rowan, G. Cagnoli, D. R. Crooks, A. Gretarsson, G. M. Harry, J. Hough, S. D. Penn, P. H. Sneddon, and S. P. Vyatchanin. Thermoelastic dissipation in inhomogeneous media: loss measurements and displacement noise in coated test masses for interferometric gravitational wave detectors. *Phys. Rev. D*, 2004.

[118] E. D. Black, A. Villar, and K. G. Libbrecht. Thermoelastic-Damping Noise from Sapphire Mirrors in a Fundamental-Noise-Limited Interferometer. *Physical Review Letters*, 2004.

[119] P. R. Saulson. Thermal noise in mechanical experiments. *Phys. Rev. D*, 1990.

[120] J. E. Logan, J. Hough, and N. A. Robertson. Aspects of the thermal motion of a mass suspended as a pendulum by wires. *Physics Letters A*, 1993.

[121] S. Mukherjee and L. S. Finn. Removing Instrumental Artifacts: Suspension Violin Modes. In S. Meshkov, editor, *American Institute of Physics Conference Series*, volume 523 of *American Institute of Physics Conference Series*, page 362, 2000.

[122] S. Rowan, J. Hough, and D. R. M. Crooks. Thermal noise and material issues for gravitational wave detectors [rapid communication]. *Physics Letters A*, 2005.

[123] W. A. Edelstein, J. Hough, J. R. Pugh, and W. Martin. Limits to the measurement of displacement in an interferometric gravitational radiation detector. *Journal of Physics E Scientific Instruments*, 11:710–712, 1978.

[124] W. Winkler, K. Danzmann, A. Rüdiger, and R. Schilling. Heating by optical absorption and the performance of interferometric gravitational-wave detectors. *Phys. Rev. A*, 44:7022–7036, 1991.

[125] V. I. Panovo V. B. Brasinsky, V. P. Mitrafanov. *Systems with Small Dissipations*. University of Chicago Press, 1986.

[126] S. Rowan, S. M. Twyford, R. Hutchins, J. Kovalik, J. E. Logan, A. C. McLaren, N. A. Robertson, and J. Hough. Q factor measurements on prototype fused quartz pendulum suspensions for use in gravitational wave detectors. *Physics Letters A*, 233:303–308, 1997.

[127] S. Rowan, S. M. Twyford, J. Hough, D.-H. Gwo, and R. Route. Mechanical losses associated with the technique of hydroxide-catalysis bonding of fused silica. *Physics Letters A*, 246:471–478, 1998.

[128] D. R. M. Crooks, P. Sneddon, G. Cagnoli, J. Hough, S. Rowan, M. M. Fejer, E. Gustafson, R. Route, N. Nakagawa, D. Coyne, G. M. Harry, and A. M. Gretarsson. Excess mechanical loss associated with dielectric mirror coatings on test masses in interferometric gravitational wave detectors . *Classical and Quantum Gravity*, 19:883–896, 2002.

[129] LIGO Scientific Collaboration. Test Mass Material Down-select Plan, http://ligo.caltech.edu/∼gari/ligoii/downselect/index.html.

[130] H. J. Pain. *The Physics of Waves and Vibrations 5th Edition*. J. Wiley and Sons, 1998.

[131] NI labVIEW website http://www.ni.com/labview/.

[132] ANSYS, Inc. Corporate Homepage http://www.ansys.com.

[133] G. W. McMahon. Experimental study of vibrations of solid, isotropic, elastic cylinders. *Journal of Accoustical Society of America*, 36:85–92, 1964.

[134] A. P. French. *Vibrations and Waves, M. I. T. Introductory Physics Series*. Van Nostrand International, 1965.

[135] D. R. M. Crooks, P. Sneddon, G. Cagnoli, J. Hough, S. Rowan, M. M. Fejer, E. Gustafson, R. Route, N. Nakagawa, D. Coyne, G. M. Harry, and A. M. Gretarsson. Excess mechanical loss associated with dielectric mirror coatings on test masses in interferometric gravitational wave detectors . *Classical and Quantum Gravity*, 2002.

[136] K. Srinivasan. Coating strain induced distortion in LIGO optics LIGO document number: LIGO-T970176-00-D. 1997.

[137] D. R. M. Crooks, G. Cagnoli, M. M. Fejer, A. Gretarsson, G. Harry, J. Hough, N. Nakagawa, S. Penn, R. Route, S. Rowan, and P. H. Sneddon. Experimental measurements of coating mechanical loss factors. *Classical and Quantum Gravity*, 2004.

[138] Laboratoire des Matériaux Avancés http://lma.in2p3.fr/lmagb.htm.

[139] S. Tamura. Empirical correlations between the compressibility and the atomic radius or the cohesive energy for elements. *Journal of Materials Science Letters*, 18(21):1753–1754, 1999.

[140] G. Harry. Thermal noise from optical coatings, http://www.ligo.caltech.edu/docs/g/g030337-00/g030337-00.pdf, 2003.

[141] D. J. Sharp, J. K. G. Panitz, and D. M. Mattox. Applications of a kaufman ion source to low energy ion erosion studies. *Journal of Vacuum Science and Technology*, 16(6):1879–1882, 1979.

[142] SSP research Summary http://www.ssp.gla.ac.uk/ressum/nanocharacterisation.htm.

[143] G. M. Harry, M. R. Abernathy, A. E. Becerra-Toledo, H. Armandula, E. Black, K. Dooley, M. Eichenfield, C. Nwabugwu, A. Villar, D. R. M. Crooks, G. Cagnoli, J. Hough, C. R. How, I. MacLaren, P. Murray, S. Reid, S. Rowan, P. H. Sneddon, M. M. Fejer, R. Route, S. D. Penn, P. Ganau, J.-M. Mackowski,

C. Michel, L. Pinard, and A. Remillieux. Titania-doped tantala/silica coatings for gravitational-wave detection. *Classical and Quantum Gravity*, 2007.

[144] CSIRO Materials Science and Engineering http://www.tip.csiro.au/imp/optical/coatingsindex.htm.

[145] M. Gross. Private communication, 2007.

[146] M. E. Wieser. Atomic weights of the elements 2005. *Pure Appl. Chem.*, 78(11):20512066, 2006.

[147] M.S.W. Vong Y. Sun and P.A. Sermon. Sol-gel chemistry of tantala HR coatings: Structure and laser-damage resistance. *Journal of Sol-Gel Science and Technolog*, 8:493–497, 1997.

[148] D. Roberts T. Remmel M. Raymond E. Luckowski S. Kalpat C. Barron R. Ramprasad, M. Sadd and M. Miller. Oxygen vacancy defects in tantalum pentoxide: a density functional study. *Microelectronic Engineering*, 69:190–194, 2003.

[149] J.-Y. Zhang, I. W. Boyd, V. Dusastre, and D. E. Williams. RAPID COMMUNICATION: Ultraviolet annealing of tantalum oxide films grown by photo-induced chemical vapour deposition. *Journal of Physics D Applied Physics*, 1999.

[150] M.-P. Houng, Y.-H. Wang, J.-H. Horng, and R.-C. Huang. Effects of Annealing on Tantalum Pentoxide Films in N_2 and N_2O Gas Environments. *Japanese Journal of Applied Physics*, 2001.

[151] Photoelectron Spectroscopy http://www.chem.qmul.ac.uk/surfaces/scc/scat5_3.htm.

[152] G. Harry. Coating project update www.ligo.caltech.edu/docs/g/g060384-00/g060384-00.pdf, 2006.

[153] G. Harry. Ligo coating project www.ligo.caltech.edu/docs/g/g060504-00/g060504-00.pdf, 2006.

[154] H. Armandula. Private communication.

[155] S. Rowan, S. M. Twyford, J. Hough, D.-H. Gwo, and R. Route. Mechanical losses associated with the technique of hydroxide-catalysis bonding of fused silica. *Physics Letters A*, 246:471–478, 1998.

[156] D. H. Gwo. Ultraprecision bonding for cryogenic fused-silica optics. In J. B. Heaney and L. G. Burriesci, editors, *Proc. SPIE Vol. 3435, p. 136-142, Cryogenic Optical Systems and Instruments VIII, James B. Heaney; Lawrence G. Burriesci; Eds.*, volume 3435 of *Presented at the Society of Photo-Optical Instrumentation Engineers (SPIE) Conference*, pages 136–142, 1998.

[157] D. H. Gwo. Hydroxide-catalyzed bonding, united states patent no. us 6,548,176 b1, 2003.

[158] J. Mester, S. Buchman, A. M. Cruise, D. Debra, H. Dittus, C. W. F. Everitt, B. Foulon, G. M. Keiser, B. J. Kent, J. Lipa, N. Lockerbie, J. M. Lockhart, F. Loeffler, B. Muhlfelder, B. Parkinson, C. Pegrum, M. Sandford, C. C. Speake, T. J. Sumner, M. Taber, R. Torii, P. Touboul, J. Turneaure, S. Vitale, W. Vodel, and P. W. Worden. Gravitational Experiments in Space: Gravity Probe B and STEP. *Nuclear Physics B Proceedings Supplements*, 134:147–154, 2004.

[159] E. J. Elliffe, J. Bogenstahl, A. Deshpande, J. Hough, C. Killow, S. Reid, D. Robertson, S. Rowan, H. Ward, and G. Cagnoli. Hydroxide-catalysis bonding for stable optical systems for space. *Classical and Quantum Gravity*, 22:257, 2005.

[160] E. J. Elliffe. *Aspects of Thermal Noise Modeling in Ground-based Gravitational Wave Detectors and Developments of Hydroxide Catalysis Bonding for Space-based Gravitational Wave Detectors and other Optical Applications*. PhD Thesis, University of Glasgow, 2005.

[161] S. Reid, G. Cagnoli, E. Elliffe, J. Faller, J. Hough, I. Martin, and S. Rowan. Influence of temperature and hydroxide concentration on the settling time of hydroxy-catalysis bonds. *Physics Letters A*, 363:341–345, 2007.

[162] R. K. Iler. *The chemistry of silica*. John Wiley and Sons, New York, 1979.

[163] J. A. Lier, P. L. De Bruyn, and J. T. Overbeek. The solubility of quartz. *Journal of Physical Chemistry*, 64:1675–1682, 1960.

[164] S. Reid. *Studies of materials for future ground-based and space-based interferometric gravitational wave detectors*. PhD Thesis, University of Glasgow, 2006.

[165] J. Gwo. Private communication.

[166] Welcome to Corning Speciality Materials www.corning.com/specialtymaterials/.

[167] Heraeus Quartz America, LLC: Heraeus Optics Products http://www.heraeusoptics.com/products/p_productsoptics.cfm.

[168] K. Numata, K. Yamamoto, H. Ishimoto, S. Otsuka, K. Kawabe, M. Ando, and K. Tsubono. Systematic measurement of the intrinsic losses in various kinds of bulk fused silica. *Physics Letters A*, 327:263–271, 2004.

[169] A. M. Gretarsson. *Thermal noise in low loss flexures*. PhD thesis, Syracuse University, 2002.

[170] A. Ageev, B. C. Palmer, A. De Felice, S. D. Penn, and P. R. Saulson. Very high quality factor measured in annealed fused silica. *Classical and Quantum Gravity*, 21:3887–3892, 2004.

[171] S. D. Penn, G. M. Harry, A. M. Gretarsson, S. E. Kittelberger, P. R. Saulson, J. J. Schiller, J. R. Smith, and S. O. Swords. High quality factor measured in fused silica. *Review of Scientific Instruments*, 72:3670–3673, 2001.

[172] A. M. Gretarsson and G. M. Harry. Dissipation of mechanical energy in fused silica fibers. *Review of Scientific Instruments*, 70:4081–4087, 1999.

[173] S. D. Penn, A. Ageev, D. Busby, G. M. Harry, A. M. Gretarsson, K. Numata, and P. Willems. Frequency and surface dependence of the mechanical loss in fused silica. *Physics Letters A*, 352:3–6, 2006.

[174] J. Wiedersich, S. V. Adichtchev, and E. Rössler. Spectral Shape of Relaxations in Silica Glass. *Physical Review Letters*, 84:2718–2721, 2000.

[175] H. Armandula. Silicate bonding procedure (hydroxide-catalysis bonding), http://www.ligo.caltech.edu/docs/e/e050228-00.pdf.

[176] General Optics: A world of ultra precision optics http://www.generaloptics.com/.

[177] Model 15 Diamond Wire & Disc Saw http://www.logitech.uk.com/mod15.asp.

[178] Hitachi Tabletop Microscope TM-1000 http://www.hht-eu.com/pls/hht/wt_show.text_page?p_text_id=7929.

[179] PM5 Precision Lapping and Polishing Machine http://www.logitech.uk.com/pm5.asp.

[180] Focused Ion Beam (FIB) System http://www.knc.gla.ac.uk/FIB.htm.

[181] Kelvin Nanocharacterisation Centre http://www.knc.gla.ac.uk.

[182] Atomic force microscopy http://www.nanoscience.com/education/AFM.html.

[183] The new nanaoanalytical TEM facility http://www.knc.gla.ac.uk/TEMNanoanalysis.htm.

[184] H. Armandula, C. A. Cantley, and S. Rowan. Bonding and visual inspection of preliminary test ears (serial numbers 0005, 0006, 0015 and 0016), http://www.ligo.caltech.edu/docs/t/t050210-00.pdf.

[185] ANSYS Inc. ANSYS academic research release v. 11.0. documentation for ANSYS, help system, BEAM189.

[186] ANSYS inc. ANSYS academic research release v. 11.0. documentation for ANSYS, help system, SOLID95.

[187] P. G. Murray. Finite element analysis of the strain energy stored in hydroxide-catalysis bonded fused silica samples, http://www.physics.gla.ac.uk/∼pmurray/presentations.html.

[188] V.S. Shiyan V.P. Mitrofanov. *Kristallografiya*, 24:307, 1979.

[189] Crystal Systems - HEM - Heat Exchanger Method http://www.crysys.com/hem.html.

[190] S. Rowan, G. Cagnoli, P. Sneddon, J. Hough, R. Route, E. K. Gustafson, M. M. Fejer, and V. Mitrofanov. Investigation of mechanical loss factors of some candidate materials for the test masses of gravitational wave detectors. *Physics Letters A*, 265:5–11, 2000.

[191] Crystal Systems, Inc. http://www.crysys.com/.

[192] G. Harry. Material downselect: Rationale and directions, LIGO doc. g050088-00-r. LSC Meeting LLO, 2005.

[193] Gregg Harry Bill Kells Helena Armandula, GariLynn Billingsley. Core optics components conceptual design document, ligo doc no. t000098-02-d. Technical report, LIGO Scientific Collaboration, 2004.

[194] D. E. McClelland, D. G. Blair, and R. J. Sandeman. AIGO: A Southern Hemisphere Second Generation Gravitational Wave Observatory. In R. T. Jantzen, G. Mac Keiser, and R. Ruffini, editors, *Proceedings of the Seventh Marcel Grossman Meeting on recent developments in theoretical and experimental general relativity, gravitation, and relativistic field theories*, page 1415, 1996.

[195] B. A. Auld. *Acoustic Fieds and Waves in Solids*, volume 1. John Wiley and Sons, 1973.

[196] A. Long (University of Glasgow). Private communication.

[197] Super Polishing Crystals
http://www.acpo.csiro.au/superpolishing.htm.

[198] Precision Spheres for GP-B Experiment
http://einstein.stanford.edu/content/topics/pg4.html.

[199] M. R. Kozlowski, J. Carr, I. D. Hutcheon, R. Torres, L. M. Sheehan, D. W. Camp, and M. Yan. Depth profiling of polishing-induced contamination on fused silica surfaces. In G. J. Exarhos, A. H. Guenther, M. R. Kozlowski, and M. J. Soileau, editors, *Proc. SPIE Vol. 3244, p. 365-375, Laser-Induced Damage in Optical Materials: 1997, Gregory J. Exarhos; Arthur H. Guenther; Mark R. Kozlowski; M. J. Soileau; Eds.*, volume 3244 of *Presented at the Society of Photo-Optical Instrumentation Engineers (SPIE) Conference*, pages 365–375, 1998.

[200] D. Crooks. Private communication.

[201] R. Lawrence, M. Zucker, P. Fritschel, P. Marfuta, and D. Shoemaker. Adaptive thermal compensation of test masses in advanced LIGO . *Classical and Quantum Gravity*, 19:1803–1812, 2002.

[202] C. C. Lam *et. al.* D. F. McGuigan. Measurements of the mechanical Q of single-crystal silicon at low temperature. *Journal of Low Temperature Physics*, 30:621, 1978.

[203] K. Tsubono. Measurement of the mechanical loss of crystalline samples using a nodal support. *Physics Letters A*, 284:162–171, 2001.

[204] Y. S. Touloukian and C. Y. Ho. *Thermal conductivity. Nonmetallic solids.* Thermophysical properties of matter - The TPRC Data Series, New York: IFI/Plenum, 1970 -, edited by Touloukian, Y.S. —e(series ed.); Ho, C.Y. —e(series tech.ed.), 1970.

[205] Y. S. Touloukian and C. Y. Ho. *Thermal expansion. Nonmetallic solids.* Thermophysical properties of matter - The TPRC Data Series, New York:

IFI/Plenum, 1970 -, edited by Touloukian, Y.S. —e(series ed.); Ho, C.Y. —e(series tech.ed.), 1970.

[206] P. Beyersdorf R. Schnabel A. Bunkowski, O. Burmeister and K. Danzmann. All-reflective optics for gravitational wave detectors
ligo-dcc no: Ligo-g040386-00-z. LSC-Meeting, Hanford Observatory, 2004.

[207] Prolog Semicor Ltd
http://www.semicor.ukrpack.net/.

[208] SPANOPTIC MRF finishing services
http://www.spanoptic.com/mrf.php.

[209] V. P. Mitrafanov. Private communication.

[210] LCGT Collaborations. Large scale cryogenic gravitational wave telescope. *Nuclear Physics B Proceedings Supplements*, 138:439–442, 2005.

[211] S. Rowan, R. L. Byer, M. M. Fejer, R. K. Route, G. Cagnoli, D. R. Crooks, J. Hough, P. H. Sneddon, and W. Winkler. Test mass materials for a new generation of gravitational wave detectors. In M. Cruise and P. Saulson, editors, *Gravitational-Wave Detection. Edited by Cruise, Mike; Saulson, Peter. Proceedings of the SPIE, Volume 4856, pp. 292-297 (2003).*, volume 4856 of *Presented at the Society of Photo-Optical Instrumentation Engineers (SPIE) Conference*, pages 292–297, 2003.

[212] A. Giazotto and G. Cella. Some considerations about future interferometric GW detectors. *Classical and Quantum Gravity*, 21:1183, 2004.

[213] S. Reid, G. Cagnoli, D. R. M. Crooks, J. Hough, P. Murray, S. Rowan, M. M. Fejer, R. Route, and S. Zappe. Mechanical dissipation in silicon flexures. *Physics Letters A*, 351:205–211, 2006.

[214] S. Nietzsche, R. Nawrodt, A. Zimmer, M. Thürk, W. Vodel, and P. Seidel. Cryogenic Q-factor measurement of optical substrate materials. *Journal of Physics Conference Series*, 2006.

[215] AS Scientific Products Ltd.
http://www.asscientific.co.uk.